Toward Real-time Earth Observation with Satellite Constellation Crosslinks and Propulsion

by
Manwei Chan
B.S., Johns Hopkins University (2016)
M.A., Johns Hopkins University (2016)
S.M., Massachusetts Institute of Technology (2019)

Submitted to the Department of Aeronautics and Astronautics
in partial fulfillment of the requirements for the degree of
Doctor of Philosophy in Aeronautics and Astronautics
at the
MASSACHUSETTS INSTITUTE OF TECHNOLOGY
February 2024

Author .....
Department of Aeronautics and Astronautics
September 5th, 2023

Certified by .....
Olivier De Weck
Professor of Astronautics and Engineering Systems, MIT
Thesis Supervisor

Certified by .....
Kerri Cahoy
Professor of Aeronautics and Astronautics, MIT
Thesis Supervisor

Certified by .....
Alessandro Golkar
Full Professor, Technical University of Munich
Thesis Supervisor

Accepted by .....
Jonathan How
Chair, Graduate Committee

Toward Real-time Earth Observation with Satellite Constellation Crosslinks and Propulsion

by

Manwei Chan

Submitted to the Department of Aeronautics and Astronautics
on September 5th, 2023, in partial fulfillment of the
requirements for the degree of
Doctor of Philosophy in Aeronautics and Astronautics

Abstract

The development of remote sensing small satellite constellations has created the potential for high-resolution Earth-observation data to reach end users faster. This work investigates how propulsion and intersatellite links enable constellations to continuously collect and deliver data faster than constellations without these capabilities.

This work has four contributions. The first contribution is a constellation simulation framework that is based on open-source libraries. This simulation framework can propagate satellites and execute propulsive maneuvers. The second contribution is a planning and scheduling algorithm for propulsive maneuvers, target observation times, and optimal data routing paths. The third contribution is the development of high performance constellation designs with respect to constellation cost and the following metrics: age of information, system response time, and total pass time. The cost model is developed from two separate models: the Small Satellite Cost Model (SSCM) and a launch cost model developed in this work. The fourth contribution is a set of cost-estimating relationships (CERs) that models the trade-off between cost and system performance in terms of the aforementioned metrics.

The new simulation framework of contribution 1 is verified against the industry-standard software Systems Tool Kit (STK). The simulation framework is used to run 21 different constellation designs, 3 different satellite models, and 432 distinct ground targets. These scenarios are run during each of the four seasons to eliminate geometric biases for a total of 108,864 individual scenario simulations. A single satellite executing the reconfiguration algorithm produces up to a 125% increase in pass time over seven days when compared to an identical satellite without propulsive capabilities. For an access cone with a nadir half-angle of 20°, the reconfiguration algorithm produces a 67% increase in pass time. Comparing the cost of inter-satellite link (ISL) and reconfiguration-capable satellites versus (i) only ISL-capable satellites and (ii) a baseline satellite without ISL or reconfigurable capabilities, a Pareto optimal analysis revealed 29% of designs had both propulsion and intersatellite link capabilities when optimizing for age of information, 7% of designs had both propulsion and intersatellite link capabilities when optimizing for system response time, and 33% of

designs had both propulsion and intersatellite link capabilities when optimizing for total pass time. The CERs show that for constellations costing between $150M and $1B (FY24), age of information can be reduced by 32 seconds for every million dollars spent, system response time can be reduced by 35 seconds for every million dollars spent, and total pass time over 3 days can be increased by 2 seconds for every million dollars spent.

Thesis Supervisor: Olivier De Weck
Title: Professor of Astronautics and Engineering Systems, MIT

Thesis Supervisor: Kerri Cahoy
Title: Professor of Aeronautics and Astronautics, MIT

Thesis Supervisor: Alessandro Golkar
Title: Full Professor, Technical University of Munich

Acknowledgments

The author would like to acknowledge several colleagues and mentors for their contributions to this work. Thesis committee members, Oli de Weck, for his overall support and guidance, Kerri Cahoy, for her technical expertise and direction, and Alessandro Golkar, for providing core structural and creative ideas in this work. Thanks to all the members of the MIT community, especially members of both STARLAB and the Engineering Systems Lab who defined my PhD experience through academic exchanges and extracurricular excursions. This thesis would also never have been finished without the support from the boys of Elm and Columbia Street. Lastly, as always, thanks to my family for always supporting me through my endeavors.

This work is supported by the National Science Foundation Graduate Research Fellowship (award numbers 1745302 and 2141064), Greg Wyler through Wafer/Wildstar/E-space, and the generous contributions of STARLAB (Kerri Cahoy) and the Engineering Systems Lab (Oli de Weck).

THIS PAGE INTENTIONALLY LEFT BLANK

Contents

THIS PAGE INTENTIONALLY LEFT BLANK

List of Figures

List of Tables

THIS PAGE INTENTIONALLY LEFT BLANK

Chapter 1

Introduction

1.1 Motivation

The advent of proliferated small satellite remote sensing constellations has enabled information to become more timely, which is defined as reducing the time between information request and the use of that information to inform a decision [5] [6] [7]. This work investigates methods to improve the timeliness of information, bringing information to end-users faster. Two metrics, age of information (AoI) and system response time (SRT), are helpful when describing a system's ability to deliver timely information. SRT defines how quickly the first useful data takes to get to an end-user while AoI measures the freshness of data over a period of time. In addition, the amount of data captured can be evaluated using the total pass time metric. A more in-depth discussion of these metrics can be found in Section 3.5.

Table 1.1 lists scenarios that benefit greatly when end-users receive timely information. For example, timely information after a disaster in a populated area provides situational awareness to first responders, such as information on potentially dangerous areas. Having imagery both before and after the event allows responders to assess damage, including critical infrastructure such as roads, bridges, energy grids (electrical, gas, and water), and medical facilities that will affect response and rescue plans [8]. Critical infrastructure is often localized, such as a power plant, and obtaining the status of such a facility may be access limited, such as by road and bridge damage.

The faster this information comes in, the more likely it is for responders to prevent secondary fires and flooding resulting from destroyed infrastructure [8].

Disasters in non-populated areas, such as oil spills, can also benefit from timely information. Traditionally, oil spill response utilize experienced airborne observers to recognize spatial patterns and distinguish between thin and thick oil.[1] However, the logistical concerns of getting an airborne observer to the desired location may be complex. Using satellite-based imagery would reduce the number of personnel needed to travel to the spill itself, reducing logistical time and costs.

In search and rescue scenarios such as the Malaysia Airline tragedy in 2014, timely data could have helped pinpoint the location of the event and narrow search areas for responders. When observing illegal activities, low SRT allows authorities to respond quickly so perpetrators do not have the time to change locations and evade capture. Similarly, lower AoI allows responders to monitor how disasters evolve, better monitor the movement of animals, or even monitor humans conducting illegal activities.

However, the unpredictability of disasters can make it difficult to provide timely data. For example, severe weather events such as tornadoes and flash floods can currently only be predicted a few hours out. Hurricanes often change paths unexpectedly [10]. Other events such as earthquakes and wildfires are also unpredictable, while disasters such as terrorist attacks or plane crashes cannot be predicted by the organizations responsible for response and rescue. With current satellite technology, the ability to provide timely data is dependent on pre-determined orbital dynamics as many satellites cannot currently alter their orbits to view a certain area on command. This work looks at methods to enable the capability to adjust satellite orbits as well as route data through a network of satellites in order to respond to disasters in a more timely way. Examples of the performance of current state of the art satellite systems can be found at the beginning of Section 3.5. Disasters are also very expensive, with tropical cyclones averaging $20.3B, wildfires averaging $6.2B, flooding averaging $4.7B, and severe storms averaging $2.3B per event [11]. While

[1]Thick oil is oil that is actionable, meaning it can be cleaned using booms and skimmers while thin oil cannot be cleaned with current technologies[9].

timely information will not be prevent all damage, it can help mitigate some costs and more importantly save lives.

Table 1.1: Selection of events that require responsive, remote sensing constellations.

Event	**Example**	**Need for timeliness**
Natural Disasters	Earthquake, tsunami, volcano, wildfire, flood, landslide, hurricanes	• Situational awareness for first responders • Damage assessment of critical infrastructure, homes, and businesses
Man-made disasters	Oil spills, Terrorist attacks (9/11), Malaysia airline crash	
Environmental monitoring	Illegal logging, illegal fishing, animal migrations	• Quick response to illegal activities • Animal tracking

Timely data is beneficial for environmental monitoring. Timely monitoring of illegal logging and fishing activities can help catch perpetrators before they leave the scene of their transgressions [12][13][14][15][16]. The ability to get images at particular places and times is paramount in these policing activities. Lastly, biologists can track the migrations of large populations of animals such as whales using high-resolution Earth observation (EO) satellites [17]. Having frequent passes on the order of hours or even days, allows for continual tracking of animal behaviors, and reduces the possibility of losing important migratory information [18].

Satellite based remote sensing systems have advantages over airborne remote sensing systems when responding to the scenarios in Table 1.1. Independence from local infrastructure allows satellite-based systems to always respond to disasters, which often compromise the support systems needed by ground and air-based remote sensing systems. Compared to air-based systems, satellite systems are independent from local airports, which can affect the responsiveness of aircraft and unmanned aerial vehicles (UAV) due to airport proximity and fueling needs. Ground-based sensing systems are dependent on local infrastructure, such as power availability and network

connection, both of which are vulnerable to the damage caused by disasters. Due to their higher altitude, satellites can also have greater command and communication ranges, allowing satellite operators to communicate with their assets from a location safely removed from the disaster. Satellite systems are also difficult to detect when overhead, and may be able to observe criminals more successfully than ground and air-based systems.

1.2 Background Capabilities

1.2.1 Low-Earth orbit constellations

Designers must consider the trade-off between orbital altitude and coverage. Given the same sensing payload, the payload at a higher altitude will have a larger ground footprint, allowing the payload to see a larger surface area. However, this design choice sacrifices spatial resolution in terms of ground sample distance. Constellations at lower altitudes, such as those in LEO, will have higher spatial resolution in their acquired images, but will require more satellites to achieve comparable coverage to higher altitude constellations. For the use cases detailed in Table 1.1, high-resolution imagery is necessary. The industry adoption of small satellites has allowed constellation designers to move into the space of proliferated low altitude remote sensing constellations as evidenced by ventures such as Planet and BlackSky [19] [20] [21]. One area of improvement for future LEO remote sensing constellations will be to make them more responsive and their data more timely. One approach to achieving this goal is to include two capabilities: intersatellite links and propulsion.

1.2.2 Intersatellite links

Traditionally, remote-sensing satellites collect data, and then the same satellite that collected the data downlinks the data to a ground station. The timeliness of this data is then dependent on when the satellite passes over a ground station. The inclusion of inter-satellite link (ISL) capabilities allows the satellite that collected the data to

transfer that data to another satellite that passes over a ground station earlier than the original satellite would have, reducing the lag between data collection and data downlink to the end-user.

An intersatellite link example is the original Iridium constellation, which consisted of 66 satellites at 781 km and an inclination of 86.4°. The constellation utilized continuous, in-plane intersatellite links to transmit voice and data globally [22] [23]. This capability has been expanded to include out-of-network satellites as studied by Claybrook and demonstrated by the PicoPanther satellite [24] [25]. Beyond Iridium, ISLs have been demonstrated with the Globalstar constellation with out-of-network satellites transferring data to the Globalstar network [26] [27]. It should be noted that the Globalstar satellites are bent-pipe repeaters and do not have ISL capabilities between Globalstar satellites. This work looks to build upon existing ISL technologies to develop a remote-sensing constellation that utilizes ISLs to deliver data more quickly.

1.2.3 Propulsion

Satellites do not necessarily have propulsion systems, but when they do, they can be used for a variety of purposes. For many satellites, propulsion is used for station-keeping: to counteract perturbative forces in order to stay in a desired orbit [28]. Satellites can also use propulsion to raise their orbits after launch insertion, like in the case of SpaceX's Starlink satellites [29] [30]. Recently, with the advent of satellite servicing missions such as Northrop Grumman's Mission Extension Vehicles, satellites can also use propulsion to conduct rendezvous and proximity operations [31]. This work investigates the use of propulsion to conduct reconfiguration maneuvers which move satellites in and out of repeat ground track (RGT) orbits through orbit raising and lowering in order to make satellite constellations more responsive.

1.3 Literature review

This work focuses on the planning, scheduling, and design of a reconfigurable and responsive satellite constellation for high-resolution (sub-meter ground resolved distance) monitoring of a particular ground location. The constellation design works in tandem with a planner and scheduler (see Section 4) to deliver low SRT and low AoI performance metrics (see Section 3.5). In order to achieve these metrics, constellation satellites are given defined roles as either observing or relay satellites. Relevant research references are split into three areas: (i) planning and scheduling, (ii) reconfigurable and responsive constellations, and (iii) multi-purpose and distributed systems. A selection of the most influential research with respect to this work are shown in Figure 1-1.

1.3.1 Reconfigurable constellations, responsive constellations, and constellation design

Reconfigurable systems can be changed repeatedly and reversibly in order to meet requirements or adapt to different operating conditions [32]. Satellites can be reconfigured in many ways, including retrofitting satellites with new components [33], reconfiguring constellations to accommodate a staged-launching strategy [34] [35], and right ascension of the ascending node (RAAN) phasing [36]. However, this work focuses on reconfiguration of satellite constellations to alter ground target coverage and ISL opportunities.

Reconfigurable constellations

In order to adjust constellation coverage, recent work on reconfigurable constellations focuses on moving satellites into RGT orbits to improve revisit times. In nominal operation, the reconfigurable satellites idle in a global observation mode (GOM) that provides global coverage. When an on-demand request is made, the satellites transition into RGT orbits to allow periodic revists in a regional observation mode (ROM). After completing an observation mission in ROM, the satellites return to GOM. Satel-

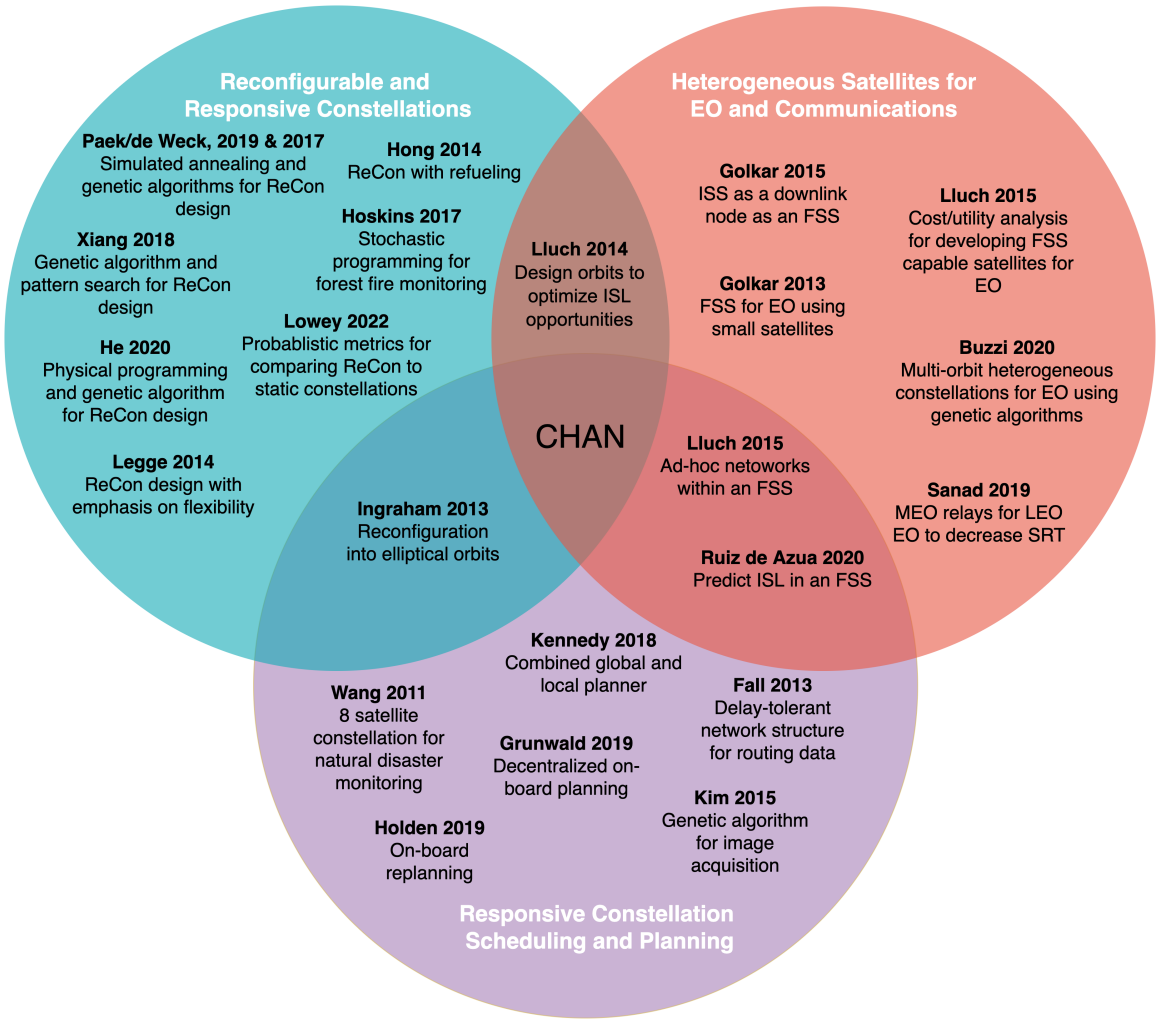

Figure 1-1: Literature review split into three main fields: planning and scheduling, reconfigurable constellations, and multi-purpose satellites. ReCon refers to the particular reconfiguration strategy of moving satellites into RGT orbits to improve revisit times.

lites return to GOM because GOM provides better staging orbits for moving into new RGT orbits.

RGT orbits are designed so that the combined effects of Earth's J2 perturbative effects with Earth's rotation generate ground tracks that repeat after an integer number of sidereal days. RGT orbits do not necessarily ensure short revisit times on the order of 1 or 2 days. For example, each LandSat satellite orbit has 16 day revisit periods [37]. This time can be decreased by phasing satellites within the same orbit, so the system comprised of LandSat 7 and 8 satellites would revisit ground locations every 8 days when phased 180 degrees apart in true anomaly.

A substantial amount of research has been conducted in designing RGT reconfiguration constellations, which are also referred to as ReCon. Legge's thesis presented a methodology to design, optimize, and operate reconfigurable satellite constellations [38]. Constellation designs are evaluated using the persistence metric, which incorporates utility based on ground sample distance and revisit time, with diminishing utility for revisiting an area too frequently. The investigation into optimal designs found that this methodology favored prograde orbits with an inclination of 60°. In terms of cost, reconfigurable constellations cost 20% to 70% less than similarly performing static (non-reconfigurable) constellations. Using the persistence metric, there is a diminishing increase in performance as the number of satellites in a constellation increases. The cost difference between a reconfigurable system and a static system drops from 27.5% to 12.2% as constellation designs increase from 36 to 60 total satellites. Legge's work demonstrates that 60° inclination constellations with fewer satellites provide the most utility per constellation cost for reconfigurable systems under the simulation environment in his thesis. Lowey's thesis compared reconfigurable constellations to static designs, finding that 74.2% of reconfigurable designs outperform their counterparts with a confidence level of 90% or higher [39]. Straub included additional considerations for designing reconfigurable constellations, including off-nadir targeting, different propulsion systems, and alternative launch strategies [40]. Straub found that using electric propulsion failed to reach 70% of the performance of chemical propulsion in reconfigurable constellations. Even just using electric propul-

sion to return to GOM was not deemed beneficial as the mass and power required to support an additional electric propulsion system outweighed the mass savings in fuel reduction. Morgan's research focused on using reconfigurable constellations to track mobile targets such as hurricanes [41].

Other researchers explored designing ReCon systems using Walker constellations with 60° inclination orbits. Paek and de Weck explored staged deployments for ReCon using a weighted-sum genetic algorithm [42]. Paek et al also compared finding optimal ReCon designs using a gradient based method, simulated annealing, and genetic algorithms to co-optimize satellite design and orbits, finding that the population based genetic algorithm performed best [43]. Their analysis produced two different designs using the genetic algorithm, one for a three-plane constellation and one for a five-plane constellation. The three-plane constellation had four satellites per plane and a sensor field of regard of 46.8° while the five-plane constellation had 2 satellites per plane and a field of regard of 47.1°. Both constellations were at 60° inclination, repeating their ground tracks once a day after 15 orbits.

Research in ReCon is not limited to 60° inclination Walker constellations. Hong et al studied constellation architectures utilizing sun-synchronous orbit (SSO) for disaster monitoring [44]. Their work included exploring the trade study involved with including on-orbit propellant depots in order to refuel their maneuvering satellites. He et al used a combination of both physical programming and a genetic algorithm to explore a case study of a constellation with 90° inclination orbits. Their optimization resulted in a 5 plane constellation at an altitude of 597 km, which was very close to a 90°:5/5/3 Walker [2] constellation [45]. Hoskins et al also looked at similar constellations for forest fire monitoring and used both a stochastic programming model and an accelerated L-shaped decomposition approach to design a reconfigurable satellite constellation, resulting in 5 satellites in evenly spaced orbital planes with an orbital period slightly above 15 revolutions around the Earth per day [46]. Yingguo et al developed a new self-adaptive variable-size multi-objective differential evolution algorithm to design their reconfigurable satellite system [47]. These works use coverage as

[2]Walker constellation notation details found in section 2.7

the guiding metric when designing reconfigurable constellations, and this work aims to build upon previous work by including intersatellite communication and downlink considerations in the design.

Responsive Constellations and Earth observation constellations

Researchers have investigated responsive constellations that can image an area quickly after being tasked. Wertz provided an overview of various responsive constellations including the elliptical Cobra Orbit, the critically inclined Magic Orbit, the more common sun-synchronous orbit (SSO), the Fast Access Orbit, and the Repeat Coverage Orbit [48]. Li et al propose a different circular orbit that revisits a ground target on consecutive ascending and descending portions of an orbit [49]. This allows one satellite to image a ground site with a revisit time close to 6 hrs between two pass opportunities, but generates a large temporal gap between revisit passes otherwise. Ingraham studied reconfiguring satellites from circular orbits to elliptical orbits, planning the maneuvers so that the perigee of the elliptical orbit is over the target ground location, offering higher spatial resolution imaging than if the satellite stayed in the higher circular orbit [50]. Over a ten day scenario, the ΔV cost for these missions was 1.2 km/s. Sengupta et al studied the maintenance cost of responsive orbits, presenting a semi-analytical approach technique to evaluate coverage and ΔV maintenance requirements [51][52].

In addition to special orbits, researchers investigated responsive designs of entire constellations. Xu et al propose a new constellation architecture that utilizes both J2 and J4 perturbations to fix the interval between successive revisits of ground sites at all latitudes, which they name Practical Time Resolution Constellations [53]. Xiang et al developed a constellation design tool using both genetic algorithms and a pattern search algorithm [54]. Their design rules incorporate responsive orbits using ground track adjustments to pass over targets that are otherwise unreachable. Using propulsion, each satellite has a reachable domain, which is a function of the true anomaly of the satellite within its orbital plane. Navabi took a different approach to responsive systems by studying how to choose ground stations, tackling the issue of data down-

link [55]. Hinds studied the Pareto frontier for 1 to 6 satellite Walker constellations for regional latitude coverage [56]. Grogan and Stern developed a platform to develop observing strategies at global and local scales using the concepts of co-simulation and service-oriented architectures [57]. The research in this work incorporates RGT orbits and communication requirements into the study of responsive constellations.

For generic design of Earth Observation satellites, Nag et al explored the design space for Earth Observation satellites using STK and MATLAB, describing the cost of the missions, and in particular looking at agile remote sensing Cubesats [58][59][60]. Singh et al researched 4-satellite constellations that utilize orbital perturbations that sacrifice coverage over certain latitudes in exchange for a 60% reduction in propellant mass budget for geostationary orbit (GEO) satellites [61]. Sugrue also researched tactical satellite systems to observe a small region on the Earth for military theater operations and targets [62]. Beyond Walker constellations, Mortari, Avendano, et al have looked into Flower constellations, which encompass Walker constellations and provide another mathematical method to describe constellation designs [63][64][65][66]. Krueger et al investigated a rapidly deployable Earth observation constellation using the Continuous Responsive Imaging System in Space (CRISIS) software to find that eight satellites at 600 km altitude in two perpendicular planes can satisfy both resolution (1 meter) and responsiveness (in-theater) requirements [67].

1.3.2 Planning and scheduling

Planning and scheduling for satellite constellations focus on improving the utilization of satellites by applying optimization methodologies [68]. These works primarily come in one of two areas. The first involves algorithms for network routing, enabling satellite constellations to downlink observing data through means such as ISLs, and the second involves algorithms designed to schedule image acquisition. This work will utilize elements from both of these areas.

Network routing

In 2003, Fall defined a Delay Tolerant Network architecture for networks in challenging environments where long delay paths and intermittent routing between network nodes cause performance degradation in traditional algorithms [69]. The challenging environment described by Fall is especially relevant in near-Earth satellite communications where orbital dynamics, terrain, and weather cause connectivity interruptions between Earth and space.

Satellite orbits are predictable to a certain degree. Kennedy devised a planner and scheduler for an Earth-Observing Small Satellite Constellation [70]. Kennedy tested the planner and scheduler on two different constellation architectures; The first consisted of 10 satellites in a singular SSO with a semi-major axis of 6978 km and three polar ground stations. The second consisted of 30 satellites in a 30°:30/3/1 Walker-Delta constellation also with a semi-major axis of 6978 km and nine ground stations distributed between ±30° latitude. Both scenarios included 40 observation targets scattered between ±30° latitude. Kennedy used mixed-integer linear programming (MILP) for both the centralized global planner and the distributed local planner. To evaluate the planner's performance in his simulations, Kennedy utilized the average AoI metric, a measure of information freshness defined by Kaul et al. [71] and also defined in Kennedy's thesis. In Kennedy's Walker scenario, the AoI was a little less than 2 hours, enabling timely updates of the ground sites in question. Kennedy's scenario also produced an average latency of about 10 minutes between the start of the simulation and the first 100 Mb of downloaded data. These metrics were enabled by the dense seeding of satellites and ground stations within a tight latitude band, which was necessary to test the power and data capacity limits of the constellation.

Grunwald built upon this work, introducing a decentralized Coupled Constraints Consensus Based Bundle Algorithm which improves computational run time by 94% and data downlink volume by 4% when compared to a centralized planner [72]. Holden also built upon this framework by implementing on-board replanning, reducing the penalties associated with arbitrary activity failures by a factor of 6 [73]. Yao et al in-

vestigated on-line task allocation strategies using a support vector machine [74]. This work differentiates itself by introducing propulsion into the planning and scheduling, as well as focusing on scenarios with few or singular ground sites of interests as opposed to multiple targets of interest.

There has also been substantial research on network and routing protocols within a Federated Satellite System (FSS) where individual satellites can share unused capacity like bandwidth to increase the overall performance of the system itself [75]. Lluch et al leveraged existing Mobile Ad-Hoc Network (MANET) techniques using Optimized Link State Routing (OLSR) and store-and-carry-forward Better Approach to Mobile Ad-Hoc Networking (BATMAN) routing to improve network latency from 41 minutes to 3.7 minutes in a 40 spacecraft FSS [76]. A series of papers by Ruiz de Azua and colleagues explores the Internet of Satellites (IoSat), a satellite network which does not use a common network interface to route data from source to destination, often using multiple hops [77] [78]. They also investigated predicting ISLs using linearized equations of relative motion to prepare satellites for data transfer [79] as well as crosslink and downlink opportunities to improve the performance of polar satellite EO missions using the OLSR protocol [80]. This line of research is also being tested through hardware on FSSCAT A and B, two 6U CubeSats launched in 2020 [81] [82]. The research presented in this work looks to build upon this work by predicting and creating ISL opportunities through propulsive phasing maneuvers.

Image Acquisition

The other subfield within planning and scheduling deals with optimizing image acquisition of target areas. Kim and Chang developed an optimal scheduler using a genetic algorithm to simulate imaging an area in Korea using four satellites in four planes at a 47° inclination orbit [83]. The satellites in the constellation had no propulsion but were able to image different areas of the target area by pointing their payload using attitude control. Kim also used system response time (SRT) as a figure of merit (FOM), calculating how long it would take for the constellation to receive an uplinked command, image the target area and downlink the corresponding data. However, Kim

did not simulate data transfer routes and timing for computational efficiency, instead using an expected uplink time to 10 minutes and downlink time to 1 hour and 50 minutes. For a 30 by 30 km ground target, SRT was 18 hours while for a 100 by 100 km target, SRT was 173 hours. Kim also utilized repeat coverage orbits (RCO), which are orbits with an inclination a few degrees higher than the ground target, to generate imaging opportunities on 4 to 5 consecutive overhead passes [48].

Other authors have pursued image acquisition planning with less of an emphasis on SRT, but focusing instead on various optimization techniques. Wang et al worked on tasking observation activities and download scheduling for disaster alert and environmental damage analysis, implementing a nonlinear model with a priority-based heuristic to generate task timetables [84]. Feng et al used support vector machines, a particular supervised learning model, to develop a cooperative planning system for autonomous satellite tasking [85]. Niu et al used a multi-objective genetic algorithm, non-dominated sorting genetic algorithm-II (NSGA-II), to plan satellite imaging of a large area to be used during the response phase of a natural disaster [86]. These works on image acquisition scheduling use satellites that have rotational pointing capabilities, but do not consider planning if the satellites have a propulsive capability. This work develops a scheduler for propulsion-enabled satellites as well as incorporates both data routing and image acquisition.

1.3.3 Heterogeneous and dual-use satellites for Earth observation and communications

Federated Satellite Systems

Early satellites were built with little to no compatibility with other satellites; however, recent works investigate the ability for satellite interaction. For example, FSS is a research area investigating ways to utilize unused capacity on satellites [87]. Golkar and Lluch studied using the International Space Station (ISS) as a data relay node, developing a business case where the ISS hosted an optical communications payload to service a market valued at millions of euros [88]. Lluch and Golkar also implemented

their FSS framework on 17 existing EO missions to find that the overall utility, which is heavily pegged to data throughput, can be increased by 8% at the cost of an additional 170 kg of communications equipment per mission [89]. To enable ISL within FSS, Lluch and Golkar studied an approach to launch satellites in orbit, maximizing satellite to satellite interaction opportunities with a previously established satellite constellation [90]. Akhtyamov et al. also looked into retrofitting satellites with equipment to incorporate them into an existing ISL network and running balloon experiments with software defined radios to prove feasibility [33][91].

Heterogeneous Orbits

Homogeneous satellite systems utilize similar satellites in orbits at the same inclination and altitude. Heterogeneous satellite systems combine the capabilities of spacecraft with different primary functions and are often placed in orbits with varying parameters. One of the most relevant works with respect to this work is by Sanad and Michelson [92] [93]. Their research investigates an approach to reduce SRT of LEO EO satellites by introducing a Medium Earth Orbit (MEO) relay constellation. Sanad and Michelson conducted two case studies, one with 4 satellites in SSO orbit at 600 km altitude and the second with 4 satellites at 45° inclination at 575 km. Both configurations used an optical sensor with a 40° field-of-view. The MEO relay consisted of 4 equatorial satellites at 8000 km altitude. Using this configuration, their simulation achieved a SRT between 8 and 26 hours. This work builds upon their work by including more than one ground station for downlink, including link budget communication constraints, and using ISLs to schedule and command satellite observing.

Li et al also use SRT to measure the performance of an EO system with Tracking and Data Relay Satellite System (TDRSS) as a communications relay [94]. Using a K-shortest path genetic algorithm to schedule data transmissions, Li et al scheduled data transmissions between 10 LEOsatellites, one TDRSS satellite, and 8 ground stations to achieve a SRT of a little over 0.5 hour. Others have also studied using heterogeneous orbits to improve constellation coverage. The communications constel-

lation explored by Chan et al consist of a backbone of LEO satellites in polar 780 km orbits [95]. A set of elliptical RGT orbits supplement the LEO backbone to provide communications to high-demand areas. Their model was designed using conditional Pareto analysis. Buzzi and Selva also investigated heterogeneous orbits to improve constellation coverage for EO applications [96]. Using a genetic algorithm that optimizes over mean revisit time, mean response time, coverage, and cost, they found that symmetric hybrid Walker constellations, which are a combination of multiple Walker constellations at different altitudes and inclinations, perform better than asymmetric heterogeneous satellite constellations. This work differs from previous works by including reconfiguration and RGT orbits for persistent data collection, data rate simulation, and does not include a MEO or TDRSS relay to transmit data.

1.4 Thesis overview

1.4.1 Research gaps and motivation

In the field of timely remote sensing, work has been done in reconfigurable constellations which utilize propulsion to move satellites into RGT orbits over a particular target of interest, and enable frequent data collection. There has also been a lot of work done in utilizing ISLs to downlink the collected information as quickly as possible. This work incorporates both of these design factors to explore constellations that can use RGT orbits in order to achieve higher high-quality revisit rates of a ground target and additionally tap into a network of ISLs in order to reduce the latency between the time the data is taken and when it can be accessed by an end-user.

In order to simulate these scenarios, a planner and scheduler are developed that handle both propulsive maneuvers and data routing paths. An open-source simulation framework is developed to run the planner and scheduler. The constellation design space is evaluated using a cost/metric model that enables the best designs to be evaluated via a Pareto front. As reconfigurable and ISL capable constellations have not been studied in combination before, the planner and scheduler, open-source simula-

tion framework, and optimal design selection combine to form a unique contribution to the field.

1.4.2 Thesis contributions

There are 4 primary contributions in this work:

1. Create an open-source simulation framework that simulates satellite propagation and execution of propulsive maneuvers and also allows for analysis of data routing pathways.

2. Develop a planning and scheduling algorithm to generate timely data for specific scenarios by implementing both constellation reconfiguration and optimal data routing through ISL.

3. Select the optimal constellation designs with regards to constellation cost and the metrics of age of information, system response time, and total pass time.

4. Generate cost estimating relationship (CER)s to aid constellation designers in understanding the cost versus performance trade-off for age of information, system response time, and total pass time.

1.4.3 Thesis roadmap

The following chapters present the work and conclusions that support the thesis contributions. Chapter 2 provides an overview of the technical background that underpins the work in this thesis. Chapter 3 describes the framework and approach used to develop the Python simulation environment. Chapter 4 walks through the algorithms that schedule the burns to put satellites into repeat ground tracks and also schedules the data transfers between various nodes in the network. Chapter 5 details the sensitivity of the analysis to the parameters and constraints. Chapter 6 presents the results of the thesis work, the optimal constellation designs, as well as the CERs derived from the simulation runs. Chapter 7 includes a summary of the findings and future directions for this research.

THIS PAGE INTENTIONALLY LEFT BLANK

Chapter 2

Technical Background

This chapter details the fundamental concepts and approach upon which this work is built. The orbital mechanics section (Section 2.1) describes the physics that underpin the propagation, propulsion, and access features of the simulation framework (contribution 1). The time conventions (Section 2.2) as well as the time and orbit geometry (Section 2.3) sections are both essential to the development of the planning and scheduling algorithm (contribution 2). The link budgets section (Section 2.4) defines the fundamental constraints of the ISL capabilities within the simulation (contribution 1) and the scheduling and planning algorithm (contribution 2). The relative motion equations section (Section 2.5) defines the constraints which determine when ISLs are feasible in the simulation (contribution 1) and the planning and scheduling algorithm (contribution 2). The Dijkstra's algorithm section (Section 2.6) describes the search method that the data routing planning algorithm is based on (contribution 2). The section on Walker constellations (Section 2.7) defines a constellation convention, making it easier to compare the best performing constellation designs within this work and with works by other researchers (contribution 3). The rocket equation section (Section 2.8) defines the fuel use for propulsive maneuvers, which ultimately affects the planning and scheduling algorithm (contribution 2) and the CERs (contribution 4).

2.1 Orbital mechanics

2.1.1 Keplerian elements

The Keplerian elements are commonly used to describe the state of a satellite with parameters $(a, e, i, \Omega, \omega, \nu)$ representing semi-major axis, eccentricity, inclination, RAAN, the argument of periapsis, and true anomaly respectively. The angular elements are depicted in Figure 2-1. The first two elements a and e describe the shape of the orbit. In classical two-body orbits, a is the distance between the center of mass for both bodies while e describes how elongated the ellipse is compared to a circle. i and Ω describe the orientation of the orbital plane. i is defined as the angle between the reference plane, which is the equatorial plane for Earth-centered satellites, and the orbital plane. Ω is the angle between the reference direction, which is the First Point of Aries in this work, and the ascending node, which is the point where the satellite passes upward through the reference plane. ω describes the orientation of the elliptical orbit with respect to the orbital plane and is defined as the angle between the ascending node and the point of periapsis. ν describes the position of the satellite within the elliptical orbit and is the angle between periapsis and the satellite position. Since this work deals with circular orbits with no defined periapsis, ν will refer to the argument of latitude, which is defined as the angle between the ascending node and the satellite's position. Lastly, mean anomaly (M) is interchangeable with ν in this work as mean anomaly equals true anomaly for circular orbits.

From the Keplerian elements, it is useful to derive the angular rate of change of the satellite around the orbit, or the mean motion, n. This value can be calculated using:

$$n = \sqrt{\mu/a^3} \tag{2.1}$$

μ is the gravitational parameter: $\mu = GM_{Earth}$, where G is the gravitational constant and M_{Earth} is the mass of the Earth.[1]

[1] M_{Earth} is technically the mass of the body that the satellite rotates around, but M_{Earth} is used to avoid confusion since only Earth-orbiting satellites are considered, and the variable M is already

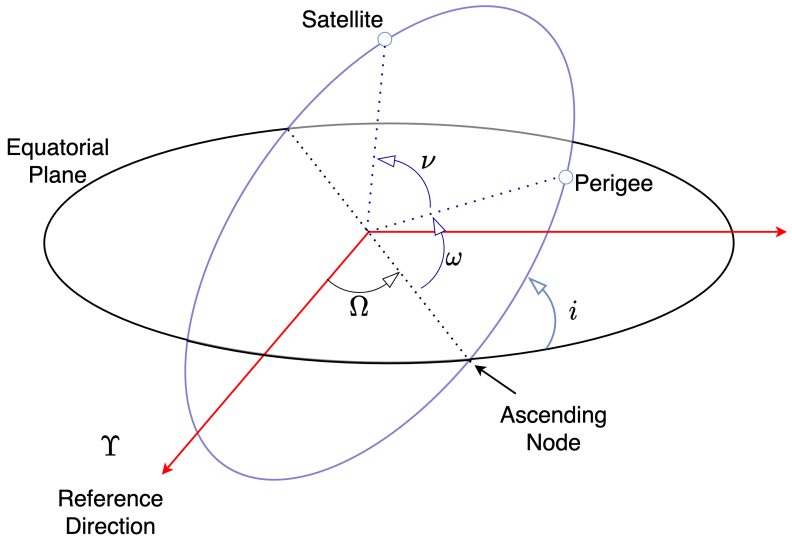

Figure 2-1: The four angular Keplerian elements. Figure created by the author and based on figures in both Wertz [1] and Vallado [2].

It takes six degrees of freedom to describe an orbit with the six Keplerian elements. The six Keplerian elements are useful because they help visualize orbits geometrically. However, for computational purposes, it is often easier to transform the Keplerian elements into a state vector comprised of 3-dimensional position and velocity. The conversion from Keplerian elements to position and velocity vectors can be found in many textbooks, including Vallado's "Fundamentals of Astrodynamics and Applications" (Algorithm 10: COE2RV) [2].

2.1.2 Orbital perturbations

In a classical two-body orbit, both bodies are modeled as point masses. In reality, satellites are perturbed from these classical orbits due to external forces in orbit such as gravitational non-uniformity from the Earth's shape, atmospheric drag (dependent on the shape of the satellite and atmosphere in LEO), 3rd body effects from the moon and sun, and solar radiation pressure. Seen in Figure 2-2, the J2 term due to the gravitational field generated by the oblateness of the Earth is two orders of magnitude

given to mean anomaly.

greater than any other perturbation force in LEO at altitudes greater than 200 km[2]. For altitudes less than 200 km, atmospheric drag would be a major perturbative force.

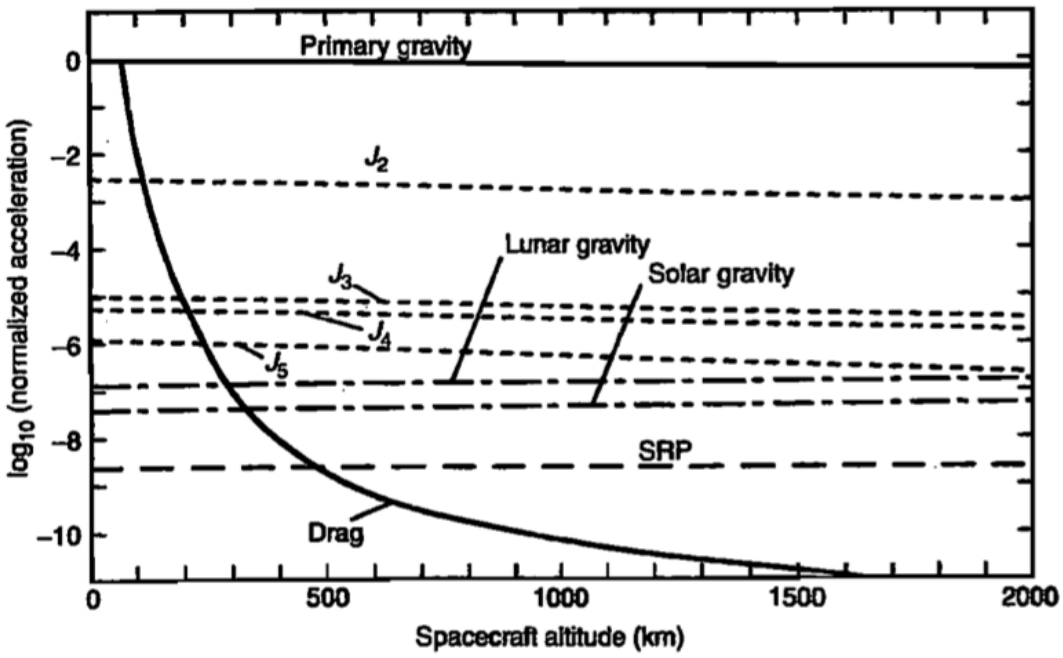

Figure 2-2: Magnitude of perturbation forces in LEO. Figure from Fortescue [3].

Due to its relative strength in LEO altitudes from 400 km to 700 km, this work considers J2 perturbations, while neglecting the lower magnitude perturbations. J2 perturbations alter a satellite's RAAN, argument of periapsis, and mean anomaly. Equations 2.2, 2.3, and 2.4 detail the Keplerian element precession rates caused by J2 perturbations [97]:

[2]Using Poliastro's atmospheric drag exponential model, a 550 km altitude, 60 deg inclination, BlackSky Satellite propagated with drag would have an altitude difference of 0.8 km compared to a BlackSky Satellite propagated without drag over the course of 3 days, the length of the trade study simulations in Chapter 6.

$$\dot{\Omega} = -\frac{3nR_{\oplus}^2 J_2}{2p^2}\cos(i) \tag{2.2}$$

$$\dot{\omega} = \frac{3nR_{\oplus}^2 J_2}{4p^2}(4 - 5\sin^2(i)) \tag{2.3}$$

$$\dot{M} = \frac{-3nR_{\oplus}^2 J_2\sqrt{1-e^2}}{4p^2}(3\sin^2(i) - 2) \tag{2.4}$$

where $\dot{\Omega}$, $\dot{\omega}$, $\dot{M}$ are the rate of change of RAAN, argument of periapsis, and mean anomaly, respectively. e and i are eccentricity and inclination, respectively. p is defined as:

$$p = a(1 - e^2) \tag{2.5}$$

where a is the semi-major axis.

n is the mean motion of the orbit:

$$n = \sqrt{(\mu/a^3)} \tag{2.6}$$

where μ is the gravitational parameter of the central body (Earth). $R_{\oplus}$ is the equatorial radius of the central body (Earth), and $J2$ is the zonal harmonic coefficient (1.082627×10^{-3} for Earth [2]) that describes the oblateness of the Earth.

In Equation 2.2, the cosine term dictates that RAAN drift rate increases with lower inclinations, and there is no RAAN drift for 90° inclination orbits. Also with the p term in the denominator, it is seen that as semi-major axis increases, which is directly related to increasing altitude for circular orbits, the satellite will experience less RAAN precession. The further a satellite is away from the Earth, the more the Earth seems to be a perfect sphere to the satellite as opposed to an oblate spheroid. Concerning eccentricity, the more circular an orbit is, the less RAAN precession the satellite experiences. In Equation 2.3, it is seen from the sine term that $\dot{\omega}$ is zero for inclinations of 63.435° and 116.565°, providing the foundational astrodynamics for Molniya orbits [1]. Like RAAN, precession decreases if an orbit is more circular and at higher altitudes. In Equation 2.4, there is no anomaly precession at inclinations

of 54.736° and 125.264°. Like RAAN and $\dot{\omega}$, precession decreases if an orbit is more circular and at higher altitudes.

2.1.3 Propagation

For a satellite and planet under the influence of gravity and no other perturbations, the system follows the two-body equation:

$$\ddot{\vec{r}} = -\frac{\mu}{r^2}\frac{\vec{r}}{r} \tag{2.7}$$

where $\vec{r}$ is the position vector between both bodies, r is the magnitude of the position vector, $\ddot{\vec{r}}$ is the acceleration, and μ is the gravitational parameter.

In order to include the J2 perturbation in our propagation, this work uses Cowell's Formulation, which is described in many texts including Vallado [97]. The two-body equation is rewritten as:

$$\ddot{\vec{r}} = -\frac{\mu}{r^2}\frac{\vec{r}}{r} + \vec{a}_{perturbed} \tag{2.8}$$

where $\vec{a}_{perturbed}$ is the total acceleration caused by all external perturbations. This equation can be rewritten as six first-order differentials:

$$\overline{\boldsymbol{X}} = \begin{bmatrix} \vec{r} \\ \vec{v} \end{bmatrix} \tag{2.9}$$

$$\dot{\overline{\boldsymbol{X}}} = \begin{bmatrix} \vec{v} \\ -\frac{\mu}{r^2}\frac{\vec{r}}{r} + \vec{a}_{perturbed} \end{bmatrix} \tag{2.10}$$

The work in this work utilizes the python library, Poliastro, to implement Cowell's method [98]. The Poliastro library uses the Dormand & Prince method of order 8 from the SciPy python library to solve Equations 2.9 and 2.10. In the Poliastro 0.14.0 documentation, this formulation is validated against an analytical solution to a tangential perturbation thrust.[3]

[3]https://poliastro-py.readthedocs.io/en/latest/examples/Propagation%20using%20Cowells%20formulation.html

2.1.4 Repeat ground track orbits

RGT orbits are designed so that a satellite ground track repeats N_0 orbits over N_d sidereal days, where N_0 and N_d are integers. These orbits offer repeated coverage of certain ground locations, sacrificing global coverage for coverage frequency. An example set of RGT orbits is shown in Figure 2-3.

To design an RGT orbit, the longitudinal rotation of the Earth cancels out the nodal precession of the orbit over N_0 orbits and N_d days. Mathematically, this can be described as:

$$N_0|\Delta L_1 + \Delta L_2| = N_d 2\pi \tag{2.11}$$

where ΔL_1 is defined as the longitudinal shift in ground track over an orbit due to Earth's rotation

$$\Delta L_1 = -2\pi \frac{T}{T_{SD}} \tag{2.12}$$

where T_{SD} is the duration of a sidereal day and T is the orbital period

$$T = 2\pi\sqrt{a^3/\mu} \tag{2.13}$$

The longitudinal shift in ground track over a period due to nodal precession is defined as ΔL_2:

$$\Delta L_2 = -\frac{3\pi J_2 R_\oplus^2 \cos(i)}{p^2} \tag{2.14}$$

which is Equation 2.2 times the orbital period, T. The semi-major axis, a, of an RGT orbit can then be solved iteratively using an algorithm such as Algorithm 71 in Vallado's Fundamentals of Astrodynamics and Applications [97]. Figure 2-4 shows a selection of RGT orbits for various N_0/N_d ratios, inclinations, and altitudes.

2.1.5 Hohmann transfers

This work uses Hohmann transfers to perform orbital maneuvers. Hohmann transfers use two impulsive burn maneuvers to transfer a spacecraft between two circular

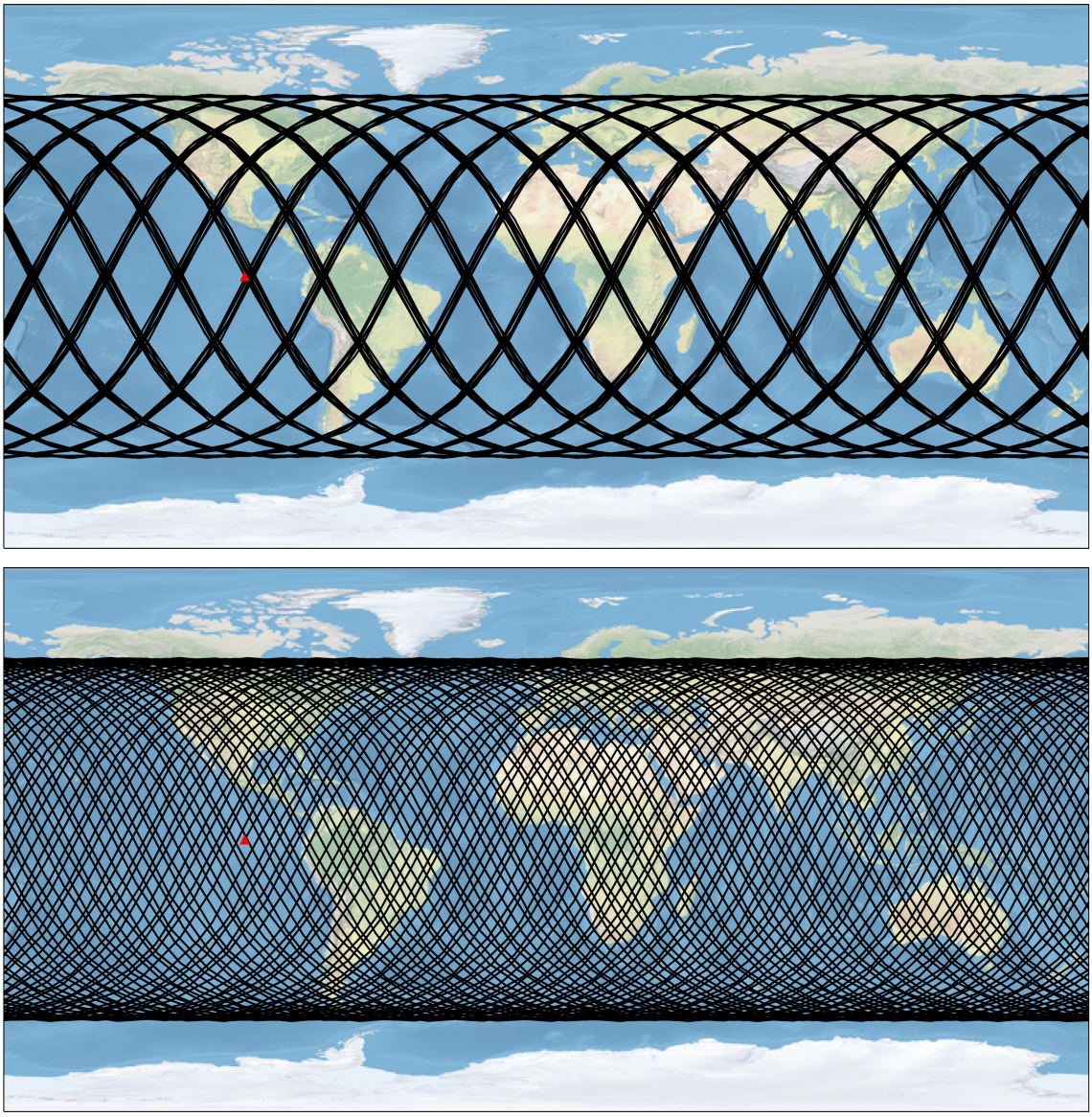

Figure 2-3: These figures display 100 orbits of a satellite at 60° inclination. The top figure is at an RGT altitude of 505.844 km (an RGT orbit), while the bottom is at an altitude of 600 km (not an RGT orbit). Figures generated using Python and the Poliastro and the Cartopy libraries.

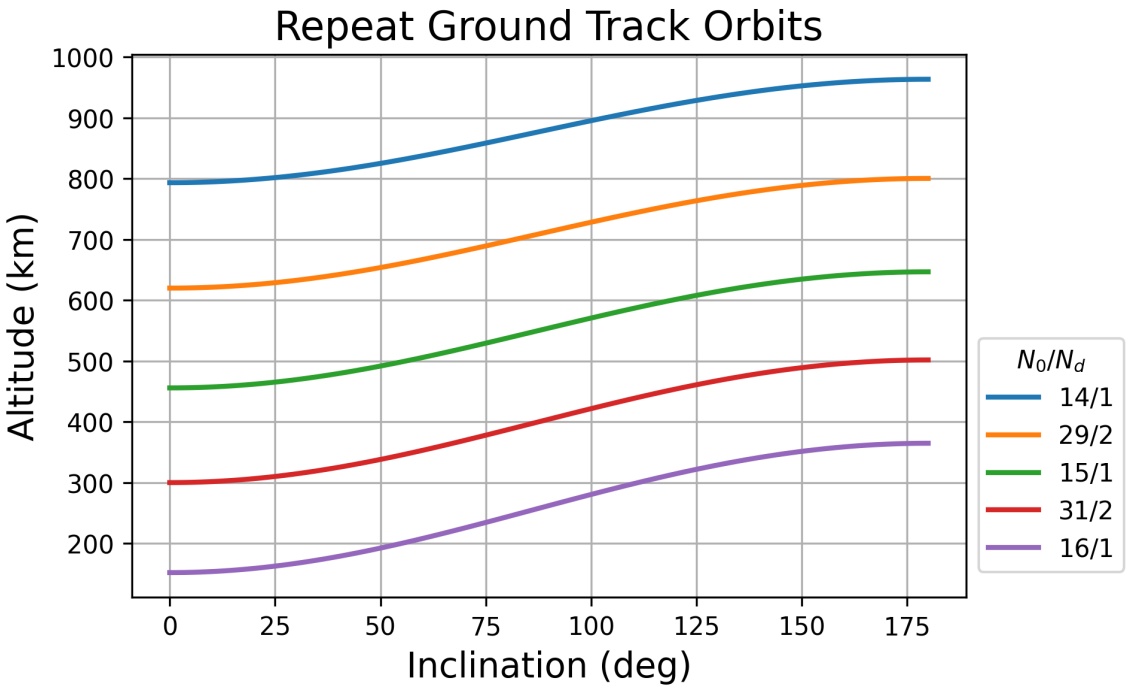

Figure 2-4: RGT altitude increases as inclination increases as well as when N_0/N_d decreases.

orbits. This work uses Hohmann transfers to allow satellites to change altitudes and is depicted in Figure 2-5. Given an initial circular orbit with semi-major axis a and a desired final circular orbit with semi-major axis b, an initial burn with value Δv_a will push the satellite into an elliptical orbit. Hohmann transfers are often the most efficient maneuvers in terms of fuel, but this efficiency often comes at the expense of time.

$$\Delta v_a = \sqrt{\frac{2\mu}{a} - \frac{\mu}{a_{trans}}} - \sqrt{\frac{\mu}{a}} \tag{2.15}$$

where μ is the gravitational parameter and

$$a_{trans} = \frac{a+b}{2} \tag{2.16}$$

A second burn with value

$$\Delta v_b = \sqrt{\frac{\mu}{b}} - \sqrt{\frac{2\mu}{b} - \frac{\mu}{a_{trans}}} \tag{2.17}$$

circularizes the orbit.

The total ΔV to complete a Hohmann transfer is therefore:

$$\Delta v_{Hohmann} = |\Delta v_a| + |\Delta v_b| \tag{2.18}$$

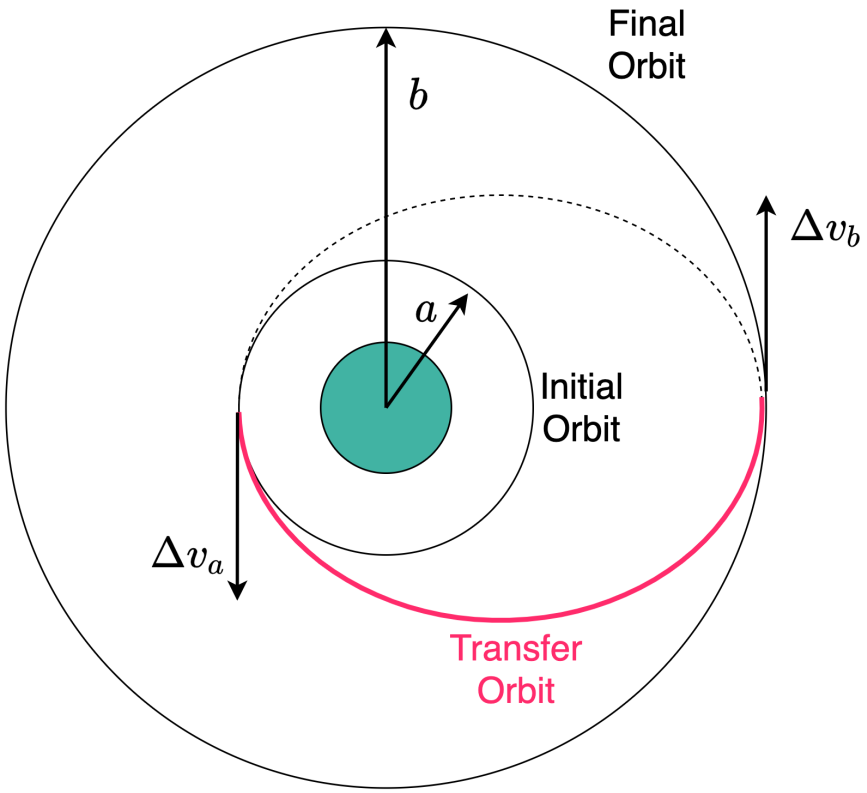

Figure 2-5: Hohmann transfer orbit (red) to move a satellite from a circular orbit with semi-major axis a to a circular orbit with semi-major axis b. Figure created by author.

2.1.6 Access calculations

Access as defined in this work is the capability for data to be transferred between a ground location and a satellite. The data is often a communications link or the ability for a sensor aboard a satellite to remotely observe a ground location. This work investigated two different methods of calculating access. The first is by using ground range calculations, the second is using trigonometry to determine elevation

and nadir angles. The first method described here uses native Poliastro functions. For this work, the second method is primarily used because it is more easily understood in terms of elevation angle and nadir angle constraints.

Ground Range Method

Calculating ground range The ground range Λ is defined as the shortest central angle between two points on the surface of a spherical body. The following is equivalent to equation 11-2 in Vallado's 4th edition astrodynamics textbook (on page 854) [2]:

$$\cos(\Lambda) = \sin(\phi_1)\sin(\phi_2) + \cos(\phi_1)\cos(\phi_2)\cos(\Delta\lambda) \tag{2.19}$$

where ϕ_1 and ϕ_2 are the latitudes of points 1 and 2, respectively and $\Delta\lambda$ is equal to $\lambda_2 - \lambda_1$, where λ_2 and λ_1 are the longitudes of points 1 and 2, respectively.

Calculating ground range of a sensor To determine if a ground location has access to a satellite, this work once again refer to Vallado's book from pages (853 - 860) [2], which has been conveniently written up in the poliastro.earth.sensors.min_and_max_ground_range() function in the poliastro python library [98]. The inputs to min_max_ground_range are the satellite altitude, total field of view of the sensor on the satellite, the boresight angle of the sensor, and the equatorial radius of the sphere, which by default is the Earth. The poliastro function min_max_ground_range returns the central angle from the satellite nadir point to the edge of the field of view of a nadir pointing sensor on the satellite. For a nadir pointing satellite (boresight angle of 0°), the min and max ground range output by this function should be equal.

Calculating Access Access between the ground location and the satellite can be calculated by finding the ground range using Equation 2.19 and comparing it to the max ground range generated by min_max_ground_range, which will call the sensor derived ground range. If the sensor derived ground range is larger than the ground

range between the ground location in question and the nadir location of the satellite, then access is available. This access calculation ensures the spherical central angle between the satellite nadir point and the ground location in question is less than the spherical central angle between the satellite nadir point and the edge of the sensor footprint on the sphere.

Considerations The methodology for ground range can be extended beyond just a sensor to Earth scenario. For example, the sensor field of view input to min_max_ground_range can be analogous to other constraints. Given a minimum elevation angle constraint for a ground station, an equivalent subsatellite nadir angle can be derived that is equivalent to a nadir pointing sensor field of view constraint.

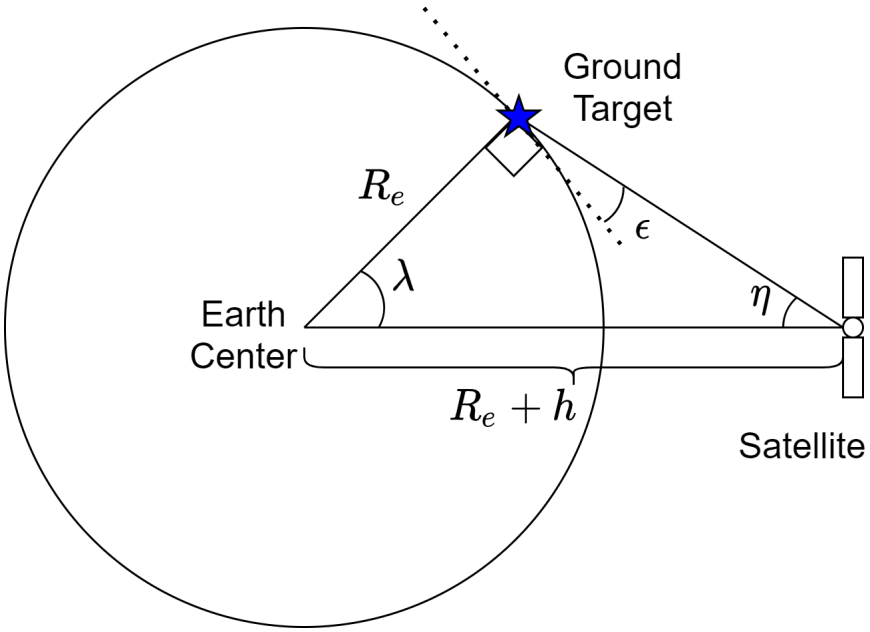

Figure 2-6: λ is the Earth central angle between the ground target and the satellite vector, ϵ is the elevation angle from the ground target, η is the nadir angle measured from the spacecraft, R_e is the radius of the Earth and h is the altitude of the satellite.

To equate an elevation angle constraint with a pointing sensor field of view constraint, the law of sines is used. From Figure 2-6, the law of sines is used to find either η or ϵ as long as the satellite altitude h and either η or ϵ are given. Using Equation 2.21, sensor field of view constraints and elevation angle constraints can be equated. For an in-depth explanation of this particular Earth geometry, see Section

8.3.1 equation 8-26 from SME SMAD [1].

$$\frac{\sin\eta}{R_e} = \frac{\sin(90+\epsilon)}{R_e+h} \tag{2.20}$$

$$\frac{\sin\eta}{R_e} = \frac{\cos(\epsilon)}{R_e+h} \tag{2.21}$$

Limitations Both Equations 2.20 & 2.21 assume a perfectly spherical Earth, which is not exactly accurate given Earth's oblate shape. In practice, when calculating using the min_max_ground_range function, the average altitude is used to reduce computation time. This is a fair assumption if the satellite in question is in a circular orbit. To increase the fidelity of this simulation, an oblate Earth model should be used, and the ground range can be calculated using the satellite's altitude at every propagation step.

Vector trigonometry method

Algorithm to determine elevation and nadir half-angles Referring back to Figure 2-6, if a satellite's altitude and the Earth Central Angle, λ, are known, both the elevation angle and nadir half-angle can be calculated to determine if the satellite in its current position can access the ground target given either an elevation or nadir half-angle constraint. Assuming knowledge of the position vectors of the satellite and the ground target, usually easiest if everything is in the Earth-centered Earth-fixed (ECEF) frame, the Earth Central Angle, λ, can be found using the cosine formula for dot product. These formulas are referenced from Space Mission Engineering: The New SMAD equations (8-26) to (8-32) [1].

$$\cos\lambda = \frac{\vec{r}_{sat}\cdot\vec{r}_{gs}}{|\vec{r}_{sat}|\,|\vec{r}_{gs}|} \tag{2.22}$$

In Equation 2.22, $\vec{r}_{sat}$ and $\vec{r}_{gs}$ are the position vectors for the satellite and ground location respectively. Next define a variable, ρ

$$\rho = \frac{R_e}{R_e + h} \tag{2.23}$$

The half-nadir angle η can then be solved using

$$\tan \eta = \frac{\rho \sin \lambda}{1 - \rho \cos \lambda} \tag{2.24}$$

Lastly the elevation angle, ϵ can be found using

$$\epsilon = \pi/2 - \eta - \lambda \tag{2.25}$$

Now with both elevation angle, ϵ, and nadir angle, η, defined, the potential accesses are calculated given a satellite position and ground station vector. The elevation angle is useful because ground stations cannot close links with satellites at low elevation angles due to obstacles such as buildings and trees.

2.2 Time conventions

Establishing time conventions is essential when considering orbit problems. An epoch designates a particular point in time, better known as a date. At a particular date, the position and orientation of other celestial bodies such as the Earth are known. Because a satellite's six orbital parameters are independent of date, an epoch must be introduced when describing a satellite orbit. The epoch describes the orientation of the rotating Earth and determines which latitudes and longitudes on Earth the satellite will fly above.

It is also important to distinguish solar and sidereal time. A solar day is defined as the time it takes for the sun to cross the local meridian on successive passes, which defines the conventional 24 hour day. Sidereal time is the time it takes for successive transits of stars over a local meridian and is shorter, at roughly

23 hours 56 minutes 4 seconds. These times are often described in hour angles, which equates 24 hour angles to 360°. It is often easier to describe satellite orbits in sidereal time; without external perturbations, these orbits would stay put with respect to the stars. However, for practical purposes, solar time is often preferred because it lines up with human cycles and also helps define when locations are illuminated by the sun, which is useful for certain types of remote sensing applications. An illustration of the difference between solar and sidereal time is shown in Figure 2-7.

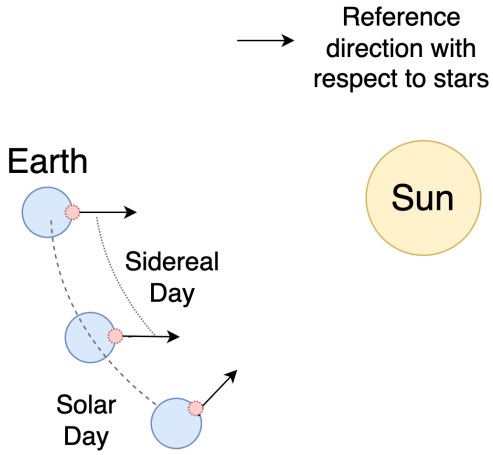

Figure 2-7: Not to scale, exaggerated for clarity. A sidereal day is the time it takes for a reference direction, with respect to the stars, to transit a particular meridian (represented by the red dot). Solar time is the transit of the sun over a particular meridian, which takes roughly 4 minutes longer than sidereal day. A meridian is the locus of points connecting points of equal longitude. In this figure, as viewed from Polaris, the Earth rotates counter-clockwise about its axis and also counter-clockwise around the sun.

This work uses Coordinated Universal Time (UTC) as the standard for solar time as it is commonly used around the world. UTC is determined using both International Atomic Time and UT1, which implements adjustments for both Earth's polar motion and apparent movements of the sun. UTC is able to use International Atomic Time, which is derived from atomic clocks, to correct for the slowing rotation of the Earth. More information on time conventions can be found in Vallado chapter 3.5 [2].

2.3 Time and orbit geometry

The relationship between time and orbit geometry is important in this work as the targeting algorithms have to not only target a particular set of orbital parameters, but also must target a particular epoch to ensure the satellite passes over a particular Earth location.

Given an orbit with inclination (i) and RAAN (Ω), and a ground location with longitude (λ) and latitude (ϕ), sidereal can be converted to solar time and vice-versa. The Greenwich mean sidereal time, θ_{GMST}, is defined as:

$$\theta_{GMST} + \lambda = \Omega + \Delta\lambda \tag{2.26}$$

where $\Delta\lambda$ is found by approximating the angle using spherical geometry:

$$\Delta\lambda = \arcsin\left(\tan\phi / \tan i\right) \tag{2.27}$$

The geometry depicting these relationships is shown in Figure 2-8.

In order to convert from sidereal time to solar time, one needs to know the location of the Earth in orbit around the sun. Pegging sidereal midnight to the First Point of Aries and the vernal equinox in the Northern Hemisphere, ΔD is defined as the fraction of a year that has transpired since the last vernal equinox. For example, 30 days after the vernal equinox on a non-leap year (365 days) would result in $\Delta D = 0.0822$. Greenwich mean solar time, θ_{GMT} is then defined as:

$$\theta_{GMT} = \theta_{GMST} - 2\pi\Delta D + \pi \tag{2.28}$$

The extra factor of π is added because Greenwich mean time is referenced to noon while Greenwich sidereal time is referenced to midnight. Local mean time θ_{LMT} can be retrieved by adding the local longitude in hour angles to Greenwich solar time.

$$\theta_{LMT} = \theta_{GMT} + \lambda \tag{2.29}$$

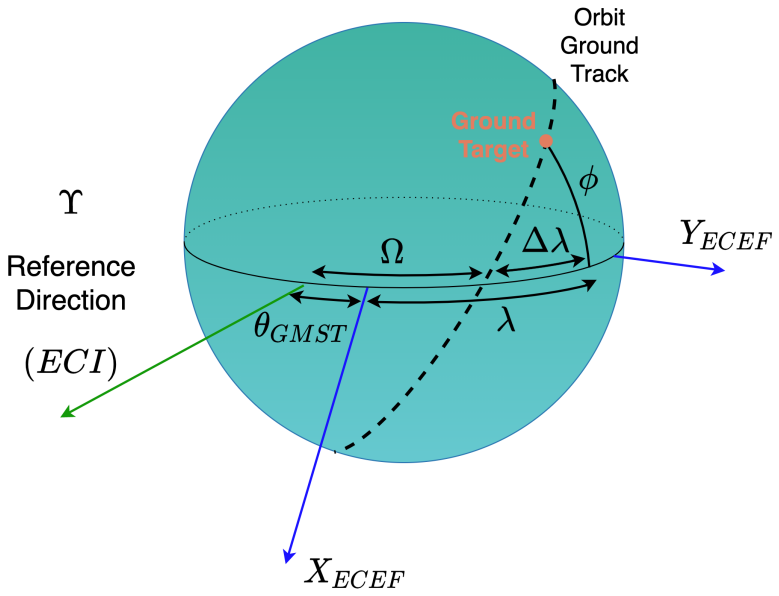

Figure 2-8: Geometric illustration of the relationship between solar and sidereal hour angles. ECI refers to the Earth Centered Inertial coordinate system, pegged to the First Point of Aries, while ECEF refers to the Earth Centered Earth Fixed coordinate system, the conventional latitude and longitude coordinates. Figure created by author using Draw.io.

2.4 Link budgets

The following section provides a high-level overview of radio frequency communication link budgets, and for a more in-depth review, please refer to Maral and Bousquet's textbook [99]. Link budgets are tools used to determine the achievable data rates given a communication system with a transmitter and receiver and are based on the Friis equation. E_b/N_0, or energy per bit over noise power density is a commonly used ratio, characterizing the performance of the link. It is defined as:

$$E_b/N_0 = \frac{P_{tx}G_{tx}L_{space}L_{other}G_{rx}}{kT_{sys}R} \tag{2.30}$$

where P_{tx} [Watts] is the transmit power, G_{tx} [unitless] is the gain of the transmit antenna, L_{space} [unitless] is the free space path loss, L_{other} [unitless] are other losses including, but not limited to, pointing loss, atmospheric loss, and line losses, $\frac{G_{rx}}{T_{sys}}$ [1/Kelvin] is the receive antenna gain to system noise temperature, k [Joules/Kelvin] is the Boltzmann constant, and R [bits per second] is the data rate. E_b is in units of energy per bit [Watt Seconds] and N_0 is noise spectral density [Watt/Hertz].

The transmitter's performance can be assessed using effective isotropic radiated power (EIRP), which is equal to:

$$EIRP = P_{tx}G_{tx} \tag{2.31}$$

L_{space} is dependent on both the distance between transmitter and receiver and also the frequency (wavelength) of communication:

$$L_{space} = \left(\frac{4\pi R}{\lambda}\right)^2 \tag{2.32}$$

where R is the distance between transmitter and receiver, and λ is the wavelength. As one would expect, the greater the distance, R, the larger L_{space} becomes. Additionally, shorter wavelengths have larger losses. While shorter wavelengths can carry higher data rates, other link budget parameters must make up for the higher free space path

losses. Often, link designers use transmit antennas with higher gain, which would then require greater pointing accuracy, in order to close the link.

L_{other} is a term to capture the other losses between transmitter and receiver in the system. For example, atmospheric losses, which are highly dependent on wavelength, must be considered in space to ground and ground to space links but can be ignored when dealing with intersatellite links. Pointing losses are dependent on the antenna beam pattern as well as the attitude control system of the satellite and pointing system of a ground terminal.

Note the equations above are not described in decibel units, hence the multiplication and division instead of the addition and subtraction commonly seen in decibel link budget equations.

2.5 Relative motion equations

This section lays out useful equations to describe relative motion between two objects. For this work, these equations pertain to the relationship between satellites and determine whether or not interactions are feasible between satellites as well as between satellites and ground stations.

2.5.1 Relative position and velocity

Given two vectors $\vec{r}_1$ and $\vec{r}_2$, the relative position $\vec{r}_{12}$ can be found using

$$\vec{r}_{12} = \vec{r}_1 - \vec{r}_2 \tag{2.33}$$

Similarly, the relative velocity $\dot{\vec{r}}_{12}$ can be found using

$$\dot{\vec{r}}_{12} = \dot{\vec{r}}_1 - \dot{\vec{r}}_2 \tag{2.34}$$

where the dot represents the derivative.

2.5.2 Line of sight

In this work, the line of sight refers to whether there is a vector, $\vec{r}_{12}$, that does not intercept the Earth, which is simplified to a perfect sphere for the following analysis. With line of sight, two satellites can establish a communication link between them if given infinite transmit power. The calculation to determine whether a line of sight exists between two satellites follows Vallado's method in Chapter 5.3.3 of his textbook [2].

Given two position vectors, $\vec{r}_1$ and $\vec{r}_2$, the angle between them, θ, can be calculated using the law of cosines:

$$\cos\theta = \frac{\vec{r}_1 \circ \vec{r}_2}{|\vec{r}_1||\vec{r}_2|} \tag{2.35}$$

The threshold for line of sight occurs when the relative position vector is perfectly tangent to the spherical obstacle (Earth). See Figure 2-9 for a geometric interpretation.

In the threshold case, the line connecting the center of the Earth with the intersection of $\vec{r}_{12}$ and the Earth forms a right angle with $\vec{r}_{12}$. The two half-angles, θ_1 and θ_2, can then be calculated using trigonometry:

$$\cos(\theta_1) = \frac{R_{earth}}{|\vec{r_1}|} \tag{2.36}$$

$$\cos(\theta_2) = \frac{R_{earth}}{|\vec{r_2}|} \tag{2.37}$$

It is seen that if $\theta_1 + \theta_2 > \theta$, there is no line of sight. Geometrically, one can imagine that as the triangle is becoming more obtuse, holding the magnitudes of $\vec{r}_1$ and $\vec{r}_2$ constant, the relative position vector $\vec{r}_{12}$ will eventually intersect the Earth sphere. If $\theta_1 + \theta_2 \leq \theta$, the triangle becomes more acute, and the the two satellites will have a direct line of sight.

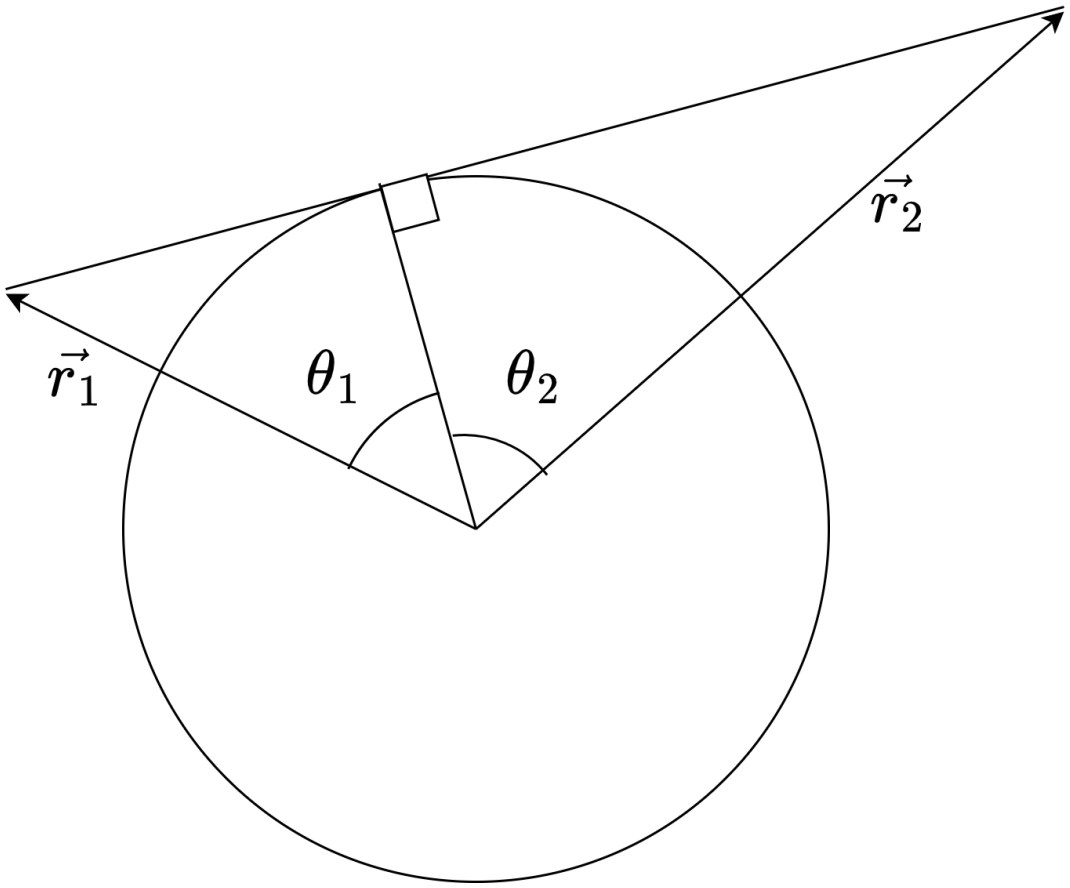

Figure 2-9: The threshold case where line of sight exists.

2.5.3 Slew rate

This work assumes that the satellites have body-fixed antennas for inter-satellite links. In order to establish an inter-satellite link, satellites must track the line of sight between two communication nodes. The rate at which this tracking occurs is referred to as the slew rate and dependent on the attitude determination and control system onboard the spacecraft. Some spacecraft will not be able to track at high rates, so a slew rate threshold is implemented to determine when satellites will be able to maintain a communication link.

The slew rate can be calculated using:

$$\vec{\omega}_{12} = \frac{\vec{r}_{12} \times \dot{\vec{r}}_{12}}{|r_{12}|^2} \tag{2.38}$$

where the magnitude of $\vec{\omega}_{12}$ is the slew rate. The derivation of this equation can be found in Dahl's report [100].

2.6 Dijkstra's algorithm

This work uses Dijkstra's algorithm to solve the data routing problem. Routing problems are often visualized as a graph, which is a mathematical structure comprised of nodes and edges. For example, a graph can be built to solve the problem of the shortest driving route from New York to Los Angeles. Each city in the US is made into a node and each edge represents the distance needed to drive between each city. Each edge is given a weight or cost, and in this scenario, the cost is the distance traveled.

Dijkstra's algorithm finds the shortest path between two nodes in a graph [101]. Given a starting node, Dijkstra's algorithm investigates the costs of reaching each neighboring node in the first step. The costs to reach each neighboring node are recorded. In the second step, the algorithm begins a neighboring node search from the node that was the lowest cost to reach. Again the costs to reach each neighboring node are recorded. Each subsequent step begins a search at the next least costly

node to reach, which would have been investigated in a previous step. This search continues until all nodes have been reached. The result is a set of the shortest paths to every node in the graph from the designated starting node. Dijkstra's algorithm pseudocode can be seen in Algorithm 2.

Algorithm 2 Dijkstra's algorithm

Require: $startNode, graph(edges, nodes)$
  $Q \leftarrow nodes$ ▷ Assign all nodes to Q as unvisited
  $shortestPaths[n] \leftarrow \infty \; \forall \; n \in nodes$
  $shortestPaths[startNode] \leftarrow 0$ ▷ Assign all paths to ∞ except startNode
  while $Q \neq \{\}$ **do**
    Let $u \in Q$ *be the node s.t.* $shortestPaths[u] == min(shortestPaths)$
    for $e \in neighboringEdges$, s.t. e connects u and $neighboringNode$ **do**
      $valueTentative = shortestPath[u] + weight(e)$
      if $valueTentative < shortestPath[neighboringNode]$ **then**
        $shortestPath[neighboringNode] = valueTentative$
      end if
    end for
    $Q \setminus u$ ▷ Remove u from Q
  end while

There are multiple variations of Dijkstra's algorithm, which are used to solve a variety of problems. The particular modifications to the general Dijkstra's algorithm that will be used for data routing in the satellite constellation system are described in Section 4.2.

2.7 Walker constellations

Walker or Walker Delta constellations are satellite constellations defined by four parameters, i, t, p, and f, corresponding to inclination, total satellites, orbit planes, and relative spacing between adjacent planes [3][102]. Walker parameters are displayed using the i: $t/p/f$ notation. All orbits have the same inclination and altitude. The number of satellites per plane can be derived from t/p. f can take a value between 0 and $p-1$. The phase difference in true anomaly in degrees between adjacent planes is calculated as $f \times \frac{360}{t}$. See Figure 2-10 for an example Walker constellation. Walker constellations are used as the standard design in this work for ease of comparison and

familiarity.

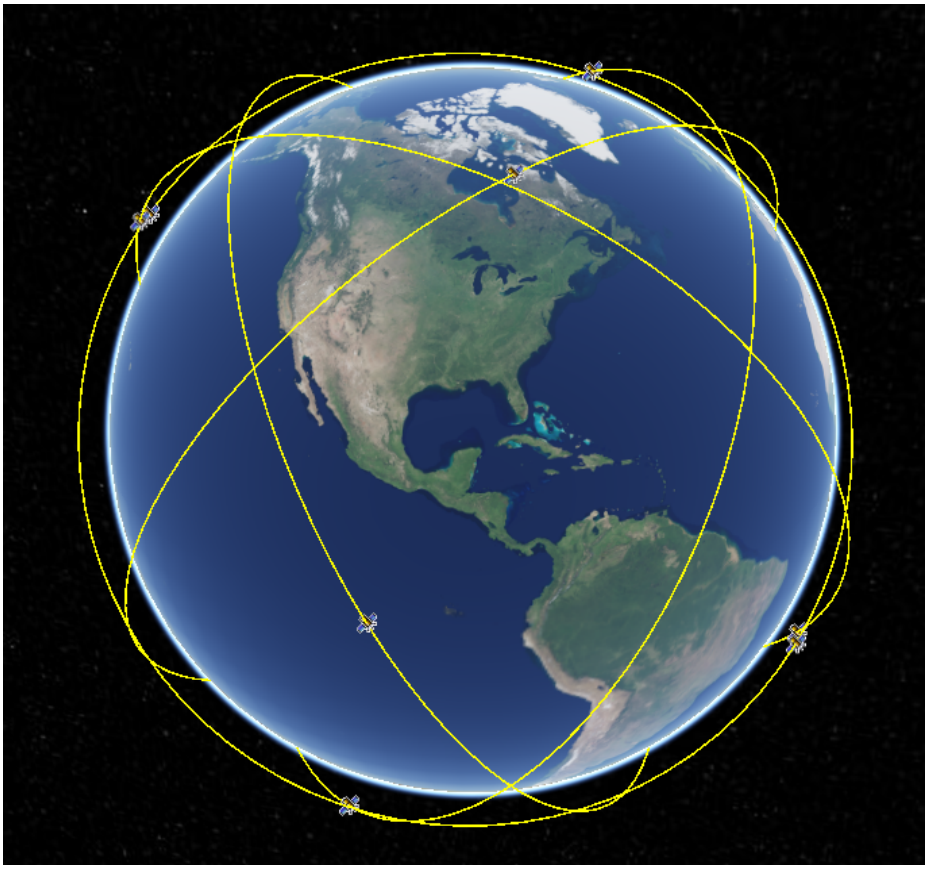

Figure 2-10: An example 60°: 10/5/1 Walker constellation displayed in Cesium.

2.8 Rocket Equation

The rocket equation describes the relationship between dry mass, wet mass, and a spacecraft's ΔV budget, which is the total sum of velocity changes that a spacecraft can undergo using propulsion. A spacecraft's dry mass does not include propellant mass while wet mass does. The rocket equation is defined as:

$$m_0 = m_f e^{\frac{\Delta V}{g_0 * isp}} \tag{2.39}$$

where m_0 is the initial or wet mass, m_f is the final mass, g_0 is gravitational acceleration, and isp is the specific impulse. Depending on the variables of interest, common

variations include substituting $m_0 = m_p + m_f$, where m_p is the propellant mass as well as $V_0 = g_0 * isp$, where V_0 is the propellant exhaust velocity. For this work, the rocket equation is primarily used to determine how much propellant is needed to perform the maneuvers that are required during its mission life time.

THIS PAGE INTENTIONALLY LEFT BLANK

Chapter 3

Simulation, models, and analysis tools

This chapter describes the approach used to develop and verify the Python simulation, models, and analysis tools. Sections 3.1 and 3.2 detail how propagation and satellite access are verified in the simulation. Section 3.3 describes the organization and the function of each individual tool or module within the simulation. Section 3.4 details the satellite and link budget models and the constraints imposed by them. Section 3.5 defines the metrics that are used to analyze the constellation performance within the simulation. Section 3.6 specifies the cost model used to estimate the cost of the constellations that are investigated in this work.

3.1 Propagation verification

The simulation relies on the poliastro Python library [98] for orbit propagation. In this section, the poliastro library is compared with STK [103], which is an industry standard software package. A position error of less than 0.1% over one day is desired. For the constellations in this work, the lowest altitude satellites orbit at 505 km. This altitude equates to a radial distance of 6883 km from the center of the Earth, which is also the origin of the coordinate frame used to calculate satellite positions. Positional error over one day would then have to be less than 6.883 km over one day to satisfy the 0.1% error criteria.

3.1.1 Verification

To verify the Poliastro propagator, identical satellite state vectors (position and velocity) are input into both Poliastro and STK propagators, both using identical 1 min propagation time steps. The difference in satellite position between both propagators will be compared, using the STK positions as truth.

Poliastro implements Cowell's method for numerical J2 propagation. STK has many different propagation options. For this comparison, STK propagation is run using the High-Precision Orbit Propagator (HPOP), which is a numerical propagator, with only the J2 perturbation activated. It should be noted that STK also has an analytical J2 perturbation propagation which applies perturbations directly to the orbital elements of RAAN, argument of perigee, and mean anomaly. Comparison with the analytical propagator creates errors on the order of 700 km over a day, which makes sense since these propagators are fundamentally different (Poliastro's numerical propagator compared to STK's analytic propagator).

Workflow

In order to ensure identical initial satellite conditions, the satellite was first propagated in STK. The position and velocity of each time step was then exported to a CSV file and imported into Python to ensure significant digits were preserved. Given the nature of numerical propagators, deviations in significant digits can lead to large propagation discrepancies. In Python, the initial conditions were extracted from the CSV file and input into the Poliastro propagator. The positions at each time step for each propagator are compared to ensure that they never deviate more than 6.993 km. The workflow for this verification test is described in Table 3.1.

3.1.2 Results: STK and Poliastro results

Over the course of a day, the Poliastro and STK propagated satellites drift apart by a little over 1 km as shown in Figure 3-2, which is on the order of magnitude of two-line element (TLE)/SGP4 propagators in Shuster's work [104]. Shuster achieved an error

Table 3.1: Workflow for propagation verification

Step	**Description**
Step 1	Create an orbit in STK (see Figure 3-1)
Step 2	Propagate the orbit for 1 day using the STK numerical propagator with J2 perturbation
Step 3	Export the position and velocity data of the orbit to a .csv file
Step 4	Import the .csv file into Python
Step 5	Extract the initial conditions from the .csv file and initialize orbit in Poliastro
Step 6	Propagate the Poliastro orbit for 1 day
Step 7	Compare the position and velocity of the STK result and the Poliastro result at each time step

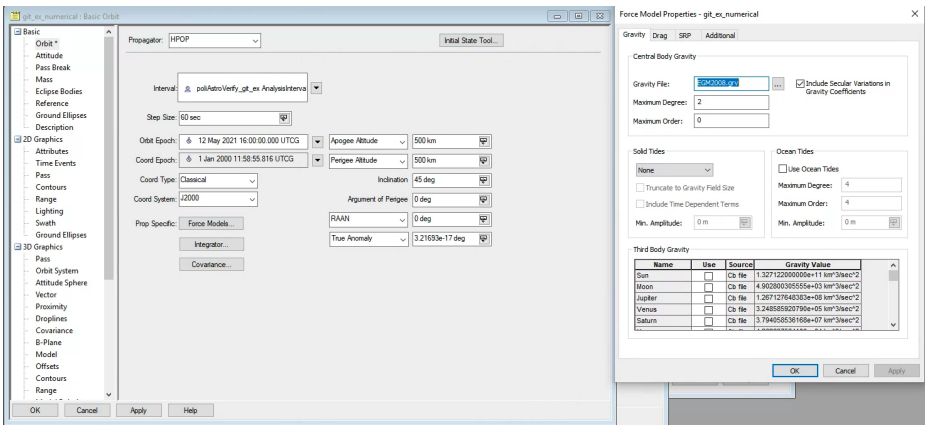

Figure 3-1: STK parameters for the test orbit. All other perturbation forces were turned off.

of 1 km using a TLE/SGP4 propagator with daily TLE updates over the course of a week.[1]

The discrepancy between the STK and Poliastro orbits can be attributed to the differences in the numerical integrators. Poliastro uses Scipy's scipy.integrate.solve_ivp with the Dormand-Prince 8th order integration method ('DOP853'). A dense output is also used, which interpolates a 7th order polynomial. STK, on the other hand, utilizes a 7th order Runge-Kutta-Fehlberg (RKF) numerical solver. 1 km of error leads to an acceptable discrepancy between this work's access calculations and STK's access calculations (see Section 3.2). Access calculation timing is crucial to this work because it underpins all of the metrics: AoI, SRT, and total pass time.

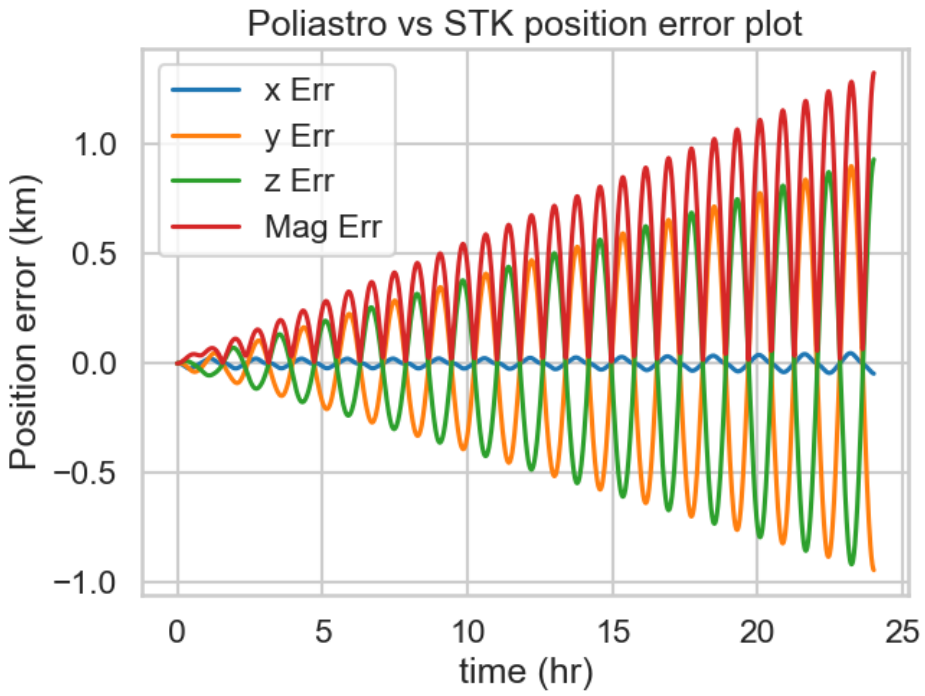

Figure 3-2: Position discrepancy between STK and Poliastro propagators over a day. Error plotted is root mean squared error.

[1]The main analysis in this work propagates satellites for 3 days.

3.2 Access calculation verification

After verifying satisfactory performance with the Poliastro propagator, access calculations were tested to be satisfactory as well. The total access time should be within 1% of the total access time calculated by STK[2], and this section shows that the total access time accuracy is 0.6%.

3.2.1 Scenario Set-up

In STK, a circular satellite orbit was initialized with orbital parameters seen in Table 3.2:

Table 3.2: Orbital parameters for access verification

Orbital parameter	**Value**
Altitude	500 km
Eccentricity	0
Inclination	45 degrees
RAAN	0 degrees
Argument of Latitude	0 degrees
Epoch	January 1st, 2000 12:00:00 UTC

The satellite was equipped with with a 45° (half-angle) nadir pointing sensor with a ground station placed at 39° latitude and 127° longitude. The satellite is propagated using a numerical propagator that includes J2 perturbations and a 1 sec time step interval. This scenario is recreated with the Python simulation code. A screenshot of the STK orbit initial conditions can be seen in Figure 3-3. The satellite in both STK and the Python simulation are propagated for 4 days, and access to the ground station is calculated.

3.2.2 Access time comparison between STK and poliastro

The Python simulation generates the access intervals in Figure 3-4. The times generated by the Python simulation differ at most by 2 seconds compared to the STK access calculations. The absolute differences for each interval start and stop time are

[2]Kennedy's work with the PROPAT orbit propagator achieved agreement to within 5% [70].

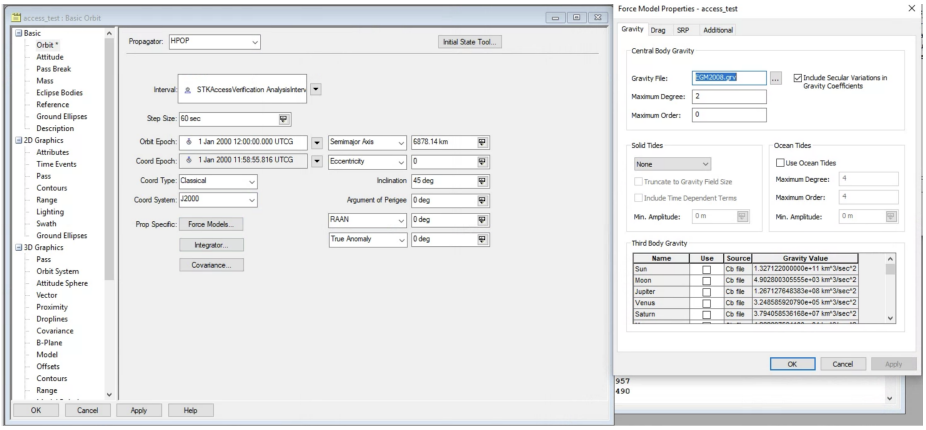

Figure 3-3: STK scenario orbit conditions

shown in Figure 3-5. The differences in start/stop intervals can be attributed to the minor differences in the numerical propagators, leading to slightly different positions, and to the STK model using a higher-fidelity WGS84 globe model for access calculations. Errors on the order of one to two seconds will have minimal effect on the analysis in this work since imaging and downlink access intervals are on the order of at least 30 seconds. The total access time calculated by STK is 1382 s, and the difference in total access time between poliastro and STK is 8 sec, leading to a total access time discrepancy of 0.58%.

3.3 Simulation Tools

This section describes the Python simulation tools used to run, simulate, and analyze constellations with both propulsion and ISL capabilities. An overview of each of the main software phases can be seen in Figure 3-6. The first part runs the burn scheduler to plan the propulsive maneuvers that allow the satellites to enter a RGT over the target location. The simulator then propagates the satellites and collects a data set that can be used for the routing algorithm in the second part of the software architecture. Once the routing has been determined, the final metrics can be extracted from the data set.

```
Access Interval 0
Start: 2000-01-01T12:14:45.000
Stop:  2000-01-01T12:17:17.000
Access Interval 1
Start: 2000-01-01T17:12:53.000
Stop:  2000-01-01T17:15:27.000
Access Interval 2
Start: 2000-01-02T11:50:34.000
Stop:  2000-01-02T11:53:07.000
Access Interval 3
Start: 2000-01-02T16:48:43.000
Stop:  2000-01-02T16:51:17.000
Access Interval 4
Start: 2000-01-03T11:26:23.000
Stop:  2000-01-03T11:28:57.000
Access Interval 5
Start: 2000-01-03T16:24:33.000
Stop:  2000-01-03T16:27:06.000
Access Interval 6
Start: 2000-01-04T11:02:12.000
Stop:  2000-01-04T11:04:46.000
Access Interval 7
Start: 2000-01-04T16:00:22.000
Stop:  2000-01-04T16:02:55.000
Access Interval 8
Start: 2000-01-05T10:38:01.000
Stop:  2000-01-05T10:40:36.000
```

Figure 3-4: Access times generated by simulation.

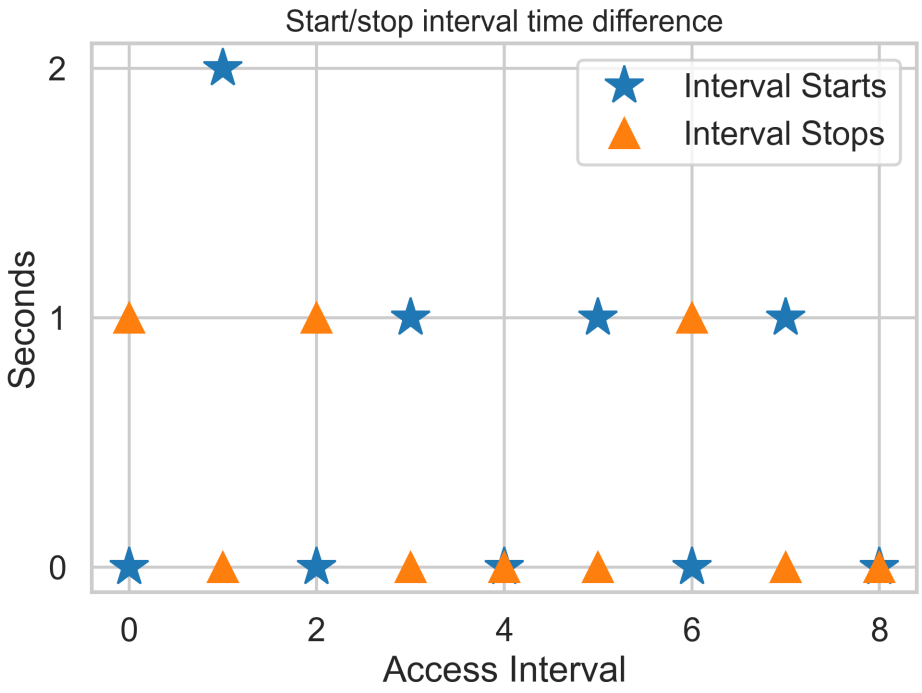

Figure 3-5: The difference in start and stop times for access intervals calculated by STK and the Python simulation.

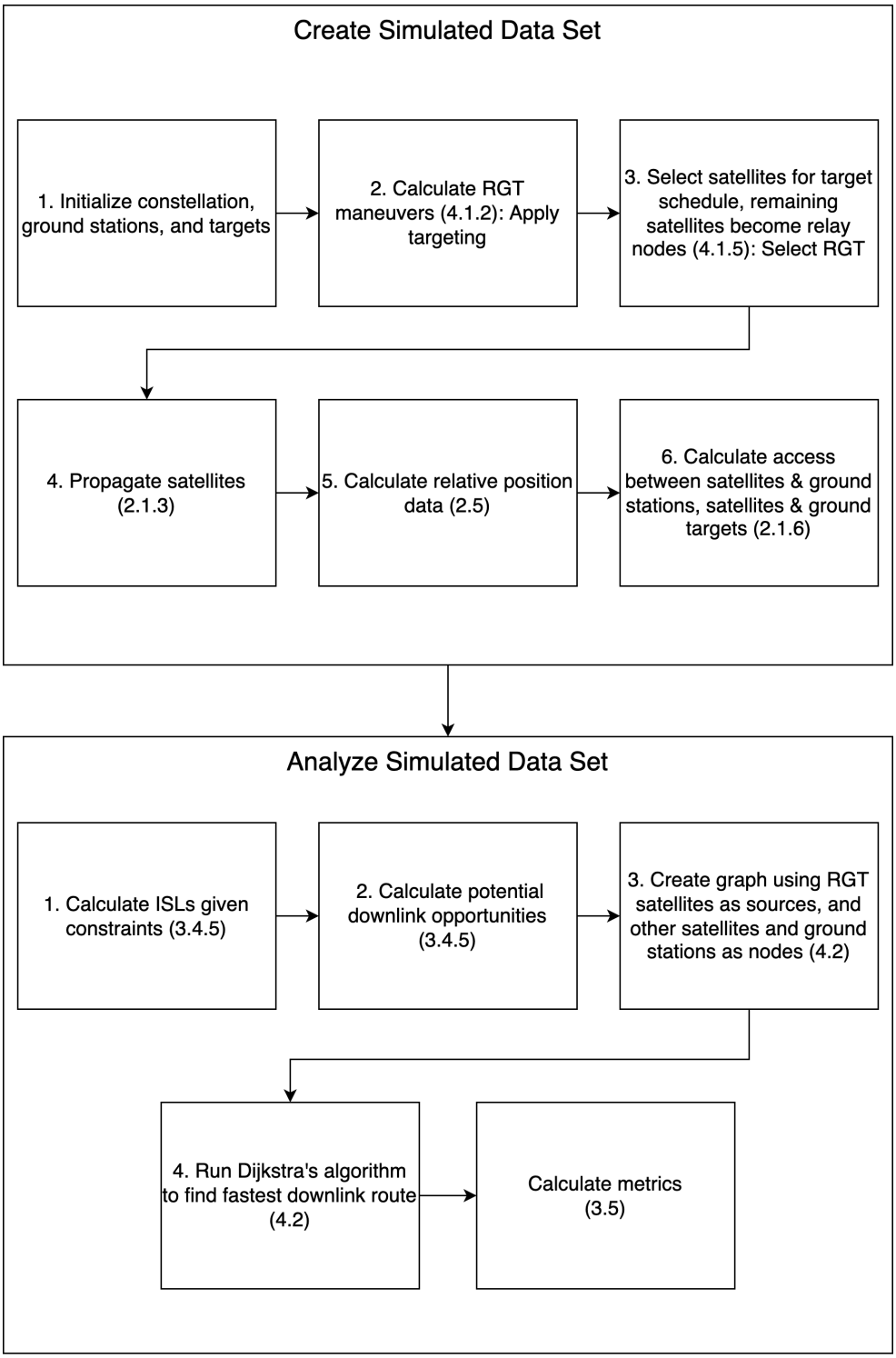

Figure 3-6: Summary of the steps in the Python simulation tool. Relevant sections of the dissertation are noted in parentheses.

3.3.1 Description of simulation tool functions

The first set of tools creates a simulated data set (Upper portion of Figure 3-6). The individual tools are described and relevant sections are listed below.

1. Initialize constellation, ground stations, and ground target: The first phase of the software architecture initializes the satellite constellation, ground stations, and the ground target of interest. For a constellation designer or operator, the constellation and ground stations will be known *a priori*. The ground target of interest represents an unplanned event such as a natural or man-made disaster that cannot be known *a priori*.

2. Calculate burn schedules for RGT maneuvers (Section 4.1.2): The planner determines the burns that will move all satellites into a RGT orbit that will overfly the ground target of interest.

3. Select best satellites to enact schedule (Section 4.1.5): The scheduler selects the best satellites to perform the scheduled burns to enter into a RGT orbit by evaluating the required drift times. The other satellites are tasked to be potential relay nodes.

4. Propagate satellites (Section 2.1.3): All satellites are propagated, including the ones selected to perform the propulsive burns that will allow them to observe the ground target of interest.

5. Calculate relative position data (Section 2.5): Using the position data from the satellite propagation, the software calculates data fields such as line of sight between satellites, relative position vectors, relative velocities, and relative slew rates.

6. Calculate access (Section 2.1.6): The satellite position data is used to determine access intervals between satellites and ground stations as well as satellites and the ground target of interest.

The second set of tools analyzes the simulated data set (Lower portion of Figure 3-6).

1. Apply constraints for ISL (Section 3.4.5): Constraints derived from satellite models and technological limitations (Table 3.8) are applied to the generated data set to determine when there are feasible crosslink opportunities.

2. Apply constraints for downlink opportunities (Section 3.4.5): Constraints derived from satellite models and technological limitations are applied to the generated data set to determine when there are feasible downlink opportunities from satellite to ground station.

3. Create graph (Section 4.2): Generate a graph over the simulated time of 3 days where satellites that can image the ground target of interest are considered sources, other satellites are considered nodes, and ground stations are sink nodes.

4. Run Dijkstra's algorithm (Section 4.2): Using the generated graph, run the modified Dijkstra's algorithm to find the fastest route to downlink the information to a ground station.

5. Calculate metrics (Section 3.5): With routing established, the software then calculates the metrics: age of information, system response time, and total pass time.

3.4 Simulation models

3.4.1 Satellite models

Base satellite (no propulsion or ISL capability)

The satellites in the simulation are based on both the BlackSky Global satellites (55 kg) and the Planet SkySats (110 kg) [4][19]. Satellites in this weight class are

chosen due to their ability to support larger amounts of propellant, enabling multiple reconfiguration maneuvers.

For the simulation, the remote sensing satellites can only collect images within a 40° cone (full angle) centered on the satellite's nadir vector. The half angle between the subsatellite point and the edge of the cone (off-nadir angle) is 20°. This constraint is a conservative estimate from ESA's Newcomers' Earth Observation Guide that states a typical maximum off-nadir angle for optical imagery is 30° [105].

BlackSky satellites take 179.4 MB RBG images in TIFF format [21]. Each satellite can take 3 images per minute [106]. Conservatively, the longest pass the satellite makes over a ground target with the 20° half angle nadir constraint at the RGT altitude of 505 km is 2 min, which equates to a maximum of 6 images taken during a pass. Making another conservative estimate that each image can be 200 MB, each satellite has a maximum of 1.2 GB, or 9.6 Gb of data to transfer per pass. The smallest image footprint for a BlackSky satellite as of 2022 are taken by Global 3, 7, and 8, which average 26 km^2 per image, while the largest image footprint is from Global 2, which averages 59 km^2 per image [106]. With 6 images, and assuming no overlap, a pass can cover 156 km^2 to 354 km^2 of surface. The satellites have a 1 m resolution [21].

The baseline satellite is modeled after the BlackSky Global satellites. Table 3.3 describes the baseline satellite model, which does not have ISL or reconfiguration capabilities.

ISL capable satellite (No propulsion)

Adding ISL capabilities to the baseline satellite will increase the size of multiple subsystems. The link budget for ISLs in section 3.4.2 is the main driver behind the subsystem changes. It is seen in Table 3.6 that the ISL link budget requires 43 W of transmit power. This model conservatively estimates the mass increase to the power system by assuming two more batteries are needed (3.2 kg total) as well as another kilogram of solar cells (baseline satellite model has 0.58 kg of solar cells) for an additional mass of 4.2 kg. This number is rounded up to 5.0 kg to ensure a

Table 3.3: Baseline satellite model and major subsystems

Specification	**Value**	**Justification**
Dry Mass	50.6 kg	[4]
Wet Mass	55.1 kg	4.4 kg of liquid water propellant [4] 146 g of FE-36 (Pressurant) [4]
ADCS Subsystem Mass	3.06 kg	2 Star trackers (0.16 kg each)[4] 4 Reaction Wheels (0.23 kg each)[4] 3 Magnetorquers (0.42 kg each)[4] 3 Inertial Measurement Units (0.055 kg each)[4] 2 Magnetometers (0.08 kg each)[4] 6 Coarse Sun Sensors (0.005 kg each)[4] 1 Fine Sun Sensor (0.035 kg)[4] 1 GPS (0.24 kg) [4]
C&DH Mass	3.98 kg	Flight Computer (3.98 kg) [4]
Comms (Downlink) Mass	1.14 kg	X-band radio (1.0 kg) [4] X-band antenna (0.14 kg) [4]
Payload Mass	10.9 kg	Telescope (8.32 kg) [4] Baffle (1.0 kg) [4] Mirror (1.3 kg) [4] Camera (0.32 kg) [4]
Power Subsystem Mass	4.77 kg	2 COTS Li-Ion Batteries (1.6 kg each) [4] 1 Power Control Unit (0.99 kg) [4] 72 GaAs Solar Cells (0.008 kg each) [4]
Thermal Subsystem Mass	1.4 kg	2 Radiating Side Panels (0.7 kg each) [4]
TT&C Mass	0.40 kg	UHF Radio (0.14 kg) [4] UHF Whip Antenna (0.0005 kg) [4] UHF Whip Cover (0.0065 kg) [4] S-band Antenna (0.055 kg) [4] S-band Radio (0.2 kg) [4]
Orbit Average Power	80 W	Estimate compared to public SkySat data [107]
Comms (Downlink) Band	X band	[4]
TT&C Band	UHF S	(Space to Ground) [4] (Ground to Space) [4]

conservative estimate. For the communications system, in order to enable ISLs, an X-band radio and X-band antenna are added for an additional 2.73 kg. During routing, links will only be in one direction, and it is assumed the radio can be programmed as both a transmit or receive radio, eliminating the need for an additional X-band radio and antenna combination. To be conservative, this number is rounded up to 2.9 kg (6% margin) to include the weight of peripherals such as cables and extra structure. Lastly, 0.1 kg is added to the thermal subsystem mass to deal with the extra power dissipated by the ISL capability. Table 3.4 contains the satellite model details.

Recon and ISL capable satellites

A propulsion system is added to enable satellite reconfiguration capabilities. In order to minimize maneuver time, the satellite is equipped with the Moog MONARC-22-12 monopropellant thruster. This thruster creates 22 N of force, weights 0.69 kg, has a specific impulse of 228.1 s, and consumes 30 W of power. This thruster was chosen for its size, weight, and power requirements, which is appropriate for a microsatellite. See Appendix A.3 for the complete data sheet.

To determine how much fuel each satellite needs, the ΔV for a reconfigurable maneuver is calculated. The satellite is designed to make at least 5 complete reconfiguration maneuvers over its lifetime. There are three different Hohmann transfers to consider in each reconfiguration maneuver. Figure 4-1 shows the first two maneuvers (GOM to drift, and drift to RGT) but leaves out the last maneuver (RGT to GOM).

The first maneuver takes the satellite from GOM to a drift orbit. Legge investigated drift orbits that differed from GOM orbits by -50 km to +50 km. To increase the speed of the phasing maneuver while also conserving enough fuel to allow the satellites to complete 5 reconfiguration maneuvers, drift orbits 100 km away from the GOM orbits are chosen for this work. For the Walker constellations that are investigated in this work, GOM is at 550 km altitude and the drift orbit is 100 km above at 650 km. Using Equation 2.18, the ΔV is calculated to be 54.15 m/s for the first part of this maneuver (see Appendix C).

The second maneuver takes the satellite from the drift orbit to the specified RGT

Table 3.4: ISL capable satellite model and major subsystems

Specification	**Value**	**Justification**
Dry Mass	58.6 kg	8.0 kg more than baseline satellite 5.0 kg added to power 2.9 kg added to comms 0.1 kg added to thermal
Wet Mass	62.1 kg	4.4 kg of liquid water propellant [4] 146 g of FE-36 (Pressurant) [4]
ADCS Subsystem Mass	3.06 kg	2 Star trackers (0.16 kg each) [4] 4 Reaction Wheels (0.23 kg each) [4] 3 Magnetorquers (0.42 kg each) [4] 3 Inertial Measurement Units (0.055 kg each) [4] 2 Magnetometers (0.08 kg each) [4] 6 Coarse Sun Sensors (0.005 kg each) [4] 1 Fine Sun Sensor (0.035 kg) [4] 1 GPS (0.24 kg) [4]
C&DH Mass	3.98 kg	Flight Computer (3.98 kg) [4]
Comms (Downlink) Mass	1.14 kg	X-band radio (1.0 kg) [4] X-band antenna (0.14 kg) [4]
Comms (ISL) Mass	2.9 kg	X-band radio (1.0 kg) [4] X-horn 23 X-band antenna (1.73 kg) [App A.2] Additional 6% margin
Payload Mass	10.9 kg	Telescope (8.32 kg) [4] Baffle (1.0 kg) [4] Mirror (1.3 kg) [4] Camera (0.32 kg) [4]
Power Subsystem Mass	9.77 kg	4 COTS Li-Ion Batteries (1.6 kg each) [4] 1 Power Control Unit (0.99 kg) [4] 72 GaAs Solar Cells (0.008 kg each) [4] Additional 23% margin
Thermal Subsystem Mass	1.5 kg	0.1 kg more than baseline satellite Accommodating higher power dissipation from ISL
TT&C Mass	0.40 kg	UHF Radio (0.142 kg) [4] UHF Whip Antenna (0.0005 kg) [4] UHF Whip Cover (0.0065 kg) [4] S-band Antenna (0.055 kg) [4] S-band Radio (0.2 kg) [4]
Orbit Average Power	123 W	Additional 43 W compared to baseline satellite (Table 3.6)
TT&C Band	UHF S	(Space to Ground) [4] (Ground to Space) [4]
Comms (Downlink) Band	X band	[4]

orbit. This Hohmann transfer takes the satellite from 650 km to 505 km and requires 78.91 m/s of ΔV (see Appendix C).

The third maneuver returns the satellite from the RGT orbit at 505 km back to a GOM orbit at 550 km and requires 24.75 m/s of ΔV (see Appendix C). In total, the ΔV required to complete an entire reconfiguration cycle is the addition of all three Hohmann transfers and equals 157.82 m/s. To allow each satellite to perform 5 complete reconfiguration maneuvers, the tanks are sized to contain 1000 m/s of hydrazine. This allows for 5 and potentially 6 reconfiguration maneuvers with margin for maneuvers such as station-keeping and collision avoidance. It should be noted that some station-keeping water propellant is already included in the baseline satellite model.

To calculate the theoretical maximum number of events a constellation can cover, the following equation is used:

$$max(N_{events}) = \frac{satellites\ per\ plane}{2} \times max(n_{maneuvers}) \tag{3.1}$$

where N_{events} is the number of events the satellite constellation can cover, and $n_{maneuvers}$ is the amount of maneuvers a single satellite can make. The first term on the right of the equation is constrained by the fact that during each event, only two satellites per plane should enter an RGT orbit given that there is only an ascending and a descending pass per plane (See Section 4.1.1).

In order to size the tank for hydrazine, first additional weight is estimated for each subsystem. The propulsion subsystem, without fuel, is estimated to weigh 7.06 kg, including the 0.69 kg thruster, the tank mass, which will be estimated to be 5 kg (shown in Equations 3.2 to 3.9), and 16% margin. The propulsion mass, 7.06 kg, also happens to be the minimum in-range weight for a propulsion system in the Small Satellite Cost Model (Section 3.6.1). An additional 0.5 kg is added to the thermal subsystem, which places the total thermal subsystem mass at 2 kg. With a final dry weight of 76.65 kg (shown in Equations 3.2 to 3.10), the thermal subsystem mass takes up 2.6% of the total weight, in line with the estimated range of 2% to 5% of

dry weight quoted in SMAD [1]. Additional weight of 0.94 kg is added to the ADCS system and 5.23 kg added to the power subsystem. Adding this weight to the dry mass of the ISL capable satellite (58.6 kg) brings the dry mass of the recon and ISL capable satellite, excluding the tank, to be 72.33 kg.

The following equations outline the methodology for estimating the hydrazine tank mass, satellite dry mass, and satellite wet mass. Starting with Equation 2.39:

$$m_0 = m_f e^{\frac{\Delta V}{g_0 * isp}} \tag{3.2}$$

substituting

$$m_0 = m_f + m_h \tag{3.3}$$

where m_0 is the initial or wet mass, m_f is the final or dry mass, and m_h is the mass of hydrazine propellant. Making the following substitution for m_f:

$$m_f = m_s + m_{tank} \tag{3.4}$$

where m_s[3] is the dry mass without the tank and m_{tank} is the mass of the empty hydrazine tank. One more substitution can be made if the mass fraction of the tank mass to propellant mass is estimated. Looking at an example ArianeGroup hydrazine tank, it can be seen that for 78 L of hydrazine, the tank weighs 6.85 kg (see Appendix A.4). The density of hydrazine at 45°F is 63.59 lbs per cubic foot or 1018.6 kg per cubic meter [108]. Converting to metric units, 78 L of hydrazine equates to 0.078 m^3 of hydrazine, which weighs 79.45 kg. The tank to hydrazine mass ratio is therefore 8.6%. For the tank sizing analysis, the tank is conservatively estimated to be 10% of the hydrazine mass. With this information, substitute the following:

$$m_{tank} = 0.1 \times m_h \tag{3.5}$$

[3] s subscript used for 'structural' mass.

Substituting Equation 3.5 into Equation 3.4:

$$m_f = m_s + 0.1m_h \tag{3.6}$$

Plugging in equations 3.3 and 3.6 into equation 3.2:

$$m_s + 1.1m_h = (m_s + 0.1m_h)e^{\frac{\Delta V}{g_0 * isp}} \tag{3.7}$$

Since the mass of the satellite structure is determined, $m_s = 72.33$ kg, ΔV= 1000 m/s, $g_0 = 9.8$ m/s^2, and $isp = 228.1$ s, m_h can be solved for:

$$m_h = \frac{m_s(e^k - 1)}{1.1 - 0.1e^k} = 43.24\ kg \tag{3.8}$$

From equation 3.5:

$$m_{tank} = 4.32 \text{ kg} \tag{3.9}$$

The total dry mass is then:

$$m_f = m_s + t_{tank} = 76.7 \text{ kg} \tag{3.10}$$

and wet mass:

$$m_0 = m_f + m_h = 119.9 \text{ kg} \tag{3.11}$$

The final satellite design parameters for the reconfigurable and ISL satellite can be seen in Table 3.5.

Table 3.5: Recon and ISL capable Satellite Model and Major Subsystems

Specification	**Value**	**Justification**
Dry Mass	76.7 kg	See Equation 3.10. Includes hydrazine tank.
Wet Mass	119.9 kg	See Equation 3.11. Includes 1 km/s hydrazine.
ADCS Subsystem Mass	4.0 kg	2 Star trackers (0.16 kg each) [4] 4 Reaction Wheels (0.23 kg each) [4] 3 Magnetorquers (0.42 kg each) [4] 3 Inertial Measurement Units (0.055 kg each) [4] 2 Magnetometers (0.08 kg each) [4] 6 Coarse Sun Sensors (0.005 kg each) [4] 1 Fine Sun Sensor (0.035 kg) [4] 1 GPS (0.24 kg) [4] Additional 29% margin
C&DH Mass	3.98 kg	Flight Computer (3.98 kg) [4]
Comms (Downlink) Mass	1.14 kg	X-band radio (1.0 kg) [4] X-band antenna (0.14 kg) [4]
Comms (ISL) Mass	2.9 kg	X-band radio (1.0 kg) X-horn 23 X-band antenna (1.73 kg) [App A.2] Additional 6% margin
Payload Mass	10.9 kg	Telescope (8.32 kg) [4] Baffle (1.0 kg) [4] Mirror (1.3 kg) [4] Camera (0.32 kg) [4]
Power Subsystem Mass	15.0 kg	4 COTS Li-Ion Batteries (1.6 kg each) [4] 1 Power Control Unit (0.99 kg) [4] 72 GaAs Solar Cells (0.008 kg each) [4] Additional 53% margin over ISL-only model.
Propulsion Subsystem Mass	7.06 kg	Monopropellant thruster (0.69 kg) [App A.3] Fuel tank (4.32 kg) [See Equation 3.9] Additional 41% margin
Thermal Subsystem Mass	2.0 kg	0.5 kg more than ISL satellite for propulsion thermal dissipation
TT&C Mass	0.404 kg	UHF Radio (0.142 kg) [4] UHF Whip Antenna (0.0005 kg) [4] UHF Whip Cover (0.0065 kg) [4] S-band Antenna (0.055 kg) [4] S-band Radio (0.2 kg) [4]
Orbit Average Power	150 W	Additional 27 W compared to ISL satellite for propulsion system
TT&C Band	UHF S	(Space to Ground) [4] (Ground to Space) [4]
Comms (Downlink) Band	X band	[4]

3.4.2 Link budgets

The following section describes the link budgets used to determine communication link feasibility in the Python simulation.

ISL link budget

The communications subsystem on the ISL-capable satellites enable communications at large distances and fast data rates up to 80 Mbps. The high level design requirements for the ISL are:

1. Distance: The ISL shall close a link at a minimum of 1250 km to ensure enough time to transmit data.

2. Data Rate: The ISL shall transmit at a minimum 80 Mbps.

3. Frequency: The ISL shall operate in the X-band.

Table 3.6 shows the link budget used to verify the ISL requirements using a 3 dB margin. The link budgets uses the same horn to transmit and receive in the X-band. The power required to close the link (43 W) drives the difference in orbit average power between the baseline and ISL capable satellites.

Space to ground link budget

For the space to ground link, the ground stations are modeled after the Atlas ground station with the lowest X-band G/T, which is in Dubai, UAE, and has a G/T value of 25.4 dBi/K (Appendix A.1). For the space to ground link, the satellites are also designed to use their X-band antenna and radio. See Table 3.7 for the link budget used to model the space to ground, image downlink link. The high level requirements for the space to ground link are:

1. Elevation Angle: The link shall close at a minimum elevation angle of 25° as seen from the ground station.

Table 3.6: Max distance ISL link budget (worst case)

Field	**Unit**	**Value**	**Justification**
Frequency	GHz	8	X-band communication link
Wavelength	m	0.0375	$\lambda = \frac{c}{f}$
Power Input	W	42.66	Required to close budget
Power Input	dBW	16.3	dB conversion: $[dBW] = 10\log_{10}([W])$
Antenna Gain	dBi	23.0	[Appendix A.2]
EIRP	dBW	37.3	Equation 2.31
Distance	km	1250	Requirement
Free Space Path Loss (FSPL)	dB	172.4	Equation 2.32
Other Losses	dB	6	Pointing and line losses
Receiver Gain	dBi	23	[Appendix A.2]
System Temperature	K	125	Example numbers from section 5.5.5 and Table 5.3 in Maral [99]
System Temperature	dBK	21	dB conversion equation
G/T	dBi/K	-2.9	Receiver Gain - System Temp (dBK)
Received Power	dBW	-137.0	EIRP - FSPL - Other Losses + G/T
Boltzmann Constant	dBW/K/Hz	228.6	Constant
Data Rate	Mbps	80.0	Requirement
Data Rate	dBHz	79.0	dB conversion equation
Eb/No	dB	12.5	Equation 2.30
Eb/No Required	dB	9.5	QPSK 10^{-5} BER. Figure 4.29 in [99]
Margin	dB	3.0	(Eb/No) - (Eb/No Required)

2. Data Rate: The link shall transmit at a minimum 400 Mbps. Conservative estimate based on Planet SkySat data rate of 580 Mbps [19].

3. Frequency: The link shall operate in the X-band.

Table 3.7: Worst case (max distance): Space to ground link budget

Field	**Unit**	**Value**	**Justification**
Frequency	GHz	8	X-band communication link
Wavelength	m	0.0375	$\lambda = \frac{c}{f}$
Power Input	W	1.51	Required to close budget
Power Input	dBW	1.8	dB conversion: $[dBW] = 10\log_{10}([W])$
Antenna Gain	dBi	23.0	[Appendix A.2]
EIRP	dBW	24.8	Equation 2.31
Distance	km	1213	Assumes worst case with 600 km altitude orbit with 25° ground station elevation cutoff angle
Free Space Path Loss (FSPL)	dB	172.2	Equation 2.32
Other Losses	dB	8	Pointing, line, and atmospheric loss
G/T	dBi/K	25.4	See Atlas ground station in Appendix A.1.
Received Power	dBW	-129.9	EIRP - FSPL - Other Losses + G/T
Boltzmann Constant	dBW/K/Hz	228.6	Constant
Data Rate	Mbps	400.0	Requirement
Data Rate	dBHz	86.0	dB conversion equation
Eb/No	dB	12.6	Equation 2.30
Eb/No Required	dB	9.5	QPSK 10^{-5} BER. Figure 4.29 in [99].
Margin	dB	3.1	(Eb/No) - (Eb/No Required)

3.4.3 Contact time constraints

There are three cases when objects in the simulation can exchange data: (i) Ground target observation: the satellite collects images of the Earth's surface; (ii) Satellite to satellite: satellites send images from one satellite to another through an ISL; (iii) Satellite to ground: a satellite downlinks information to a ground station. A set of

constraints is implemented to determine when data can move from one object in the simulation to another. This following section details the constraints that are used in the simulation.

Ground target observation

In order for a satellite to observe and image a ground target, the target has to be within the 20° off-nadir cone specified in Section 3.4.1. Additionally, a simple lighting constraint is implemented in the simulation. Since the satellite has an optical camera payload, the target has to be illuminated for a valid observation. The simulation implements a filter that calculates the dot product between the position vector of the ground location and the sun in the Earth-centered frame:

$$\vec{r}_{gt} \circ \vec{r}_{sun} > 0 \tag{3.12}$$

where $\vec{r}_{gt}$ is the position of the ground target and $\vec{r}_{sun}$ is the position of the sun, both with respect to the center of the Earth. A dot product greater than 0 indicates that the ground target is illuminated, allowing the satellite to successfully capture an image.

Satellite to satellite

For satellite to satellite links, this work implements distance, slew rate, and contact time constraints. The distance constraint requiring contact within 1250 km is specified in the link budget (See Table 3.6).

For slew rates, the instantaneous slew rate between the two satellites must be less than 3° per second. See Section 2.5.3 for slew rate calculations. The communications antennas are body-mounted (no gimbal), and therefore the entire satellite bus must be able to slew at this rate to maintain a communications link. This requirement is derived as a conservative estimate as Shell notes in his study that 12U cubesat designs can accommodate 3° per second slew rates while larger 250 kg satellites can achieve 5° per second slew rates [109]. Since the satellite models in this work all fall

between the 12U and 250 kg class of satellites, the conservative value of 3° per second is used.

In order to transfer images between satellites, a continuous contact time of at least 2.5 min must be maintained. From Section 3.4.1, each satellite can obtain up to 9600 Mb of data per pass when collecting images. From Table 3.6, an ISL link can obtain a data rate of 80 Mbps, meaning it would take 2.0 min to transfer 6 images (200 MB or 9600 Mb per 6 images). A buffer of 30 seconds (25%) was added to the constraint to account for processes such as link acquisition. Because this work does not simulate advanced networking algorithms that would allow for piecemeal sending of data, only continuous contact intervals that last longer than 2.5 min are considered valid. If the contact interval is less than 2.5 min, no information is transferred between satellites.

Satellite to ground station downlink

For satellite to ground station transmission, the simulation implements an elevation angle constraint and a contact time constraint. The satellite must be 25° above the horizon to initiate a contact interval as specified by the requirement in the space to ground link in Table 3.7. With a downlink data rate of 400 Mbps, it would take 24 seconds to downlink 9600 Mb of data from a satellite. For the space to ground link, again a 25% buffer is added, so it will take 30 seconds to complete a downlink. Similar to the satellite to satellite link, if the valid contact interval is less than 30 seconds, no information is transferred in the simulation.

3.4.4 High level simulation parameters

Generally, the simulation time resolution is 15 seconds when propagating satellites. However, when there is a scheduled burn, the time resolution is changed so that burns can be simulated on time in the following manner:

1. Let t_n and t_{n+1} be two time steps 15 seconds apart.

2. Let t_b be the scheduled burn time where $t_n < t_b < t_{n+1}$

3. At t_n, the satellite is propagated to t_b

4. At t_b, the burn (ΔV) is applied to the satellite state simulating an instantaneous burn[4]

5. The satellite is then propagated, with the new state velocity, from t_b to t_{n+1}

6. The satellite is then propagated to t_{n+2}, which is $t_{n+1} + 15s$

A time step of 15 seconds is chosen as it is half as long as the shortest contact interval (30 seconds for a space to ground downlink). A shorter time step, while offering higher simulation resolution, would also be more computationally expensive.

The simulation is run for 3 days from ground target initialization to simulate the critical 3 day emergency time window and its importance. This time frame was chosen because according to Zhang and Kerle, the availability of image-derived products is generally low for the first 3 days after a disaster. In an emergency response situation, the most challenging issue is obtaining imagery of areas of interest within the 3 day emergency window [110]. Additionally, a survey of 45 state emergency management agencies found that 91% indicated a need for remote sensing data within the first 3 days [111].

3.4.5 Parameters and constraints summary

Table 3.8 summarizes the simulation parameters and constraints.

[4]An instantaneous burn is used to approximate the monopropellant thruster.

Table 3.8: Simulation parameters and constraints

Simulation Parameter	**Value**
Time Step	15 seconds. Section 3.4.4.
Time Length	3 days. Section 3.4.4.
Simulation Constraint	**Value**
Reconfiguration altitude change	+100 km. Section 3.4.1.
Ground station minimum elevation angle	25°. Section 3.4.2.
Satellite field of view for ground observation	20° half-angle for nadir cone. Section 3.4.1.
Max ISL distance	1250 km. Section 3.4.2.
Max relative slew rate	3° per second. Section 3.4.3.
Minimum time for successful ISL link	2.5 minutes. Section 3.4.3.
Minimum time for successful space to ground downlink	30 seconds. Section 3.4.3.
Lighting Constraint	Ground target must be illuminated. Section 3.4.3.

3.5 Performance Metrics

Three main metrics are used to evaluate the performance of the simulated reconfigurable, inter-satellite-link enabled remote sensing constellations: AoI, SRT, and total pass time. These metrics evaluate the responsiveness and overall monitoring capability of the systems.

The three metrics are not industry standard published information. However, insight can be gleaned from published performance statistics. Planet's SkySat constellation claims to be able to provide actionable insights up to 7 times per day while taking 3 hours to downlink an image after capture [112]. The minimum (best performing) average AoI is estimated to be 3.42 hrs, which is derived from their stated value of 7 downlinks per day. NASA's Land, Atmosphere, Near real-time Capability for EOS (LANCE) also provides imagery 3-5 hours after observation, which estimates to an average AoI of greater than 3 hrs since AoI also incorporates the time it takes to task and observe a target [113]. BlackSky claims to be able to visit mid-latitude locations a maximum of 15 times a day and received first images after launch within 24 hrs [114][115]. The minimum average AoI is estimated to be 1.6 hrs at mid-latitude locations. The reader should note that these statistics are provided by Planet and BlackSky, so they are biased to provide the best performing examples and highlight the highest-end of the respective system's performance estimate. To obtain a more direct estimated performance, the BlackSky constellation was input into the same simulator used by this work. The BlackSky constellation produced an average AoI of 15.3 hrs, SRT of 15.7 hrs, and total pass time of 4.4 min. See section 6.4.5 for more details.

3.5.1 Age of information (AoI)

AoI measures the freshness of data collected from a given observation target. It is a better metric than average revisit time for determining useful, periodic status updates of a target. Legge highlighted the issues with average revisit time as there are statistical features that may contribute to a misunderstanding of the usefulness

of passes [38]. For example, revisits that are clumped together can lower the average revisit time metric, however; the amount of new information may be limited if the observed phenomena changes on a time scale longer than the time between revisits. An observer will receive more useful information regarding a phenomena that changes on an hourly basis if they receive updates every hour, rather than 3 updates within the first hour, and 3 more updates in the fifth hour. Legge devises a new metric that he coined persistence, which is not skewed by statistical outliers that affect average and maximum revisit time.

Legge's persistence metric pertains to satellite passes over a target area, and AoI builds upon persistence by including the time it takes to downlink the image, capturing the utility provided to the end users to the data. In addition to closing the data collection and transfer loop, AoI also differs from persistence in a few ways. The most important difference is that the metrics have inversely desired values: The persistence metric wants to be maximized while AoI should be minimized for better performance. Additionally, persistence sets a desired temporal resolution where observations at the desired cadence produce a maximum utility function value of 1. Any observation that occurs before the desired pass time is capped at a function value of 1. Conversely, overdue passes continually increase the AoI as there is no cap in metric value. Lastly, there is no benefit in persistence to observing at a higher frequency than the desired temporal resolution, while AoI continually benefits from higher frequency passes as long as the data can be downlinked in a timely fashion.

AoI is also used by Kennedy in his work, and this work explores the effect of reconfigurable constellations on this metric [70]. An example graphical representation of AoI can be seen in Figure 3-7.

To evaluate the performance of the constellation over the course of the simulation, this work uses the average AoI. The average value of the AoI function, Δt, is seen in Equation 3.13:

$$\overline{AoI} = \frac{1}{T}\int_0^T \Delta t dt \tag{3.13}$$

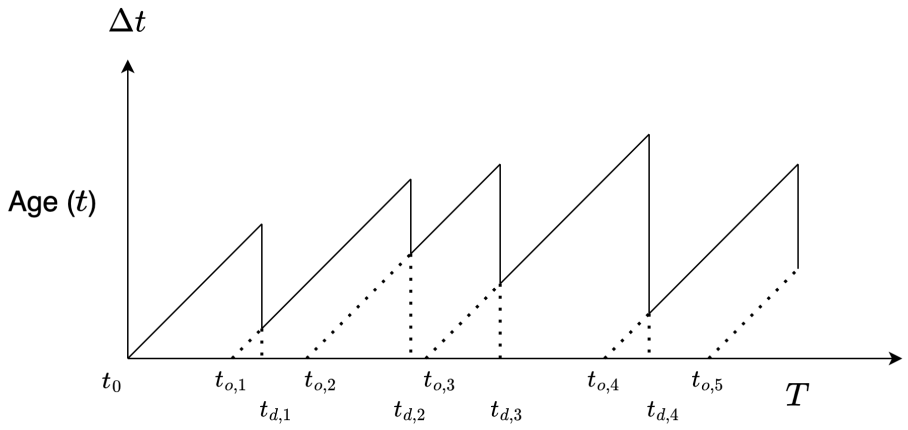

Figure 3-7: The sawtooth function that characterizes Age of Information, Δt. t_0 is the time at the initiation of the phenomena to observe, $t_{o,n}$ is the nth observation of the target, $t_{d,n}$ is the downlink of the nth observation, and T is the length of the observation interval. Note, because both x and y axes are in units of time, the slope of the sawtooth is equal to 1, except at the downlink times.

Equation 3.13 can be simplified because the slope of the sawtooth is 1. This allows us to break down the sawtooth function into a series of isosceles triangles that make up half a square, with the diagonal of the square as hypotenuse. Using this information, Equation 3.13 can be calculated using Equation 3.14, where T is the length of the observation interval, and N is the number of observation/downlink pairs.

$$\overline{AoI} = \frac{1}{T}\sum_{i}^{N}\frac{(t_{d,i} - t_{o,i-1})^2 - (t_{d,i-1} - t_{o,i-1})^2}{2} \tag{3.14}$$

One should note the two edge cases at the beginning and end of the simulation. For the first term in the summation, only the first term in the numerator is used to capture the time from the simulation start to the first downlink so that $t_{d,i} = t_{d,1}$, $t_{o,i-1} = t_0$, and the second term in the numerator is being ignored. The second term is ignored since there were no previous downlinks or observations.

At the end of the simulation, a substitution is made: $t_{d,i} = t_f$, where t_f is the time at the end of the simulation. This ensures that AoI calculations for every scenario end at a standard stopping point. If this last term is ignored and the metric purely followed Equation 3.14, then the last term would be calculated with the last downlink.

However, the last downlink may occur 2 days or 30 seconds before the end of the simulation, so keeping track of the time until the end of the simulation ensures the metric is not skewed.

In this work, the average AoI is reduced by reconfiguring the constellation into repeat ground track orbits, which will increase the number of passes over the target location. Additionally, intersatellite links are utilized to decrease the time from observation and downlink. Lowering the AoI will allow responders to disasters to have updated, pertinent information to make informed decisions.

3.5.2 System response time

Like AoI, system response time (SRT) is a measure of a system's responsiveness. However, unlike AoI, SRT is a more acute metric that measures the time from the incident start to when the first image is downlinked. AoI, on the other hand, includes the ability to monitor the ground target. Separating out the first pass and image downlink is important because in many cases, the first image will give the most information about how the target has changed. For example, an image before and after an earthquake or mudslide occurs can provide valuable information to what infrastructure is damaged or unusable. Further imaging may provide progressively less valuable information. However, there are continually evolving events where obtaining a lower average AoI will be more valuable than a shorter SRT. For instance, a wildfire will need to be constantly monitored for evolutions in intensity and direction of spread, and each progressive downlinked image will provide continually relevant updates of the situation.

The activities that are considered in calculating SRT can be seen in Figure 3-8. A description of each activity is also described here:

1. Incident occurs: This is the time that the network becomes aware of a target and decides to send commands to initiate monitoring of this location. Time lapse considered negligible for this step.

2. Transfer commands to ground station: The observation task is sent through the

terrestrial network to a ground station which can communicate the task to a satellite in GEO. Time along the terrestrial route is considered negligible.

3. Uplink command to GEO satellite: Command is uplinked to a network of GEO satellites such as the Tracking and Data Relay Satellite (TDRS), which will have access to all the satellites in LEO. This method is based off of Capella Space's own tasking strategy which routes image scheduling through Inmarsat's GEO communications constellation [116]. Transmit time from ground to GEO and from GEO to LEO takes hundreds of milliseconds at most. Time during this step is also considered negligible when compared to SRTs calculated in this work, which is on the order of and hours.

4. GEO satellites task EO satellites in LEO, transmitting thruster activation times (burn schedules) and image tasking. The satellites stay in contact to update data routing as needed. Again, this is performed using radio transmissions so transmit time is negligible.

5. Select EO satellites move into RGT orbits: Satellites that are chosen as observers move into their respective drift orbits and then their respective RGT orbits. The time spent during this leg is dependent on the amount of phasing the satellite has to complete in order to attain the correct argument of latitude for the desired RGT orbit.

6. Image tasking: Once in the desired RGT orbit, the satellite waits until it passes over the ground target to image the location. Time in this leg depends on the target location. The RGT orbits are expected to make a direct pass over the target location once a day.

7. Route image to downlink satellite: Image is sent via radio transmission through the planned route, which may include other satellites or may be sent direct to the ground station. Time is dependent on when satellites have communication contact with other satellites in the network, the size of the image, and the link data rate.

8. Image downlink: The image is downlinked to the ground network. Time depends on when the downlinking satellite passes a ground station.

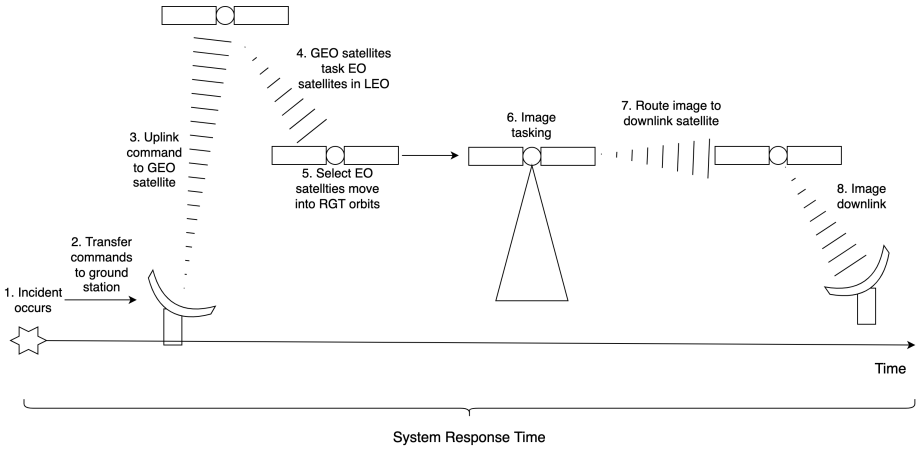

Figure 3-8: The system response time chain that is considered when calculating this metric. Figure created by author.

3.5.3 Total pass time

The total pass time metric is used to evaluate the imaging opportunities a constellation has of the target ground site. Total pass time is defined as the total amount of time a satellite has access to a ground target site. In this work, the constraint requires that the ground target site falls within the payload nadir cone, which defines where a remote sensing payload can acquire images. Like SRT, total pass time indirectly affects AoI, since more passes allows average AoI to be lower as long as the data is downlinked. Looking at raw total pass time provides an intuitive way to evaluate scenarios. Factors such as the number of passes and the quality of passes affect raw total pass time. More passes would increase total pass time, and passes that occur closer to zenith from a ground target are longer, also increasing total pass time. RGT orbits are specifically designed to improve pass quality by targeting direct overpasses, increasing the average time of each pass, and by increasing the number of overall passes of the ground target. From an end-user standpoint, more pass time would equate to more data per pass, which could translate to greater coverage area or more angles to view an area of interest.

3.6 Cost Model

This section describes the models used to estimate the cost of deploying the constellations being studied in this work. There are three basic methods to estimate costs: bottom-up cost estimation, analogy-based estimation, and parametric estimating. The first method, bottom-up estimating, requires identifying the required parts and labor and estimating their costs. This method is often used when the design of a project has matured, reducing the amount of uncertainty in parts and labor estimates. The second method, analogy-based estimation, references the cost of a similar object or project, and then adjusts the estimate for the current object or project for size and complexity. The third method, parametric estimating, uses cost estimating relationship (CER)s, which are mathematical equations that express cost as a function of parameters [1]. Parametric estimating is also often referred to as top-down estimating, as costs are derived from high-level design specifications and requirements.

This work uses a combination of all three methods. Some specific parts, such as the antenna horn, are picked out and used as part of the satellite model in Section 3.4.1, leading to some bottom-up cost estimation. Other parameters such as the power subsystem mass for the ISL and reconfigurable capable satellites use the second method, analogy-based estimation, because the value is relative to the size required for the ISL-only capable satellites. Lastly, the final costs in this work are derived from parametric estimation through the Small Satellite Cost Model (SSCM) software.

Other cost models that were considered include USCM8, which is modeled off a database of larger satellites and is not as accurate for small satellites, and COCOMO 81, which is used for estimating software costs. SSCM is chosen because it estimates the costs of satellites in the same class as the satellite models in Section 3.4.1, and also because it is free to obtain and use for US citizens [117].

3.6.1 SSCM

The SSCM is developed by the Aerospace Corporation to estimate the costs of small satellites up to 1000 kg. It was originally developed in the 1990s, as the industry shifted towards building smaller satellites with commercial off-the-shelf components. The heritage cost models predict the costs of small satellites poorly, so NASA sponsored the Aerospace Corporation to develop small satellite CERs until the late 1990s when funding for SSCM switched over to Aerospace Corporation Internal Research and Development Funds [118][119].

The Aerospace Corporation gathered data from 83 small-satellite programs in order to develop the CERs that underpin the cost estimates in SSCM [120]. SSCM takes in various inputs such as satellite wet mass and beginning of life power to provide cost estimates for each individual subsystem, broken down into power, structure, attitude determination and control system (ADCS), propulsion, telemetry and telecommand (TT&C), command and data handling (C&DH), and thermal. Additionally, cost estimates are provided for assembly, integration, testing, program management, systems engineering, launch support, and orbital operations support. Ground station, radio frequency licensing, and propellant costs, while not explicitly stated in the SSCM manual, are all assumed to be included in the SSCM cost output for this work. Lastly, SSCM provides cost estimates for both recurring and non-recurring satellite costs, a feature very useful for constellation cost estimating where recurring costs drive the overall cost as multiple satellites are being built.

SSCM cost estimates

The satellite models in Section 3.4.1 were input into SSCM to obtain an estimate for the recurring and non-recurring costs for the mission for the 2024 fiscal year. For the baseline satellite (Table 3.3), SSCM also requires an estimate for development time, which is estimated as 18 months. For the ISL capable satellite (Table 3.4), the development time is increased by 6 months to 24 months total. For the ISL and reconfiguration capable satellite, the development time is increased by 3 months to

27 months total. For satellites larger than 100 kg, which applies to the ISL and reconfiguration capable satellite but not the baseline or ISL-only capable satellite, SSCM also requires an estimate for mission design life, which was estimated to be 24 months. The results output by SSCM are shown in Table 3.9.

Table 3.9: SSCM cost outputs in FY24

Costs (FY24$M)	**First Unit**	**Recurring**	**Non-Recurring**
Baseline Satellite	8.7 ± 1.1	4.7 ± 0.6	4.0 ± 0.5
ISL Capable	11.3 ± 1.5	6.1 ± 0.8	5.2 ± 0.7
ISL and Recon Capable	45.2 ± 8.4	25.1 ± 4.7	20.1 ± 3.7

The costs in Table 3.9 are adjusted for inflation using SSCM's NASA inflation model for the 2024 fiscal year. The cost error associated with the first unit is a standard error (standard deviation) that is derived from the variance associated with SSCM's models and provided in the software. The errors associated with both recurring and non-recurring costs are not provided by the software, but are proportionally calculated and derived from the first unit error. A few points to note:

1. The baseline satellite model has a recurring cost of $4.7M. The model is based off the BlackSky satellites, and this value agrees with BlackSky's COO claim that BlackSky satellites will cost $3 to $5 each [121].

2. According to SSCM, adding ISL capabilities increases costs by around 30% compared to the baseline satellite, while adding ISL and propulsion capabilities increases satellite costs by 400% relative to an ISL-only capable satellite.

3. The ISL and Recon capable satellite is the only model over 100 kg, and SSCM uses a different set of inputs and CERs for satellites in this weight class. This is one contributing factor as to why the costs are dramatically higher than the other satellite models. For example, the downlink data rate of 400 Mbps is an input for SSCM models greater than 100 kg, but is not an input factor for satellites less than 100 kg. This means that the baseline satellite and ISL-only capable satellite are not penalized for having a high downlink data rate while the ISL and Recon capable satellite is.

4. SSCM has ranges for their input values that statistically fit their models, and a 400 Mbps downlink is 166% greater than their upper limit. For the ISL and recon capable satellites, the C&DH and TT&C subsystems together make up 56% of the subsystem costs, while in the only-ISL capable and baseline satellite models, the two subsystems make up 22% and 14% of the total subsystem costs, respectively. However, it should be noted that a 400 Mbps downlink is possible for remote sensing satellites of this weight class as the Planet SkySats claim to achieve a 580 Mbps X-band downlink, and one could reasonably expect that the C&DH and TT&C subsystems do not make up greater than 50% of the subsystem cost [19]. Improving the communication system's performance with respect to cost will make ISL and recon capable satellites more competitive on a cost basis.

3.6.2 Launch Model

Two different baseline launch strategies are analyzed in this work. The first involves only SpaceX Falcon 9 launches, and the second involves only Rocket Lab Electron launches. While there are cost-saving alternatives by mixing and matching launch vehicles, this approach creates a repeatable baseline for comparison between constellations.

In order to determine how many satellites can fit in a rocket fairing, the satellite size must be estimated. According to the BlackSky FCC application, the physical dimensions of the satellite are 55 cm by 67 cm by 87 cm. This volume will be used for both the baseline and the ISL-only capable satellite model. In order to estimate the size of the ISL and recon capable satellite, the size of the fuel tank must be determined. From 3.4.1, the satellite model has 43.25 kg of hydrazine. A density of 1018.6 kg per cubic meter results in 43,250 cm^3 of hydrazine [108]. Assuming a cylindrical tank with a radius of 27.5 cm (half the shortest dimension of the BlackSky satellite), a cylindrical volume would have to be 18.2 cm in height. Rounding up to 20 cm for tank width, the final dimensions of the ISL and recon capable satellite is estimated to be 55 cm by 67 cm by 107 cm.

Falcon 9 Launch Model

The Falcon 9 is a medium-lift launch vehicle with a 5.2 m diameter fairing with a lift capacity of 22,800 kg to LEO at a price point of $67M (estimate FY24) [122]. Because the Falcon 9 can lift multiple BlackSky-class satellites into a single orbit, a space tug that enables the satellites to move into their respective final orbits is included. This work uses the MOOG COMET as a reference space tug, as there is a publicly available data sheet at the time of writing (See Appendix A.5).

The work makes a conservative assumption that a space tug can fit four satellites. The largest of these is the ISL and reconfigurable satellite, which gets mounted with the shortest side radially outward. The bus has a 31 inch radius, so radially the COMET and satellite (55 cm or 21.7 in) extend roughly 52.7 inches. The diameter of the COMET and satellite structure is estimated to be 105.4 inches.

The Falcon 9 fairing usable dimensions can be found in Appendix A.6. At 380 inches above the bottom of the usable volume, the diameter of the fairing is 132 inches. The largest dimension in the MOOG/satellite structure is the COMET height (42 inches), so 9 COMET ensembles can fit in the fairing comfortably, allowing the Falcon 9 to launch 36 satellites per launch. Using the ISL and recon capable satellites as the upper mass limit, the wet mass of the COMET can be determined. Starting with equations 3.2 and 3.3:

$$m_f + m_h = m_f e^{\frac{\Delta V}{g_0 * isp}} \tag{3.15}$$

where m_f is the dry mass of the COMET plus the mass of the satellites:

$$m_f = 518 \text{ kg} + 4 \times (119.9 \text{ kg}) = 997.6 \text{ kg} \tag{3.16}$$

$\Delta V = 350$ m/s as stated in the data sheet (Appendix A.5) and $isp = 228.1$ s since the COMET uses hydrazine. Solving for hydrazine propellant (m_h):

$$m_h = m_f(e^{\frac{\Delta V}{g_0 * isp}} - 1) = 429.2 \text{ kg} \tag{3.17}$$

making the total mass of the COMET/satellite ensemble equal to 1427 kg. The total payload mass of 9 of these ensembles would then equal 12,841 kg, which is well within the lift capacity to LEO. Repeating the analysis for the ISL only and baseline satellites return ensemble weights of 1,096 kg and 1,056 kg, respectively. In this configuration the launcher is volume-constrained as opposed to mass-constrained.

The next part of the cost model determines if it is worth launching 36 satellites on a Falcon 9 due to the required orbital plane separations for constellation deployment. Using differential RAAN drift (See equation 2.2), the cost model requires that the final constellation plane can be reached in 6 months after launch. The model also assumes the Falcon 9 deploys the COMET/satellite ensemble at 350 km altitude and 60° inclination, with the final orbit in GOM at 550 km and 60° inclination. The main contributing factor for RAAN drift is then the difference in altitude of 200 km. Psuedocode for the Falcon 9 cost model can be seen in Algorithm 3.

Algorithm 3 Falcon 9 launcher cost model

$\dot{\Omega}_{350km} \leftarrow Equation\ 2.2(350km\ altitude, 60°\ inclination)$
$\dot{\Omega}_{550km} \leftarrow Equation\ 2.2(550km\ altitude, 60°\ inclination)$
$COST_{f9} = \$67M$
$planeSeparation = RAAN\ difference\ between\ planes\ (defined\ by\ constellation)$
$constellationPlanes = Defined\ by\ constellation$
$satellitesPerPlane = Defined\ by\ constellation$
$maxSatellitesPerLaunch = 36$
$maxDriftTime = 6\ months$
if $satellitesPerPlane > satellitesPerLaunch$ **then**
    $launchesPerPlane = ceiling(satellitesPerPlane/satellitesPerLaunch)$
else
    $launchesPerPlane = 1$
end if
$\Delta\dot{\Omega} = \dot{\Omega}_{350km} - \dot{\Omega}_{550km}$
$maxDrift = \Delta\dot{\Omega} \times maxDriftTime$
$planesPerLaunch = floor(maxDrift/planeSeparation)$
if $planesPerLaunch == 0$ **then**
    $planesPerLaunch = 1$
end if
$totalLaunches = ceil(constellationPlanes/planesPerLaunch) \times launchesPerPlane$
$totalCost = totalLaunches \times COST_{f9}$

One of the major drawbacks of this algorithm is that it assumes dedicated Falcon 9 launches, so all the Falcon 9's capacity is not necessarily used. For example, a

36/6/0 Walker constellation would require 6 launches with 6 satellites on each launch. Because the cost model doesn't account for concepts such as ride-sharing, these prices can be somewhat more expensive than reality.

Rocket Lab Cost Model

The second launch model is based on dedicated Rocket Lab Electron launches. The Electron rocket is a small satellite launcher with a lift capacity of 300 kg to LEO [123] at a price point of $7.5M (assuming FY24) [124]. For launches specific to this work, Figure 12 in 2020 Rocket Lab's Payload User Guide shows a capability to launch 240 kg to a 550 km, 60° inclination orbit [123]. The price point may also be an underestimate as it is a price given in 2022, yet the author assumes this price for the 2024 fiscal year. This launcher is also volume-constrained as opposed to mass-constrained. It should be noted that BlackSky launched with Rocket Lab, but in order to do so, Rocket Lab had to use an expanded fairing, as two nominal BlackSky satellites will not fit in the fairing according to the Rocket Lab Electron Payload User Guide [125][123]. In order to stay consistent with the public $7.5M FY24 price point, the model in this work does not use an expanded fairing, so only one satellite is launched per Electron. The total cost launch cost is then:

$$totalCost = totalSats \times \$7.5M \tag{3.18}$$

3.6.3 Cost model summary

The cost model has two major inputs, the cost to construct and operate the satellites and the cost to launch the satellites. The SSCM is used to estimate the satellite costs in fiscal year 2024 dollars, while two launcher models, Falcon 9 and Rocket Lab Electron, are used to model the launcher costs. Ground station, radio frequency licensing, and propellant costs are all assumed to be included in the SSCM cost output.

THIS PAGE INTENTIONALLY LEFT BLANK

Chapter 4

Scheduling and planning approach

This chapter describes the approach used to develop the scheduler and planner. The scheduler and planner consists of two parts: The first moves satellites into a RGT orbit that passes over a select ground location and the second part decides the data routing path to get images down to a ground station. The RGT acquisition maneuver consists of three segments, which takes a satellite from its standby orbit (global observation mode (GOM)), into a drift orbit, and finally into a RGT orbit (regional observation mode (ROM)). See Figure 4-1 for an illustration. The data routing approach utilizes a modified Dijkstra's algorithm with time-varying edge weights.

4.1 Repeat ground track acquisition overview

This section describes each segment in the sequence of maneuvers that allows a satellite to acquire the desired RGT orbit, as seen in Figure 4-1. Satellites in reconfigurable constellations begin in global observation mode (GOM), an orbit that the satellites stay in until tasked otherwise. Since GOM is a non-RGT orbit, it allows satellites to acquire desirable RGT orbits. When tasked, satellites begin to maneuver into the desired RGT orbit. When satellites have acquired their RGT orbits, the constellation is in regional observation mode (ROM). The maneuver into ROM is achieved through an intermediate drift orbit, which allows the satellite to phase to the correct orbit location to insert into the desired RGT orbit. The reconfiguration planner, described

in Section 4.1.5, decides which satellites are sent to ROM from GOM.

If selected, the satellite immediately conducts a Hohmann transfer to the designated drift orbit in Segment 1. Segment 1 is conducted as soon as the satellite receives the task. The drift orbit is designed so that the Δa (semi-major axis) between the drift orbit and ROM is larger than the Δa between the GOM and ROM. This design generates a condition where a satellite in the drift orbit will acquire a ROM ground track quicker than if the satellite remained in GOM [38].

The satellite remains in the drift orbit for a predetermined amount of time in segment 2. The drift time varies depending on the initial positions of the satellite and is timed so that one more Hohmann transfer from the drift orbit to ROM altitude will allow the satellite to acquire the desired RGT orbit that passes over the desired ground location. As long as the drift orbit altitude and ROM altitude are known, then the time the satellite spends in each of the Hohmann transfers is known, leaving the drift time as the main variable to solve for in this targeting algorithm [38].

Segment 3 takes the satellite from the drift orbit to ROM. As mentioned above, the time and cost of this Hohmann maneuver is known.

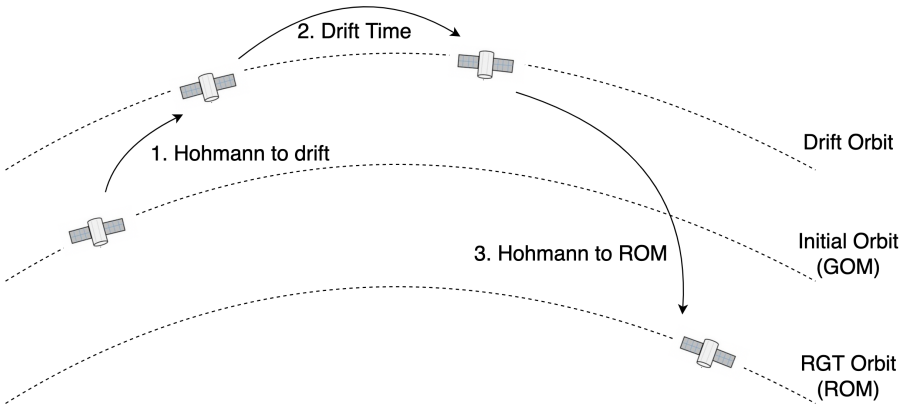

Figure 4-1: Satellite reconfiguration strategy to move from GOM to ROM.

4.1.1 Targeting overview

This section describes how the targeting algorithm is implemented. Referring to Figure 4-1, segment 1 takes a satellite from GOM to drift orbit, segment 2 is the time

spent in the drift orbit, and segment 3 takes a satellite from drift orbit to the desired RGT orbit. Segment 1 is conducted immediately and consists of a Hohmann transfer, for which the time and ΔV costs are known. Since segment 1 is a known quantity in time as well as cost and takes the satellite into the desired drift orbit, the targeting algorithm described here focuses on taking a satellite in the drift orbit down to ROM.

Determining the desired repeat ground track orbit

Determining the desired repeat ground track orbit involves finding the orbit parameters that allow a repeat pass over a point in latitude/longitude. Defining an orbit requires defining the classical orbital elements and then pegging that particular orbit to an epoch.

Eccentricity, Inclination, Argument of Perigee This approach finds a circular RGT orbit with an eccentricity of 0; the argument of perigee is undefined. In order to save propellant, the maneuver will not consist of any expensive inclination changes. Inclination perturbations, such as those from third-bodies such as the moon, are assumed to be negligible on the order of days, which is the timescale used. The target inclination of the RGT is assumed to be the same as the inclination of the satellite moving into the desired RGT.

Altitude Given an eccentricity and inclination, the desired RGT altitude can be set by defining the two RGT parameters N_0 and N_d, which are the number of orbits before the ground track repeats and the number of days before the ground track repeats, respectively. The algorithm targets ground tracks with $N_0 = 15$ and $N_d = 1$, which result in satellite altitudes around 500 to 600 km, as shown in Figure 2-4. Repeat ground tracks with $N_0 = 14$ produce altitudes around 900 km, which result in a larger ground resolved distance in images. Repeat ground tracks with $N_0 = 16$ result in satellite altitudes around 200 to 300 km, which are low enough for drag to quickly bring down satellites unless the satellites spend precious fuel continuously conducting station-keeping maneuvers.

RAAN In order to find the epoch for the orbital parameters, begin with Equation 2.26. This equation calculates the Greenwich Mean Sidereal Time of a RGT given a specific RAAN. For this particular algorithm, the RAAN (Ω_A) of the maneuvering satellite is used. Any RAAN can be chosen, however, making this algorithm applicable to a broader variety of scenarios. A different RAAN would alter the θ_{GMST}, as defined in Equation 2.26. Each combination of RAAN and θ_{GMST} that satisfies Equation 2.26 generates a RGT that passes over the targeted ground location. Solving Equation 2.26 provides a RGT that passes over the target location while the orbit is ascending. In order to solve for the corresponding RAAN for a descending pass, Equation 2.26 can be rearranged as seen in Equations 4.1 and 4.2.[1] Examples of ascending and descending passes can be seen in Figure 4-2.

$$\theta_{GMST} = \Omega_A + \Delta\lambda - \lambda \tag{4.1}$$

$$\Omega_D = \theta_{GMST} + \Delta\lambda + \lambda + \pi \tag{4.2}$$

Epoch Solving Equations 4.1 and 4.2 provide the RAANs of the ascending and descending RGT orbits, Ω_A and Ω_D respectively. It also provides a time, θ_{GMST}, which can be converted into a more conventional time by first converting θ_{GMST} into θ_{GMT} using Equation 2.28, then converting θ_{GMT} into an angle (hour angle recommended). This hour angle can be added to the day of the pass to get the epoch that the satellite will be overhead the targeted ground location. [2]

For example, a satellite with a RAAN of 0° and inclination of 60° desires to pass over a point with latitude 30° and longitude 40° on July 22nd, 2022. $\Delta\lambda$ as defined by Equation 2.27 is calculated to be 19.47°. Plugging into Equation 4.1, θ_{GMST} =-25.53°

[1] It should be noted that using geocentric latitude (instead of geodetic latitude) in the calculation of $\Delta\lambda$ provides results about 0.2° more accurate when using the Astropy WGS84 ellipsoid model.

[2] Note, this particular approach produced the best results when pegging the reference time (when the ECI x-axis is pointed at the sun for noon) to be March 22nd, 2022. It should be noted that the official vernal equinox in 2022 is on March 20th. Additionally, this approach produced marginally better results when the satellite was initiated at an epoch within a few years of the reference time. That is to say, the reference time should be changed to the current year of mission planning if possible.

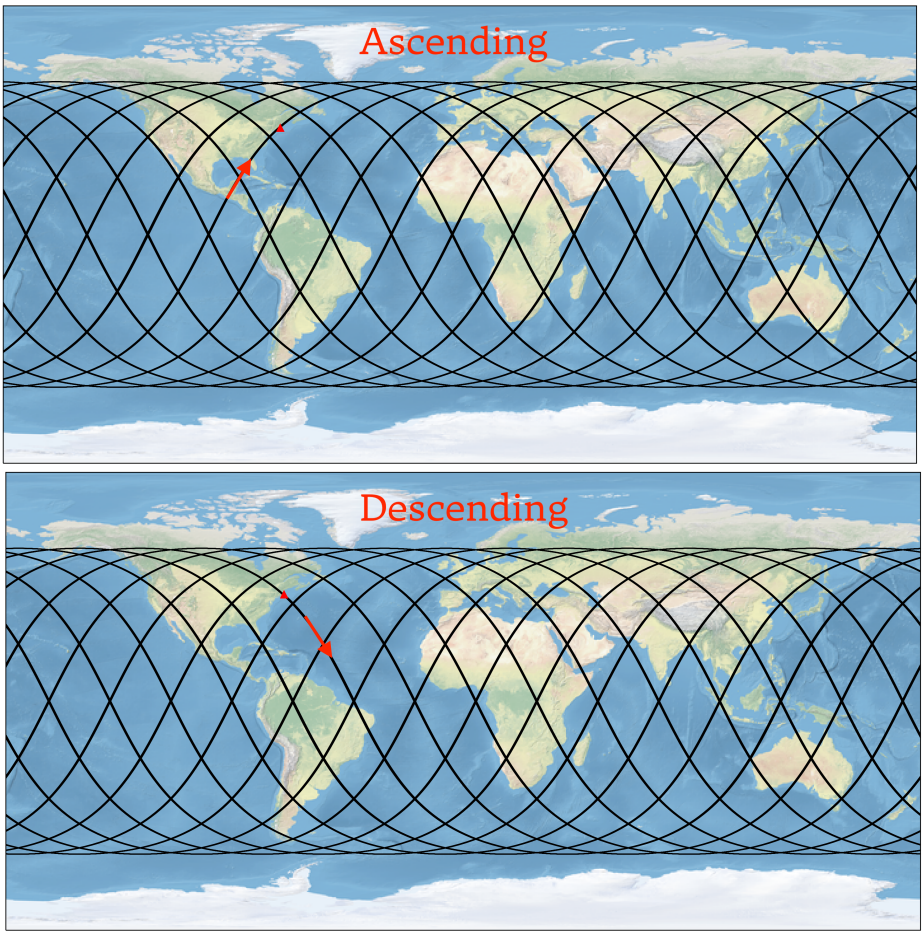

Figure 4-2: The top plot shows a repeat ground track orbit with ascending pass over Boston (red triangle), while the bottom plot shows a repeat ground track with descending pass over Boston.

is calculated. Next, set the reference vernal equinox to March 22nd, 2022 to find that July 22nd, 2022 is 0.3345 years after the reference date. Plugging that value as ΔD into Equation 2.28, the Greenwich mean solar time (θ_{GMT}) is calculated to be 34.02°, which is equivalent to 2.27 hour angles. A satellite with a RAAN of 0° and inclination of 60° will then pass over the target ground location on July 22nd, 2022 at 02h16 GMT.

Argument of Latitude Because the satellites follow circular, inclined orbits, the argument of latitude must be defined. Calculate this angle using the formula for great circles on a sphere. First choose two points on the circle, $\vec{n}_1$ and $\vec{n}_2$. For simplicity, set $\vec{n}_1$ to the unit vector in the direction of RAAN and $\vec{n}_2$ to be the unit vector of the ground location in question. Let $\boldsymbol{G} = [G_x, G_y, G_z]$ be the location of the ground location in Earth-Centered Inertial (ECI) and $\overline{G}$ be the magnitude of G.

$$\boldsymbol{n}_1 = \begin{bmatrix} \cos(\Omega) \\ \sin(\Omega) \\ 0 \end{bmatrix} \tag{4.3}$$

$$\boldsymbol{n}_2 = \frac{1}{\overline{G}} \begin{bmatrix} G_x \\ G_y \\ G_z \end{bmatrix} \tag{4.4}$$

With these two vectors defined, the argument of latitude can then be defined using the following equation:

$$v = \arctan\left(\frac{|\boldsymbol{n_1} \times \boldsymbol{n_2}|}{\boldsymbol{n_1} \cdot \boldsymbol{n_2}}\right) \tag{4.5}$$

where v is the true anomaly of the satellite when it is overhead the ground target.

RGT orbit parameters

The eccentricity, inclination, and argument of perigee are either already known or not applicable. The altitude of the orbit is defined by the constraints that govern an RGT orbit. RAAN and orbit epoch are closely tied together and can be solved using spherical geometry given a desired target location. Similarly, the argument of latitude of the orbit can be solved using great-circle geometry given a desired target location. With this information, the parameters can be defined and pegged to an epoch to generate the desired RGT orbit.

4.1.2 Maneuver planning

Maneuver planning in this work follows Aorpimai et al's methodology to enable a satellite in a drift orbit to target a desired RGT orbit[126]. For every targeted ground location, there are two possible RGT orbits, an ascending pass and a descending pass (see Figure 4-2). Maneuvers are calculated for both ascending and descending passes, and the option requiring the least drift time is selected.

Finding equator crossings

The targeting algorithm is based on the fact that RGT orbits cross the same point on the equator every N_d times (in this work N_d is 1 day). The methodology in Section 4.1.1 defines the RGT orbit. A satellite in this orbit can then be propagated until it crosses Earth's equatorial plane. The longitude of this crossing is one of the equatorial crossings for this particular RGT orbit. The other equatorial crossing points are separated by longitudinal angles of $360°/N_0$, where N_0 is the number of orbits per repeat period N_d.

These equatorial crossings are used for the targeting algorithm when calculating how long a satellite stays in the drift orbit (segment 2 in Figure 4-1). Within the context of this work, the drift orbit is already defined as 100 km higher than GOM. Satellites move into drift orbit immediately using a Hohmann transfer when image tasking is received. The satellite position at the time it receives the task can be

predicted, and therefore true anomaly is also known. The predicted satellite position in the drift orbit is then propagated until it crosses Earth's equatorial plane. The equatorial crossing of the predicted drift orbit, combined with the equatorial crossings of the desired RGT orbit provides information on how far off the satellite in the drift orbit is from its final RGT orbit.

Longitudinal angle

With the equatorial crossing of the RGT orbit and the equatorial crossing of the drift satellite, the longitudinal angle that must be covered until the ground track of the drift orbit overlaps with the ground track of the RGT orbit can be calculated. For a drift orbit with an altitude greater than the desired RGT orbit, the drift orbit ground track moves westward. A drift orbit with an altitude less than the desired RGT orbit has a ground track that drifts eastward. See Figure 4-3 for an illustration.

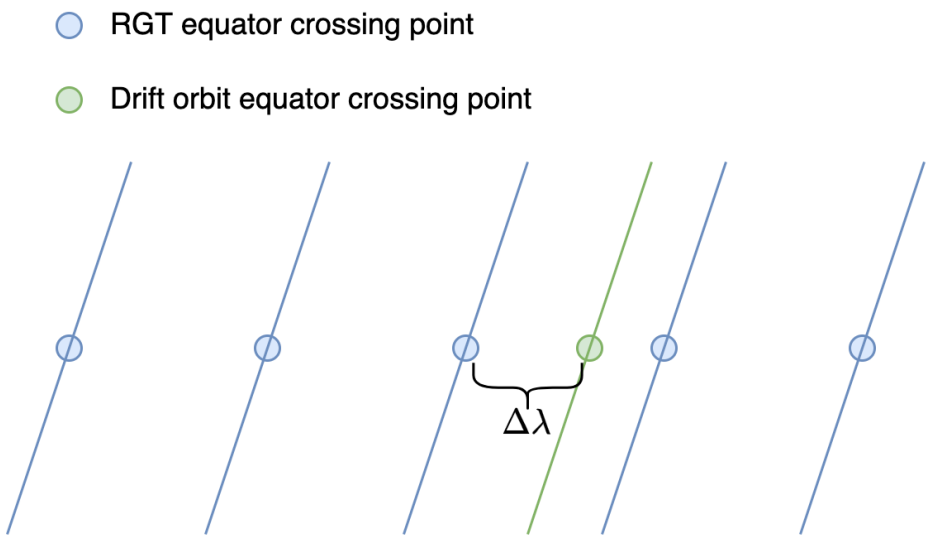

Figure 4-3: A visual of how to calculate the longitudinal distance $\Delta\lambda$ that must be traveled before the satellite ground track overlaps the desired RGT. In this case, the drift orbit is higher than the desired RGT orbit so the nearest westward equatorial crossing is chosen.

Drift time

Every orbit, the relative drift rate between a satellite's current orbit and the desired RGT ground track drifts is [126]:

$$\Delta L = \frac{3}{2} P_{N_0} (\omega_e - \dot{\Omega}_0) \frac{\Delta a}{a_0} \tag{4.6}$$

where ΔL is the relative drift rate per nodal period between the desired RGT and the current drift orbit. P_{N_0} is the period of the desired RGT, ω_e is the rotation rate of the Earth, $\dot{\Omega}_0$ is the drift rate of right ascension of the ascending node of the desired RGT orbit (see Equation 2.2), Δa is the difference in altitude between the current (drift) orbit and RGT, and a_0 is the semi-major axis of the desired RGT.

The average drift rate, $\Delta \dot{L}$, is the drift rate per orbit: ΔL divided by the nodal period of the current orbit.

$$\Delta \dot{L} = \frac{\Delta L}{P_N} \tag{4.7}$$

where P_N is the nodal period of the drift orbit.

The total longitudinal angle that must be traversed is a function of the drift orbit, drift time, Hohmann transfer orbit, and Hohmann transfer time.

$$\Delta \lambda = \Delta \dot{L}_{DRIFT} \times t_{DRIFT} + \Delta \dot{L}_{HOHMANN} \times t_{HOHMANN} \tag{4.8}$$

Except for t_{DRIFT}, all variables in this equation are known, so solving for t_{DRIFT} allows us to calculate the last missing piece of the targeting algorithm:

$$t_{DRIFT} = \frac{\Delta \lambda - \Delta \dot{L}_{HOHMANN} \times t_{HOHMANN}}{\Delta \dot{L}_{DRIFT}} \tag{4.9}$$

4.1.3 Targeting algorithm summary

The maneuvers take a satellite from GOM to ROM, and a summary of these burns can be seen in Table 4.1. The first step involves immediately taking the satellite in GOM to a predetermined drift orbit using a Hohmann transfer. For this work, a drift orbit of 650 km is chosen as it is 100 km greater than the GOM altitude of 550 km. The maximum altitude difference was selected because this work focuses on responsiveness, measured by AoI and SRT, and greater altitude change decreases drift time, improving system responsiveness. This approach then determines the longitudinal drift required to acquire the desired RGT orbit and calculates the required drift time for the acquisition. The planner schedules another Hohmann transfer after the drift time to take the satellite from the drift orbit to the desired RGT.

4.1.4 Maneuver verification

In order to ensure the maneuvers function as expected, they are tested over a variety of ground targets. The results are evaluated based on the amount of total access time available to a satellite that executed the targeted algorithm versus the same satellite that did not make the maneuvers.

Example scenario

The example satellite is at an altitude of 550 km, an eccentricity of 0, an inclination of $60°$, a RAAN of $90°$, and an argument of latitude of $-10°$.

A series of ground targets are selected, each with a longitude of $-57°$ and latitudes from $-60°$ to $60°$ in steps of $5°$. Since average satellite pass times are dependent on latitude but not longitude, longitude was not varied to save computation time. A detailed discussion on the mathematical equations governing access time dependence on latitude and longitude can be found in Washburn's work [127].

Two satellites, one that performs maneuvers, and one that did not perform maneuvers, propagate for 7 days with 15 second time steps. The total access times over the selected ground target were calculated and compared.

At Time	Definition	Calculation	Notes
$t_{H1-Elliptical}$: Time at tasking.	Time when moving satellite into elliptical orbit during 1st Hohmann transfer to move from GOM to drift orbit	Hohmann elliptical transfer burn to predetermined drift orbit	In elliptical transit orbit for time $t_{H1-transit}$
$t_{H1-Circular} = t_{H1-Elliptical} + t_{H1-transit}$	Time when circularizing orbit at drift altitude during 1st Hohmann transfer	Hohmann circularizing burn at drift orbit	Remains in drift orbit for t_{drift}, which is calculated in Section 4.1.2
$t_{H2-Elliptical}$: $t_{H1-Circular} + t_{drift}$	Time when moving satellite into elliptical orbit during 2nd Hohmann transfer to move from drift orbit to ROM	Hohmann elliptical transfer burn from drift to desired RGT	In elliptical transit orbit for $t_{H2-transit}$
$t_{H2-Circular}$: $t_{H2-Elliptical} + t_{H2-transit}$	Time when circularizing orbit at ROM altitude during 2nd Hohmann transfer	Hohmann circularizing burn at RGT altitude	At desired RGT orbit

Table 4.1: The four maneuvers to take a satellite from GOM to ROM.

To get a better understanding of the sensitivity of maneuver planning to a satellite sensor's field-of-view, the access calculations are repeated using satellite nadir cone access half angles from 5° to 90°.

Maneuver Results

The first set of results in Figure 4-4 show a single set of runs where the target latitude is varied, with a nadir half angle constraint of 25° (the full angle field of view covers 50°). Reconfigurability is less useful for latitudes that are near the inclination of the satellite orbit. This can be explained by looking at the non RGT ground tracks in

Figure 2-3. There is more dense coverage at latitudes closer to the inclination of the orbit. The density indicates that there is a higher chance for an access pass at these latitudes, even if the satellites are not in an RGT orbit. Depending on the satellite sensor's field of view, when in a non-RGT, a satellite can achieve access on subsequent passes, but only one pass per day is expected while in an RGT orbit.

There are also cases where the satellite in GOM has slightly more access time than the satellite after moving into ROM. This is due to the fact that the targeting algorithm does not account for J2 perturbations in its Hohmann transfers, which results in orbits that are occasionally inaccurate enough to provide sub-optimal results. The case at 20° latitude is an example of this phenomenon where the RGT satellite has a total pass time of slightly over 2 min but the GOM satellite has a total pass time of a little over 3 min. One last factor is that the satellite in GOM is at a higher altitude than the reconfigured satellite, allowing it to have a larger access footprint on the Earth and increasing the probability of an access pass.

Nadir half angle variation The same target latitude scenario is used, but the size of the nadir half angle is varied. The results are shown in Figure 4-5. While ROM provides higher total access time compared with GOM across these half angles, the access time improvement does not reach more than 5 minutes.

Intentional miss Additionally, a scenario was tested where the ground target was moved to $-45°$ longitude. The shift from $-57°$ longitude is 12° to the west or half the distance between equator crossings of the desired RGT. For this international miss case, the satellite still targets the $-57°$ degree target, so the orbit track separation is 12° between the intentional miss satellite and the satellite in the correct RGT. The total access time between the satellite that intentionally misses its target and the satellite in the correct RGT orbit is compared.

The results of the intentional miss are shown in Figure 4-6. The first observation is that as the nadir half angle constraint increases for an on-target RGT (orange), the usefulness of reconfigurability decreases. This is because when nadir angle constraints

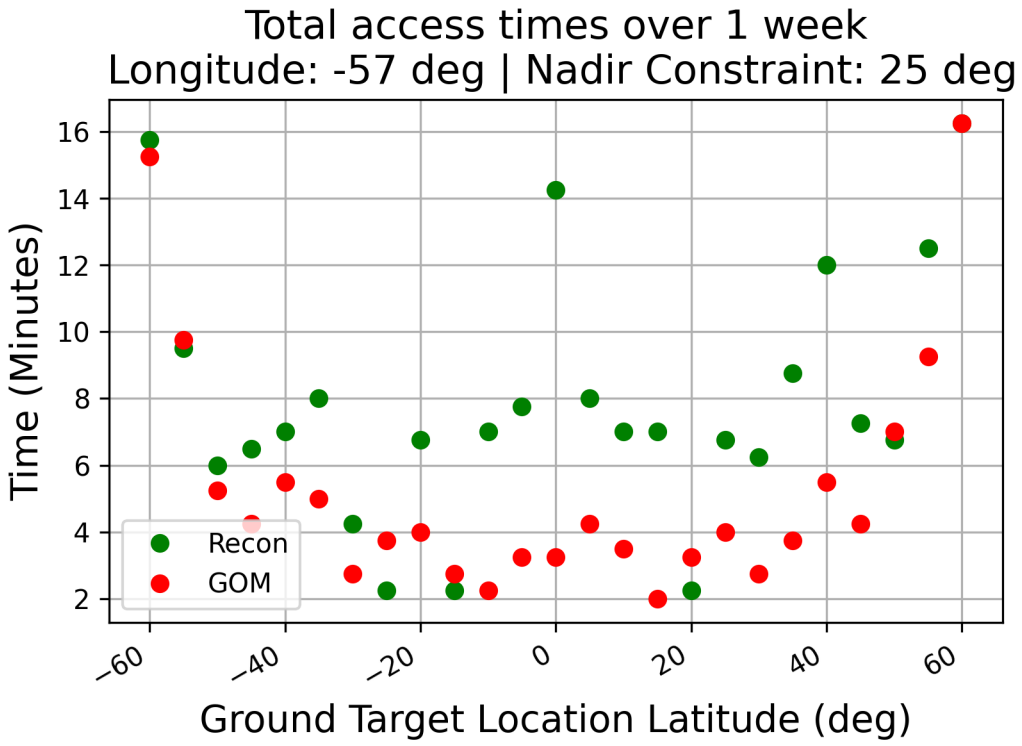

Figure 4-4: The total access times of a satellite implementing the targeting algorithm versus a satellite with no propulsive maneuvers, varied over different target latitudes. At mid-latitudes, post maneuver accesses (green) are higher than accesses without using maneuvers to reconfigure. The nadir constraint is defined by the half angle field of view.

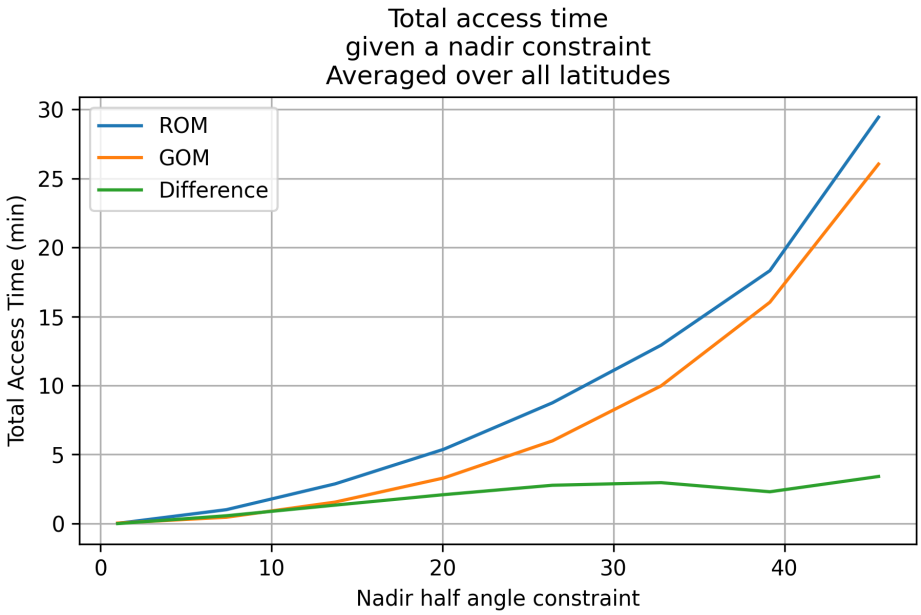

Figure 4-5: The total access time of a satellite in GOM versus a satellite that maneuvers into ROM, averaged over all ground location latitudes.

are large, more ground under the orbit track is seen. With a narrow half-angle nadir constraint of 7 deg, a satellite in an on-target RGT orbit outperforms a satellite in GOM by 125 %, while a satellite designed to purposely miss the ground target under performs a satellite in GOM by 30% at all latitudes. However, any advantage given by an on-target RGT disappears by the time the half-angle nadir constraint exceeds 58°. The curves also coincide and plateau at high nadir angle constraints because increasing nadir accessibility at these angles does not actually provide a larger view of the ground in the field of view, as these angles extend the access cone above the Earth's surface. It is also interesting to note that for large half-angle nadir constraints (such as >70°), being in RGT actually slightly under performs GOM because GOM is at a higher altitude, and therefore has a larger footprint.

4.1.5 Repeat ground track selection

Selection overview

This section describes two approaches to select which satellites will move into a RGT orbit. The maximum number of satellites per plane that should be maneuvered into

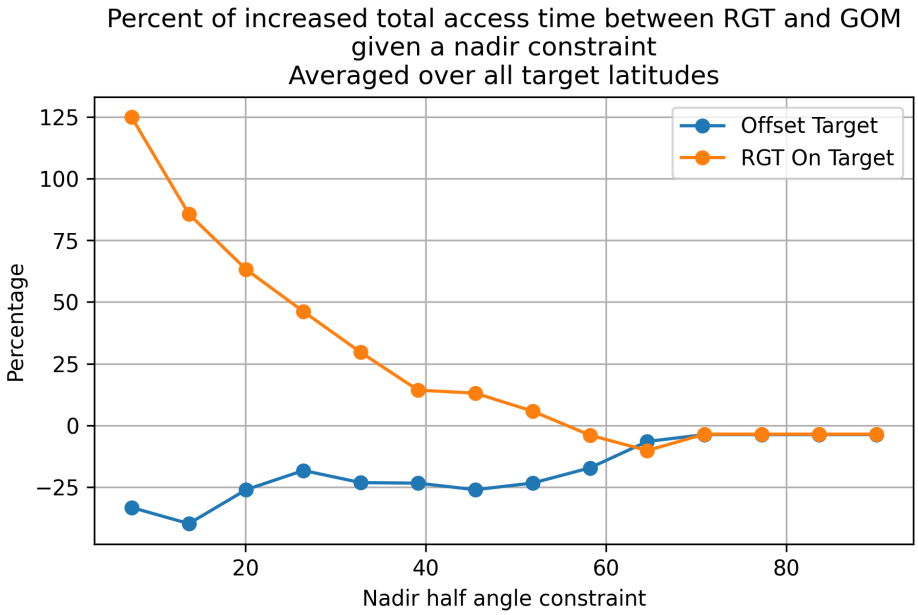

Figure 4-6: The curves show the percentage access change between a satellite in GOM and one that maneuvers to an RGT. The access calculator is also run with an offset ground target (blue), which is 12° to the west, and demonstrates significantly worse performance, as expected. Target latitudes varied between -60° to 60°.

the RGT orbit is 2, since for any given RAAN and inclination, there are only two true anomaly values that would lead to the desired RGT passes: an ascending pass and a descending pass (See Figure 4-2). The first approach selects one satellite in each plane to move into a RGT orbit, irrespective of whether the pass is ascending or descending. The second approach selects two satellites in each plane to move into two RGT orbits, with one satellite moving into a ascending pass orbit and the other into a descending pass orbit.

Both approaches first calculate the targeting solution to acquire the RGT, as described in Section 4.1.2, for each satellite in the plane. The first, simpler, approach selects one satellite per plane to maneuver into the RGT, while the second, improved algorithm selects two satellites per plane. Both selections choose the satellite schedule with the least drift time, which corresponds to the least amount of anomaly change for a satellite to move into the RGT orbit. The selected satellite(s) then execute the RGT acquisition burn and move into observing mode.

Expected Results

There are only two locations per orbital plane that result in a direct overpass of a particular ground location, corresponding to an ascending and descending pass, and this is true as long as the target latitude is less than the orbit inclination. Other edge cases will be discussed below.

For the first approach, only moving one satellite per orbital plane, the expected average revisit time should be:

$$\bar{T}_{revisit} = \frac{24 \text{ hrs}}{p} \tag{4.10}$$

where $\bar{T}_{revisit}$ is the average revisit time, defined as the average time between passes, and p is the number of planes in the constellation.

For the second approach that schedules two satellite maneuvers per plane, there is an expected average revisit time of:

$$\bar{T}_{revisit} = \frac{24 \text{ hrs}}{2p} \tag{4.11}$$

Individual Passes

One interesting point to note is that even though the average revisit times for 2 maneuvering satellites per orbital plane follow Equation 4.11, the actual time between passes is not necessarily uniform. This work analyzes the behavior through the two equations derived from Equation 2.26 [38]. Equation 2.26 describes an ascending node, and the expression for the descending pass can be found by subtracting π.

Note these equations are first order approximations that assume a spherical Earth or no perturbation drifts, but are useful for designing constellations.

$$\theta_{GMST}(ascending) = \Omega + \Delta\lambda - \lambda \tag{4.12}$$

$$\theta_{GMST}(descending) = \Omega - \Delta\lambda - \lambda - \pi \tag{4.13}$$

The relationship between the hour angles of the ascending and descending passes, $\Delta\theta_{GMST}$, can be described as:

$$\theta_{GMST}(ascending) - \theta_{GMST}(descending) = \Delta\theta_{GMST} \tag{4.14}$$

Plugging in Equations 4.12 and 4.13 into Equation 4.14:

$$(\Omega + \Delta\lambda - \lambda) - (\Omega - \Delta\lambda - \lambda - \pi) = \Delta\theta_{GMST} \tag{4.15}$$

Simplifying and substituting $\Delta\lambda$ with Equation 2.27:

$$2\Delta\lambda + \pi = \Delta\theta_{GMST} \tag{4.16}$$

$$2\left(\arcsin\left(\frac{\tan\phi}{\tan i}\right)\right) + \pi = \Delta\theta_{GMST} \tag{4.17}$$

It can be seen from equation 4.17 that the hour angle between ascending and descending passes is a function of both ϕ, the target latitude, and i, the orbit inclination. To find the time to the subsequent pass, find:

$$\theta_{GMST}(descending) - \theta_{GMST}(ascending) = \Delta\theta_{GMST2} \tag{4.18}$$

which results in:

$$-2\left(\arcsin\left(\frac{\tan\phi}{\tan i}\right)\right) - \pi = \Delta\theta_{GMST2} \tag{4.19}$$

The two Equations, 4.17 and 4.19, can be combined into one expression:

$$2\left(\arcsin\left(\frac{\tan\phi}{\tan i}\right)\right) + \pi = \pm\Delta\theta_{GMST} \tag{4.20}$$

Equation 4.20 reveals a set of interesting edge cases and limits. The first limit is defined by the arcsin term. The domain of arcsin is bounded between $[-1, 1]$, so in order for arcsin to stay defined, ϕ must be less than i, which makes sense as an orbit with an inclination less than the latitude of a ground location cannot pass directly

overhead.

Another edge case is when $\phi = i$, driving $\Delta\theta_{GMST}$ equal to 2π, where $\theta_{GMST}(ascending)$ and $\theta_{GMST}(descending)$ are the same. In this case, there is only one direct overhead pass location, which makes sense when the orbit inclination equals the target latitude. The overpass of the target position is when the satellite's argument of latitude equals the target latitude at either the highest or lowest argument of latitude of the orbit.

Yet another interesting edge case is defined when $\Delta\theta_{GMST} = \pi$, indicating that ascending and descending passes are exactly 12 hrs apart. This implies that the arcsin term is equal to 0. In order for the arcsin term to be 0, one of two things must be true. One is that the numerator goes to 0, which means the target latitude is 0°. This means that the orbit's ascending and descending nodes coincide with the ascending and descending RGT passes. The other instance that sends the arcsin term to 0 is when $\tan i$ goes to ∞ so that:

$$\lim_{i \to \pi/2} \frac{tan\phi}{\tan i} = 0 \tag{4.21}$$

which corresponds to an orbit with an inclination of 90°. This also makes sense, as a ground location, regardless of latitude (excluding the 90° latitude case), would have to rotate 180° before passing under the orbit again. Unless the satellite is in one of these scenarios, the time between ascending and descending passes will not be equal.

4.1.6 Repeat ground track selection verification

The selection algorithm was tested using several Walker constellations. The Walker parameters are varied as seen in Table 4.2:

This combination of parameters generates 2678 different constellations. The drift altitude for the reconfiguration is set to 650 km. The target location is set at 42 deg latitude and 72 deg longitude. The RGT targeting and selection algorithm from Section 4.1.2 is then run in each scenario and the average revisit time is calculated. Only the maneuvered satellites are tasked to image the ground target. Each of the satellites are propagated from their initial epoch (See Table 4.2) for 5 days with a

Table 4.2: Walker constellation parameters used in RGT selection verification.

Variable	**Quantity**
Number of planes in constellation	1 to 24
Number of satellites per plane	2 to 10
f parameter	0 to $P-1$, where P is the number of planes in the constellation
Inclination	60°
Altitude	550 km
Epoch	January 1st, 2000 12:00:00.000 UTC

propagation time step of 15 seconds, all maneuvers propagated as well. Access is calculated given a 25° half angle nadir facing conical sensor. Time between passes is calculated by pegging a particular pass to the first propagation time step that results in access between the satellite and the ground location. Results are shown in Figure 4-7.

4.1.7 Discussion of targeting algorithm results

As the number of planes increases, the difference between the theoretical expected revisit times (Equations 4.10 and 4.11) and simulated average revisit times decreases. This can be explained by the number of data points generated by each constellation. For example, in the first approach which only re-positions one satellite over the 5 day simulation period, a constellation with one orbital plane would expect around 5 overhead passes, generating 5 data points that feed into the average revisit time. On the other hand, the constellation with 10 orbital planes would expect to generate around 50 overhead pass data points over the course of 5 days, allowing the average time to converge to the desired target time.

The trade between constellation fuel and average revisit time can affect the approach. Moving 1 satellite maneuver per plane uses less propellant but results in worse revisit time, where moving 2 satellites per plane uses more fuel for a better revisit time. For the constellation designer, there are diminishing returns as the number of constellation planes increase. For example, in the approach that maneuvers 2 satellites per plane, the average revisit time increases from 30 min to 36 min if the

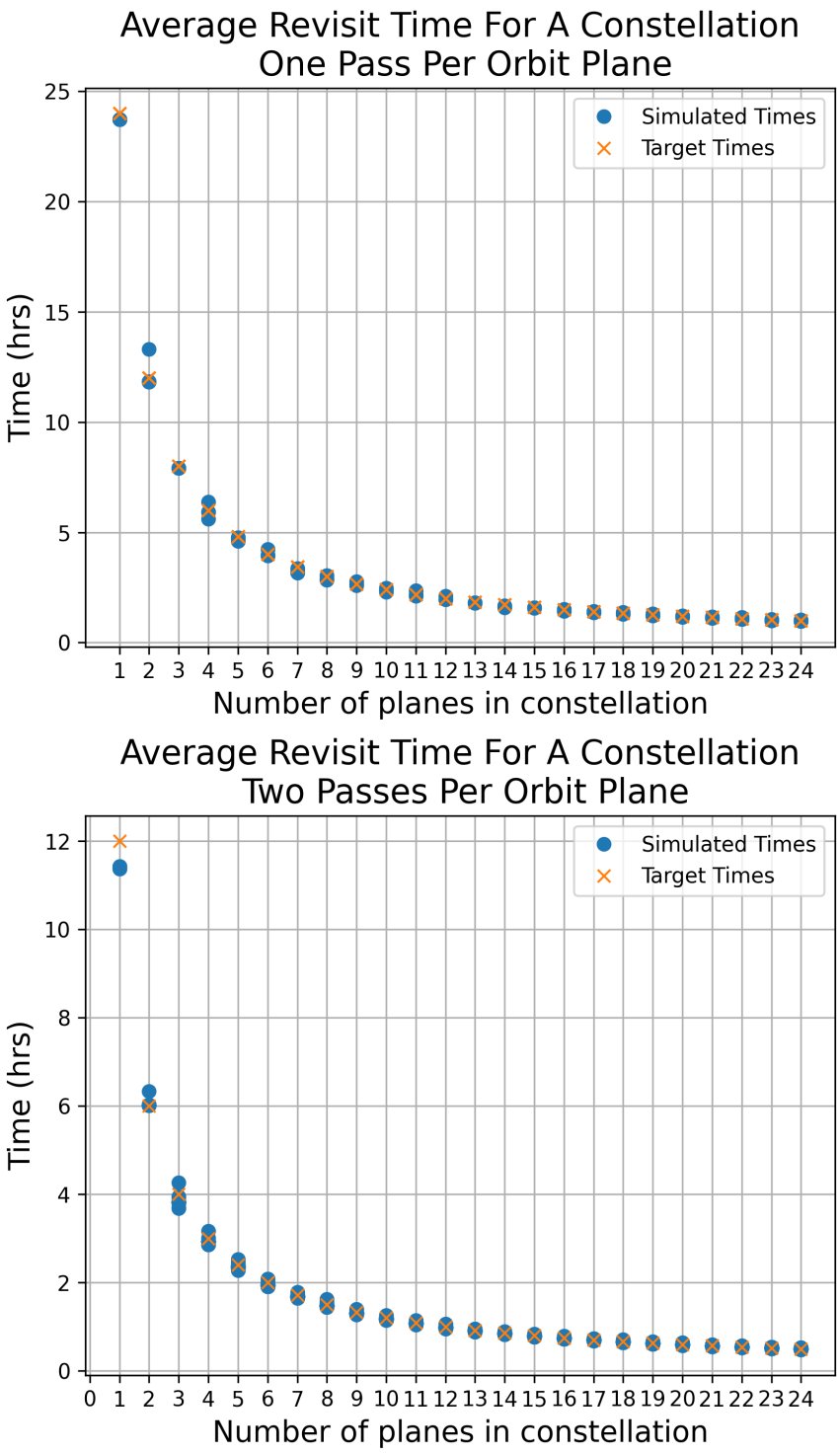

Figure 4-7: Target times are the expected average revisit times, and it can be seen that both approaches produce simulated average revisit times near the expected average revisit rates. Each blue data point represents the average revisit time for a particular constellation. Note the y-axis scales in both plots are different to accommodate the more frequent visits when the approach is to maneuver 2 satellites per plane.

number of planes decreases from 24 to 20 planes. That 6 min increase in revisit time may not be worth the cost of deploying satellites to 4 more planes.

The approximations provided in Equation 4.20 are also seen to be accurate in this simulation. Take the Walker constellation 60°:10/1/0 (i:t/p/f), which had an average time between passes seen in Table 4.3:

Table 4.3: Values for pass time intervals: Predicted and simulated

Time between pass	Predicted	Sim
Descending to ascending (Eq: 4.17)	16.18 hrs	15.89 hrs
Ascending to descending (Eq: 4.19)	7.82 hrs	7.77 hrs

The results in Table 4.3 show that the simulated times are less than the predicted times. This is because the predicted times use a spherical globe model and do not take into account the RAAN drift due to the J2 perturbation. The J2 perturbation would cause the RAAN to decrease by 3.5° per day, partially explaining the shorter time between passes. While not perfectly accurate, for this simulation, Equation 4.20 is still useful as a first-order design tool.

4.2 Routing

Dijkstra's algorithm, from section 2.6, is adaptable to satellite data routing. The nodes of the graph are the satellites and ground stations that transmit and receive data. Dijkstra's algorithm can be applied and modified for various uses within the field of satellite routing. If the satellite nodes are always in communication contact, the algorithm can assume communication between each node is always available, and Dijkstra's algorithm can determine the shortest path to the destination. In this work, the satellites are not always in communication contact and instead, comprise a delay tolerant network where data must be stored on a satellite before it passes the data on to the next node when a contact is available [69].

In order to formulate the problem so that Dijkstra's algorithm finds the quickest downlink route in a delay-tolerant network, the edge weights are set to the time to the next contact with a neighboring node. The minimum value route is then equivalent to

the quickest route in terms of time. However, one major modification must be made regarding the graphs of the original Dijkstra's algorithm. Algorithm 2 works when the edge weights are invariant. In a graph derived from a delay-tolerant network, the time to contact between nodes varies. Dijkstra's algorithm must then be modified to Algorithm 4, where the edge weight is a time-dependent function, and the starting value of the starting node can be set to the current simulation time. While small, these adjustments allow the algorithm to find the shortest downlink times given a network of dynamic nodes.

Algorithm 4 Time-dependent Dijkstra's algorithm

Require: $startNode, graph(edges, nodes), startTime$ ▷ Modification here
  $Q \leftarrow nodes$
  $shortestPaths[n] \leftarrow \infty \; \forall \; n \in nodes$
  $shortestPaths[startNode] \leftarrow startTime$ ▷ Modification here
  while $Q \neq \{\}$ **do**
    Let $u \in Q$ *be the node s.t.* $shortestPaths[u] == min(shortestPaths)$
    for $e \in neighboringEdges$, s.t. e connects u and $neighboringNode$ **do**
      $valueTentative = shortestPath[u] + weight(e, t)$ ▷ Modification here
      if $valueTentative < shortestPath[neighboringNode]$ **then**
        $shortestPath[neighboringNode] = valueTentative$
      end if
    end for
    $Q \setminus u$
  end while

This algorithm is coined the "Earliest Delivery" method by Jain [128]. In order to solve for the variable edge weights, the algorithm must have knowledge of the time-dependent contacts between all nodes, which can be found through satellite propagation and access calculations (Section 2.1.6). The "Earliest Delivery" method is optimal if there are no queued messages at the nodes or the bandwidth between nodes is sufficiently large, allowing all messages to flow through without impediment. In this work, this condition is ensured by filtering out satellite-to-satellite and satellite-ground contacts that are not long enough to transfer all the data in one pass/contact. Graphically, the difference between Algorithms 2 and 4 can be seen in Figure 4-8.

In practice, the time-dependent graph is implemented by setting the starting node value to be the time that routing begins. The algorithm then calculates the time to

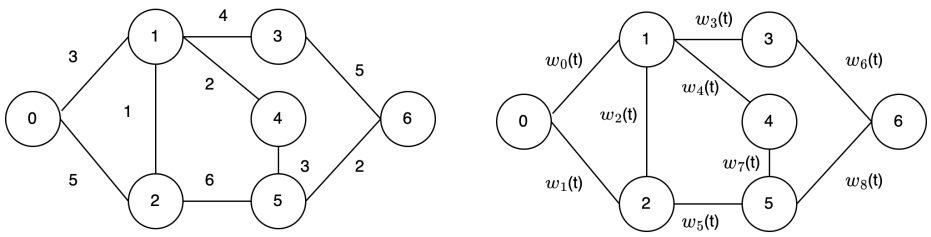

Figure 4-8: A graph with time-independent edge weights on the left where the optimal path from node 0 to node 6 is $0 \rightarrow 1 \rightarrow 4 \rightarrow 5 \rightarrow 6$. However, with delay-tolerant satellite networks, the edge weights are time-varying, as seen on the right.

next contact between the starting node and neighboring nodes. When the algorithm moves on to investigate the next node, the contact times must be recalculated in order to take into account the data arrival time from the previous node.

THIS PAGE INTENTIONALLY LEFT BLANK

Chapter 5

Simulation sensitivity to parameters and constraints

This chapter details the sensitivity of this work to various parameters. Section 5.1 analyzes the sensitivity of the AoI and SRT metrics to parameters that affect ISLs, namely the maximum ISL distance and the minimum amount of time required to transfer data. Section 5.2 analyzes the sensitivity of the maneuver planning approach to the Walker constellation parameters.

5.1 Sensitivity to ISL constraints

In order to understand the sensitivity of the algorithm to the ISL-related constraints, simulations are run varying the maximum ISL distance and minimum time for successful ISL links. Both of these constraints can be directly altered by changing constellation, satellite, or communications subsystem models. Maximum ISL range and contact time are coupled to each other as a longer ISL range will generate longer contact times between satellites. The minimum time for successful ISL links is dependent on the achievable data rate in the link budget. A higher data rate allows the minimum time for successful ISL links to decrease.

Keeping data rate constant and communication frequency constant, the maximum ISL distance is directly dependent on the design parameters for transmit power and

antenna gain. A satellite designer can increase the maximum ISL distance by implementing more solar panels or using a larger gain antenna coupled with appropriate pointing capabilities.

5.1.1 Simulation setup

The constraint analysis simulates the BlackSky constellation and ground stations as outlined in their 2019 FCC application [4]. The satellite initialization parameters are listed in Table 5.1. All satellites are assumed to be circular (eccentricity=0) orbits. It should also be noted that the satellites are initialized in three phases, with subsequent deployments 90 days and 180 days after the first 4 satellites are initialized. After initialization, the simulation propagates all satellites to the same epoch (2020-09-27 00:00:00.000).

The ground station network is also taken from the 2019 FCC application, and is displayed in Table 5.2. An interesting point to note is that the ground station at Svalbard, and also potentially Fairbanks, is at a latitude that is unreachable by the satellites in the proposed constellation given the maximum satellite inclination of 60°.

To test sensitivity, the constellation is initialized and run over the scenarios and constraints as seen in Table 5.3. The constellation is run over 432 different ground targets. For each ground target, the constraints are varied between the 7 max ISL distance values and 11 minimum times for successful ISL links for a total of 33,264 data points.

5.1.2 Sensitivity Study Results

The results from the sensitivity study are shown in Figures 5-1 and 5-2.

As the constraints are relaxed (i.e. higher maximum ISL distance or lower minimum time for successful ISL) the performance of the system improves (both AoI and SRT are decreasing). For AoI, the tightest constraints produced an average of 593.5±224.7 minutes over all 432 ground targets while the most relaxed constraints produced an average of 535.3±184.3 minutes over all 432 ground targets. By relaxing

Table 5.1: Simulated BlackSky Satellite Initialization Parameters [4]

Satellite	**Altitude**	**Inclination**	**RAAN**	**Argument of Latitude**	**Epoch**
Global 5	550 km	45°	0°	0°	2020-01-01 00:00:00.000
Global 6	550 km	55°	0°	0°	2020-01-01 00:00:00.000
Global 7	385 km	45°	0°	0°	2020-01-01 00:00:00.000
Global 8	550 km	55°	0°	0°	2020-01-01 00:00:00.000
Global 9	600 km	35°	0°	0°	2020-03-31 00:00:00.000
Global 10	600 km	60°	0°	0°	2020-03-31 00:00:00.000
Global 11	385 km	35°	0°	0°	2020-03-31 00:00:00.000
Global 12	385 km	60°	0°	0°	2020-03-31 00:00:00.000
Global 13	600 km	35°	0°	0°	2020-09-27 00:00:00.000
Global 14	600 km	60°	0°	0°	2020-09-27 00:00:00.000
Global 15	385 km	35°	0°	0°	2020-09-27 00:00:00.000
Global 16	385 km	60°	0°	0°	2020-09-27 00:00:00.000

Table 5.2: Simulated BlackSky Satellite Ground Station Parameters [4]

Location	**Latitude**	**Longitude**
Guam	13.5° N	144.8° E
Fairbanks	64.8° N	147.5° W
Svalbard	78.2° N	15.4° E
Usingen	50.3° N	8.5° E
Invercargill	46.5° S	168.4° E
Chitose	42.8° N	141.6° E

Table 5.3: Sensitivity Simulation Parameters

Parameter	**Range**	**Resolution**
Ground target longitude	-175 to 175 degrees	Every 10 degrees
Ground target latitude	-55 to 55 degrees	Every 10 degrees
Max ISL distance	500 km to 2000 km	Every 250 km
Minimum time for successful ISL link	30 sec to 630 sec	Every 60 sec

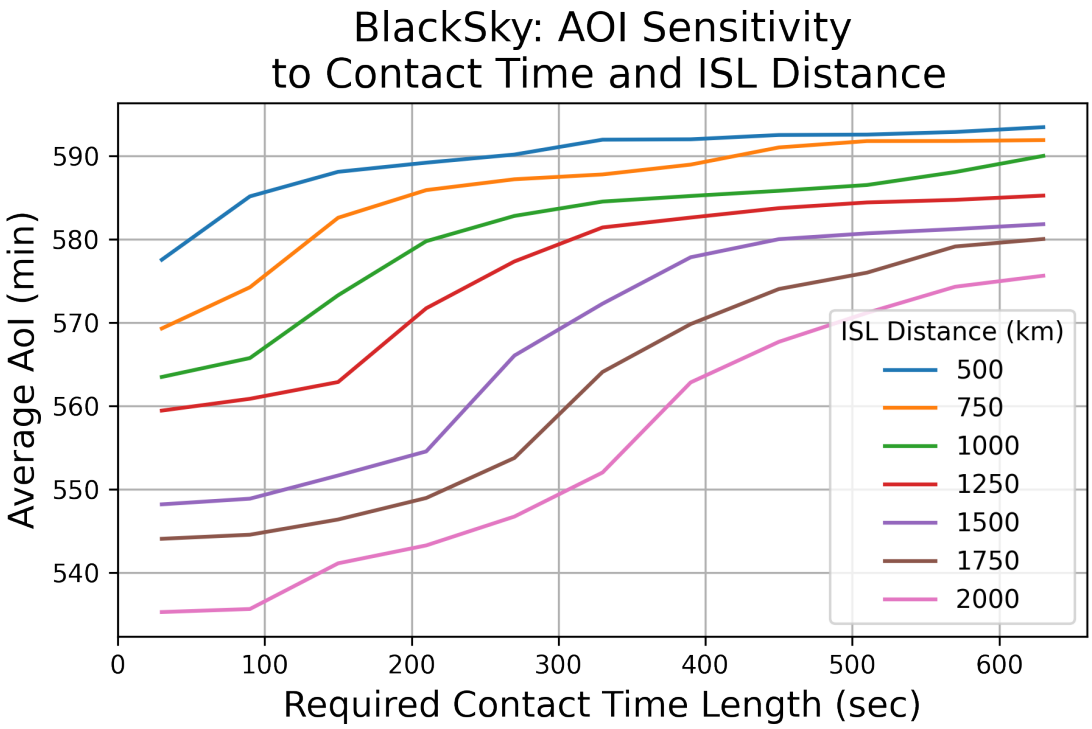

Figure 5-1: The sensitivity of the AoI metric to maximum ISL distance and minimum time for successful ISL links. Lower AoI through lower contact times and greater ISL distances are desirable.

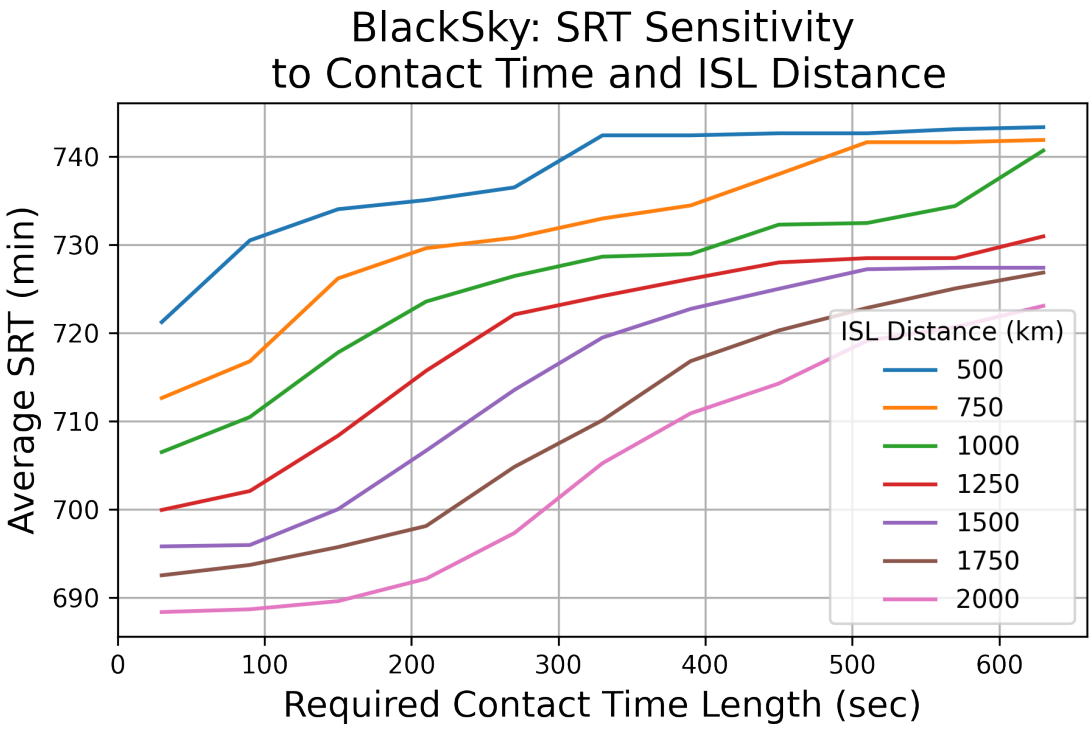

Figure 5-2: The sensitivity of the SRT metric to maximum ISL distance and minimum time for successful ISL links. Lower SRT through lower contact times and greater ISL distances are desirable.

constraints, an improvement of 9.8% can be achieved in average AoI.

The same analysis for SRT finds that the tightest and loosest constraints produced values of 743.3±455.0 min and 688.3±450.6 min, respectively. Loosening the constraints (ISL distance from 500 km to 2000 km and minimum contact time from 630 sec to 30 sec) produces an improvement of 7.4% in SRT. The analysis for overall pass time is not done as overall pass time is not dependent on ISL performance.

For both SRT and AoI, both maximum values fall within the standard deviation of their respective minimum values. This statistical feature suggests that while overall performance of a metric improves with looser constraints, it does not change the metric results by more than 10%. Any combination of the parameters chosen for max ISL distance and minimum time for a successful ISL link would provide results in the ballpark of any other combination of parameters. This analysis suggests the limiting factor is constellation design, which is varied in Chapter 6.

Another factor to keep in mind is the performance increase needed to obtain looser constraints. For example, by adjusting the link budget's power to first accommodate a 2000 km link would raise the ISL power requirement from 43 W to 110 W. To accommodate a 320 Mbps data rate that would allow 9600 Mb of data to transfer over 30 seconds would then raise the power requirement from 110 W to 437 W, keeping all things equal except for power. This particular link budget can be seen in Table 5.4. The power requirement to satisfy this link budget would be a lot harder to attain on a small satellite, as described in Section 3.4.1.

5.2 Sensitivity to Walker parameters

This section shows how the different Walker constellation design parameters affect both the drift time that the reconfiguring satellites spend between GOM and their RGT orbit, as well as the time to first pass over the ground target.

Table 5.4: Loose constraints link budget

Field	**Unit**	**Value**	**Justification**
Frequency	GHz	8	Requirement
Wavelength	m	0.0375	$\lambda = \frac{c}{f}$
Power Input	W	436.5	Required to close budget
Power Input	dBW	26.4	dB conversion: $[dBW] = 10\log_{10}([W])$
Antenna Gain	dBi	23.0	[Appendix A.2]
EIRP	dBW	49.4	Equation 2.31
Distance	km	2000	Requirement
Free Space Path Loss (FSPL)	dB	176.5	Equation 2.32
Other Losses	dB	6	Pointing and line losses
Receiver Gain	dBi	23	[Appendix A.2]
System Temperature	K	125	Example numbers from section 5.5.5 and Table 5.3 in Maral [99]
System Temperature	dBK	21	dB conversion equation
G/T	dBi/K	-2.9	Receiver Gain - System Temp (dBK)
Received Power	dBW	-131.0	EIRP - FSPL - Other Losses + G/T
Boltzmann Constant	dBW/K/Hz	228.6	Constant
Data Rate	Mbps	320	Requirement
Data Rate	dBHz	85.1	dB conversion equation
Eb/No	dB	12.5	Equation 2.30
Eb/No Required	dB	9.5	QPSK 10^{-5} BER. Figures 4.29 in [99]
Margin	dB	3.0	(Eb/No) - (Eb/No Required)

5.2.1 Simulation set up

A set of Walker Constellations is initialized with the following parameters listed in Table 5.5.

Table 5.5: Walker parameters for sensitivity study

Parameter	**Value**
Number of planes	1 to 24
Number of satellites per plane	2 to 10
f parameter (in Walker t/p/f notation)	0 to $P - 1$, where P is the number of planes
Inclination	60 degrees
Altitude	550 km
Epoch	January 1st, 2000 12:00:00 UTC

This combination of parameters generates 2678 different constellations. The drift altitude for the reconfiguration is set to 650 km. The target location is set at 42 deg latitude and 72 deg longitude. The RGT targeting and selection algorithms in Section 4.1 are then run in each scenario and the average revisit time is calculated. Only the maneuvered satellites are tasked to image the ground target. Each of the satellites is propagated from their epoch for 5 days with a propagation time step of 15 seconds, all maneuvers propagated as well. Access is calculated given a 25° half angle nadir facing conical sensor. Time between passes was calculated by pegging a particular pass to the first propagation time step that results in access between the satellite and ground location.

5.2.2 Drift time results

The drift time refers to the amount of time spent in the drift orbit at 650 km, and relates directly to the change in anomaly required to reach the desired RGT orbit. From each individual simulation, the average drift times are calculated, and the results can be seen in Figure 5-3.

The results show that as the number of satellites per plane is increased, the average drift time and the standard deviation associated with the average drift times decrease. This makes sense as the more satellites you have per plane, the chance that one of the

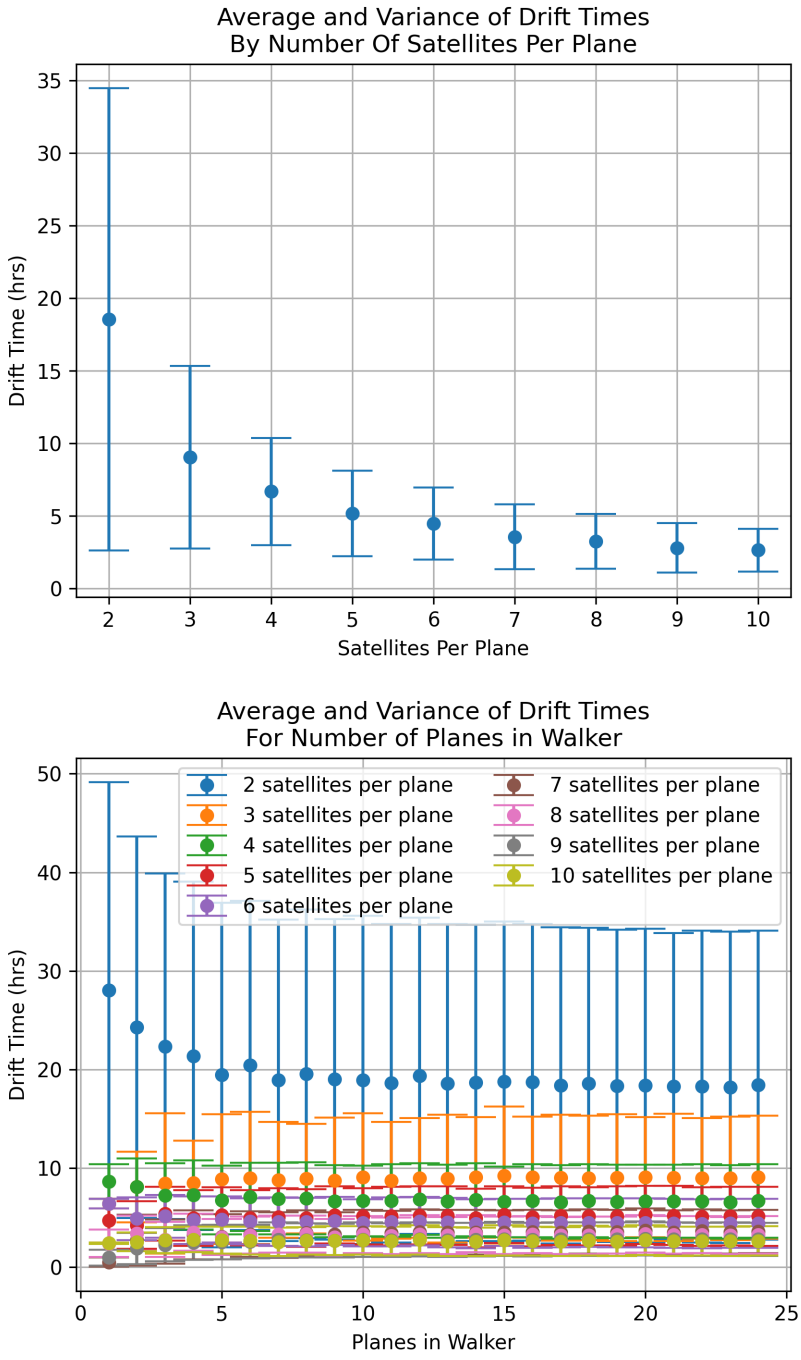

Figure 5-3: The top plot shows the average and standard deviation of drift times binned by the number of satellites per plane. The bottom plot shows the average and standard deviation of drift times binned by the number of planes in the constellation.

satellites is near the desired argument of latitude for the RGT increases; therefore, the average drift time decreases. The standard deviation also decreases since the argument of latitude between each satellite in the plane decreases. The argument of latitude between each satellite in the plane corresponds to the maximum anomaly a satellite would have to drift, since the scheduler would rather select the adjacent satellite than task a satellite to drift beyond the anomaly of its neighbor.

Beyond 5 planes in the constellation, the drift time statistics are fairly agnostic of the number of planes. This makes sense as the drift time should be most strongly coupled to the argument of latitudes of the satellites. For constellations with 1 to 4 planes, the drift time statistics are slightly higher due to initial condition biases that are not averaged out, since the number of planes is lower.

5.2.3 Time to first pass results

The time to first pass of the ground target is a good measure of the constellation responsiveness. The results from the simulation run are shown in 5-4.

The results show that the statistics for the time to first pass improve as the number of satellites increase. This makes sense as the more satellites in a constellation, the higher the chance that it will be in the right position to move into an RGT orbit to make the pass. However, binning the data by the number of planes is potentially more telling, since pass times are directly related to the orbital planes in a constellation. In this particular simulation run, the number of satellites is directly coupled to the number of planes. There is a 'knee' around 10 planes, after which an increase in the number of planes provides diminishing returns in terms of both average and standard deviation of the time to first pass.

5.2.4 The effect of the phasing parameter, f

The walker parameter, f, determines relative spacing between satellites in adjacent planes. The satellite arguments of latitude directly affect the drift time statistics and also influence the time to first pass. However, the differences that various f

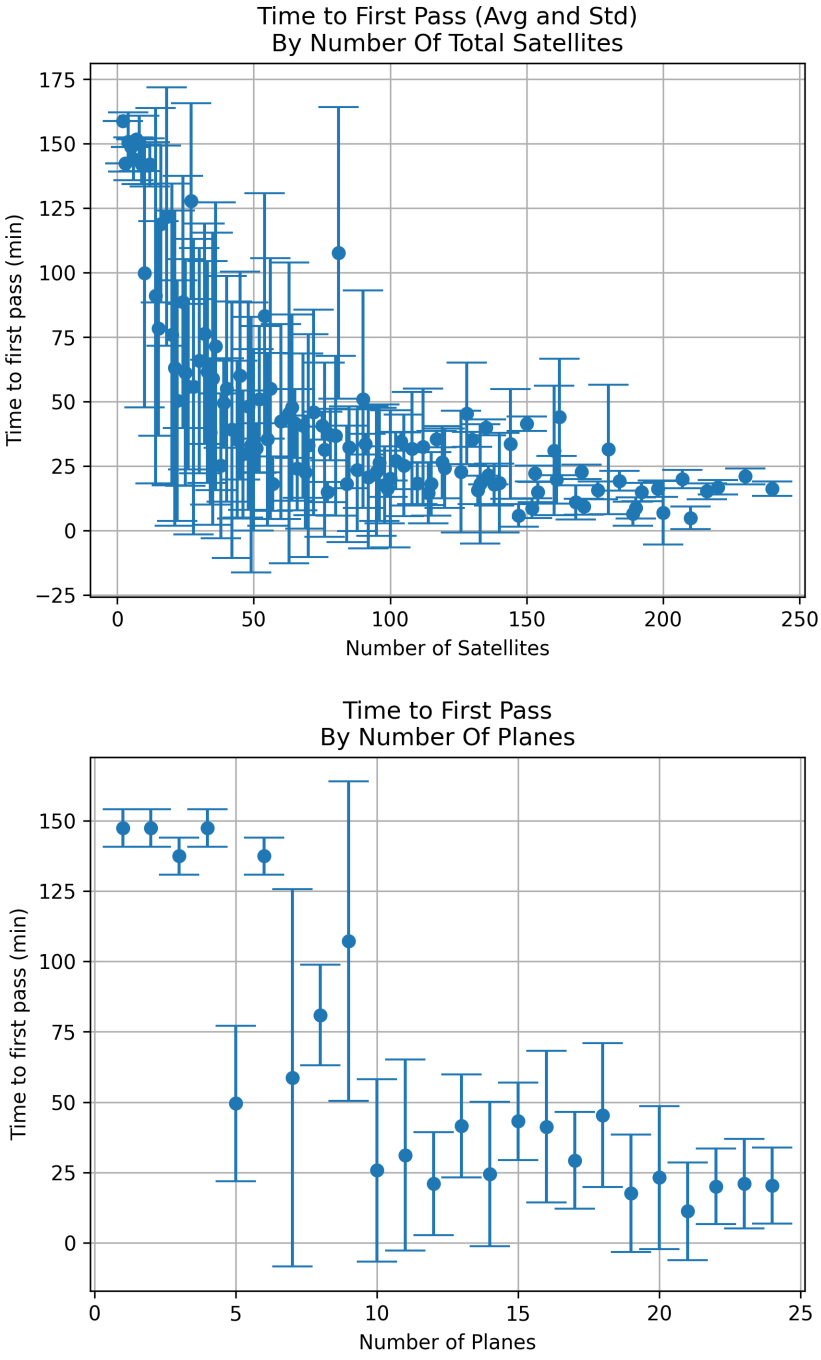

Figure 5-4: The top plot shows the average and standard deviation of the time to first pass binned by the number of satellites in the constellation. The bottom plot shows the average and standard deviation of the time to first pass binned by the number of planes in the constellation.

parameters induce should average out over multiple runs. See Figure 5-5 for a sample selection of runs that show the independence of drift time to the f Walker parameter. Showing that f has no impact over large averages will allow future simulation runs to ignore this parameter, significantly decreasing the constellation trade space, saving memory and computation time. The averages are not all equal in Figure 5-5, but they do fall within the error bars of the other averages.

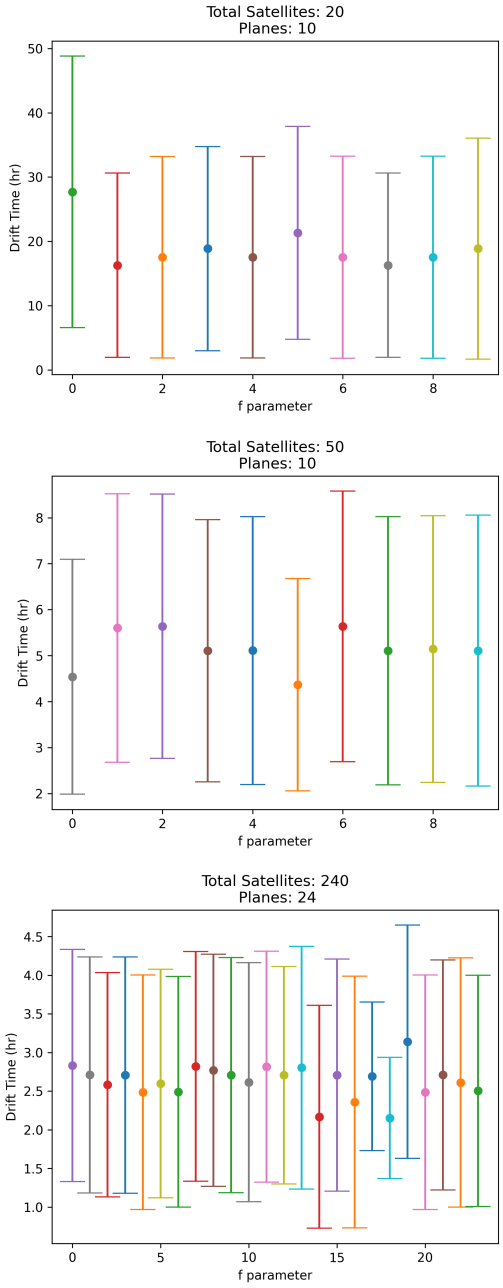

Figure 5-5: The drift times of satellites in constellations with 20, 50, and 240 satellites, as a function of changing the f Walker parameter. No notable trends are observed.

THIS PAGE INTENTIONALLY LEFT BLANK

Chapter 6

Results from Python simulation

This chapter details the results from the Python simulation that result in the highest performing constellation designs (contribution 3) as well as the CERs for the metrics: AoI, SRT, and total pass time (contribution 4). Section 6.1 details the satellite constellation trade space that is investigated. Section 6.2 explains the supercomputing resource used to run the simulations. Section 6.3 details the run time performance of the planning and scheduling algorithm. Section 6.4 contains the results of the simulation in terms of the metrics: AoI, SRT, and total pass time. Section 6.5 explains some of the outliers in the data. Section 6.6 details the cost versus performance analysis that produces the highest performing constellation designs. Section 6.7 contains the CERs that allow designers to understand the trade-off in cost versus performance.

6.1 Constellation Trades

Three different size constellations are evaluated: 12-, 36-, and 72-satellite constellations which represent small, medium, and large remote sensing constellations, respectively. There is a discernible plateau in time to first pass performance in Figure 5-4 starting around 70 satellites until the 200 satellite range. At 200 satellites, the benefits of reconfiguration are severely reduced [38]. To standardize the constellation design, only Walker constellations (Section 2.7) are chosen for this work. Two satellites per plane are moved into an RGT orbit (one for the ascending and one for the descending

pass), and at least one satellite is left in GOM to act as a relay. This requires at least three satellites per plane, as displayed in Table 6.1. The Walker phase parameter 'f' is not varied because it does not affect the drift time of satellites moving from GOM to ROM if other factors, such as ground target location, are randomized (see Section 5.2.4).

Table 6.1: Walker Constellation parameters at 60 deg inclination and 550 km GOM altitude

t	**p**	**f**		**t**	**p**	**f**		**t**	**p**	**f**
12	1	0		36	1	0		72	1	0
12	2	0		36	2	0		72	2	0
12	3	0		36	3	0		72	3	0
12	4	0		36	4	0		72	4	0
				36	6	0		72	6	0
				36	9	0		72	8	0
				36	12	0		72	9	0
								72	12	0
								72	18	0
								72	24	0

6.2 Supercomputing

All of the analysis and results presented in this chapter are run using the MIT SuperCloud. The MIT SuperCloud consists of the following computing resources: 704 nodes, 32,000 CPU cores, 448 GPUs, and 873 TB of distributed storage. There are two types of nodes, GPU capable Intel Xeon Gold 6248 nodes and non-GPU compatible Intel Xeon Platinum 8260 nodes. This work uses the latter, as no GPUs are needed. There are 480 Intel Xeon Platinum 8260 nodes, 48 cores on each node, and 192 GB of RAM on each node (4 GB RAM per core) [129]. For this analysis, the standard allocation of 16 nodes or 768 cores could be used at any given time.

The computations utilize the throughput method of supercomputing, which separates independent processes that are often run in series on a personal computer, and parallelizes them to allow several separate independent processes to run simultaneously across different cores. For example, a 'for' loop in computer programming can

be parallelized as long as each subsequent loop is not dependent on the previous loop run. In the analyses conducted in this work, each 'independent scenario' includes an initialized constellation and one specific ground target to image. The 'for' loop would loop over variables such as ground target location, constellation design, and constraint set (for the analysis in Section 5.1). At its most efficient, 768 (16 nodes with 48 cores each) of these independent scenarios could be run simultaneously, however, in practice it was often less than that due to RAM constraints.

For reference, running the full simulation set-up, planning and scheduling algorithm, and post-simulation metric analysis for a 12 satellite constellation on 9 nodes running 48 cores each for a set of 432 ground targets took 46 minutes. Only 9 nodes are needed for 12 satellite constellation runs as they provide 432 cores, one for each ground target. Given the independence of each individual simulation for each ground target, running this analysis pipeline serially would take 5.5 days. For a 36 satellite constellation, the same set of 432 ground target simulations took 3.5 hrs on the SuperCloud using 16 nodes, and would take 63 days to compute serially. For a 72 satellite constellation, the analysis pipeline took 17 hrs using 16 nodes, which equates to 306 days to run serially. To put it into perspective, as shown in Table 6.1, the constellation design space includes four 12-satellite constellations, seven 36-satellite constellations, and ten 72-satellite constellations.

6.3 Scheduling and planning algorithm performance

6.3.1 Run time

To evaluate the run time of just the planning and scheduling algorithm, the set of constellations shown in Table 6.1 are initialized on January 1st, 2019. For each constellation design, 100 random ground target locations are created between the latitudes of $-55°$and $+55°$ and longitudes of $-175°$ to $+175°$. This analysis excludes the simulation set-up and post-simulation metric analysis portions of the code mentioned in Section 6.2 because the planning and scheduling algorithm is the software that will

be implemented by constellation operators.

Two different timing milestones are recorded. The first 'maneuver' milestone is the time it takes to generate and select the RGT maneuvers (See Section 4.1). The generation and selection of maneuvers starts the entire reconfiguration process, which should occur as early as possible and gives the satellites enough information to complete up to step 6 in the SRT chain (see Figure 3-8).

The second 'routing' milestone records the time it takes to simulate the propagation of the satellites, develop the contact graph, and run Dijkstra's algorithm to find the best route. The information generated by this section of the algorithm is only usable once the satellites finish step 6 in the SRT chain (See Figure 3-8). In practice, this routing information can be sent after the information in the first 'maneuver' milestone, allowing the satellites to start maneuvers early and not get delayed waiting for the longer routing algorithms.

The results from the run time analysis are shown in Figure 6-1. As one would expect, larger constellations have longer run times. Additionally, the second milestone (routing algorithm) also takes longer than the run time of the first milestone (RGT scheduling). An important point to keep in mind is that the run time for the largest 72-satellite constellations averages less than 3 hours, below the average SRTs seen in Figures 6-7, 6-8, and 6-9, which are all at least 4+ hours. This shows that this algorithm can be run on a single core on the MIT SuperCloud and still produce schedule commands fast enough to get them to the satellites in time.

Routing for larger satellite constellations takes up a larger proportion of total run time (see Table 6.2). Larger satellite constellations have larger contact graphs, with the total number of edges expanding as a combinatorial (the number of nodes choose 2). In this work, the number of vertices is the number of nodes (ground stations and satellites) and the number of edges is equal to ${}_V C_2$, where V is the number of vertices. The time complexity of Dijkstra's algorithm as implemented is $O(|E|log|V|)$ where E is the number of edges and V is the number of vertices [130]. On the other hand, the 'maneuvers' milestone is of $O(V)$ as maneuvers are only calculated once for each satellite. The time complexity of Dijkstra's algorithm scales with the number of edges

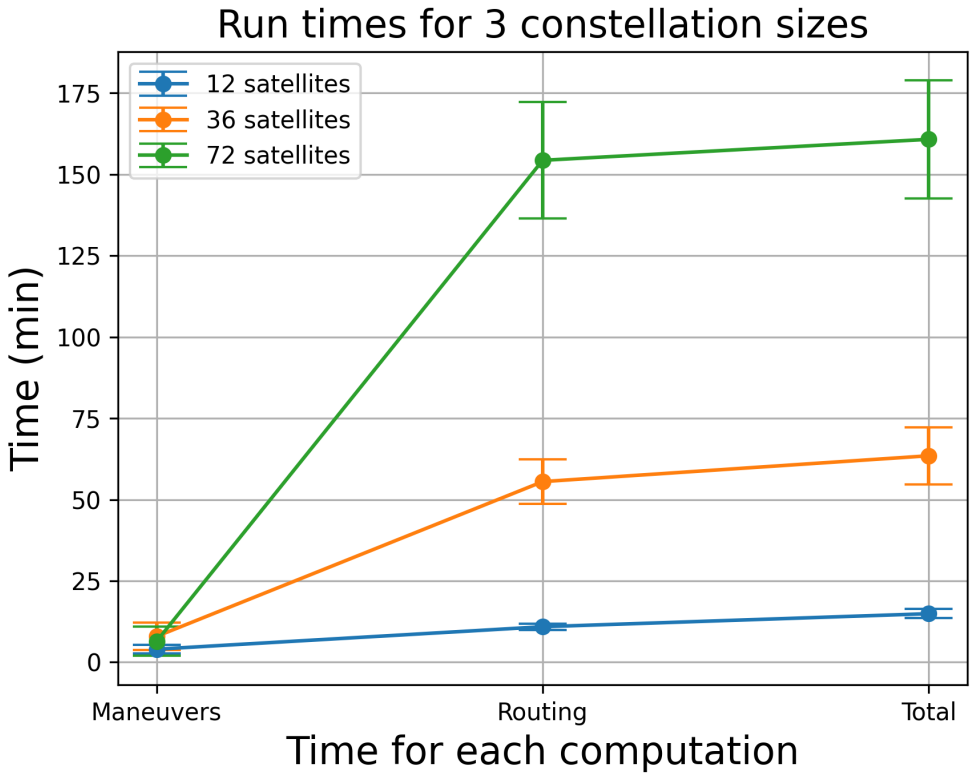

Figure 6-1: Computer run time where 'Maneuver' times indicate the runtime to first milestone, 'Routing' times indicate the runtime of the second milestone, and 'Total' shows the sum of both the 'Maneuver' and 'Routing' portions of the algorithm.

and the number of edges increases combinatorially as the number of nodes increases, so the greater the number of satellites, the longer the 'routing' milestone will take to run and the milestone will also take up a greater proportion of total run time.

Table 6.2: Percentage of total run time for each timing milestone

Constellation satellites	**Maneuvers**	**Routing**
12	27%	73%
36	13%	87%
72	4%	96%

6.4 Metric performance in constellation trade study

6.4.1 Analysis set-up

To evaluate the performance of the planning and routing algorithm, several simulations are run over scenarios initialized with each of the 21 constellation from Table 6.1 and ground stations from Table 5.1. All three satellite models are simulated: no-ISL/no-recon (baseline satellite model), ISL capable/no-recon, and ISL/recon-capable satellite models. Each constellation is then run using the same 432 ground target locations from Table 5.3, longitude ranging from -175 to +175 degrees in 10 degree increments, and latitude ranging from -55 to +55 degrees in 10 degree increments. Since the Walker constellations are all initialized with the same RAAN, resulting in the same initial conditions with respect to the sun, the simulations are run four times over the start of each season. The constellations are initialized on March 21st, 2019, June 21st, 2019, September 21st, 2019, and December 21st, 2019 in order to vary the lighting from the sun. In total, 108,864 individual scenario simulations are run.

During each scenario, the scheduling and planning algorithm from Section 4 is run, and then the metrics from Section 3.5 are calculated, taking into consideration the constraints from Table 3.4.5. In order to create comparable results, the same satellites that are tasked with imaging a particular location are identical regardless of satellite model, so if the satellite initialized in the plane at 0° RAAN at 45° argument of latitude is tasked with moving into an RGT orbit to image the ground target, that

same no-ISL/no-recon satellite is also tasked with imaging the ground target in its respective scenario.

6.4.2 Age of information

The AoI metric as calculated over all constellations, all ground targets, and all four seasons can be seen in Figures 6-2, 6-3, and 6-4. The statistics averaged over all season can be seen in Figure 6-5.

AoI improves as the number of planes increases. This makes sense, as a constellation distributed over multiple planes has a much better chance of being in the right orbit to view a broad set of imaging ground targets. For 12-satellite constellations, this performance increase is evident between 1 plane and 2+ plane constellations.

There is a geometric correlation in the data. The winter and summer initialized single-plane-constellations have larger quantile distribution than the fall and spring runs with the 75% quantile data point above 4000 min for winter and summer runs while the 75% quantile is slightly more than 2000 min for the fall and winter runs. This evidence points to the fact that the constellation is initialized in a geometrically favorable position in the fall and spring and geometrically unfavorable in the winter and summer. This exemplifies why the simulation is run over all four seasons, to eliminate geometrically introduced biases.

The error bars for the ISL and recon capable satellites are also smaller than the No Recon/No ISL (baseline) satellite model and the No Recon/ISL (ISL-only) model. Because the ISL and recon capable satellites move into targeted RGT orbits, error bars are expected to be smaller as the entire reconfiguration and routing processes are more repeatable. For the satellites with no propulsive capabilities, the ability to pass over a ground target area is purely based on *a priori* determined orbital mechanics, which may be favorable or unfavorable for the mission and result in a larger spread of data points. It should also be noted that the size of the quartile error bars decrease as the constellation includes more orbital planes. Increasing the number of planes brings diminishing returns after around 4 planes, averaged over all seasons as seen in Figure 6-5.

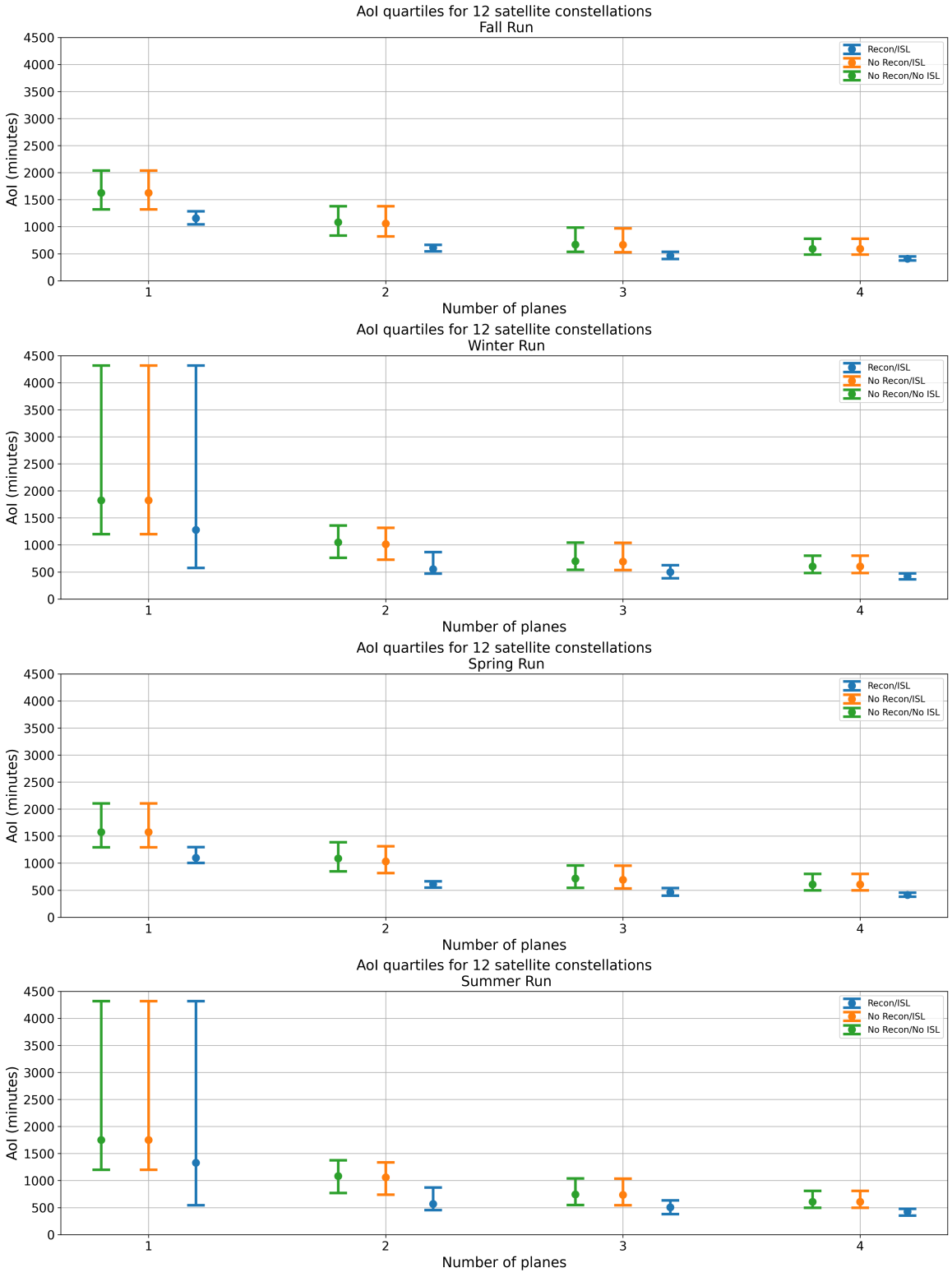

Figure 6-2: The AoI distribution for 12 satellite Walker constellations. The 25%, median, and 75% quartiles are shown by the lower bar cap, circular data point, and upper bar cap, respectively. Green and blue lines offset horizontally for clarity.

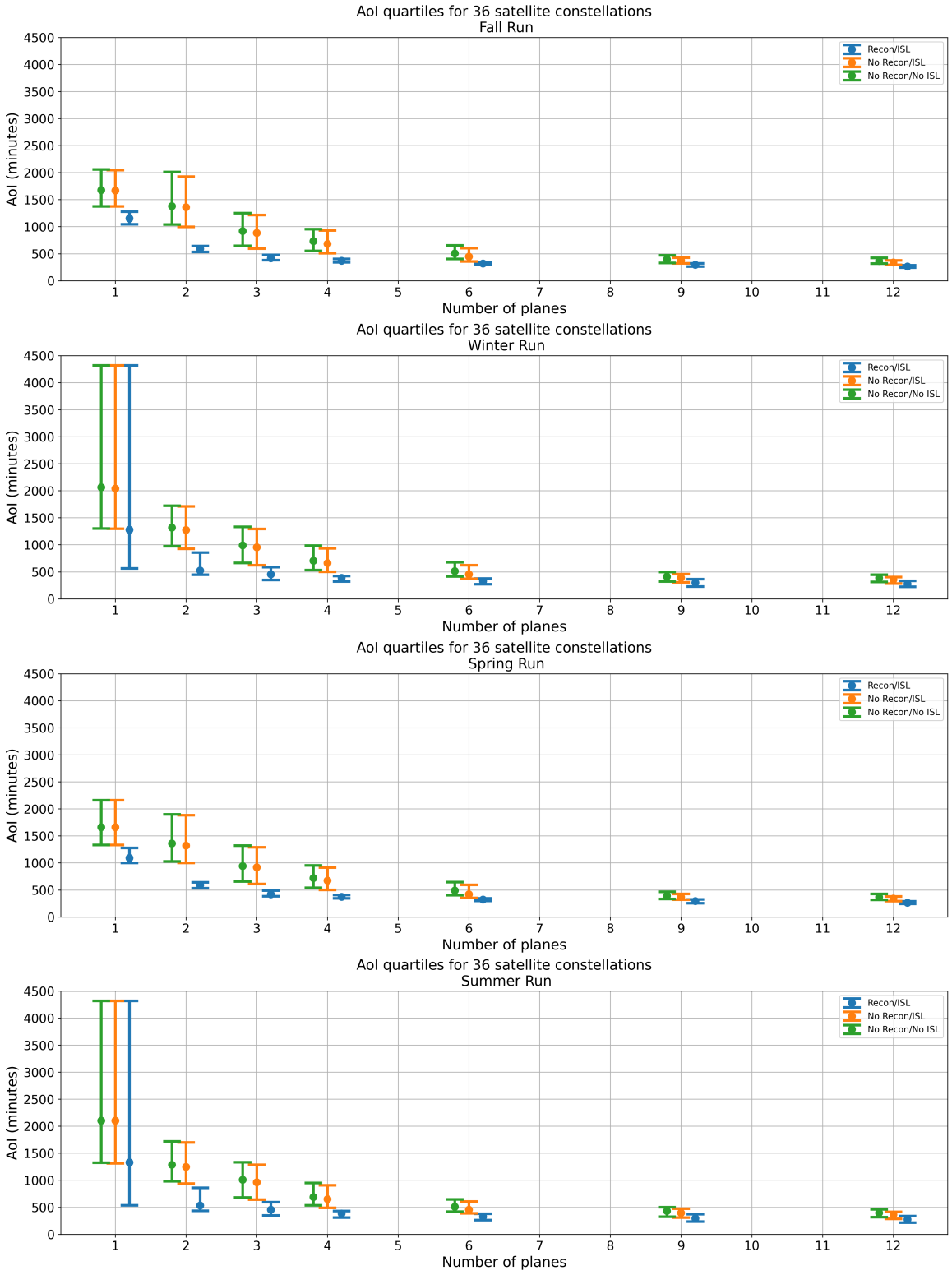

Figure 6-3: The AoI distribution for 36 satellite Walker constellations. The 25%, median, and 75% quartiles are shown by the lower bar cap, circular data point, and upper bar cap, respectively. Green and blue lines offset horizontally for clarity.

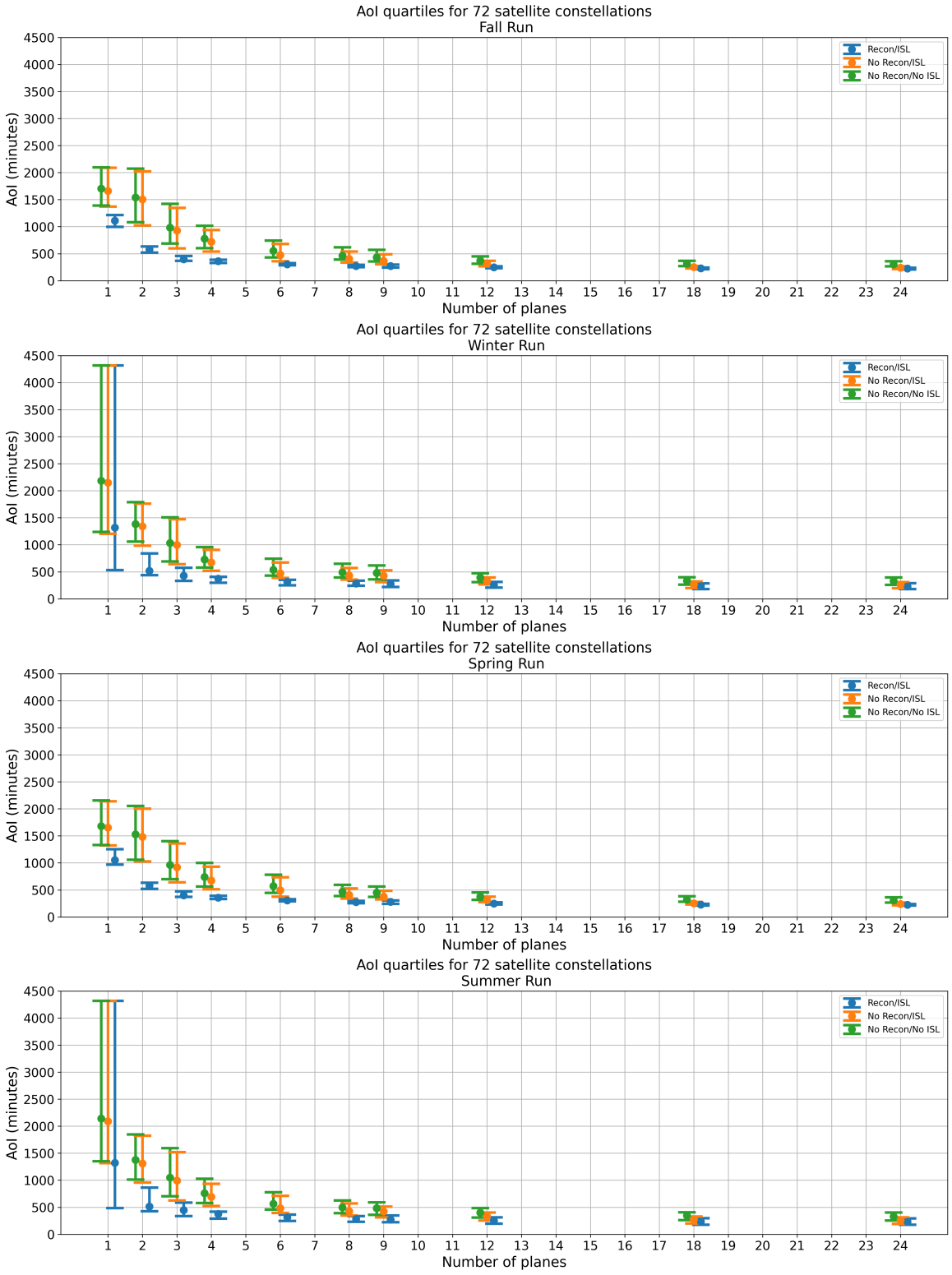

Figure 6-4: The AoI distribution for 72 satellite Walker constellations. The 25%, median, and 75% quartiles are shown by the lower bar cap, circular data point, and upper bar cap, respectively. Green and blue lines offset horizontally for clarity.

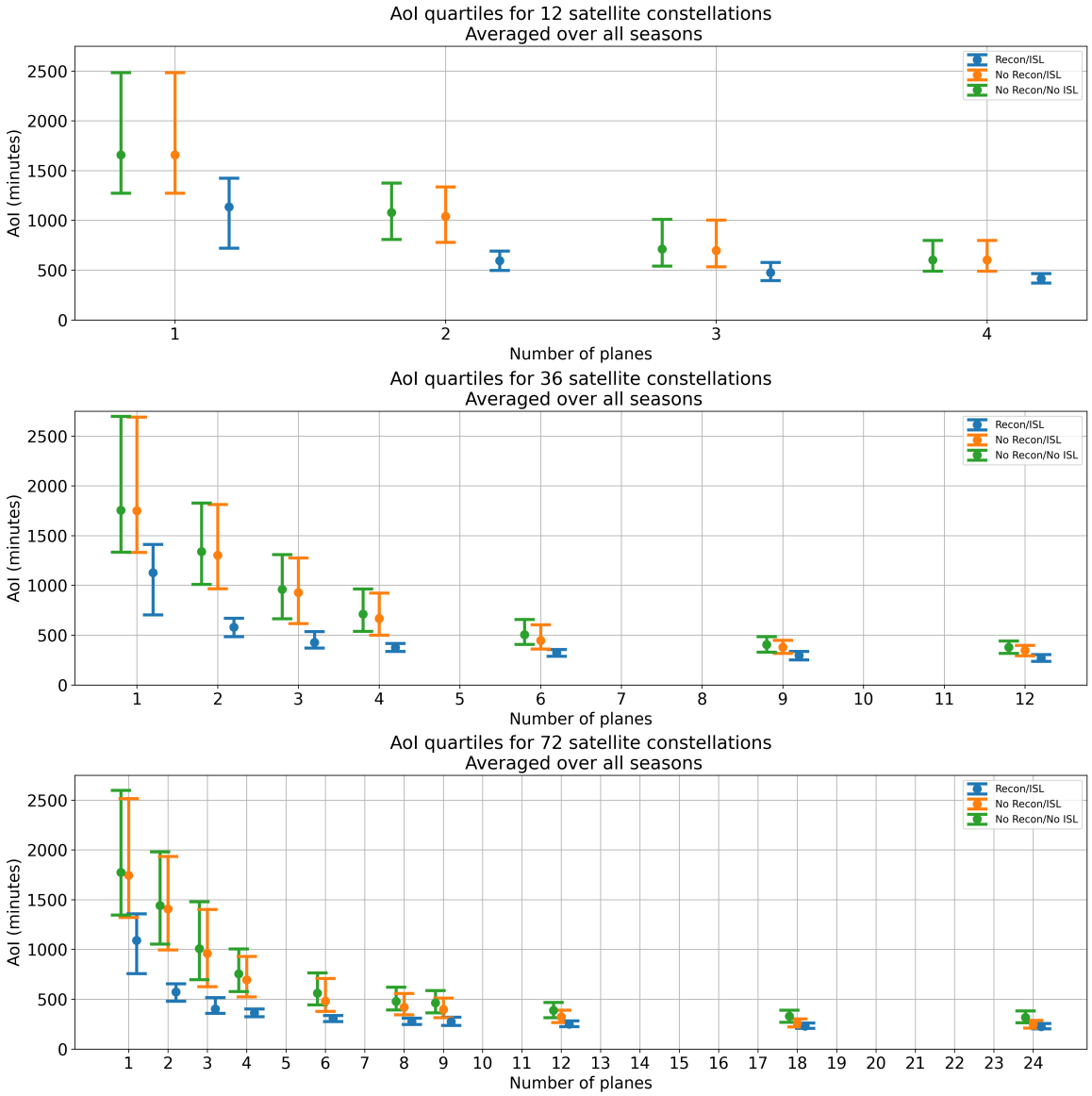

Figure 6-5: The AoI distribution for 12, 36, 72 satellite constellations taking data over all seasons. The 25%, median, and 75% quartiles are shown by the lower bar cap, circular data point, and upper bar cap, respectively. Green and blue lines offset horizontally for clarity. The performance improvement offered by ISL and reconfigurability diminish as more planes are added.

The relative improvement in AoI performance between all three satellite models is shown in Figure 6-6. Improvement is defined using two metrics: (i) Improvement in median value, with less equating to better performance; (ii) Improvement in quantile spread, defined as the difference between the 75th and 25th quantile values, with a smaller value indicating more consistent, and therefore more desirable performance. The greatest improvement can be seen in the 36- and 72-satellite constellations with 2 to 6 planes. These constellations have improvements in quantile spread around 80% and in median value around 60%.

6.4.3 System response time

The SRT metric calculated over all constellations, all ground targets, and all four seasons can be seen in Figures 6-7, 6-8, and 6-9, and the statistics averaged over all seasons are shown in Figure 6-10. SRT behaves similarly to AoI, which is to be expected, since the metrics are correlated. SRT describes the time to the first downlink, while AoI is a metric that measures the freshness of data over continuous downlinks. Similarities include larger error bars for constellations with fewer planes, especially single-plane constellations. With single-plane constellations, the spread of SRT can be attributed to the fact that the performance metric is mostly dependent on favorable/unfavorable initialization conditions. Geometrically, the satellites in the plane do not have a chance to take advantage of other orbital planes that cover different parts of the Earth. The error bars for all three constellation types also decrease as the number of planes increase, following a similar trend to the AoI averages.

Over all seasons as seen in Figure 6-10, increasing the number of planes brings diminishing returns after the number of planes increases from 1 to 2. For SRT, the largest performance increase comes from increasing the planes to 2.

Unlike AoI, ISL and recon-capable constellations do not have a distinct advantage, in terms of SRT error bars, over the ISL/no-recon and no-ISL/no-recon (baseline) satellites. This can be attributed to the fact that recon-capable constellations are designed for persistent surveillance of a ground target, which is something that the AoI metric captures but SRT does not.

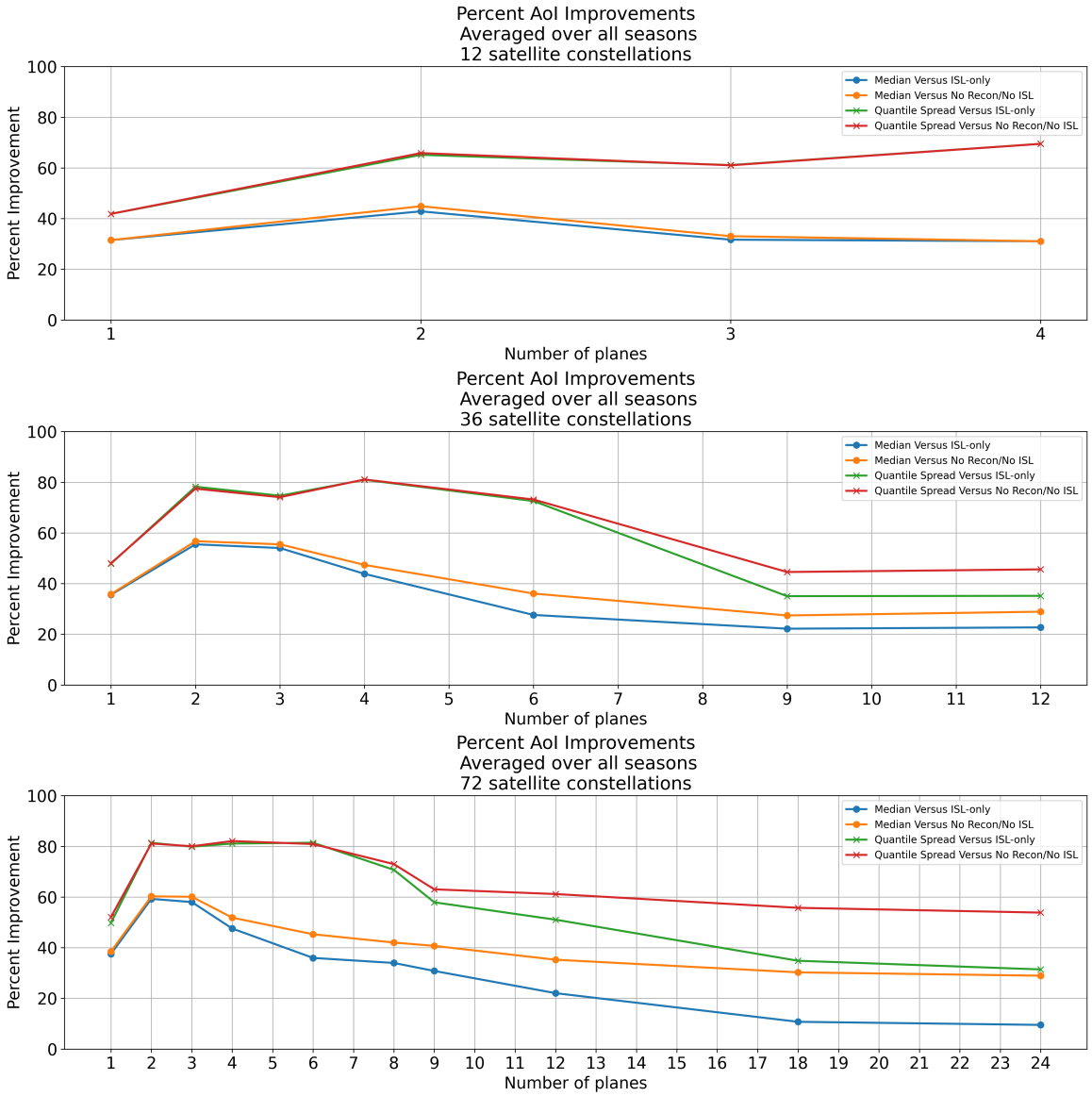

Figure 6-6: The relative improvement in AoI when introducing both ISL and reconfigurable capabilities. The improvement can be categorized by both improvement in median value and by improvement by the size of the error bars (quantile spread). The quantile spread is defined as the difference between the 75th and 25th quantiles, with a smaller value indicating more consistent, and therefore more desirable performance.

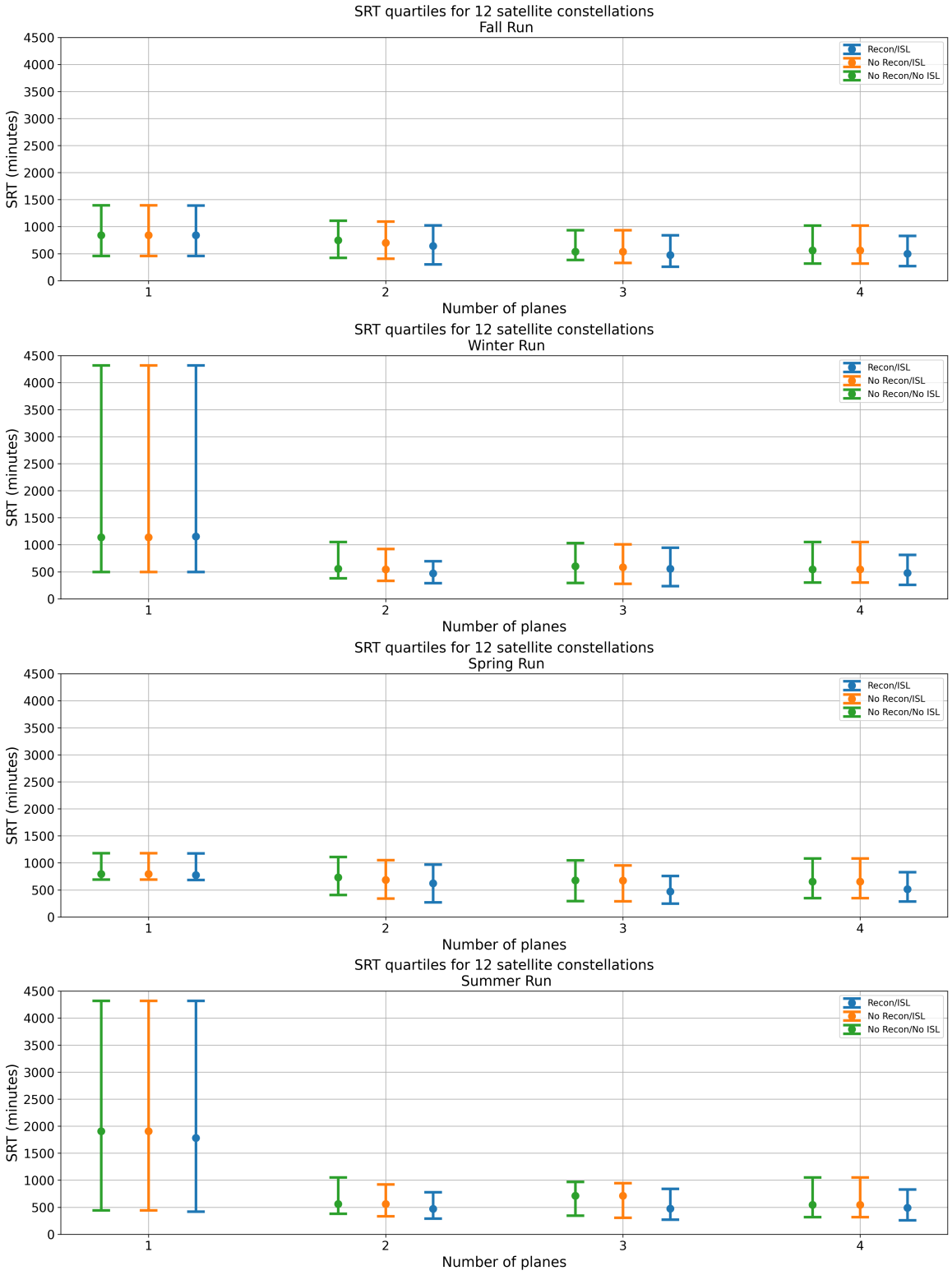

Figure 6-7: The SRT distribution for 12 satellite Walker constellations. The 25%, median, and 75% quartiles are shown by the lower bar cap, circular data point, and upper bar cap, respectively. Green and blue lines offset horizontally for clarity.

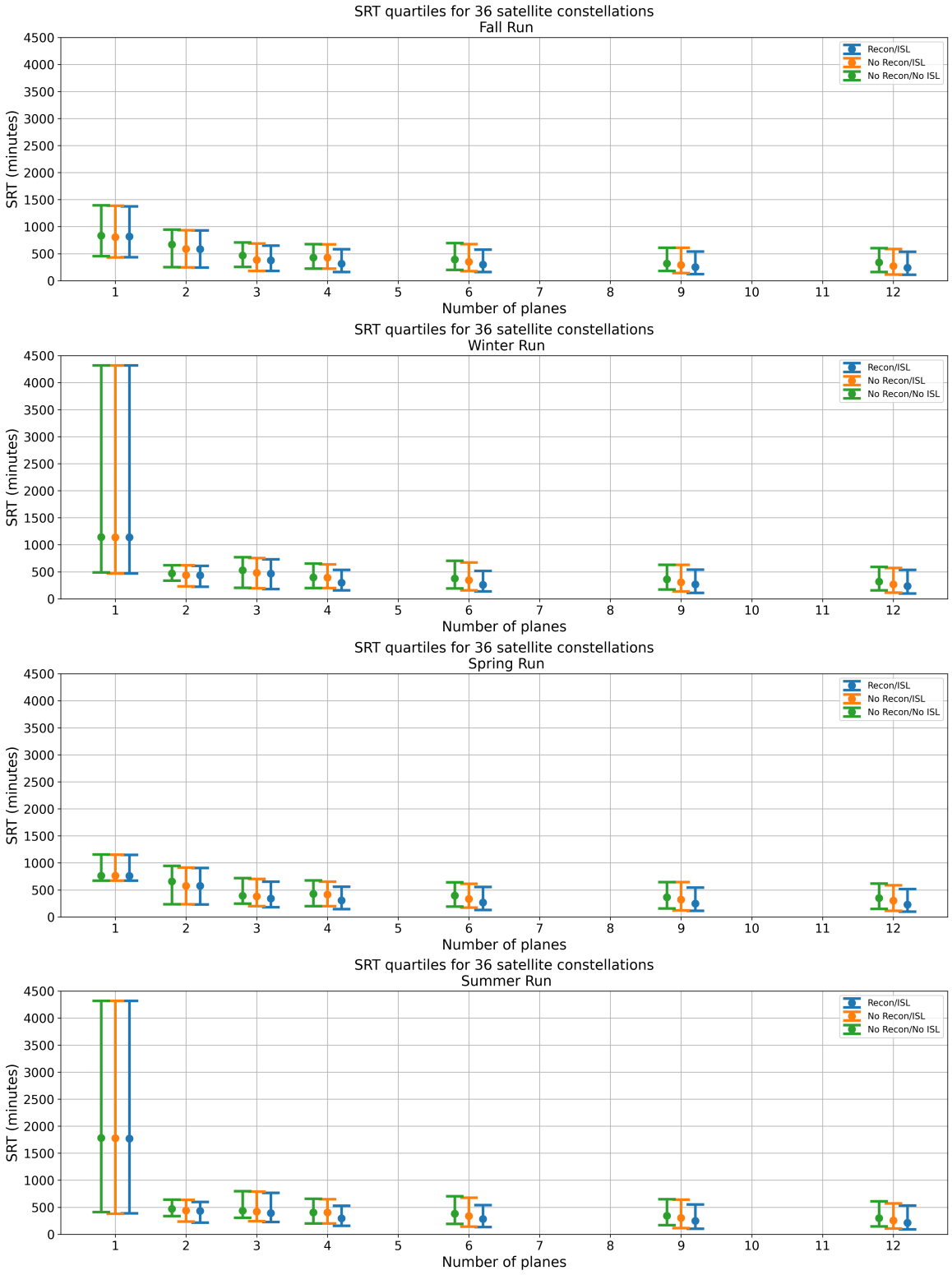

Figure 6-8: The SRT distribution for 36 satellite Walker constellations. The 25%, median, and 75% quartiles are shown by the lower bar cap, circular data point, and upper bar cap, respectively. Green and blue lines offset horizontally for clarity.

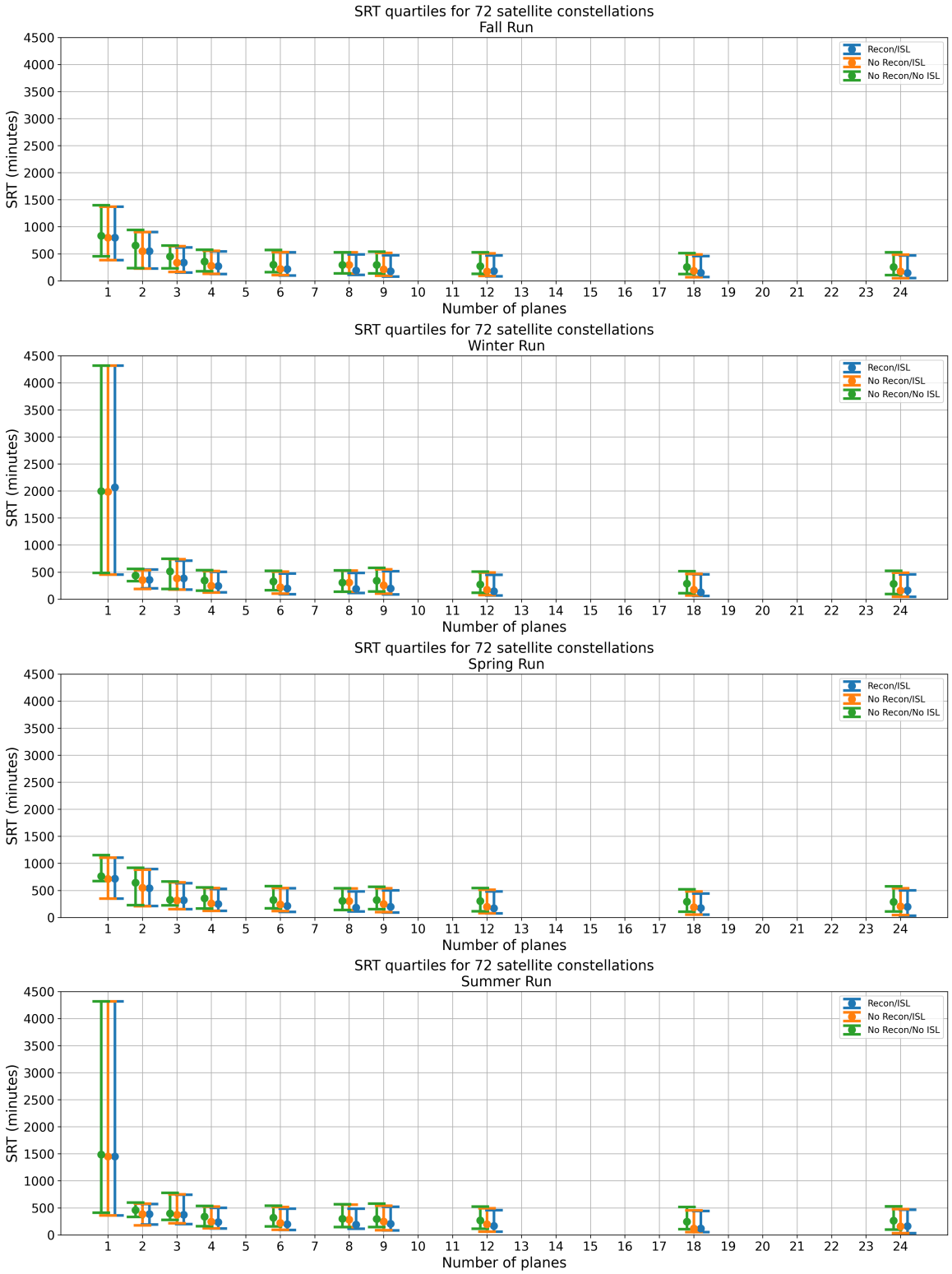

Figure 6-9: The SRT distribution for 72 satellite Walker constellations. The 25%, median, and 75% quartiles are shown by the lower bar cap, circular data point, and upper bar cap, respectively. Green and blue lines offset horizontally for clarity.

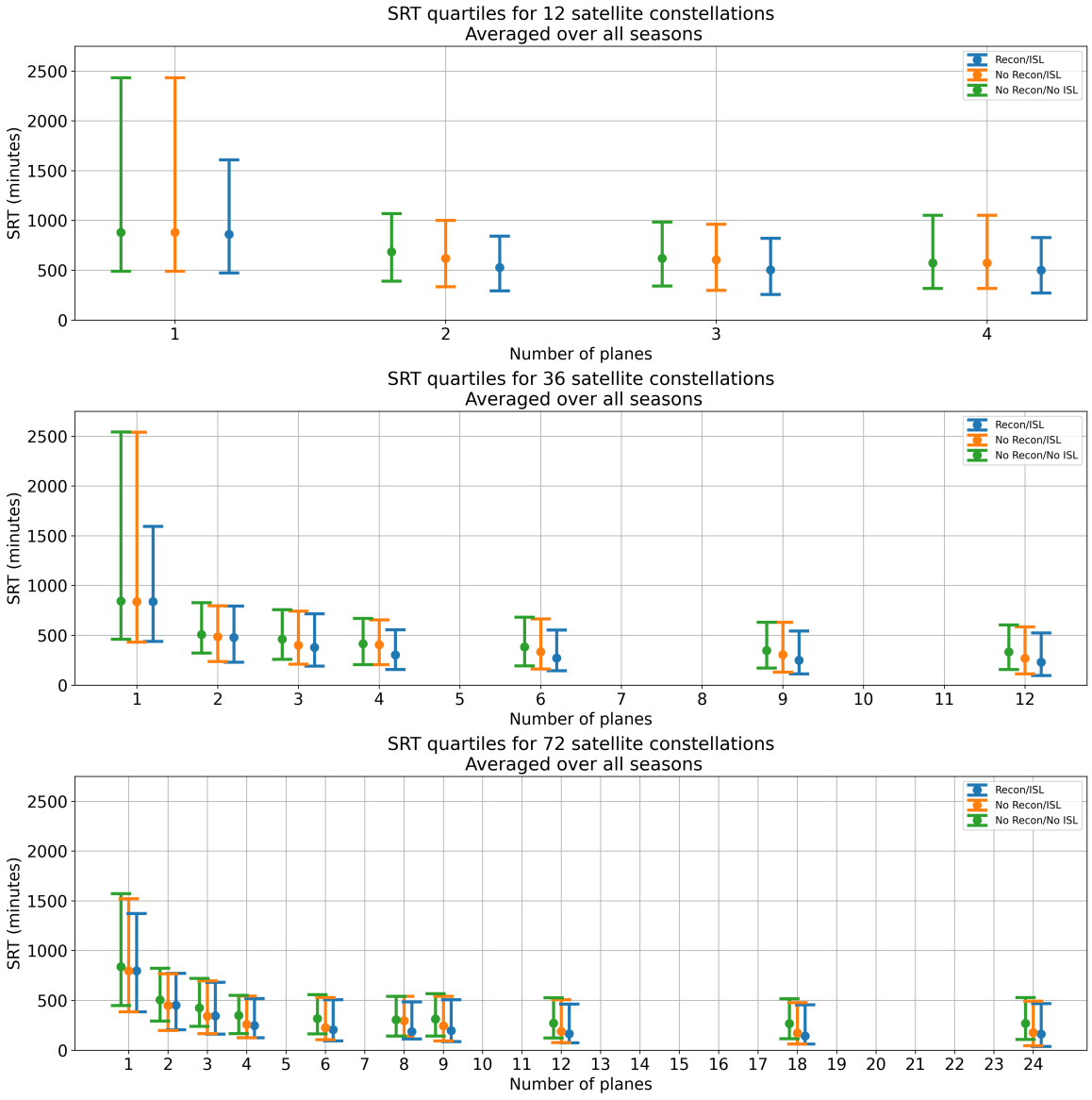

Figure 6-10: The SRT distribution for 12, 36, 72 satellite constellations taking data over all seasons. The 25%, median, and 75% quartiles are shown by the lower bar cap, circular data point, and upper bar cap, respectively. Green and blue lines offset horizontally for clarity.

Finally, SRT values tend to be higher than AoI values for ISL and recon-capable constellations for the same reason. SRT captures the time to first image, including the reconfiguration maneuver. AoI captures the constellation's performance when it has been configured correctly with RGT orbits overflying the ground target every day, which would produce a lower average data latency.

The relative improvement in SRT performance between all three satellite models is shown in Figure 6-11. Improvement is defined using two metrics: (i) Improvement in median value, with less equating to better performance; (ii) Improvement in quantile spread, defined as the difference between the 75th and 25th quantile values, with a smaller value indicating more consistent, and therefore more desirable performance. While the relative median improvement always stays positive, the quantile spread performance decreases for 36- and 72-satellite constellations at 2 and 3 planes, and at 2 to 6 planes, respectively. This can be explained as reconfiguring a constellation takes some time. A satellite might be reconfiguring during a pass time, missing the pass. Reconfigurable constellations with fewer planes would then have to wait longer for a subsequent pass, while the other satellite models with no propulsion would have already collected their first images.

6.4.4 Pass time

The pass time metric calculated over all constellations, all ground targets, and all four seasons is shown in Figures 6-12, 6-13, and 6-14, and the statistics averaged over all season can be seen in Figure 6-15. As mentioned in Section 3.5.3, the more pass time a constellation can achieve, the more data the satellites can collect. The more planes a constellation has, the more chances it has to image a ground target. This advantage increases if the constellation has reconfigurable capabilities, which can be seen in Figures 6-12, 6-13, and 6-14. More planes allows the planning and scheduling algorithm to find more satellites to move into an RGT orbit, enabling more passes of the ground target. The performance improvements due to ISL, reconfigurability, and more constellation planes all come at a higher cost (see Section 3.6). The no-ISL/no-recon and ISL/no-recon constellation models also have identical pass times,

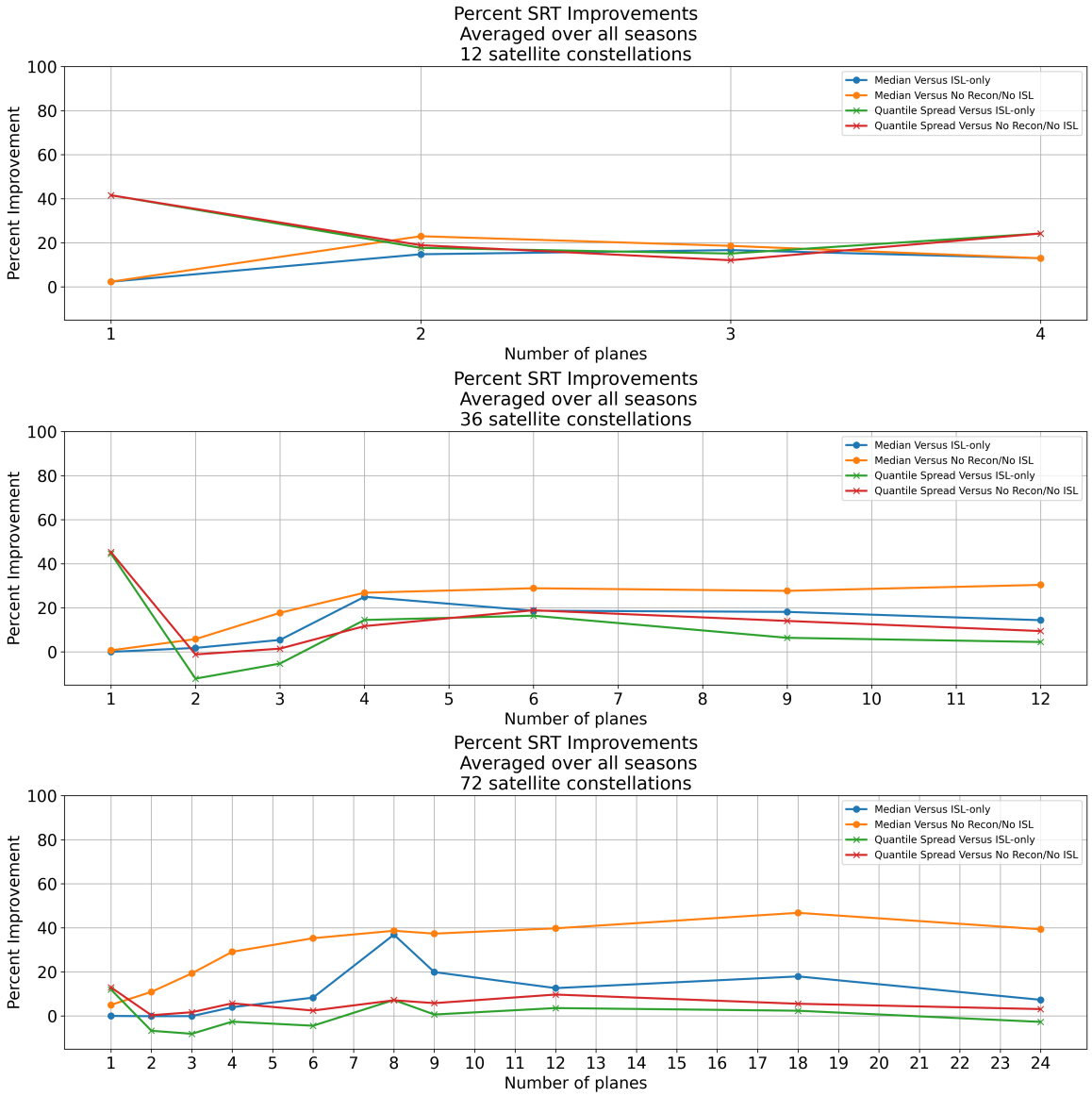

Figure 6-11: The relative improvement in SRT when introducing both ISL and reconfigurable capabilities. The improvement can be categorized by both improvement in median value and by improvement by the size of the error bars (quantile spread). The quantile spread is defined as the difference between the 75th and 25th quantiles, with a smaller value indicating more consistent, and therefore more desirable performance.

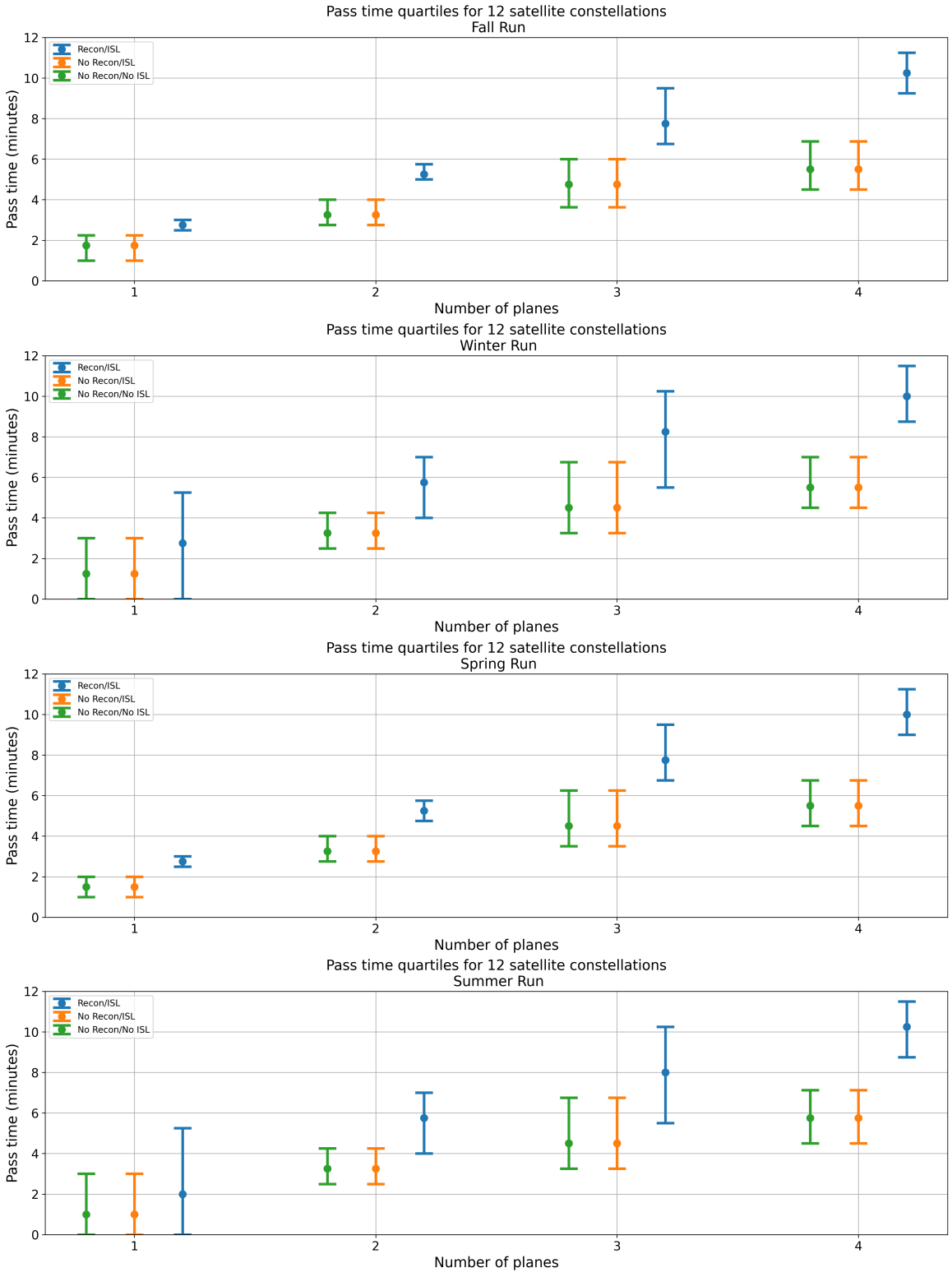

Figure 6-12: The pass time distribution for 12 satellite Walker constellations. The 25%, median, and 75% quartiles are shown by the lower bar cap, circular data point, and upper bar cap, respectively. Green and blue lines offset horizontally for clarity.

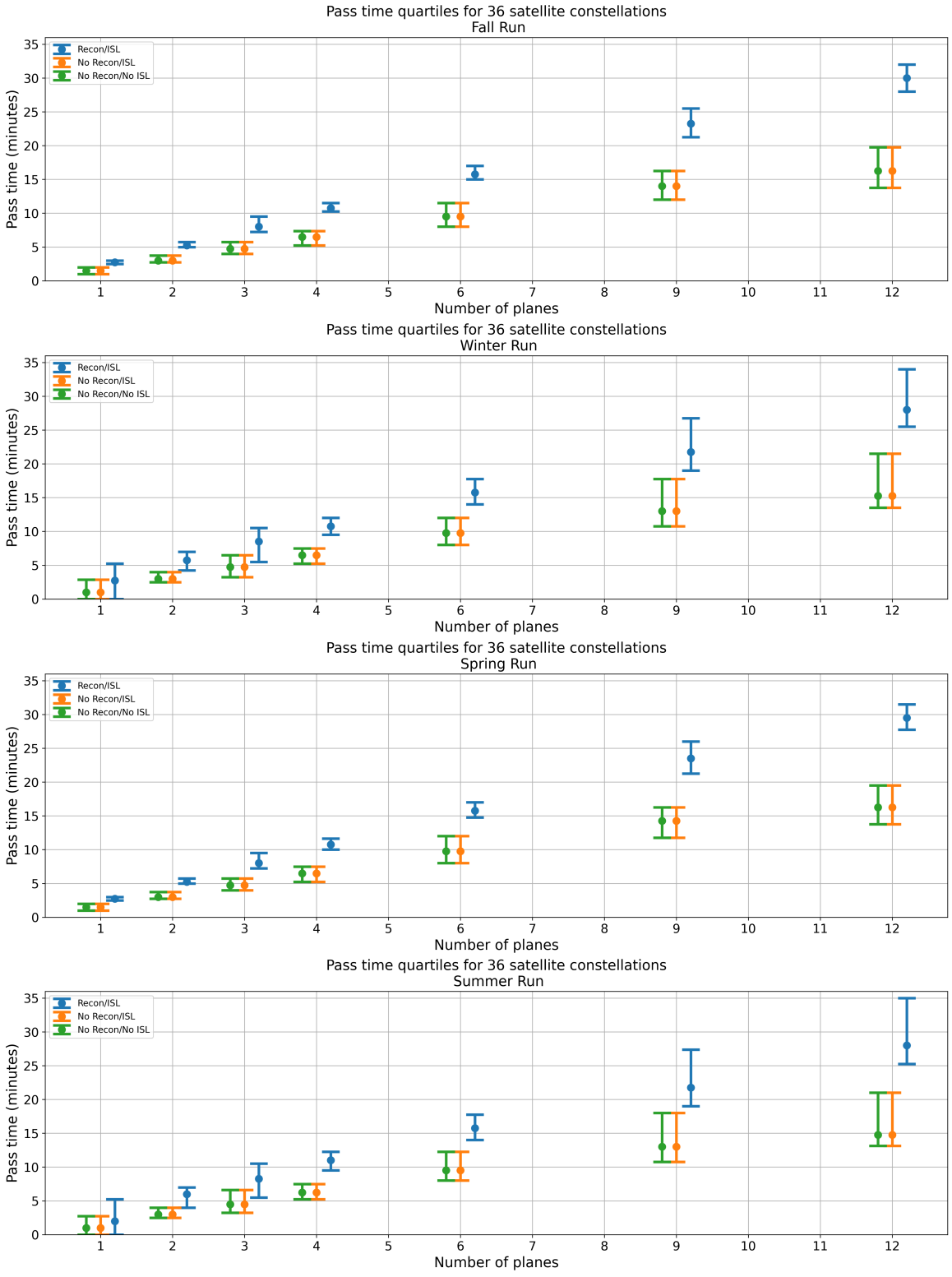

Figure 6-13: The pass time distribution for 36 satellite Walker constellations. The 25%, median, and 75% quartiles are shown by the lower bar cap, circular data point, and upper bar cap, respectively. Green and blue lines offset horizontally for clarity.

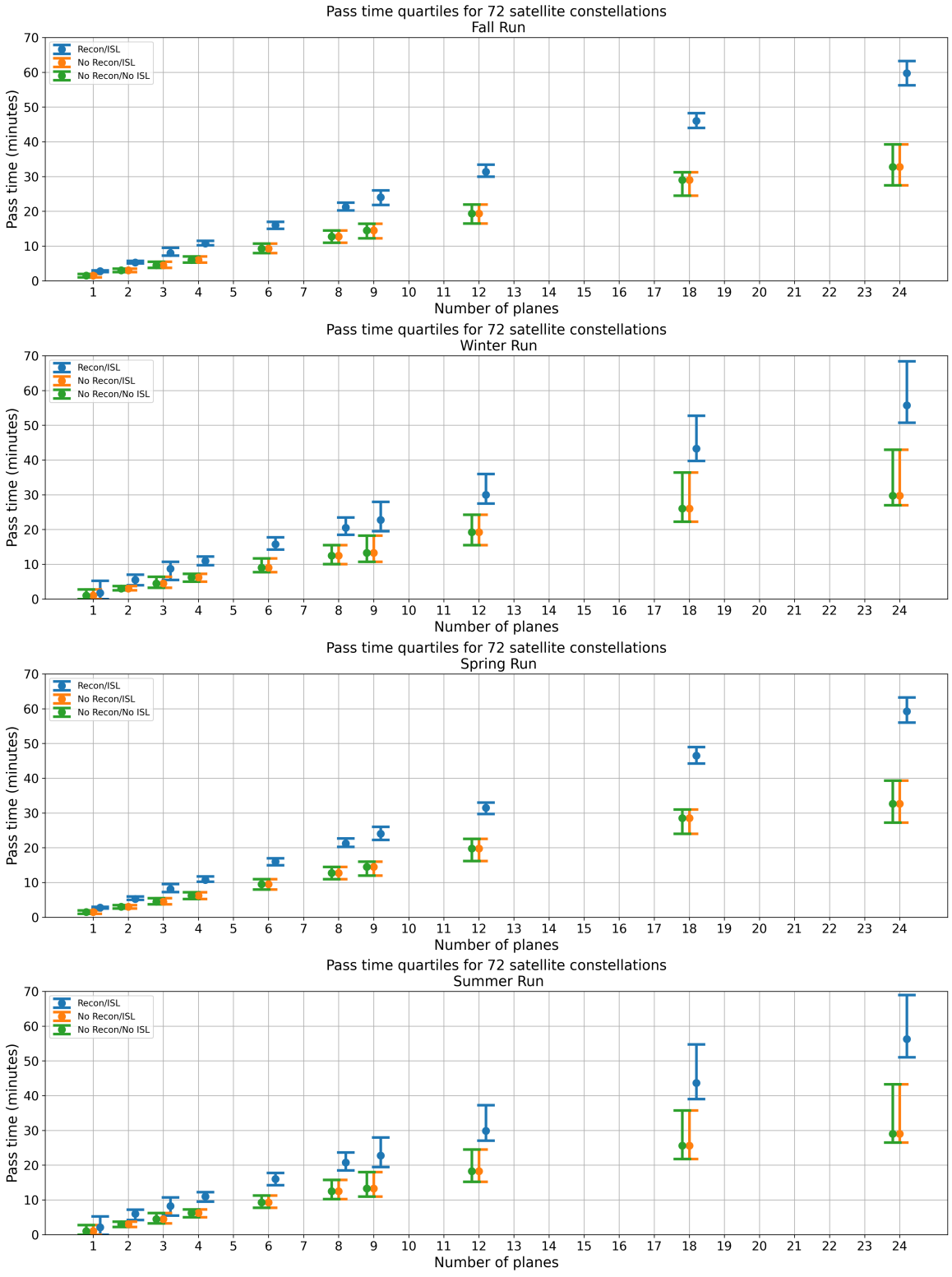

Figure 6-14: The pass time distribution for 72 satellite Walker constellations. The 25%, median, and 75% quartiles are shown by the lower bar cap, circular data point, and upper bar cap, respectively. Green and blue lines offset horizontally for clarity.

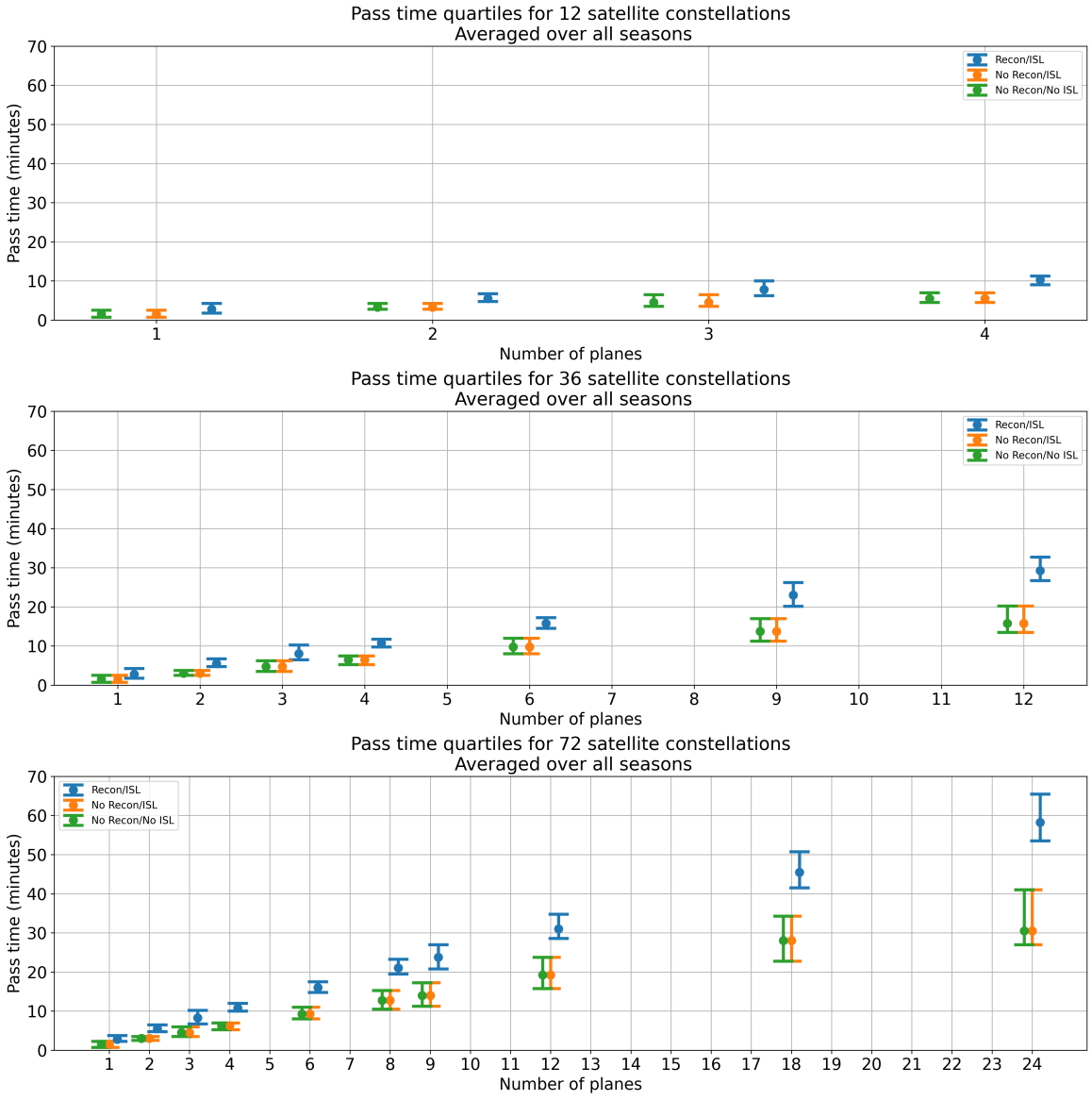

Figure 6-15: The total pass time distribution for 12, 36, 72 satellite constellations taking data over all seasons. The 25%, median, and 75% quartiles are shown by the lower bar cap, circular data point, and upper bar cap, respectively. Green and blue lines offset horizontally for clarity.

which is to be expected as their satellites do not undergo any propulsive maneuvers, and therefore are propagated identically.

The relative improvement in pass time performance between all three satellite models is shown in Figure 6-16. Improvement is defined by difference in median value, with less equating to better performance. Reconfigurable constellations perform 60% to 85% better than non-propulsive satellite models.

6.4.5 Comparison with BlackSky Constellation

A direct comparison can be made between the BlackSky Constellation system as defined in Tables 5.1 and 5.2 and the simulation run with the 60°:12/4/0 Walker constellation, as they both have the same number of satellites and planes. The BlackSky constellation does not have ISL or reconfiguration capabilities. However, for comparison, these two capabilities are included in separate simulation runs for a more direct comparison against the Walker constellation runs. The metrics can be seen in Table 6.3.

Table 6.3: Comparison between BlackSky and 12/4/0 Walker constellation

Metric	**No ISL/No Recon**	**ISL/No Recon**	**ISL/Recon**
AoI (BlackSky)	920 ± 450 min	890 ± 422 min	574 ± 217 min
AoI (Walker)	619 ± 217 min	619 ± 217 min	439 ± 169 min
SRT (BlackSky)	943 ± 840 min	902 ± 775 min	720 ± 453 min
SRT (Walker)	702 ± 518 min	702 ± 518 min	566 ± 370 min
Pass Time (BlackSky)	4.4 ± 2.9 min	4.4 ± 2.9 min	8.5 ± 3.7 min
Pass Time (Walker)	6.5 ± 3.3 min	6.5 ± 3.3 min	10.7 ± 3.3 min

From the simulation runs, it can be seen that ISL and reconfigurable capable constellations outperform the other satellite models. It can be also be seen that the Walker constellations perform better than the BlackSky constellation in every metric. One reason is due to the varied inclinations of the BlackSky satellites, which range from 35° to 60°. Since the simulated ground targets span from -55° to +55°, only a few of the BlackSky constellations can observe the targets at higher latitudes as opposed to the Walker constellation, which contains satellites with 60° inclinations. However, BlackSky may have chosen lower inclinations to gain better equatorial coverage.

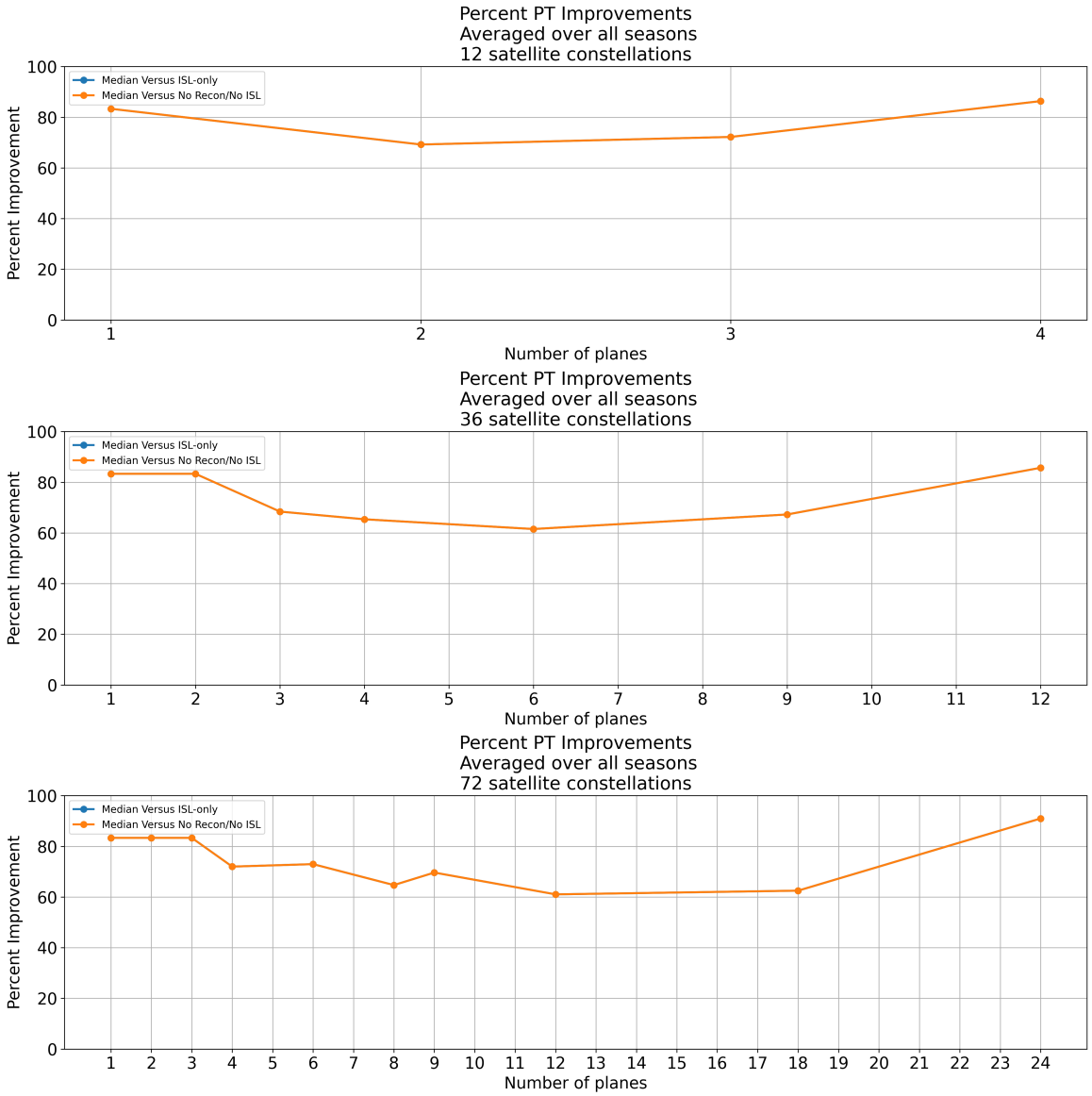

Figure 6-16: The relative improvement in pass time when introducing both ISL and reconfigurable capabilities. The improvement can be categorized by improvement in median value. Both sets of data points (blue and orange lines) are overlapped in this figure as ISL-only and baseline satellite models do not have propulsive capabilities; resulting in identical orbital propagation.

6.5 Explaining Outliers

Each simulation run has a few outliers that can be explained by unique scenario geometry and the hard simulation time cut-off. To illustrate this point, this section focuses on the summer run of the 60°:12/2/0 constellation that incorporates both reconfiguration and ISL. Figure 6-17 shows the distribution in AoI and also highlights the outliers that will be investigated in this section.

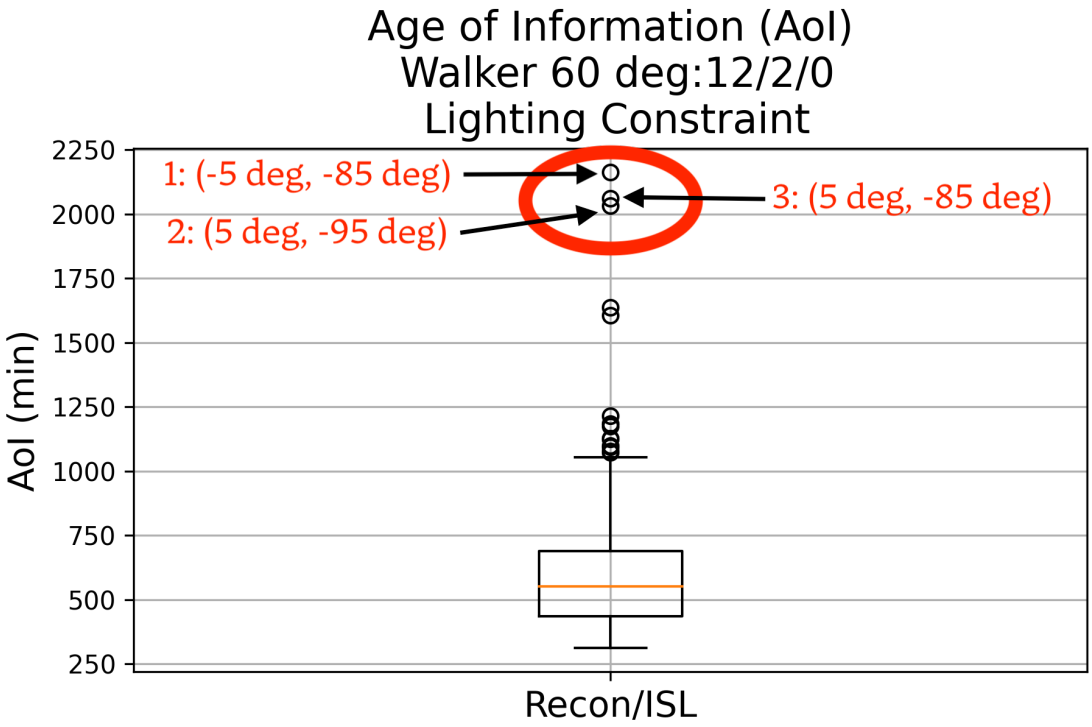

Figure 6-17: The AoI distribution for the summer run of the 60°:12/2/0 constellation. This section focuses on the outliers circled in red. The three study cases are labeled with latitude/longitude in parenthesis.

The three cases circled in red in Figure 6-17 refer to the ground target locations with latitude/longitude of:

1. -5° lat, -85° lon
2. 5° lat, -95° lon
3. 5° lat, -85° lon

This group of targets are located in relatively close proximity leading to similar geometric interactions with the satellite constellation.

6.5.1 Geometric contributions

A few geometric considerations contribute to a high overall simulation AoI. For a constellation with two planes, four satellites are expected to reconfigure into observing mode, two per plane for an ascending and descending pass. In this particular scenario, all three ground targets are located close to the equator, which would make the ascending and descending passes roughly 180° apart in true anomaly. With a separation in true anomaly of 180°, only one satellite per plane is expected to get a usable image due to the lighting constraint since if one pass occurs in daytime, the next pass should occur at night. For a three day simulation, roughly three direct overhead passes are expected per observing satellite, which totals to six passes for the two satellites that have a pass during the daytime.

6.5.2 Individual satellite example

In this particular case, the ground targets are not located on the equator so the separation in true anomaly is a little less than 180°. Taking a closer look at the reconfigured satellite in case 1 (-5° lat, -85° lon) that had initial parameters of a RAAN = 0° and true anomaly = -120°, the satellite's ground target passes end at:

1. 23:37 2019-06-21 UTC
2. 23:18 2019-06-22 UTC
3. 22:59 2019-06-23 UTC

Given a longitude of -85°, these times correspond to evening passes around 5:30 pm local. With the hard lighting constraint defined in Section 3.4.3, the first pass is considered invalid. Additionally, the last pass occurs an hour before the end of the simulation, which occurs at 00:00 2019-06-24 UTC. Due to the low number of planes, ISLs are uncommon. In this case there are no opportunities to downlink the

information before the simulation ends. This particular satellite has two successful imaging passes, but only one gets downlinked, resulting in an abnormally higher contribution to AoI.

The satellite in case 1 is scheduled to make a descending pass with two out of three passes successful in terms of lighting. The satellite in the same plane that makes an ascending pass is expected to have at least one successful imaging pass. However, this does not occur, as the target latitude is not exactly on the equator, leading to a true anomaly difference between ascending and descending passes to be slightly less than 180°. This factor, combined with the rotation of the Earth that occurs between ascending and descending passes leads to all of the satellite passes being invalidated by the lighting constraint. During the simulation, this particular plane only has one successful downlinked image due to the geometrical and simulation end time constraints, which inflates the AoI for this scenario.

6.6 Design Trades

From section 6.4, it can be seen that adding ISL and reconfiguration capabilities allows constellations to perform better than constellations that do not have those capabilities. This section includes cost in the analysis, investigating the cost/performance Pareto front in order to determine the optimal designs.

The analysis in this section takes the average of the performance metric for each Walker constellation design over all four seasonal simulations. The cost model from Section 3.6 is applied to each constellation design. Plotting cost on the x-axis and the relevant metric on the y-axis creates a figure from which a Pareto front can be calculated. The Pareto front determines the Pareto optimal designs by only including "non-dominated" designs, which are the designs that allow for the best performance given a price point. Other designs not on the Pareto front are "dominated" if they either provide worse performance than a design with equal or less cost, or the design costs more than other designs with equal or better performance.

6.6.1 Optimal designs for AoI

The cost vs AoI design space is shown in Figure 6-18 and the Pareto front designs are listed in Table 6.4. Cost errors in Table 6.6 are derived from the satellite cost uncertainties shown in Table 3.9.

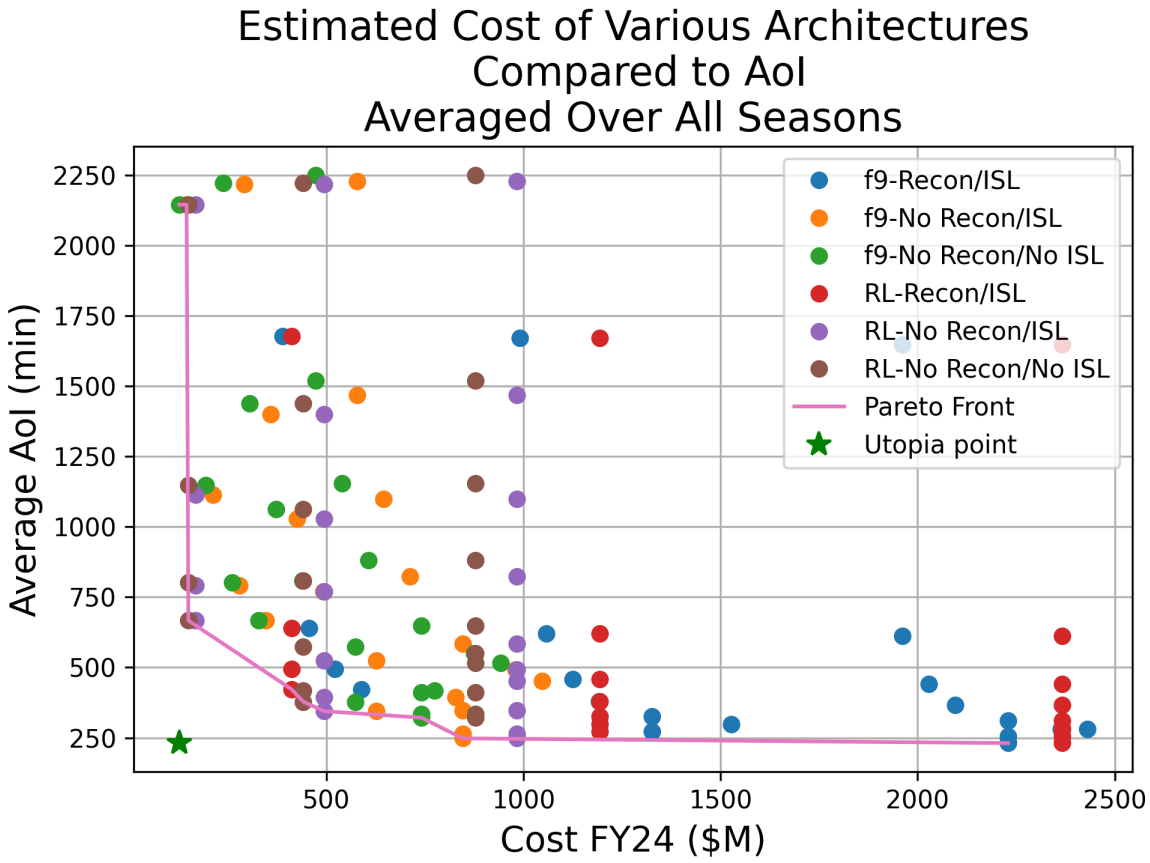

Figure 6-18: The design and cost space for AoI, showing the Pareto front in magenta. The utopia point represents the best metric performance at the lowest cost. 'f9' refers to a constellation purely launched using Falcon 9s and 'RL' for a constellation purely launched using the Rocket Lab Electron. Costs in millions of dollars.

There are a couple of interesting features to note in this design space. The first is the effect of the launcher in the cost space. Since the Rocket Lab Electron launches 1 satellite per launch, the cost is independent of the number of constellation planes, creating the vertical cost features seen in Figure 6-18. There are also three vertical features per constellation type, corresponding to the number of satellites in the constellation. For example, for a Rocket Lab-launched ISL and recon-capable constel-

Table 6.4: Pareto front points for AoI

Cost FY24 ($M)	**AoI (min)**	**Walker (t/p/f)**	**Launch Vehicle**	**Capabilities: Recon (R) | ISL (I)**
127 ± 8	1900	12/1/0	Falcon 9	N/A
328 ± 8	619	12/4/0	Falcon 9	N/A
411 ± 60	440	12/4/0	Electron	RI
441 ± 22	386	36/12/0	Electron	N/A
494 ± 30	346	36/12/0	Electron	I
846 ± 60	245	72/24/0	Falcon 9	I
2229 ± 340	236	72/24/0	Falcon 9	RI

lation (red), the 12 satellite constellations are at a price point around $400M (FY24), the 36 satellite constellations are at a price point around $1200M (FY24), and the 72 satellite constellation are at a price point around $2.3B (FY24). From Figures 6-2, 6-3, and 6-4, it can be seen that the points with higher AoI correspond to the constellations with fewer planes. If launching with Rocket Lab, it's best to launch a constellation with as many planes as possible as there is no additional cost penalty. On the contrary, the Falcon 9 cost model is dependent on the number of planes in the constellation, more specifically, the planar separation determines how many planes can be deployed per launch. Because of this, a horizontal as well as vertical spread in the cost values of Falcon 9-launched constellations is seen.

At lower price points (less than $1200M), the Pareto front generally consists of designs that do not have reconfigurable/propulsion capabilities. However, at $411M, there is a Rocket Lab-launched ISL and recon capable constellation (red) that provides a large performance boost, dropping the average AoI on the Pareto from 619 min to 440 min, a 29% performance increase. The next two points on the Pareto front are two other Rocket Lab-launched constellations (brown and purple) that do not have reconfigurable capabilities. These two constellations are also 36-satellite constellations while the recon-capable constellation (red) is only a 12-satellite constellation. This is an example of a smaller constellation providing similar performance at a comparable price to a larger constellation if given reconfiguration capabilities. Having fewer satellites is advantageous from a space sustainability standpoint but also adds

more performance risk if a satellite goes offline. In a 36-satellite constellation, the performance loss caused by a defunct satellite is more easily masked by the other satellites. Additionally, the cost uncertainties in Table 6.4 reveal that each of these three designs have comparable costs, as they overlap. The 12-satellite ISL and recon capable constellation is in the same class in both cost and performance as the 36 satellite constellations with only ISL capabilities or neither ISL nor recon capabilities. As stated in Section 3.6, the cost model does not take into account potential regulatory costs for space debris and sustainability. Including space sustainability factors into the cost model would make the contrast between the 12 satellite reconfigurable-capable constellation and the 36-satellite reconfigurable-non-capable constellations even larger.

At higher price points, the Pareto front is dominated by the ISL and recon-capable constellations, but it is interesting to note that the performance increase in AoI is only 9 min for a 1.5B$ (FY24) cost increase. The marginal performance increase can also be seen in Figure 6-4, where as the number of planes increase, the ISL only constellation becomes almost equal to the performance of the ISL and recon-capable constellation. With the Rocket Lab electron launch model, the cost for the 24-plane 72-satellite constellation is equal to the 2-plane 72-satellite constellation, as there is no launch penalty for including more constellation planes. Overall, constellations with both ISL and reconfiguration capabilities make up 29% of the Pareto front designs.

6.6.2 Optimal designs for SRT

The cost vs. SRT design space is shown in Figure 6-19 and the Pareto front designs are listed in Table 6.5. Cost errors in Table 6.6 are derived from the satellite cost uncertainties shown in Table 3.9. The SRT design space shares the same vertical Rocket Lab cost structure as the AoI design space. There is also a family of constellations with high SRTs, and these are the family of one-plane constellations, which can be seen in Figures 6-7, 6-8, and 6-9. The SRT design space differs from the AoI design space, where recon-capable constellations do not live on the Pareto front until higher price points. The 12-satellite Rocket Lab-launched constellation at $411M

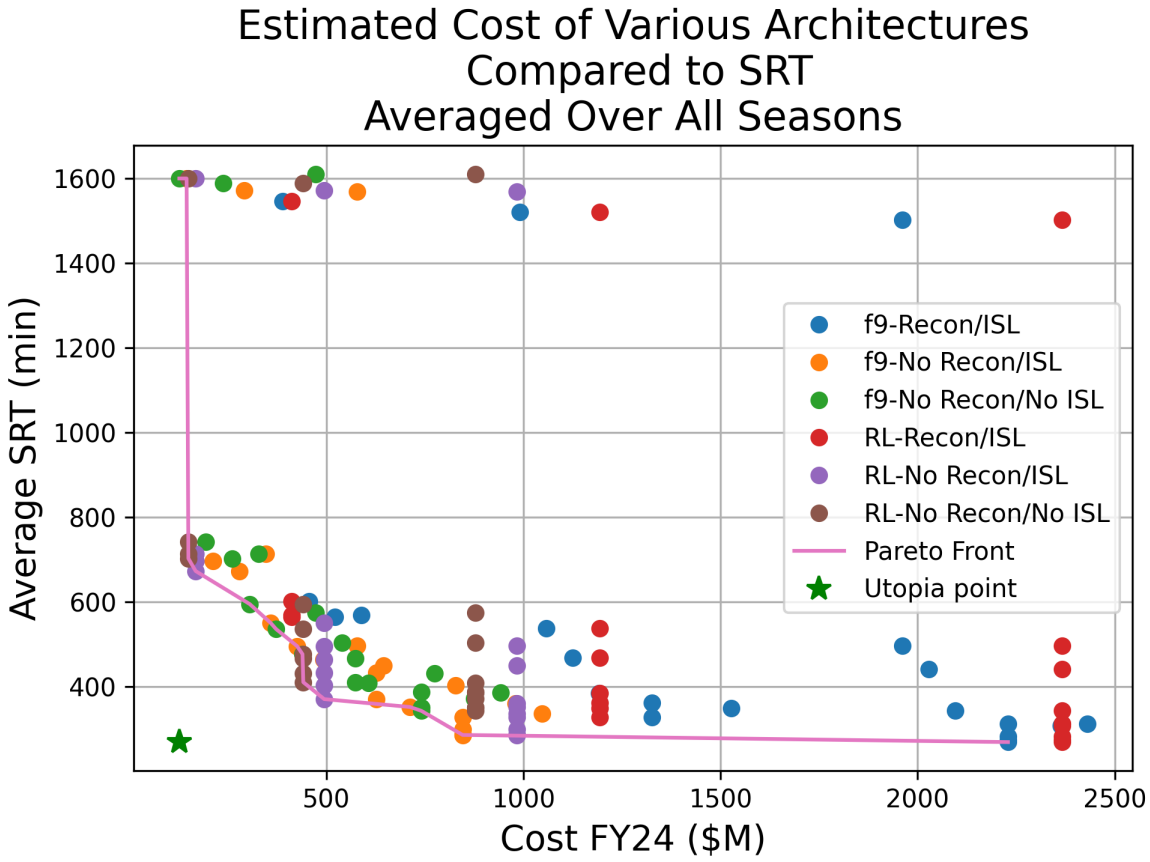

Figure 6-19: The design and cost space for SRT, showing the Pareto front in magenta. The utopia point represents the best metric performance at the lowest cost. 'f9' refers to a constellation purely launched using Falcon 9s and 'RL' for a constellation purely launched using the Rocket Lab Electron. Costs in millions of dollars.

Table 6.5: Pareto front points for SRT

Cost FY24 ($M)	**SRT (min)**	**Walker (t/p/f)**	**Launch Vehicle**	**Capabilities: Recon (R) | ISL (I)**
127 ± 8	1600	12/1/0	Falcon 9	N/A
145 ± 11	1600	12/1/0	Falcon 9	I
150 ± 8	702	12/3/0	Electron	N/A
168 ± 11	672	12/3/0	Electron	I
305 ± 22	597	36/2/0	Falcon 9	N/A
358 ± 30	551	36/2/0	Falcon 9	I
372 ± 22	536	36/3/0	Falcon 9	N/A
425 ± 30	496	36/3/0	Falcon 9	I
439 ± 22	477	36/4/0	Falcon 9	N/A
441 ± 22	410	36/12/0	Election	N/A
494 ± 30	370	36/12/0	Election	I
712 ± 60	354	72/4/0	Falcon 9	I
741 ± 44	344	72/18/0	Falcon 9	N/A
846 ± 60	282	72/24/0	Falcon 9	I
2229 ± 340	270	72/24/0	Falcon 9	RI

and SRT of 565 min is now dominated by the Falcon 9-launched 36-satellite 3-plane constellation at $388M and a SRT of 535 min. The main reason for the absence of ISL and recon-capable constellations from the lower cost constellation Pareto front is that AoI, unlike SRT, is able to measure persistent surveillance of an area, something that reconfiguration is designed for. SRT on the other hand measures immediate data latency, which reconfiguration also drives down, but the full advantages of RGT orbits are not necessarily captured in the SRT metric. The 12-, 36-, and 72-satellite ISL and recon-capable constellations do perform better in terms of SRT than constellations without reconfiguration, but their performance is bested by the constellations with more satellites, no reconfiguration capabilities, and lower price points. Again, like AoI, the higher cost models are dominated by ISL and recon-capable constellations, but the improvement of 12 min in SRT comes at a cost of 1.5B$ (FY24). Overall, constellations with both ISL and reconfiguration capabilities make up 7% of the Pareto front designs.

6.6.3 Optimal designs for pass time

The cost vs pass time design space is shown in Figure 6-20 and the Pareto front designs are listed in Table 6.6. Cost errors in Table 6.6 are derived from the satellite cost uncertainties shown in Table 3.9.

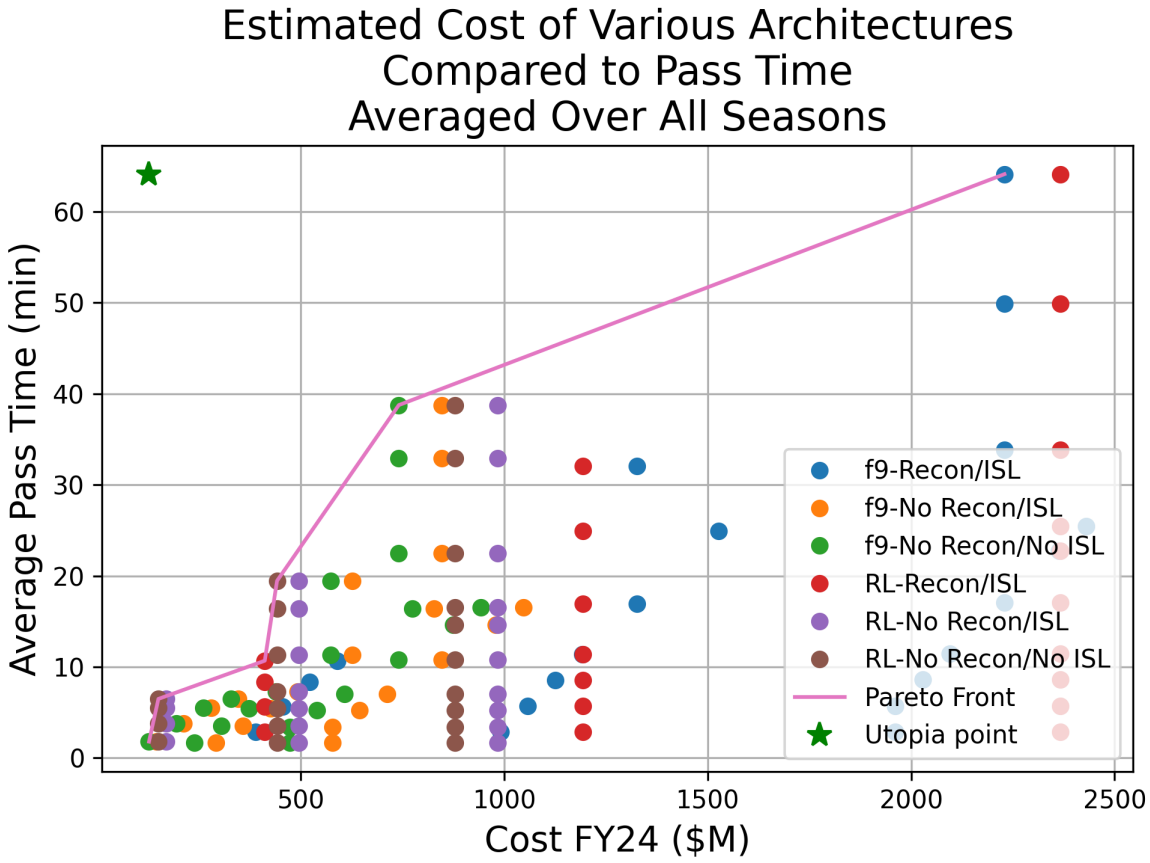

Figure 6-20: The design and cost space for pass time, showing the Pareto front in magenta. The utopia point represents the best metric performance at the lowest cost. 'f9' refers to a constellation purely launched using Falcon 9s and 'RL' for a constellation purely launched using the Rocket Lab Electron. Costs in millions of dollars (FY24).

Similar to the other metrics, the pass time Pareto front at lower cost points is dominated by constellations that do not have reconfigurable capabilities. The only exception to this is again the 12 satellite Rocket Lab-launched constellation at $411M. However, unlike AoI, the improvement in pass time is quickly overshadowed in performance by the 36 satellite no ISL/no recon constellation. There are also no ISL-only capable constellations on the Pareto frontier due to the fact that there is no propul-

Table 6.6: Pareto front points for pass time

Cost FY24 ($M)	**Pass time (min)**	**Walker (t/p/f)**	**Launch Vehicle**	**Capabilities: Recon (R) | ISL (I)**
127 ± 8	1.8	12/1/0	Falcon 9	N/A
150 ± 8	6.5	12/4/0	Electron	N/A
411 ± 60	10.7	12/4/0	Electron	RI
441 ± 22	19.5	36/12/0	Electron	N/A
741 ± 44	38.6	72/24/0	Falcon 9	N/A
2229 ± 340	64.0	72/24/0	Falcon 9	RI

sion on board these satellites; therefore all the constellations without reconfiguration capability will have the exact same total pass time. The ISL-only capable constellations will have a higher price tag than the non-ISL capable constellations, keeping them at the same pass time performance metric but with a higher price tag.

Unlike SRT and AoI, the performance increase in pass time at higher price points is significant, with performance gains of over 50% over a 72 satellite constellation with no recon capabilities if using a 72-satellite ISL and recon-capable constellation. A mission designer who weighs the pass time metric heavily may decide 72-satellite reconfiguration-enabled constellations are worth the extra cost. Overall, constellations with both ISL and reconfiguration capabilities make up 33% of the Pareto front designs.

6.6.4 Optimal design summary

Using the cost model in Section 3.6 and the data generated from the simulations described in this section (Section 6.4), a number of optimal designs is revealed. For AoI and pass time, there is a sweet spot at lower price points where ISL and recon-capable constellations outperform higher satellite constellations without recon capabilities. This sweet spot does not exist in the SRT design space as SRT does not fully capture the advantages of recon capabilities. The recon capable constellations also dominate at higher price points, with marginal performance increases in AoI and SRT and major performance increases for pass time. The cost model in Section 3.6 does not account for costs related to space sustainability and space traffic as these do not exist

at the time of writing. However, there is a growing amount of literature and industry momentum to advance space sustainability, and the inclusion of potential penalties for larger, non-propulsive constellations would make the advantages of recon-capable constellations more significant [131] [132].

There are only two 'super-dominant' designs, designs that are on the Pareto front for all three metrics:

1. \$127M (FY24), 60°:12/1/0, Falcon 9 launched, no-ISL / no-reconfigurability
2. \$2.2B (FY24), 60°:72/24/0, Falcon 9 launched, ISL / reconfigurability capable

These two designs represent the two ends of the cost and performance spectrum, which essentially guarantee them a spot on the Pareto front as there are no cheaper designs or designs with higher performance. In the constellation architecture trade space that is investigated in this work, there are no 'middle-of-the-road' designs that provide Pareto optimal performance for all three metrics.

6.7 Cost of responsiveness

From the analysis in Section 6.6.1, the relationships to determine the cost associated with improving each performance metric by fitting the points on the Pareto front can be extracted.

6.7.1 Age of Information

This section produces two fits to the data. The first produces a fit over the entire domain of the Pareto frontier points, while the second produces a linear fit to the knee in the curve over the domain between \$150M (FY24)to \$1000M (FY24).

AoI fit over entire domain

The Pareto front is fit with a function

$$f(x) = \frac{a}{|x|} + b \tag{6.1}$$

where a = 241238 min $M and b = -67.81 min. The fit can be seen in Figure 6-21. A fit over the entire domain can help designers estimate the cost of a constellation

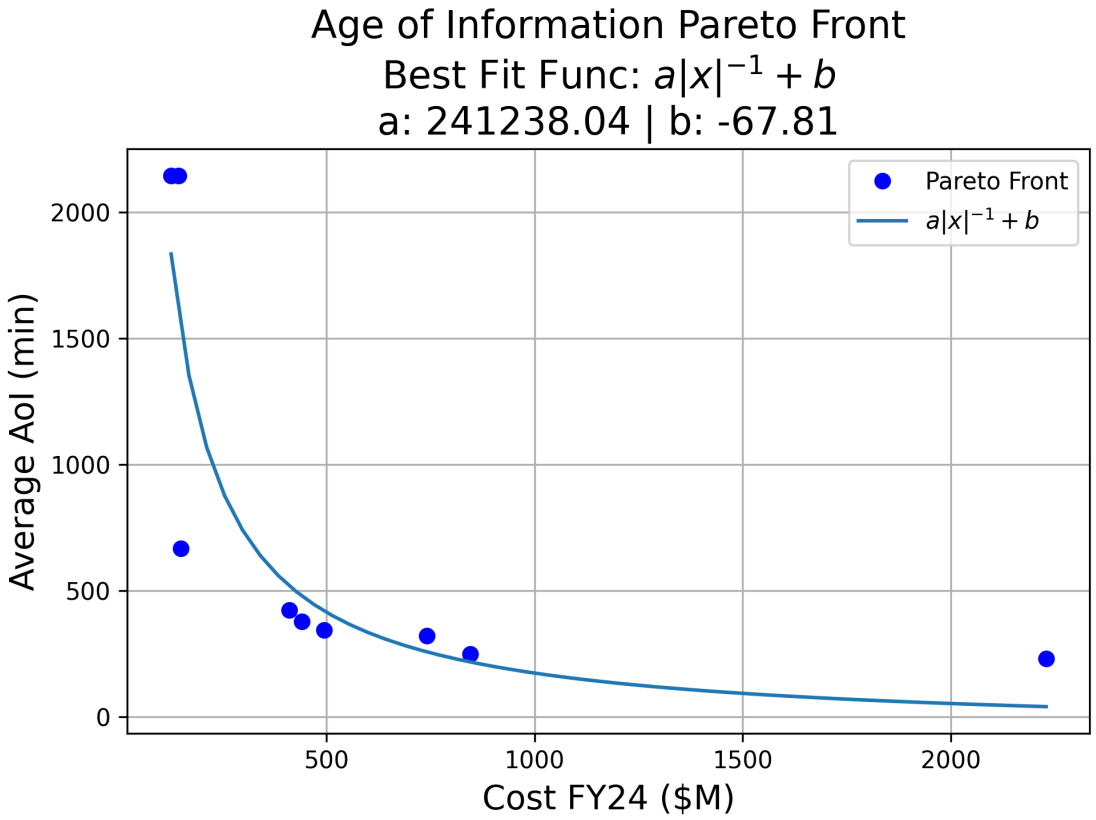

Figure 6-21: The functional fit over the entire domain for AoI

in the price range. Interestingly, the negative y-offset parameter (b) suggests that with infinite resources, AoI can be reduced to effectively 0. This can be theoretically achieved if a constellation is created where satellite cameras covers the entire surface of the Earth and where each satellite can communicate using ISLs at any time to adjacent satellites. Data can be immediately obtained and downlinked to a ground station.

AoI linear fit

While Equation 6.1 can accurately describe the cost/metric relationship over the entire cost domain, it can be illuminating to fit the subset of data in the 'knee' of the curve between costs of $150M (FY24) to $1000M (FY24). In Figure 6-22, the linear fit

excludes the two points with an average AoI of 1900 min at cost points of $126.81M (FY24) and $145.28M (FY24) and the last point with a price point of $2229.17M (FY24) and an average AoI of 236 min. The linear fit can be used by constellation

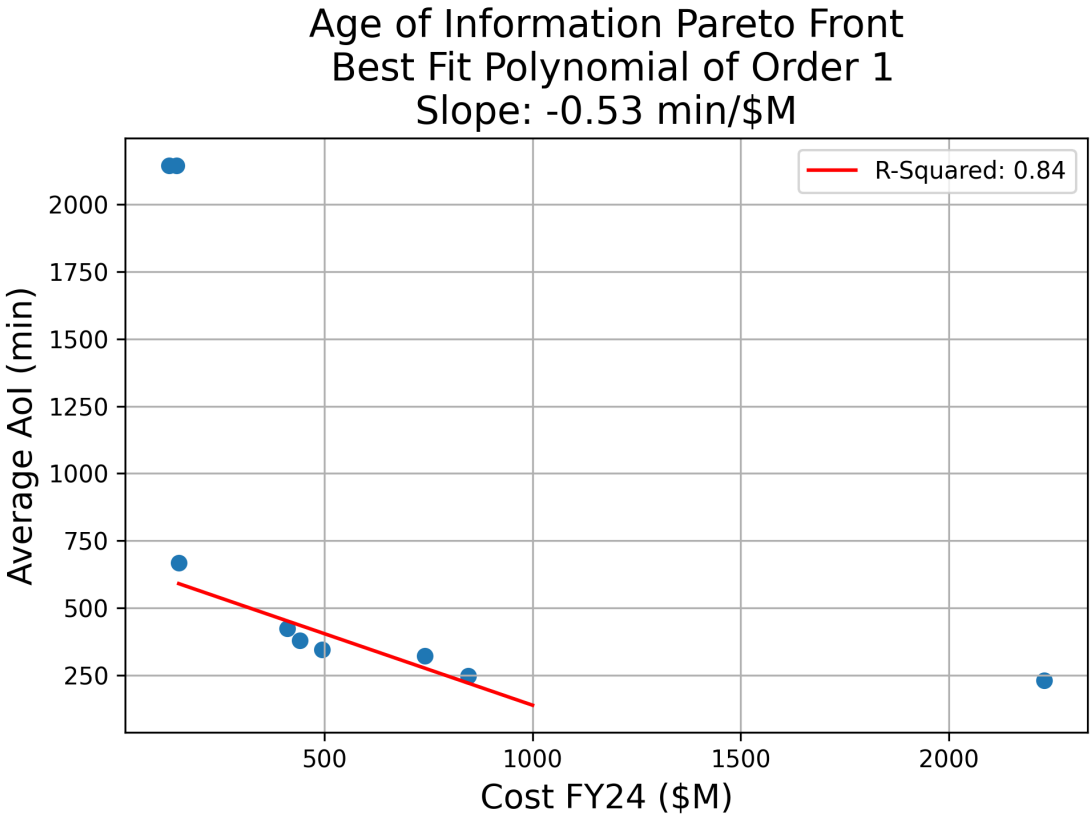

Figure 6-22: A linear fit of the points in the curve 'knee' for AoI

designers to evaluate the space between the cost range of $150M to $1000M. Within this range, every 32 seconds of improvement in AoI will cost $1M.

SRT fit over entire domain

The SRT Pareto front is also fit with Equation 6.1, with the best fit parameters are a = 155622 min $M and b = 104.68 min (See Figure 6-23). The y-offset of this fit (b) suggests that the minimum SRT achievable with infinite resources is equal to 104.61 min.

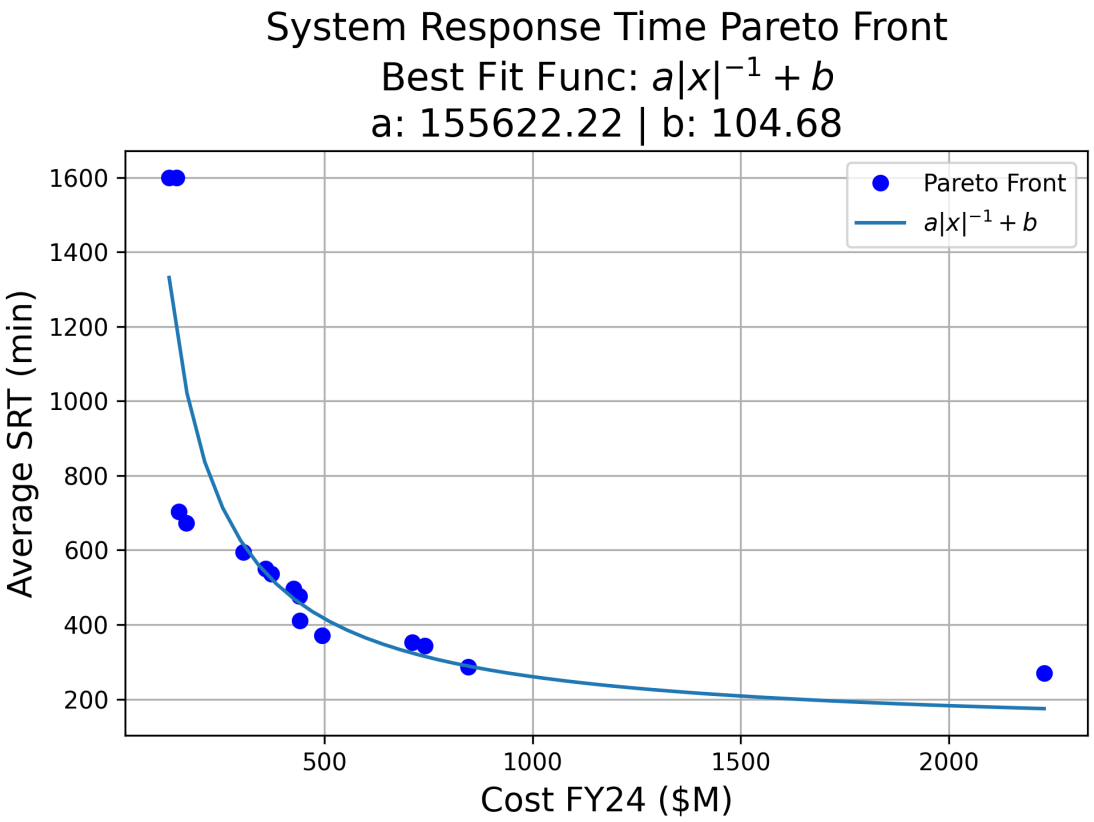

Figure 6-23: The functional fit over the entire domain for SRT

SRT linear fit

Similarly, a linear fit over the data 'knee', which excludes the first two Pareto front points at price points of $126.81M (FY24) and $145.28M (FY24) with average SRTs of 1600 min as well as the last point with a price point of $269.66M (FY24) and an average SRT of 2229 min. The fit can be seen in Figure 6-24. For SRT in the cost

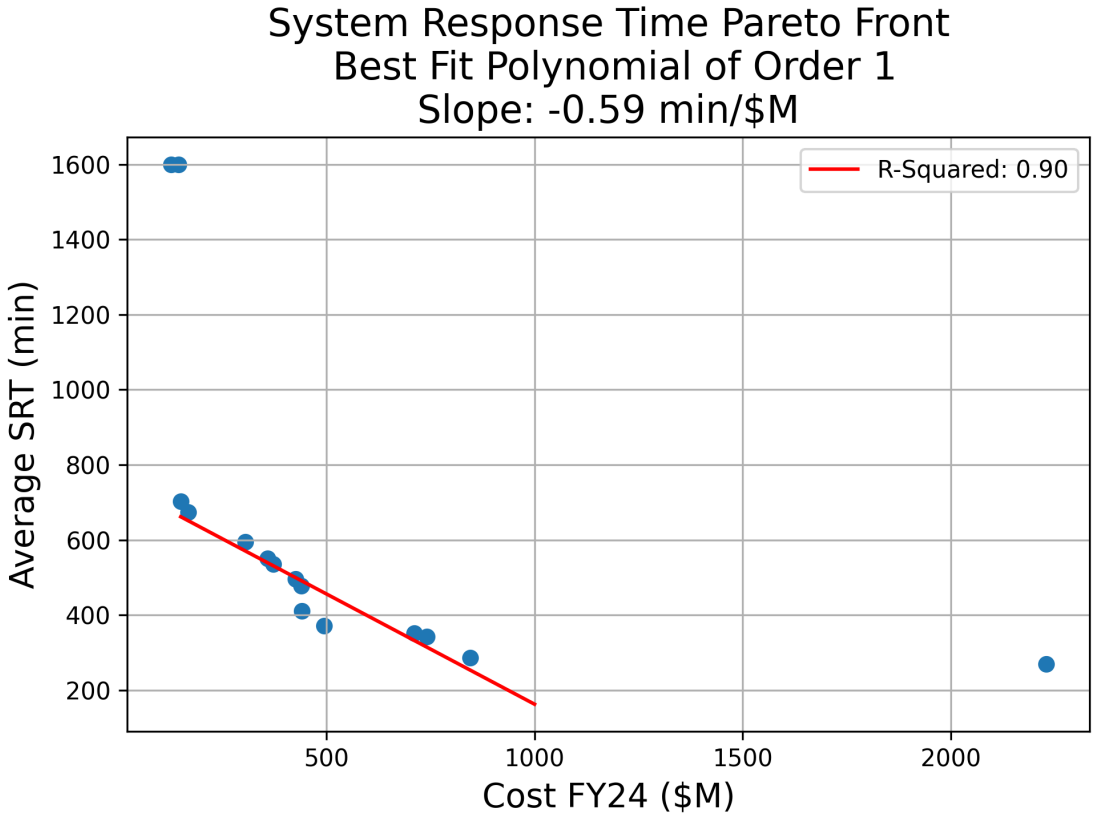

Figure 6-24: A linear fit of the points in the curve 'knee' for SRT

domain between $150M to $1000M, every 35 seconds of improvement in this metric will cost $1M.

6.7.2 Pass time

The pass time Pareto front has a different shape than both AoI and SRT, so a linear fit can be made over the entire cost domain. The results of the fit are shown in Figure 6-25. The linear pass time Pareto fit suggests that each million dollars spent improves pass time by almost 2 seconds over a 3 day time period.

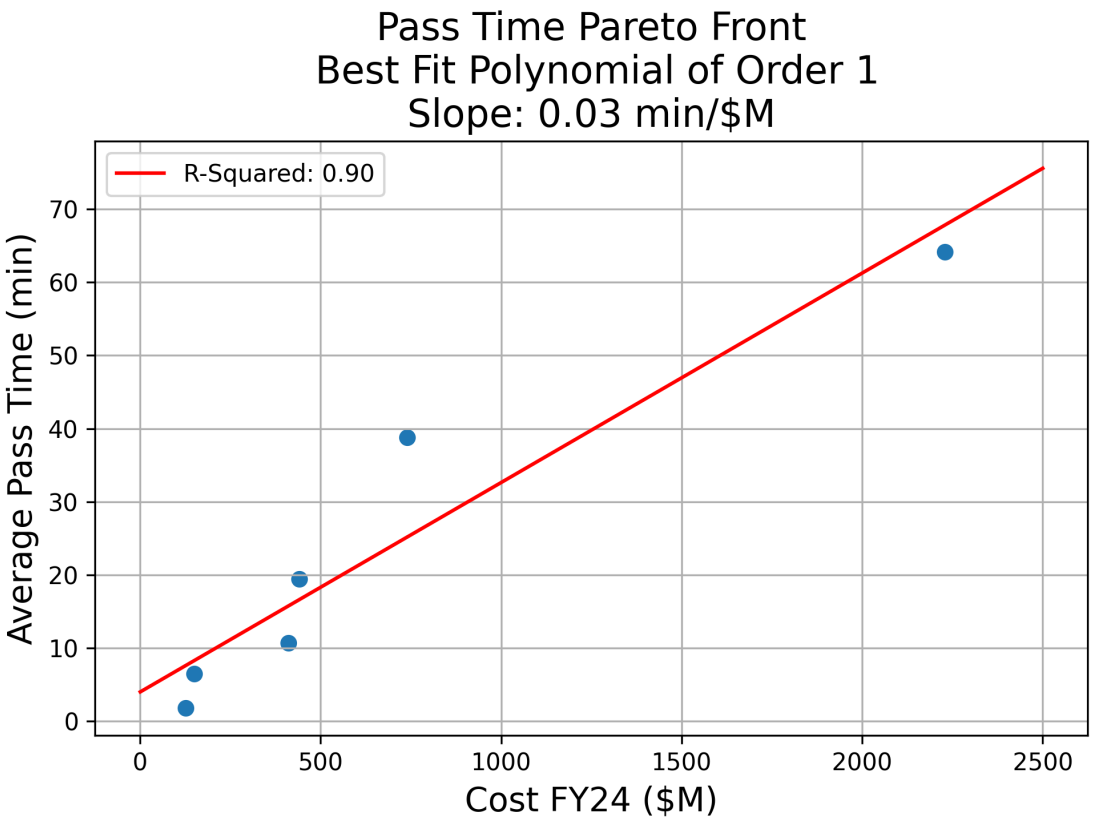

Figure 6-25: A linear fit of the pass time Pareto front.

THIS PAGE INTENTIONALLY LEFT BLANK

Chapter 7

Conclusions and future work

This work presents new tools to assess the performance and cost of a constellation that is capable of both utilizing ISL and propulsive reconfiguration in order to provide timely information. These constellations are useful for responding to natural and man-made disasters as well as for environmental monitoring. The work also describes a planning and scheduling algorithm needed to implement a constellation with ISL and propulsive capabilities. The planning and scheduling algorithm is tested in a simulation framework developed in this work, and the merits of this new type of constellation are analyzed through a Pareto front analysis as well as the development of CERs to model the relationship between constellation ability to deliver timely data and their costs. The following sections of this chapter describe the major contributions from this work as well as future directions.

7.1 Review of contributions

The major contributions of this work are:

1. Contribution 1: A completely open-source python-based constellation simulation and analysis framework is created. Unlike previous work in this field, there is no reliance on proprietary software such as MATLAB or STK. However, STK is used to verify the accuracy of the propagators and analysis functions. Additionally, this work extends previous open-source software libraries, which

often focus on single-satellite propagation, for applications using satellite constellations. The software also allows for the implementation of planning and scheduling algorithms and post-simulation analysis and extraction of metrics. Because the software has been built in a modular fashion, it also enables different propagators, planning and scheduling algorithms, and analyses to be easily implemented (see Appendix B).

2. Contribution 2: A novel planning and scheduling algorithm that reduces data timeliness for satellite constellations with both ISL and reconfiguration capabilities is described in this work. Previous works focused on either ISL routing or reconfiguration propulsive maneuvers, but did not yet integrate and subsequently test both capabilities. The reconfiguration algorithm produces up to 125% increased pass time over 7 days when compared to a satellite in GOM (see Figure 4-6) and a 67% increase in pass time at a nadir viewing half-angle of 20°. The data routing algorithm modifies the classic Dijkstra's algorithm to allow the contact graph to become time-dependent, more accurately modeling the intermittent contact between satellites and ground stations. This algorithm is considered optimal as long as there is no throughput bottleneck. No bottlenecks are modeled into the simulation framework.

3. Contribution 3: A selection of Pareto optimal constellation designs for timely data was presented. For optimizing AoI, 29% of all Pareto optimal designs are constellations with both ISL and reconfiguration capabilities. For optimizing SRT, 7% of the Pareto optimal designs are ISL and reconfiguration capable constellations, and for total pass time, 33% of designs are constellations with ISL and reconfiguration capabilities. The analysis shows that a constellation with ISL and reconfiguration capabilities can outperform a larger constellation of 36-satellites with respect to AoI if that larger constellation does not have reconfiguration capabilities. SRT on the other hand is not dominated by constellations with ISL and reconfiguration capabilities because SRT does not capture the persistent surveillance of an area that reconfigurability offers. Lastly, for

overall pass time, reconfigurable capabilities offer great performance increases, which are expected as they are a direct measurement of how often a satellite passes over a given target.

4. Contribution 4: New CERs are developed using the SSCM and launch vehicle models. These CERs produce relationships that allow constellation designers to evaluate the expected performance of their constellations with respect to cost, so they can adjust their costs to reflect customer needs and business models. For AoI and SRT, two CERs are provided, the first of which covers the entire cost domain and provides a non-linear relationship to estimate costs and performance. The second CER is limited to a smaller subset of the cost domain, but provides an easier to understand linear relationship between cost and performance. For total pass time, only a linear CER is derived.

7.2 Future work

This work develops tools and analysis for ISL and propulsive capable satellite constellations. However, the work presented is only a starting point, and there are many promising avenues to further this field of research. The following outlines future directions to take this work.

7.2.1 Planning and scheduling algorithm

The planning and scheduling algorithm can be improved in various ways, increasing its efficiency and capabilities.

1. Multiple event planning: The current planning and scheduling algorithm can only handle one event at a time. For applications such as natural and man-made disasters, this may be sufficient. However, the algorithm is not prepared for the scenario when multiple disasters occur within the observation time frame of a previous disaster. Future work can add a module to the planning and scheduling algorithm that allows it to utilize the remaining non-observing satellites in the

constellation and reconfigure them to monitor the second disaster site. Potential features of the algorithm include a weighting factor based on suspected damage to life and property for the various target sites, which could also re-allocate resources to the new target that were previously allocated to the old target. The algorithm could also handle simultaneous/near-simultaneous events where resources have yet to be allocated to a single target, so the algorithm would dictate where to send all the satellite in GOM.

2. Constellation lifetime planning: The current planning and scheduling algorithm is tailored to respond to one event. An extended planning and scheduling algorithm would be able to optimize resources over the entirety of the constellation lifetime. For example, a satellite that has already been tasked with multiple reconfigurations may be left out of the next reconfiguration in order to conserve fuel, even though that particular satellite will reach the target the fastest. During the course of the constellation lifetime, satellite performance may vary due to quality issues such as a malfunctioning payload. The algorithm would be able to assign satellites to particular roles depending on their expected performance over a long period. It would also be able to handle anomalies such as satellite failures. Additionally, the availability of on-orbit refueling depots would open up research avenues for fuel-efficient trajectories between fuel depots, ROM, and GOM as well as satellite design considerations since satellites do not have to carry as much fuel mass.

3. Resource constrained environments: The current time-dependent Dijkstra's algorithm is assumed to be optimal because given the assumptions, there are no throughput restrictions over the expected contact times, and all data can be transferred between a single contact time frame. The algorithm can be extended to handle resource constrained environments where data can be sent in packets over multiple different contact intervals. Additionally, there are other routing algorithms that can be explored for different scenarios. For example, the first contact algorithm (assumes zero apriori knowledge), the minimum ex-

pected delay algorithm with time-invariant costs (assumes knowledge of graph contacts), the earliest delivery with all queues (assumes knowledge of graph contacts), and linear programming algorithms (assume complete knowledge of the scenario) [128].

4. Expected lighting: The planning and scheduling algorithm currently does not account for the expected lighting at the time of the satellite pass. Depending on the application, the algorithm can dictate burn schedules based on the expected lighting of the target at the time of pass. Some scenarios may prefer dawn/dusk lighting for shadows while others may prefer direct overhead lighting. Given a particular scenario, the algorithm can dictate satellite movements to ensure fulfillment of the best lighting conditions.

5. Higher precision propulsion planning: The maneuver planning algorithm takes into account the J2 perturbation when calculating drift times; however, the Hohmann transfers in the maneuvers do not take into account this higher level perturbation. Accounting for higher level perturbations will make the algorithm more accurate, leading to increased pass times. Additionally, more expensive transfers such as the one-tangent burn can reduce the time to first pass if the satellite happens to be in the right orbit [2]. In terms of revisit time, the targeting algorithm can also be modified to achieve a more customizable revisit time. For example, the algorithm can select to move 1 satellite instead of 2 satellites in a plane to achieve a slower revisit time, which may be suitable for use with a slower developing phenomena. This would allow the constellation to conserve overall fuel with minimal effects on performance.

7.2.2 Analysis

The following are a few interesting analysis directions to take the work:

1. Exploration of the ground station trade space: The current work used the ground station network proposed by BlackSky. An analysis studying the placement of ground stations, in number and location, can provide information on

when it is more useful to build more ground stations versus adding reconfigurable satellites with respect to the timeliness metrics, AoI and SRT. Coupled with a ground station cost analysis, a researcher can develop a Pareto front of architectural decisions that expands this work to include ground station locations in the constellation design.

2. Incorporate space sustainability into cost model: Proponents of space sustainability are gathering momentum, but have not yet quantified the value of launching constellations with less satellites and propulsive capabilities. These two features are inherent in reconfigurable constellations as satellites have propulsive capabilities by default and also can perform similarly to constellations with more satellites. Quantifying and incorporating the sustainable merits of reconfigurable constellations would alter the Pareto optimal designs selected in this work to better reflect the direction of the regulation and policy.

3. Investigate other communication bands for performance and cost: The models in this work used X-band RF transmission given the industry heritage. Other bands could be useful for ISL links, especially higher frequency bands such as V-band. This could alter both the data transmission rate as well as the cost estimates for the constellations. Beyond RF transmission, optical intersatellite links would be an interesting case study that could also impact both data rates and cost estimates.

4. Regional constellation design: The analysis in this work utilized an equidistant grid of potential imaging targets in its analysis. However, certain countries or companies may only be interested in monitoring certain areas. For example, a company may only be interested in monitoring their own assets or a country may be focused only on monitoring a certain type of natural disaster, say forest fires or earthquakes. The addition of localized target areas into the analysis pipeline will allow constellation designers to better understand how the proposed satellite constellation systems can respond to their expected needs.

Appendix A

Data sheets

A.1 Atlas Ground Stations

The Atlas ground stations for S and X-band [133]. See next page.

ATLAS Antenna Network Spec Sheet

ATLAS' Global Antenna Network is fully integrated with our Freedom™ Software, providing users low latency, secure communications solution. Including: automated network operations, set-and-forget scheduling, mixed modem capability, real-time metrics, and single secure VPN access.

Location	Lat	Long	Antenna Size	Rx Freq (MHz)	G/T (dBi/k)	Tx Freq (MHz)	EIRP (dBW)	Polarization
Utqiagvik (Barrow), AK, USA	71.27	-156.80	3.7m	S: 2200-2300 X: 7900-8400	12.8 26.4	S: 2025-2110 -	50.0 -	R/LHCP
Sodankylä, Finland	67.37	26.63	7.3m	S: 2200-2300 X: 7750-8400	19.81 32.11	S: 2025-2110 -	54.8 -	R/LHCP
Dundee, Scotland	56.45	-2.98	3.7m	S: 2200-2400 X: 7800-8400	13.6 26.5	S: 2025-2120 -	48.0 -	R/LHCP
Brewster, WA, USA	48.14	-119.70	7.6m	S: 2200-2300 X: 7900-8500	15.0 31.0	S: 2025-2120 -	53.8 -	RHCP
Chitose, Japan	42.77	141.62	3.4m	S: 2200-2300 X: 7900-8500 UHF: 397-405	10.89 25.91 -	S: 2025-2120 - UHF: 450-460	52.0 - 32.0	R/LHCP
Mojave, CA, USA	35.06	-118.16	3.0m	S: 2200-2300 X: 7750-8500	11.31 25.93	S: 2025-2110 -	50.0 -	R/LHCP
Miami, FL, USA	25.61	-80.38	11.3m	X: 8000-8500	35.0	-	-	RHCP
Dubai, United Arab Emirates	24.94	55.35	3.7m	S: 2200-2300 X: 7900-8500	12.8 25.4	S: 2025-2120 -	50.0 -	R/LHCP
Harmon, Guam	13.51	144.82	3.7m	S: 2200-2300 X: 7900-8400 UHF: 395-405	13.68 26.15 -	S: 2025-2110 - UHF: 435-455	50.28 - 32.0	R/LHCP - RHCP
Sunyani, Ghana	7.34	-2.34	3.0m	S: 2200-2300	12.4	S: 2025-2110	50.15	RHCP
Tahiti, French Polynesia	-17.64	-149.61	3.7m	S: 2200-2300 X: 7900-8400	13.96 27.48	S: 2025-2120 -	50.0 -	R/LHCP
Mingenew, Australia	-29.01	115.34	5.0m	S: 2200-2300 X: 8025-8400	14.0 29.5	S: 2025-2120 -	55.0 -	R/LHCP
Awarua, New Zealand	-46.53	168.38	3.7m	S: 2200-2300 X: 8025-8400	13.7 27.0	S: 2025-2120 -	48.0 -	R/LHCP

Modem	Product / Number	Compatible Bit Rate	Modulation / Demodulation
Amergint	satTRAC	120 Mbps	BPSK, QPSK, SQPSK, OQPSK, 8PSK, GMSK, FSK
Kratos RT-Logic	qRadio, qFEP, QMR, MMR	1.5 Gbps	FSK, BPSK, QPSK, SQPSK, OQPSK, 8PSK, GMSK, MSK, 16 QAM, DVB-S2 16 APSK, 32 APSK

*Please note: All RF bands and transmit / receive capability and polarization can be modified to meet client needs.

10850 E. Traverse Highway, Ste. 3355
Traverse City, MI, USA, 49684

+1 (231) 598-6184
info@atlasground.com

A.2 Spaceteq X-band Horn

Spaceteq horn antenna [134]. The X-horn 23 is used to close the ISL link budget. See next page.

X BAND TRANSMIT ANTENNA
X HORN-18/23

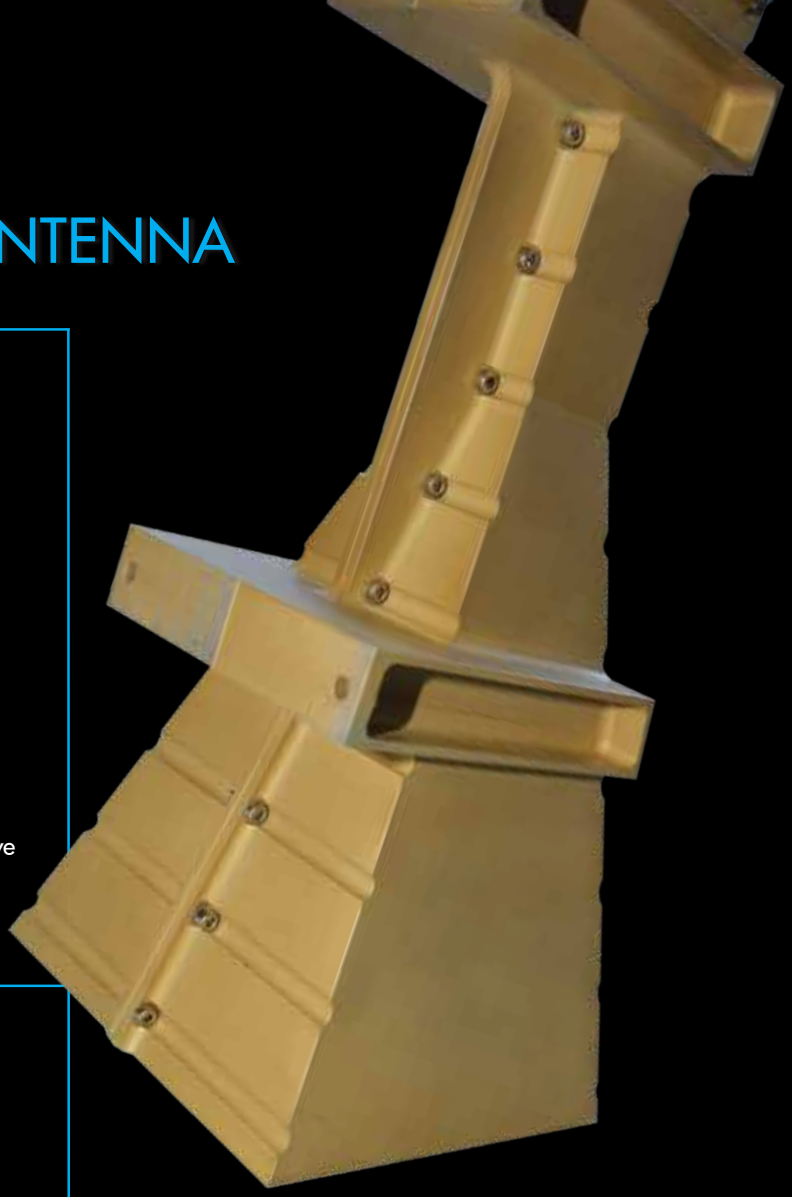

The XHorn family is a dual circularly polarised high gain rigid horn antenna. Its two feed ports are well isolated to allow for simultaneous orthogonal microwave link operation. The simple design, precision milled aluminium construction and very low parts count ensures ruggedness and high reliability.

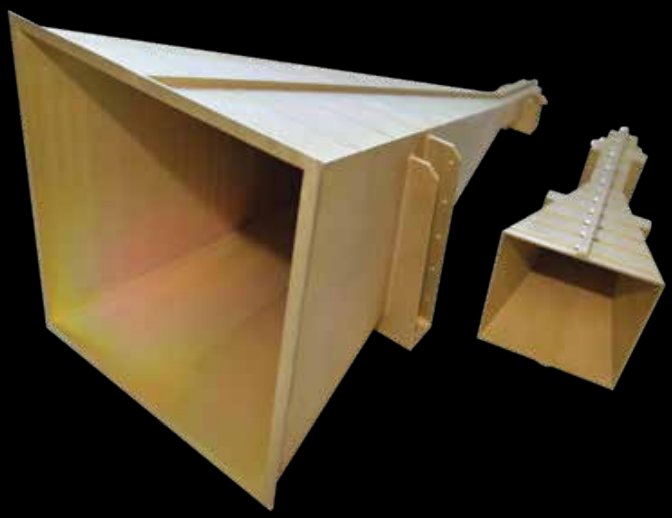

Benefits

Low cost, high performance
Simple, proven design
Improved and scaled design of heritage flight antennas
Allows lower transmitter power (lower DC power, lower heat loads, cheaper and simpler transmitter)
Allows smaller ground station antenna to be used (simpler hardware and lower cost)

Features

EO X-band window
High gain, Narrow beam
Dual circular polarised
Good port isolation
Low Axial Ratio

SPACETEQ

T +27 21 007 3001
spaceteq@spaceteq.co.za
www.spaceteq.co.za

Spaceteq
Houwteq, High Rising Road, Haasvlakte, Grabouw
PO Box 88, Grabouw, 7160, South Africa

SPECIFICATIONS	XHorn-18	XHorn-23
Performance		
Peak Isotropic Gain (RHCP & LHCP)	18 dBic	23 dBic
Cross Polar Isolation (port to port)	> 20 dB	> 25 dB
Bandwidth (S11,22 < -15 dB/ -18dB)	8000 - 8500 MHz	8000 - 8500 MHz
Axial Ratio at Boresight	< 1.5 dB	< 1.5 dB
Design Life	7 years	7 years
Mechanical		
Dimensions	252x 113.4 x 103.4 mm	547x 216.3 x 214 mm
Weight	< 450g	< 1.73 kg
Interface	4 off M4	4 off M6
Environmental		
Operating Temperature	-20°C to +60°C	-20°C to +60°C
Random Vibration (Qualification)	14g RMS	14g RMS
Radiation (component level)	> 15 kRad	> 15 kRad

SPACETEQ

T +27 21 007 3001
spaceteq@spaceteq.co.za
www.spaceteq.co.za

Spaceteq
Houwteq, High Rising Road, Haasvlakte, Grabouw
PO Box 88, Grabouw, 7160, South Africa

A.3 Moog Monopropellant Thrusters

MOOG monopropellant thruster data sheet [135]. The MONARC-22-12 is used to enable satellite reconfiguration maneuvers. See next page.

MONOPROPELLANT THRUSTERS

Moog offers a wide range of monopropellant thrusters suited for spacecraft and flight vehicle attitude control applications. These hydrazine thrusters have a long and successful heritage. Range of applications include; earth observation and communication, space exploration, and missile defense.

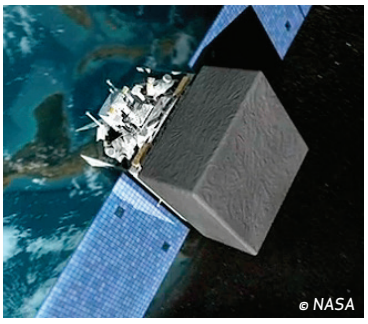

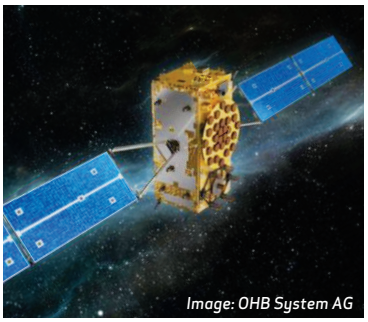

MOOG

MONOPROPELLANT THRUSTERS

PERFORMANCE CHARACTERISTICS

	MONARC-1	MONARC-5	MONARC-22-6	MONARC-22-12	MONARC-90LT	MONARC-90HT	MONARC-445
Engine					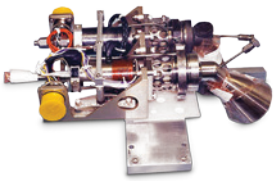		
Steady State Thrust	0.22 lbf (1N) @275 psia	1.0 lbf (4.5 N) @325 psia	5 lbf (22N) @275 psia	5 lbf (22N) @190 psia	20 lbf (90 N) @ 235 psia	26 lbf (116 N) @ 235 psia	100 lbf (445N) @ 275 psia
Feed Pressure	70 – 400 psia (4.8 – 27.6 bar)	80 – 420 psia (5.5 – 29.0 bar)	70 – 400 psia (4.8 – 27.6 bar)	70 – 400 psia (4.8 – 27.6 bar)	80 – 400 psia (5.5 – 27.6 bar)	80 – 370 psia (5.5 -25.5 bar)	70 – 400 psia (4.8-27.6 bar)
Nozzle Expansion	57:1	135:1	60:1	40:1	40:1	50:1	50:1
Valve Power	18 watts	18 watts	30 watts	30 watts	72 watts	72 watts	58 watts
Mass	0.83 lbm (0.38 kg)	1.08 lbm (0.49 kg)	1.58 lbm (0.72 kg)	1.51 lbm (0.69 kg)	2.47 lbm (1.12 kg)	2.47 lbm (1.12 kg)	3.5 lbm (1.6 kg)
Engine Length/Exit Diam	5.2 in (13.3 cm) / .2 in (0.5 cm)	9.4 in (41.8 cm) /1 in (2.5 cm)	8 in (20.3 cm) / 1.5 in (3.8 cm)	9 in (22.9 cm) / 1.2 in (5.3 cm)	12 in (30 cm) / 3.3 in (8.4 cm)	12 in (30 cm) / 3.3 in (8.4 cm)	16 in (41 cm) / 5.8 in (14.8 cm)
Specific Impulse	227.5 sec	226.1 secs	229.5 secs	228.1 secs	232.1 secs	234.0 secs	234.0 secs
Minimum Impulse Bit	0.0006 lbf-sec (2.6 mN-sec)	0.0007 lbf-sec (3.1 mN-sec)	0.07 lbf-sec (312m N-sec)	0.12 lbf-sec (526m N-sec)	0.04 lbf-sec (1.8 N-sec)	0.26 lbf-sec (1.16 N-sec)	2.59 lbf-sec (11.52 N-sec)
Total Impulse	25,000 lbf-sec (111,250 N-sec)	138,000 lbf-sec (613,852 N-sec)	120,000 lbf-sec (533,784 N-sec)	263,720 lbf-sec (1,173,085 N-sec)	786,000 (3,500,000 N-sec)	459,100 lbf-sec (2,042,178 N-sec)	1,250,000 lbf-sec (5,600,000 N-sec)
Pulses	375,000	205,000	230,000	160,000	50,000	70,000	12,000

MOOG
SPACE AND DEFENSE GROUP

6686 Walmore Road, Niagara Falls, NY, 14304-1697
Tel +1 716 731 6000
www.moog.com/space
bvogt@moog.com

linkedin.com/company/moog-sdg
facebook.com/MoogSDG.USA
twitter.com/MoogSDG

Form 500-934 0418

A.4 Hydrazine tank

Ariane group Hydrazine tank data sheet [136]. This tank model is used to estimate the mass fraction of propellant versus tank. See next page.

SURFACE TENSION TANK OST 31/0

Surface Tension Tank OST 31/0	
Tank Net Volume	104 to 177 Litres
Max. Propellant Volume	78 Litres (Blow Down 4:1)
Propellant	Hydrazine (N_2H_4)
Pressurant Gas	Helium (He) or Nitrogen (N_2)
Maximum Expected Operating Pressure (MEOP)	24.6 bar
Proof Pressure (1.5 x MEOP)	36.9 bar
Burst Pressure (2.0 x MEOP)	49.2 bar
Interface Fixation	Polar Mounting, Rigidly Fixed at Propellant Port Boss Side
Materials	
- Pressure Vessel	Ti6Al4V STA (Hemispheres 3.7164.7)
- Gas & Propellant Ports	Ti6Al4V (3.7164.1)
- Propellant Management Device	All Titanium
Tank Mass	≤ 6.85 kg
Project Application	Globalstar

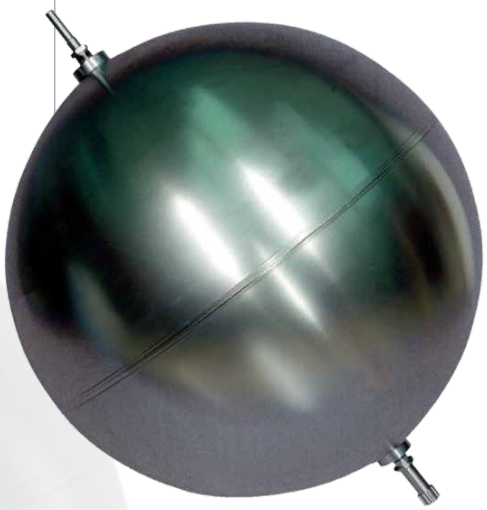

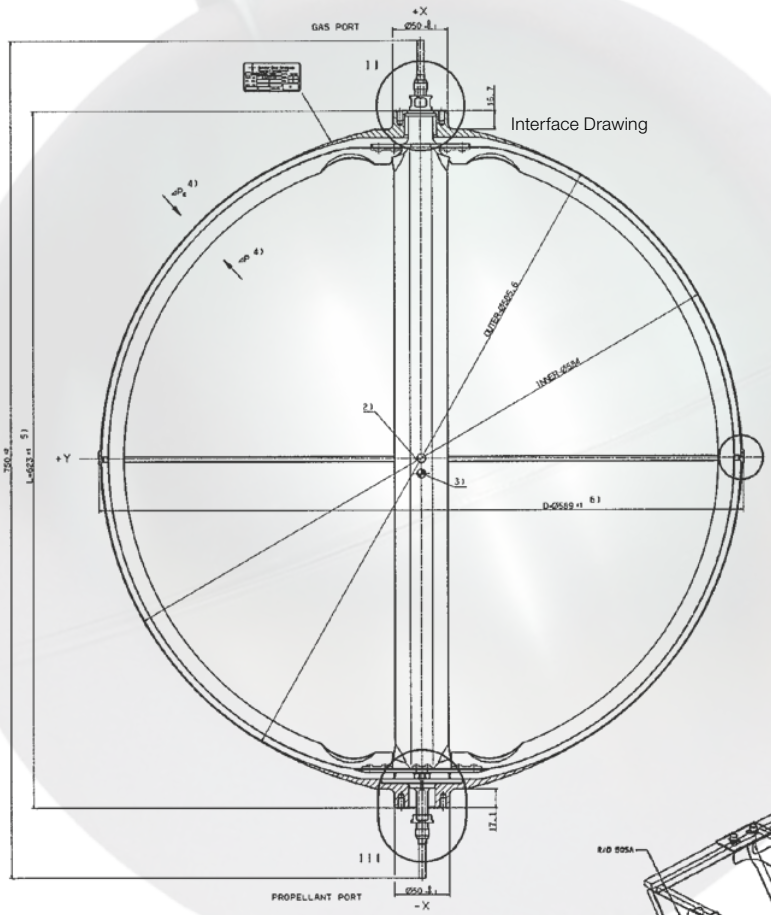

Interface Drawing

Mission Requirements

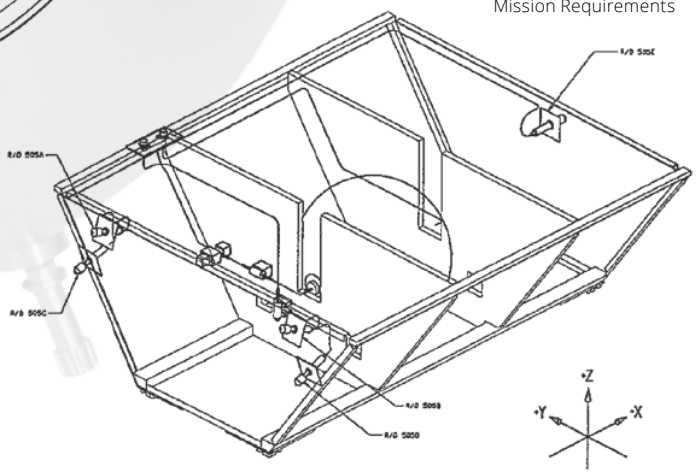

- → Propellant Pumping towards the Propellant Port
- → Steady State Pumping Rate of 2.0 cm^3/s against an Acceleration Level of $1x10^{-3}$ g_0 (g_0 = 9.81 m/s^2)
- → Expulsion of higher Flow Rates during 4 Thruster Firing DV - Manoeuvre
- → Expulsion for Attitude Control Manoeuvres

ArianeGroup - Orbital Propulsion - Robert-Koch-Straße 1 - 82024 Taufkirchen - Germany
Susana Cortés Borgmeyer - susana.cortes-borgmeyer@ariane.group - Phone: +49 (0)89 6000 29244 - www.space-propulsion.com

A.5 MOOG COMET

The MOOG COMET, which is used to model a space tug in the Falcon 9 cost model [137]. See next page.

COMET

PROPULSIVE ESPA

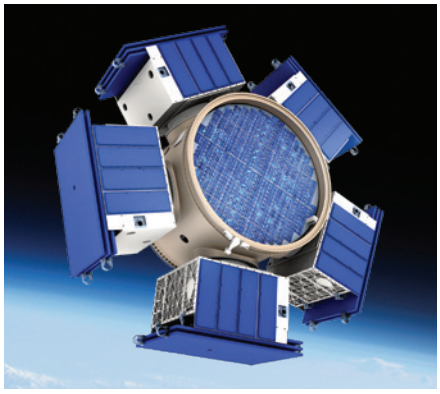

COMET is a Propulsive ESPA product family used for a variety of missions in LEO. COMET is ideal for rideshare/multi-manifest or other disaggregated mission types. COMET leverages the same core avionics from Moog's Space Vehicle family that have been demonstrated in missions from LEO to the Moon. The hydrazine propulsion system provides enough capability for several different missions including deploying multiple planes of smaller spacecraft. The simple and robust all aluminum structure based on Moog's ESPA Grande provides radiation shielding and can support a range of payload configurations. COMET can be used as a hosted payload platform further expanding the mission types.

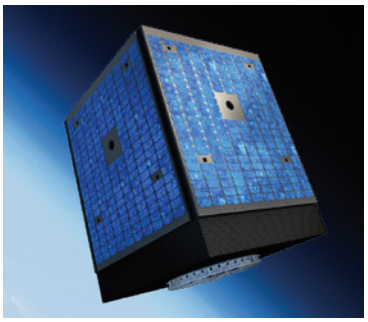

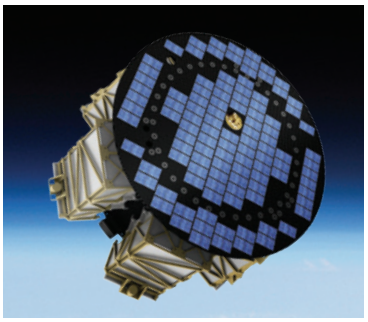

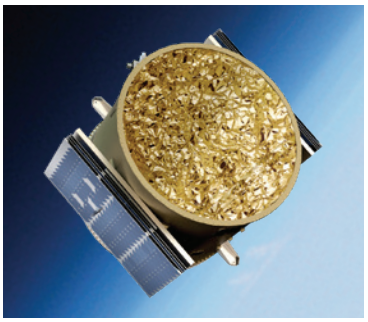

KEY FEATURES

- Avionics leveraging Moog's BRE440™ rad-hard CPU
- LEO missions, expansion to GEO missions possible
- Flexible flight software is payload and mission configurable
- High-thrust hydrazine propulsion system
- Single string but layered GNC sensor suite provides resiliency
- Can be stacked in NSSL-class launch vehicles

MOOG

COMET PROPULSIVE ESPA

SPECIFICATIONS

Characteristic	Performance / interfaces
Orbit	500 to 1200 km
Mission Life	< 1 years (based on propellant usage)
Radiation	25.5 kRad total dose with 0.200" Al shielding
Radiation Effects	Availability due to SEU of >99% over 1 year
Bus Mass	518 kg Bus Dry Mass
Bus Volume	Ø62" x 42" Tall
Orbital Position Knowledge	<4 m
Attitude Knowledge Telemetry Accuracy	<40 arc-sec (1 sigma)
Velocity Accuracy	0.1 m/s
Delta-V	>350 m/s (with 1086 kg Payload mass)
Payload Interfaces (Mechanical)	5x 42"x46"x56" (Port/Side Mounted) with Ø24" Ports 6x 42"x28"x56" (Port/Side Mounted) with Ø15" Ports
Payload Mass	5 x 300 kg (Up to 700 kg with reduced propulsion capabilities)

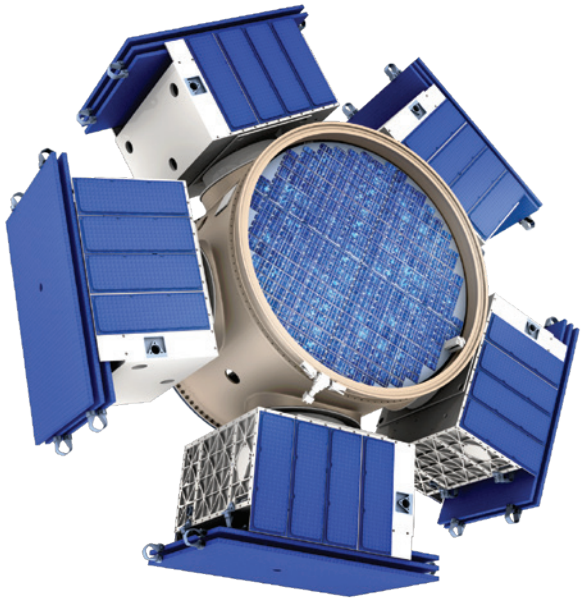

MOOG
SPACE AND DEFENSE GROUP

For More Information
Christopher Loghry
16080 Table Mountain Pkwy, Unit 500, Golden, CO 80403
cloghry@moog.com

Moog Space and Defense @MoogSDG @MoogSDG @MoogSDG @MoogInc

A.6 Falcon 9 usable volume

A page from the Falcon 9 Payload User Guide that details the usable volume of the fairing [138]. See next page.

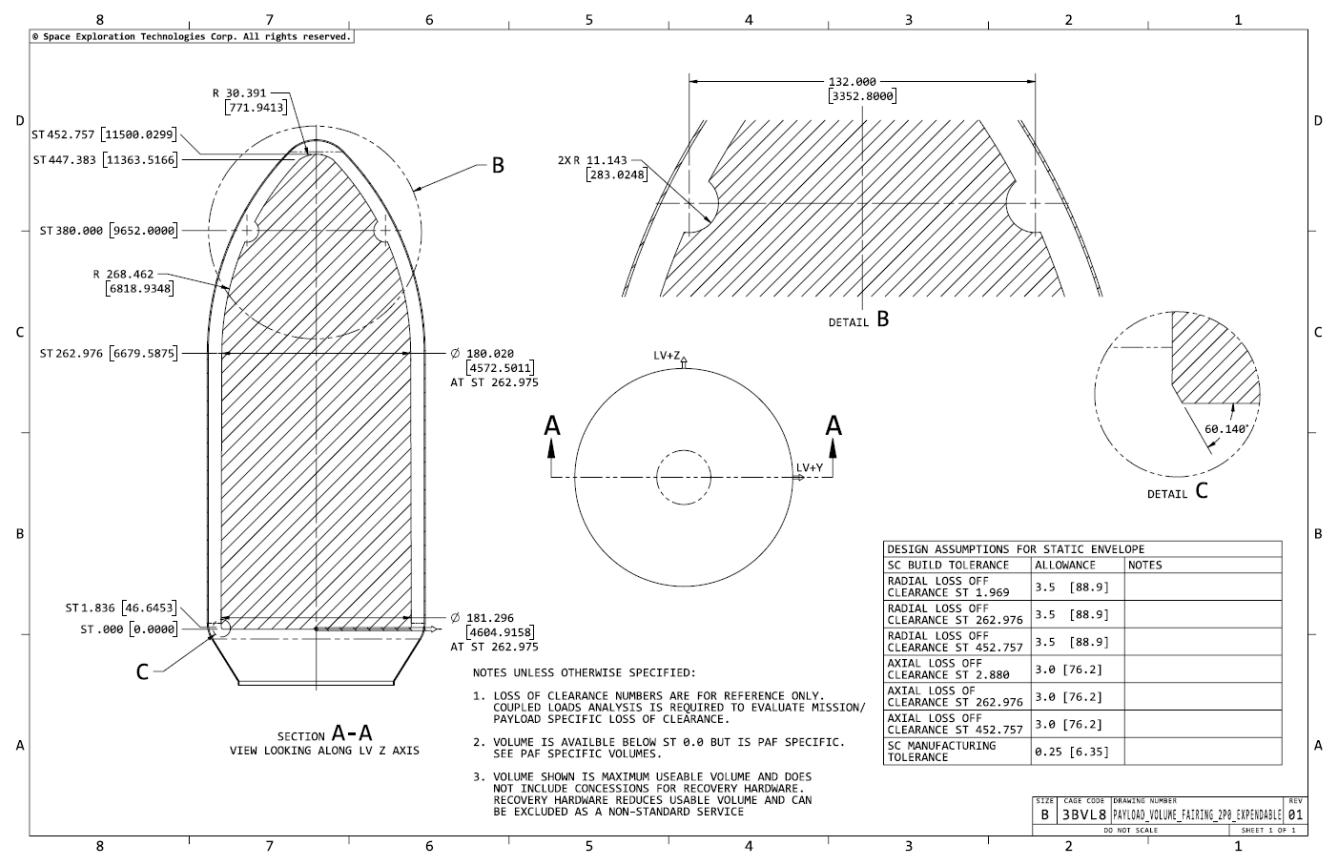

Figure 12-5: Payload static envelope (standard Falcon fairing)

THIS PAGE INTENTIONALLY LEFT BLANK

Appendix B

Github

Code for this thesis can be found on the Github site: https://github.com/manweichan/SatLib

The libraries in the repository are all open-source and include: Poliastro, Astropy, and a few libraries written by the author.

THIS PAGE INTENTIONALLY LEFT BLANK

Appendix C

Delta-V calculations

C.1 Reconfiguration maneuvers

C.1.1 GOM to drift orbit

The GOM to drift orbit maneuver takes a satellite from 550 km to 650 km. Using constants [2]:

$$r_{Earth} = 6378.1\text{km}$$

$$\mu = 3.986 \times 10^{14} \frac{\text{m}^3}{\text{s}^2}$$

we can calculate the semi-major (b) and semi-minor (a) axes of the Hohmann ellipse and plug them into Equation 2.16:

$$a = r_{earth} + 550 \text{ km} = 6928.1\text{km} \tag{C.1}$$

$$b = r_{earth} + 650 \text{ km} = 7028.1\text{km} \tag{C.2}$$

$$a_{trans} = \frac{a+b}{2} = \frac{6928.1\text{km} + 7028.1\text{km}}{2} = 6978.1\text{km} \tag{C.3}$$

Equations 2.15 and 2.17 can then be solved:

$$\begin{aligned}
\Delta v_a &= \sqrt{\frac{2\mu}{a} - \frac{\mu}{a_{trans}}} - \sqrt{\frac{\mu}{a}} \\
&= \sqrt{\frac{2 \times 3.986 \times 10^{14} \frac{\mathrm{m}^3}{\mathrm{s}^2}}{6928.1\mathrm{km}} - \frac{3.986 \times 10^{14} \frac{\mathrm{m}^3}{\mathrm{s}^2}}{6978.1\mathrm{km}}} - \sqrt{\frac{3.986 \times 10^{14} \frac{\mathrm{m}^3}{\mathrm{s}^2}}{6928.1\mathrm{km}}} \\
&= 27.13 \frac{\mathrm{m}}{\mathrm{s}} \qquad \text{(C.4)} \\
\Delta v_b &= \sqrt{\frac{\mu}{b}} - \sqrt{\frac{2\mu}{b} - \frac{\mu}{a_{trans}}} \\
&= \sqrt{\frac{3.986 \times 10^{14} \frac{\mathrm{m}^3}{\mathrm{s}^2}}{7028.1\mathrm{km}}} - \sqrt{\frac{2 \times 3.986 \times 10^{14} \frac{\mathrm{m}^3}{\mathrm{s}^2}}{7028.1\mathrm{km}} - \frac{3.986 \times 10^{14} \frac{\mathrm{m}^3}{\mathrm{s}^2}}{6978.1\mathrm{km}}} \\
&= 27.03 \frac{\mathrm{m}}{\mathrm{s}} \qquad \text{(C.5)}
\end{aligned}$$

Plugging the two values into Equation 2.18:

$$\Delta v_{Hohmann} = |\Delta v_a| + |\Delta v_b| = 27.12 \frac{\mathrm{m}}{\mathrm{s}} + 27.03 \frac{\mathrm{m}}{\mathrm{s}} = 54.15 \frac{\mathrm{m}}{\mathrm{s}} \qquad \text{(C.6)}$$

C.1.2 Drift orbit to RGT

The drift to RGT maneuver takes a satellite from 650 km to 505 km. Again we calculate the semi-major (b) and semi-minor (a) axes of the Hohmann ellipse and plug them into Equation 2.16:

$$a = r_{earth} + 505 \text{ km} = 6883.1\mathrm{km} \qquad \text{(C.7)}$$

$$b = r_{earth} + 650 \text{ km} = 7028.1\mathrm{km} \qquad \text{(C.8)}$$

$$a_{trans} = \frac{a+b}{2} = \frac{6883.1\mathrm{km} + 7028.1\mathrm{km}}{2} = 6955.6\mathrm{km} \qquad \text{(C.9)}$$

Equations 2.15 and 2.17 can then be solved:

$$\begin{aligned}
\Delta v_a &= \sqrt{\frac{2\mu}{a} - \frac{\mu}{a_{trans}}} - \sqrt{\frac{\mu}{a}} \\
&= \sqrt{\frac{2 \times 3.986 \times 10^{14} \frac{\mathrm{m}^3}{\mathrm{s}^2}}{6883.1\mathrm{km}} - \frac{3.986 \times 10^{14} \frac{\mathrm{m}^3}{\mathrm{s}^2}}{6955.6\mathrm{km}}} - \sqrt{\frac{3.986 \times 10^{14} \frac{\mathrm{m}^3}{\mathrm{s}^2}}{6883.1\mathrm{km}}} \\
&= 39.56 \frac{\mathrm{m}}{\mathrm{s}} \qquad \text{(C.10)} \\
\Delta v_b &= \sqrt{\frac{\mu}{b}} - \sqrt{\frac{2\mu}{b} - \frac{\mu}{a_{trans}}} \\
&= \sqrt{\frac{3.986 \times 10^{14} \frac{\mathrm{m}^3}{\mathrm{s}^2}}{7028.1\mathrm{km}}} - \sqrt{\frac{2 \times 3.986 \times 10^{14} \frac{\mathrm{m}^3}{\mathrm{s}^2}}{7028.1\mathrm{km}} - \frac{3.986 \times 10^{14} \frac{\mathrm{m}^3}{\mathrm{s}^2}}{6955.6\mathrm{km}}} \\
&= 39.35 \frac{\mathrm{m}}{\mathrm{s}} \qquad \text{(C.11)}
\end{aligned}$$

Plugging the two values into Equation 2.18:

$$\Delta v_{Hohmann} = |\Delta v_a| + |\Delta v_b| = 39.56 \frac{\mathrm{m}}{\mathrm{s}} + 39.35 \frac{\mathrm{m}}{\mathrm{s}} = 78.91 \frac{\mathrm{m}}{\mathrm{s}} \qquad \text{(C.12)}$$

C.1.3 RGT to GOM

The RGT to GOM maneuver takes a satellite from 505 km to 550 km. Again we calculate the semi-major (b) and semi-minor (a) axes of the Hohmann ellipse and plug them into Equation 2.16:

$$a = r_{earth} + 505 \text{ km} = 6883.1\mathrm{km} \qquad \text{(C.13)}$$

$$b = r_{earth} + 550 \text{ km} = 6928.1\mathrm{km} \qquad \text{(C.14)}$$

$$a_{trans} = \frac{a+b}{2} = \frac{6883.1\mathrm{km} + 6928.1\mathrm{km}}{2} = 6905.6\mathrm{km} \qquad \text{(C.15)}$$

Equations 2.15 and 2.17 can then be solved:

$$\begin{aligned}
\Delta v_a &= \sqrt{\frac{2\mu}{a} - \frac{\mu}{a_{trans}}} - \sqrt{\frac{\mu}{a}} \\
&= \sqrt{\frac{2 \times 3.986 \times 10^{14} \frac{\mathrm{m}^3}{\mathrm{s}^2}}{6883.1\mathrm{km}} - \frac{3.986 \times 10^{14} \frac{\mathrm{m}^3}{\mathrm{s}^2}}{6905.6\mathrm{km}}} - \sqrt{\frac{3.986 \times 10^{14} \frac{\mathrm{m}^3}{\mathrm{s}^2}}{6883.1\mathrm{km}}} \\
&= 12.39 \frac{\mathrm{m}}{\mathrm{s}} \qquad \text{(C.16)} \\
\Delta v_a &= \sqrt{\frac{\mu}{b}} - \sqrt{\frac{2\mu}{b} - \frac{\mu}{a_{trans}}} \\
&= \sqrt{\frac{3.986 \times 10^{14} \frac{\mathrm{m}^3}{\mathrm{s}^2}}{6928.1\mathrm{km}}} - \sqrt{\frac{2 \times 3.986 \times 10^{14} \frac{\mathrm{m}^3}{\mathrm{s}^2}}{6928.1\mathrm{km}} - \frac{3.986 \times 10^{14} \frac{\mathrm{m}^3}{\mathrm{s}^2}}{6905.6\mathrm{km}}} \\
&= 12.37 \frac{\mathrm{m}}{\mathrm{s}} \qquad \text{(C.17)}
\end{aligned}$$

Plugging the two values into Equation 2.18:

$$\Delta v_{Hohmann} = |\Delta v_a| + |\Delta v_b| = 12.39 \frac{\mathrm{m}}{\mathrm{s}} + 12.37 \frac{\mathrm{m}}{\mathrm{s}} = 24.75 \frac{\mathrm{m}}{\mathrm{s}} \qquad \text{(C.18)}$$

Bibliography

[1] J. R. Wertz, D. Everett, and J. Puschell, *Space Mission Engineering: The New SMAD*. Hawthorne, California: Microcosm Press, 2011.

[2] D. A. Vallado, *Fundamentals of Astrodynamics and Applications 4th Edition*, 4th ed. Hawthorne, California: Microcosm Press, 2013.

[3] P. Fortescue, J. Stark, and G. Swinerd, *Spacecraft Systems Engineering*, 3rd ed. England: Wiley, 2003.

[4] H. Goldberg and J. Wiener, "Application for Modification of License To Construct, Deploy and Operate an NGSO Earth Exploration Satellite Service Constellation System," 2019. [Online]. Available: https://fcc.report/IBFS/SAT-MOD-20190725-00067/1816346.pdf

[5] C. D. Lippitt, D. A. Stow, and K. C. Clarke, "On the nature of models for time-sensitive remote sensing," *International Journal of Remote Sensing*, vol. 35, no. 18, pp. 6815–6841, 2014.

[6] F. Ip, J. M. Dohm, V. R. Baker, T. Doggett, A. G. Davies, R. Castaño, S. Chien, B. Cichy, R. Greeley, R. Sherwood, D. Tran, and G. Rabideau, "Flood detection and monitoring with the Autonomous Sciencecraft Experiment onboard EO-1," *Remote Sensing of Environment*, vol. 101, no. 4, pp. 463–481, 2006.

[7] D. K. Davies, S. Ilavajhala, M. M. Wong, and C. O. Justice, "Fire information for resource management system: Archiving and distributing MODIS active fire data," *IEEE Transactions on Geoscience and Remote Sensing*, vol. 47, no. 1, pp. 72–79, 2009.

[8] D. A. Stow, C. D. Lippitt, L. L. Coulter, and B. A. Davis, "Time-Sensitive Remote Sensing Systems for Post-Hazard Damage Assessment," in *Remote Sensing Theory and Time-Sensitive Information*, C. Lippitt, L. Coulter, and D. Stow, Eds. New York: Springer.

[9] J. Svejkovsky, W. Lehr, J. Muskat, G. Graettinger, and J. Mullin, "Operational utilization of aerial multispectral remote sensing during oil spill response: Lessons learned during the deepwater horizon (MC-252) spill," *Photogrammetric Engineering and Remote Sensing*, vol. 78, no. 10, pp. 1089–1102, 2012.

[10] Working Group on Natural Disaster Information Systems, "Effective Disaster Warnings - Report by the Working Group on Natural Disaster Information Systems Subcommittee on Natural Disaster Reduction," National Science and Technology Council, Tech. Rep. November, 2000. [Online]. Available: digital.library.unt.edu/ark:/67531/metadc25972

[11] NOAA, "Seven things to know about NCEI's U.S. billion-dollar disasters data."

[12] M. Mahfud, L. Farsia, N. Roesa, and S. Safrina, "Satellite Image Data as Environmental Crime Evidence in the Field of Illegal Logging," *Fiat Justisia: Jurnal Ilmu Hukum*, vol. 15, no. 3, pp. 269–286, 2021.

[13] Y. Gao, M. Skutsch, J. Paneque-Gálvez, and A. Ghilardi, "Remote sensing of forest degradation: a review," *Environmental Research Letters*, vol. 15, no. 10, 2020.

[14] J. Lynch, M. Maslin, H. Balzter, and M. Sweeting, "Choose satellites to monitor deforestation," *Nature*, vol. 496, pp. 293–294, 2013.

[15] C. Corbane, L. Najman, E. Pecoul, L. Demagistri, and M. Petit, "A complete processing chain for ship detection using optical satellite imagery," *International Journal of Remote Sensing*, vol. 31, no. 22, pp. 5837–5854, 2010.

[16] A. A. Kurekin, B. R. Loveday, O. Clements, G. D. Quartly, P. I. Miller, G. Wiafe, and K. A. Agyekum, "Operational monitoring of illegal fishing in Ghana through exploitation of satellite earth observation and AIS data," *Remote Sensing*, vol. 11, no. 3, 2019.

[17] H. C. Cubaynes, P. T. Fretwell, C. Bamford, L. Gerrish, and J. A. Jackson, "Whales from space: Four mysticete species described using new VHR satellite imagery," *Marine Mammal Science*, vol. 35, no. 2, pp. 466–491, apr 2019.

[18] S. I. Corporation, "Satellite Imagery for Wildlife Monitoring & Tracking," 2022.

[19] Planet, "PLANET IMAGERY PRODUCT SPECIFICATIONS," Planet, Tech. Rep., 2020. [Online]. Available: https://assets.planet.com/docs/Planet{_}Combined{_}Imagery{_}Product{_}Specs{_}letter{_}screen.pdf

[20] K. Murthy, M. Shearn, B. D. Smiley, A. H. Chau, J. Levine, and D. Robinson, "SkySat-1: very high-resolution imagery from a small satellite," *Sensors, Systems, and Next-Generation Satellites XVIII*, vol. 9241, no. October 2014, p. 92411E, 2014.

[21] S. Saunier, F. Done, and C. Albinet, "Technical Note on Quality Assessment for BlackSky," Earthnet Data Assessment Pilot, Tech. Rep., 2021. [Online]. Available: https://earth.esa.int/eogateway/documents/20142/37627/TechnicalNoteonQualityAssessmentforBlackSky

[22] K. Maine, C. Devieux, and P. Swan, "Overview of IRIDIUM satellite network," in *Wescon Conference Record*, 1995, pp. 483–490.

[23] Iridium, "Iridium Network," 2023. [Online]. Available: https://www.iridium.com/network/

[24] C. Rodriguez, H. Boiardt, and S. Bolooki, "CubeSat to commercial intersatellite communications: Past, present and future," in *IEEE Aerospace Conference Proceedings*, vol. 2016-June, 2016.

[25] J. Claybrook, "Feasibility Analysis on the Utilization of the Iridium Satellite Communications Network for Resident Space Objects in Low Earth Orbit," Ph.D. dissertation, Air Force Institute of Technology, 2013.

[26] A. D. Santangelo and P. Skentzos, "Utilizing the globalstar network for cubesat and small satellite communications," *33rd AIAA International Communications Satellite Systems Conference and Exhibition, ICSSC 2015*, pp. 1–8, 2015.

[27] H. Voss, A. White, and S. Brandle, "Globalstar Communication Link for CubeSats: TSAT, GEARRS1, and GEARRS2," in *29th AIAA/USU Conference on Small Satellites*, 2015. [Online]. Available: https://digitalcommons.usu.edu/cgi/viewcontent.cgi?article=3300{&}context=smallsat

[28] W. Min, L. Qiang, A. Ran, and L. Xingang, "Station-Keeping Method for GEO All-Electric Propulsion Satellite to Avoid Forbidden Firing Position," in *Proceedings - 5th International Conference on Control Science and Systems Engineering, ICCSSE 2019*, 2019, pp. 122–127.

[29] J. Gonzalez Del Amo, "Electric Propulsion at the European Space Agency (ESA)," in *Space Propulsion Conference*. ESA, 2021. [Online]. Available: https://www.epic-src.eu/wp-content/uploads/Electric-Propulsion-at-ESA-2021Virtualtiket.pdf

[30] A. Alamalhodaei, "SpaceX's acquisition of Swarm is paying off with new Starlink thrusters," 2023.

[31] Northrup Grumman, "Successful docking paves the way for future on-orbit and life-extension services through robotics," 2021. [Online]. Available: https://news.northropgrumman.com/news/releases/northrop-grumman-and-intelsat-make-history-with-docking-of-second-mission-extension-vehicle-

[32] S. Ferguson, K. Lewis, A. Siddiqi, and O. L. De Weck, "Flexible and reconfigurable systems: Nomenclature and review," *2007 Proceedings of the ASME International Design Engineering Technical Conferences and Computers and Information in Engineering Conference, DETC2007*, vol. 6 PART A, no. January, pp. 249–263, 2008.

[33] R. Akhtyamov, R. Vingerhoeds, and A. Golkar, "Identifying retrofitting opportunities for federated satellite systems," *Journal of Spacecraft and Rockets*, vol. 56, no. 3, pp. 620–629, 2019.

[34] A. Siddiqi, J. Mellein, and O. L. De Weck, "Optimal Reconfigurations for Increasing Capacity of Communication Satellite Constellations," in *46th AIAA/ASME/ASCE/AHS/ASC Structures, Structural Dynamics and Materials Conference*, Austen, Texas, 2005.

[35] O. L. De Weck, U. Scialom, and A. Siddiqi, "Optimal Reconfiguration of Satellite Constellations with the Auction Algorithm," *Acta Astronautica*, vol. 62, no. 2-3, 2008. [Online]. Available: https://www.sciencedirect.com/science/article/abs/pii/S0094576507001920

[36] C. Mcgrath and M. Macdonald, "Design Of A Reconfigurable Satellite Constellation," in *66th International Astronautical Congress, IAC2015*, Jerusalem, Israel, 2015.

[37] U.S. Geological Survey, "Landsat Missions: Imaging the Earth Since 1972," U.S. Geological Survey, Tech. Rep. April, 2020. [Online]. Available: https://landsat.usgs.gov/landsat-missions-timeline

[38] R. S. Legge and D. W. Miller, "Optimization and Valuation of Reconfigurable Satellite Constellations Under Uncertainty," Ph.D. dissertation, MIT, 2014.

[39] C. E. Lowey, "Uncertainty-Based Design Optimization and Decision Options for Responsive Maneuvering of Reconfigurable Satellite Constellations by," Ph.D. dissertation, MIT, 2022.

[40] A. N. Straub, "Expanded Tradespace Analysis and Operational Considerations for Reconfigurable Satellite Constellations by," Ph.D. dissertation, MIT, 2020.

[41] S. J. Morgan, "Reconfigurable Satellite Constellations for Mobile Target Tracking," Ph.D. dissertation, MIT, 2021. [Online]. Available: https://dspace.mit.edu/handle/1721.1/139043

[42] S. W. Paek and O. Ladislas De Weck, "Concurrent design optimization of earth observation Satellites and reconfigurable constellations," *Journal of the British Interplanetary Society*, vol. 70, pp. 19–35, 2017. [Online]. Available: https://www.researchgate.net/publication/319302797

[43] S. W. Paek, S. Kim, and O. de Weck, "Optimization of reconfigurable satellite constellations using simulated annealing and genetic algorithm," *Sensors (Switzerland)*, vol. 19, no. 4, feb 2019.

[44] S. B. Hong, H. Na, and J. Ahn, "Assessment of architectural options for a dual-mode disaster monitoring constellation supported by on-orbit propellant depots," *Proceedings of the Institution of Mechanical Engineers, Part G: Journal of Aerospace Engineering*, vol. 228, no. 11, pp. 2108–2122, 2014.

[45] X. He, H. Li, L. Yang, and J. Zhao, "Reconfigurable Satellite Constellation Design for Disaster Monitoring Using Physical Programming," *International Journal of Aerospace Engineering*, vol. 2020, 2020.

[46] A. B. Hoskins, H. R. Medal, and E. Rashidi, "Satellite constellation design for forest fire monitoring via a stochastic programing approach," *Naval Research Logistics*, vol. 64, no. 8, pp. 642–661, dec 2017.

[47] Y. Chen, V. Mahalec, Y. Chen, X. Liu, R. He, and K. Sun, "Reconfiguration of satellite orbit for cooperative observation using variable-size multi-objective differential evolution," *European Journal of Operational Research*, vol. 242, no. 1, pp. 10–20, apr 2015.

[48] J. R. Wertz, "Coverage, Responsiveness, and Accessibility for Various "Responsive Orbits"," in *3rd Responsive Space Conference*. El Segundo, California: AIAA, apr 2005.

[49] T. Li, J. Xiang, Z. Wang, and Y. Zhang, "Circular revisit orbits design for responsive mission over a single target," *Acta Astronautica*, vol. 127, pp. 219–225, oct 2016.

[50] S. P. Ingraham, "DYNAMIC CONSTELLATION TASKING AND MANAGEMENT," Ph.D. dissertation, Air Force Institute of Technology, 2013. [Online]. Available: https://scholar.afit.edu/etd/831

[51] P. Sengupta, S. R. Vadali, and K. T. Alfriend, "Semi-Analytical Approach to Target Access in the Responsive Space Problem," in *6th Responsive Space Conference*, 2008.

[52] ——, "Satellite orbit design and maintenance for terrestrial coverage," *Journal of Spacecraft and Rockets*, vol. 47, no. 1, pp. 177–187, 2010.

[53] M. Xu and T. Tan, "A New Constellation Architecture for Practical Responsive Revisiting," *The Japan Society for Aeronautical and Space Sciences*, vol. 57, no. 3, 2014.

[54] X. Yu, K. Liu, and Q. Chen, "Constellation design for responsive visiting based on ground track adjustment," in *Proceedings of the Institution of Mechanical Engineers, Part G: Journal of Aerospace Engineering*, vol. 232. SAGE Publications Ltd, sep 2018, pp. 2300–2316.

[55] M. Navabi and H. B. Khamseh, "Improving in-orbit responsiveness of low earth orbit sun-synchronous satellites by selection of ground segment location," *Proceedings of the Institution of Mechanical Engineers, Part G: Journal of Aerospace Engineering*, vol. 227, no. 5, pp. 766–777, may 2012.

[56] C. A. Hinds, "A Pareto-Frontier Analysis Of Performance Trends For Small Regional Coverage LEO Constellation Systems," Ph.D. dissertation, California Polytechnic State University, 2014.

[57] P. T. Grogan and J. L. Stern, "COORDINATING OBSERVATION AT GLOBAL AND LOCAL SCALES: SERVICE-ORIENTED PLATFORM TO EVALUATE MISSION ARCHITECTURES." [Online]. Available: https://github.com/code-lab-org/cvis-propagate.

[58] S. Nag, J. LeMoigne, D. Miller, and O. de Weck, "A Framework for Orbital Performance Evaluation in Distributed Space Missions for Earth Observation," in *IEEE Aerospace Conference*, Big Sky, Montana, 2015.

[59] S. Nag, A. S. Li, and J. H. Merrick, "Scheduling algorithms for rapid imaging using agile Cubesat constellations," *Advances in Space Research*, vol. 61, no. 3, pp. 891–913, feb 2018.

[60] S. Nag, J. Lemoigne, and O. De Weck, "Cost and risk analysis of small satellite constellations for earth observation," *IEEE Aerospace Conference Proceedings*, 2014.

[61] L. A. Singh, W. R. Whittecar, M. D. DiPrinzio, J. D. Herman, M. P. Ferringer, and P. M. Reed, "Low cost satellite constellations for nearly continuous global coverage," *Nature Communications*, vol. 11, no. 1, dec 2020.

[62] K. A. Sugrue, "Optimal Orbital Coverage of Theater Operations and Targets," Ph.D. dissertation, Air Force Institute of Technology, 2007. [Online]. Available: https://scholar.afit.edu/etd/2994

[63] D. Mortari, "Flower Constellations as Rigid Objects in Space," *ACTA Futura*, vol. 2, pp. 7–22, 2006.

[64] D. Mortari and C. Bruccoleri, "The Flower Constellations The Theory of Connections View," *Article in Journal of the Astronautical Sciences*, 2004. [Online]. Available: https://www.researchgate.net/publication/241677742

[65] D. Mortari, M. De Sanctis, and M. Lucente, "Design of flower constellations for telecommunication services," *Proceedings of the IEEE*, vol. 99, no. 11, pp. 2008–2019, 2011.

[66] M. E. Avendaño, J. J. Davis, and D. Mortari, "The 2-D lattice theory of Flower Constellations," *Celestial Mechanics and Dynamical Astronomy*, vol. 116, no. 4, pp. 325–337, 2013.

[67] J. K. Krueger, D. Selva, M. W. Smith, and J. Keesee, "Spacecraft and constellation design for a continuous responsive imaging system in space," in *AIAA Space 2009 Conference and Exposition*. American Institute of Aeronautics and Astronautics Inc., 2009.

[68] S. M. Minic, "Collection Planning Management : Multi-Satellite Collection Scheduling," MDA, Tech. Rep. February, 2016. [Online]. Available: http://cradpdf.drdc-rddc.gc.ca/PDFS/unc235/p804216{_}A1b.pdf

[69] K. Fall, "A Delay-Tolerant Network Architecture for Challenged Internets," in *SIGCOMM '03: Proceedings of the 2003 conference on Applications, technologies, architectures, and protocols for computer communications*, Karlsruhe, Germany, 2003.

[70] A. K. Kennedy, "Planning and Scheduling for Earth-Observing Small Satellite Constellations," Ph.D. dissertation, MIT, 2018.

[71] S. Kaul, R. Yates, and M. Gruteser, "Real-time status: How often should one update?" in *Proceedings - IEEE INFOCOM*, 2012, pp. 2731–2735.

[72] W. Grunwald, "Decentralized On-board Planning and Scheduling for Crosslink-enabled Earth-observing Constellations," Ph.D. dissertation, MIT, 2019.

[73] B. G. Holden II, "Onboard Distributed Replanning for Crosslinked Small Satellite Constellations," Ph.D. dissertation, MIT, 2019.

[74] F. Yao, J. Li, Y. Chen, X. Chu, and B. Zhao, "Task allocation strategies for cooperative task planning of multi-autonomous satellite constellation," *Advances in Space Research*, vol. 63, no. 2, pp. 1073–1084, jan 2019.

[75] D. Selva, A. Golkar, O. Korobova, I. Lluch i Cruz, P. Collopy, and O. L. De Weck, "Distributed earth satellite systems: What is needed to move forward?" *Journal of Aerospace Information Systems*, vol. 14, no. 8, pp. 412–438, 2017.

[76] I. Lluch, U. Pica, P. Grogan, and A. Golkar, "Simulating a Proactive Ad-Hoc Network Protocol for Federated Satellite Systems," in *Proceedings from the 2015 IEEE Aerospace Conference*, Big Sky, Montana, 2015.

[77] J. A. Ruiz De Azúa, A. Calveras, and A. Camps, "Internet of Satellites (IoSat): An interconnected Space Paradigm," in *5 th Federated and Fractionated Satellite Systems Workshop*, Toulouse, France, 2017.

[78] J. A. De Azua, A. Calveras, and A. Camps, "Internet of Satellites (IoSat): Analysis of Network Models and Routing Protocol Requirements," *IEEE Access*, vol. 6, pp. 20 390–20 411, apr 2018.

[79] J. A. Ruiz-De-Azua, V. Ramirez, H. Park, A. C. Auge, and A. Camps, "Assessment of Satellite Contacts Using Predictive Algorithms for Autonomous Satellite Networks," *IEEE Access*, vol. 8, pp. 100 732–100 748, 2020.

[80] J. A. Ruiz-De-Azua, A. Camps, and A. Calveras Auge, "Benefits of Using Mobile Ad-Hoc Network Protocols in Federated Satellite Systems for Polar Satellite Missions," *IEEE Access*, vol. 6, pp. 56 356–56 367, 2018.

[81] A. Camps, A. Golkar, A. Gutierrez, J. Ruiz de Azua, J. Munoz-Martin, L. Fernandez, C. Diez, A. Aguilella, S. Briatore, R. Akhtyamov, and N. Garzaniti, "Fsscat, the 2017 Copernicus Masters' "Esa Sentinel Small Satellite Challenge" Winner: A Federated Polar and Soil Moisture Tandem Mission Based on 6U

Cubesats," in *IGARSS 2018 - 2018 IEEE International Geoscience and Remote Sensing Symposium*, 2018.

[82] J. Ruiz-de Azua, L. Fernandez, J. Munoz, M. Badia, R. Castella, C. Diez, A. Aguilella, S. Briatore, N. Garzaniti, A. Calveras, A. Golkar, and A. Camps, "Proof-Of-Concept Of A Federated Satellite System Between Two 6-Unit CubeSats For Distributed Earth Observation Satellite Systems," in *IGARSS 2019 - 2019 IEEE International Geoscience and Remote Sensing Symposium*, Yokohama, Japan, 2019. [Online]. Available: https://ieeexplore.ieee.org/abstract/document/8900099

[83] H. Kim and Y. K. Chang, "Mission scheduling optimization of SAR satellite constellation for minimizing system response time," *Aerospace Science and Technology*, vol. 40, pp. 17–32, jan 2015.

[84] P. Wang, G. Reinelt, P. Gao, and Y. Tan, "A model, a heuristic and a decision support system to solve the scheduling problem of an earth observing satellite constellation," in *Computers and Industrial Engineering*, vol. 61, sep 2011, pp. 322–335.

[85] G. Feng, W. Li, and H. Zhang, "Geomagnetic energy approach to space debris deorbiting in a low earth orbit," *International Journal of Aerospace Engineering*, vol. 2019, 2019.

[86] X. Niu, H. Tang, and L. Wu, "Satellite scheduling of large areal tasks for rapid response to natural disaster using a multi-objective genetic algorithm," *International Journal of Disaster Risk Reduction*, vol. 28, pp. 813–825, jun 2018.

[87] A. Golkar, "Federated Satellite Systems (FSS): A Vision Towards an Innovation in Space Systems Design," in *9th IAA Symposium on Small Satellites for Earth Observation*, Berlin, Germany, 2013.

[88] A. Golkar and I. Lluch I Cruz, "The Federated Satellite Systems paradigm: Concept and business case evaluation," *Acta Astronautica*, vol. 111, pp. 230–248, 2015.

[89] I. L. Cruz and A. Golkar, "Adopting the Federated Satellite Systems paradigm for Earth observation An architecting framework," in *66th International Astronautical Congress*, Jerusalem, Israel, 2015.

[90] I. Lluch and A. Golkar, "Satellite-to-satellite coverage optimization approach for opportunistic inter-satellite links," in *IEEE Aerospace Conference Proceedings*. IEEE Computer Society, 2014.

[91] R. Akhtyamov, I. L. I. Cruz, H. Matevosyan, D. Knoll, U. Pica, M. Lisi, and A. Golkar, "An implementation of Software Defined Radios for federated aerospace networks: Informing satellite implementations using an inter-balloon communications experiment," *Acta Astronautica*, vol. 123, pp. 470–478, jun 2016.

[92] I. Sanad and D. G. Michelson, "A Framework for Heterogeneous Satellite Constellation Design for Rapid Response Earth Observations," in *IEEE Aerospace Conference Proceedings*, vol. 2019-March. IEEE Computer Society, mar 2019.

[93] I. Sanad, "Reduction Of Earth Observation System Response Time Using Relay Satellite Cconstellations," Ph.D. dissertation, University of British Columbia, 2020.

[94] J. Li, H. Chen, and N. Jing, "A data transmission scheduling algorithm for rapid-response earth-observing operations," *Chinese Journal of Aeronautics*, vol. 27, no. 2, pp. 349–364, 2014.

[95] S. Chan, A. T. Samuels, N. B. Shah, J. E. Underwood, and O. L. De Weck, "Optimization of Hybrid Satellite Constellations using Multiple Layers and Mixed Circular-Elliptical Orbits," in *22nd AIAA International Communications Satellite Systems Conference*, Monterey, California, 2004.

[96] P. Garcia Buzzi and D. Selva, "Evolutionary formulations for design of heterogeneous Earth observing constellations," in *2020 IEEE Aerospace Conference*, 2020.

[97] D. Vallado, *Fundamentals of Astrodynamics and Applications*. Hawthorne, California: Microcosm Press, 2007.

[98] J. L. Cano Rodriguez, "Poliastro 0.16," 2021. [Online]. Available: https://github.com/poliastro/poliastro

[99] G. Maral and M. Bousquet, *Satellite communications systems*, 5th ed. Wiley, 2009.

[100] T. A. Dahl and B. C. Gunter, "An Evaluation of Spacecraft Pointing Requirements for Optically Linked Satellite Systems AE 8900 MS Special Problems Report Space Systems Design Lab (SSDL)," Tech. Rep., 2017.

[101] E. W. Dijkstra, "Numerische Mathematik," *Numerische Mathematik*, vol. 1, pp. 269–271, 1959.

[102] J. Walker, "Continuous Whole-Earth Coverage by Circular-Orbit Satellite Patterns," Royal Aircraft Establishment, Tech. Rep., 1977.

[103] Ansys, "Ansys STK."

[104] S. P. Shuster, "A Survey and Performance Analysis of Orbit Propagators for LEO, GEO, and Highly Elliptical Orbits," Ph.D. dissertation, Utah State University, 2017. [Online]. Available: https://digitalcommons.usu.edu/etd/6510

[105] ESA, "Newcomers Earth Observation Guide," 2020. [Online]. Available: https://business.esa.int/newcomers-earth-observation-guide

[106] "Blacksky Satellite," 2022. [Online]. Available: https://apollomapping.com/blacksky-satellite-imagery

[107] EoPortal, "SkySat," 2022. [Online]. Available: https://directory.eoportal.org/web/eoportal/satellite-missions/s/skysat

[108] NOAA, "Hydrazine," 1999. [Online]. Available: https://cameochemicals.noaa.gov/chris/HDZ.pdf

[109] J. R. I. Shell, "Imaging payload performance considerations for on-orbit servicing and active debris removal," in *Advanced Maui Optical and Space Surveillance Technologies Conference (AMOS)*, Maui, Hawaii, 2018. [Online]. Available: https://amostech.com/TechnicalPapers/2018/Space-Based{_}Assets/Shell.pdf

[110] S. Zlatanova and J. Li, *Geospatial information technology for emergency response*. London: Taylor & Francis, 2008.

[111] P. Showalter and Y. Lu, *Geospatial Techniques in Urban Hazard and Disaster Analysis*, 2nd ed. New York: Springer, 2010.

[112] Planet, "High-Resolution Imagery with Planet Satellite Tasking," 2023.

[113] N. E. Data, "LANCE: NASA Near Real-Time Data and Imagery," 2023.

[114] B. Defense, "To maximize Ukraine coverage, BlackSky shifted orbits for its newest satellites," 2022.

[115] BlackSky, "BLACKSKY ACHIEVES WORLD'S HIGHEST REVISIT, TIME-DIVERSE DAWN-TO-DUSK SATELLITE CONSTELLATION WITH THREE SUCCESSFUL LAUNCHES IN THREE WEEKS," 2021.

[116] D. Werner, "Earth imagery companies reimagine satellite tasking," 2022.

[117] A. Corp, "How to obtain the SSCM software."

[118] E. M. Mahr, "Small Satellite Cost Model 2019 (SSCM19) User's Manual," The Aerospace Corporation, Tech. Rep., 2019.

[119] E. Mahr, A. Tu, and A. Gupta, "Development of the Small Satellite Cost Model 2019 (SSCM19)," *IEEE Aerospace Conference Proceedings*, vol. 2019, 2020.

[120] "SSCM Database." [Online]. Available: https://aerospace.org/sscm-database

[121] G. Farley, "Seattle-based BlackSky to sell affordable, real time space photos," 2016.

[122] SpaceX, "Falcon Vehicles Capabilities & Services," 2022. [Online]. Available: https://www.spacex.com/media/Capabilities{&}Services.pdf

[123] Rocket Lab, "Launch: Payload User's Guide," 2020. [Online]. Available: https://www.rocketlabusa.com/assets/Uploads/Rocket-Lab-Launch-Payload-Users-Guide-6.5.pdf

[124] J. Foust, "Rocket Lab to launch remaining NASA TROPICS satellites," 2022.

[125] EoPortal, "Satellite Missions of Rocket lab," 2018. [Online]. Available: https://www.eoportal.org/other-space-activities/rocket-lab{#}love-at-first-insight

[126] M. Aorpimai and P. L. Palmer, "Repeat-groundtrack orbit acquisition and maintenance for earth-observation satellites," *Journal of Guidance, Control, and Dynamics*, vol. 30, no. 3, pp. 654–659, 2007.

[127] A. R. Washburn, "Earth Coverage by Satellites in Circular Orbit," *Calhoun: The NPS Institutional Archive*, pp. 1–18, 2013.

[128] S. Jain, K. Fall, and R. Patra, "Routing in a delay tolerant network," in *SIGCOMM '04: Proceedings of the 2004 conference on Applications, technologies, architectures, and protocols for computer communications*, 2004, p. 145.

[129] A. Reuther, J. Kepner, C. Byun, S. Samsi, W. Arcand, D. Bestor, B. Bergeron, V. Gadepally, M. Houle, M. Hubbell, M. Jones, A. Klein, L. Milechin, J. Mullen, A. Prout, A. Rosa, C. Yee, and P. Michaleas, "Interactive Supercomputing on 40,000 Cores for Machine Learning and Data Analysis," in *2018 IEEE High Performance Extreme Computing Conference, HPEC 2018*, 2018, pp. 17–22.

[130] M. Barbehenn, "A Note on the Complexity of Dijkstra's Algorithm for Graphs with Weighted Vertices," *IEEE Transactions on Computers*, vol. 47, no. 2, 1998.

[131] "Space Sustainability Rating." [Online]. Available: https://spacesustainabilityrating.org/

[132] M. Slavin, M. Jah, and D. Wood, "Developing Detectability, Identifiability, and Trackability Metrics to Evaluate Sustainability of Space Missions," in *AIAA Ascend*, 2021.

[133] ATLAS, "ATLAS Antenna Network Spec Sheet." [Online]. Available: https://atlasground.com/wp-content/uploads/2022/02/ATLAS-Network-Map{_}Specs-Feb{_}2022.pdf

[134] Spaceteq, "X band transmit antenna x horn-18/23," Tech. Rep., 2022. [Online]. Available: https://www.spaceteq.co.za/{_}files/ugd/b9bb07{_}96e5ef72e2ee443cb840d127b52c78d9.pdf

[135] MOOG, "Monopropellant thrusters," 2018. [Online]. Available: https://www.moog.com/content/dam/moog/literature/Space{_}Defense/spaceliterature/propulsion/moog-MonopropellantThrusters-Datasheet.pdf

[136] ArianeGroup, "Surface tension tank ost 31/0." [Online]. Available: https://www.space-propulsion.com/brochures/propellant-tanks/104-177lt-n2h4-tank-ost-31-0.pdf

[137] MOOG, "COMET Datasheet," 2021. [Online]. Available: https://www.moog.com/content/dam/moog/literature/Space{_}Defense/spaceliterature/space-vehicles/moog-comet-datasheet.pdf

[138] SpaceX, "Falcon User's Guide," 2021. [Online]. Available: https://www.spacex.com/media/falcon-users-guide-2021-09.pdf